Aritra Acharyya
Arindam Biswas
Hiroshi Inokawa   *Editors*

New Horizons in Millimeter-Wave, Infrared and Terahertz Technologies

Springer

Lecture Notes in Electrical Engineering

Volume 953

The book series *Lecture Notes in Electrical Engineering* (LNEE) publishes the latest developments in Electrical Engineering—quickly, informally and in high quality. While original research reported in proceedings and monographs has traditionally formed the core of LNEE, we also encourage authors to submit books devoted to supporting student education and professional training in the various fields and applications areas of electrical engineering. The series cover classical and emerging topics concerning:

- Communication Engineering, Information Theory and Networks
- Electronics Engineering and Microelectronics
- Signal, Image and Speech Processing
- Wireless and Mobile Communication
- Circuits and Systems
- Energy Systems, Power Electronics and Electrical Machines
- Electro-optical Engineering
- Instrumentation Engineering
- Avionics Engineering
- Control Systems
- Internet-of-Things and Cybersecurity
- Biomedical Devices, MEMS and NEMS

For general information about this book series, comments or suggestions, please contact leontina.dicecco@springer.com.

To submit a proposal or request further information, please contact the Publishing Editor in your country:

China

Jasmine Dou, Editor (jasmine.dou@springer.com)

India, Japan, Rest of Asia

Swati Meherishi, Editorial Director (Swati.Meherishi@springer.com)

Southeast Asia, Australia, New Zealand

Ramesh Nath Premnath, Editor (ramesh.premnath@springernature.com)

USA, Canada

Michael Luby, Senior Editor (michael.luby@springer.com)

All other Countries

Leontina Di Cecco, Senior Editor (leontina.dicecco@springer.com)

** This series is indexed by EI Compendex and Scopus databases. **

Aritra Acharyya · Arindam Biswas ·
Hiroshi Inokawa
Editors

New Horizons
in Millimeter-Wave, Infrared
and Terahertz Technologies

Editors
Aritra Acharyya 🆔
Electronics and Communication
Engineering
Cooch Behar Government Engineering
College
Cooch Behar, India

Arindam Biswas
School of Mines and Metallurgy
Kazi Nazrul University
Asansol, India

Hiroshi Inokawa
Research Institute of Electronics
Shizuoka University
Hamamatsu, Japan

Preface

The scope of this book includes a significantly long portion of the electromagnetic spectrum, starting from the mm-waves (i.e., 30 GHz) and extended up to the end of the near-IR spectrum (i.e., 450 THz). Most significant aspect of this portion of the electromagnetic spectrum is that it includes a frequency regime where the gradual technological transition from electronics to photonics can be observed; this frequency regime is nothing but the THz frequency spectrum (0.3–10 THz). This book provides detailed analysis, description, and discussion of some recently developed technologies under this extended frequency spectrum. Especially, the emphasis is given to the state-of-the-art and upcoming research going on at various parts of the globe on THz science and technology. Some significant contents of this book are Ku-band substrate integrated waveguide, gallium nitride terahertz integrated power module, heterostructure electro-optic modulator, graphene nanoribbon field effect transistors, birhythmic behavior in dual loop optielectronic oscillators, infrared sensor-based object detection circuit for computer vision applications, bandwidth management techniques in 6th generation mobile communication, noise performance of millimeter-wave impact avalanche transit time (IMPATT) oscillators, high frequency passive circuits, asymmetric junctionless dual material double gate MOSFETs, gate all round tunneling field-effect transistor (GAA-TFET) based on graphene nanoribbon (GNR), generalized distribution functions in heavily doped nanomaterials at terahertz frequencies, influence of THz frequency on the gate capacitance in two-dimensional quantum-well field effect transistors, alternative scheme of quantum optical superfast tri-state controlled-NOT gate using frequency encoding principle of light with semiconductor optical amplifier, use of frequency encoding principle for implementing nano-photonic ultrafast tri-state

Pauli X gate, etc. This book covers a very vast audience from basic science to engineering and technology experts as well as learners. This could eventually work as a textbook for engineering students or science masters programs and for researchers.

Cooch Behar, India   Aritra Acharyya
Asansol, India   Arindam Biswas
Shizuoka, Japan   Hiroshi Inokawa

Contents

Editors and Contributors

About the Editors

Dr. Aritra Acharyya is currently working at Department of Electronics and Communication Engineering, Cooch Behar Government Engineering College, Harinchawra, Ghughumari, West Bengal, 736170, India, as Assistant Professor. He was born in 1986. He received B.E. and M.Tech. degrees from IIEST, Shibpur, India, and Institute of Radio Physics and Electronics, University of Calcutta, India, in the years 2007 and 2010 respectively. Finally he obtained Ph.D. degree from Institute of Radio Physics and Electronics, University of Calcutta, in the year 2016. His research interests are high frequency semiconductor devices, nano-structures, semiconductor physics, transport phenomena, quantum mechanics, optoelectronics, etc. He has published 88 research papers in peer reviewed national and international journals, 70 research papers in national and international conference proceedings, and several book chapters. He also authored and edited 07 and 05 number of books respectively.

Dr. Arindam Biswas Assistant Professor, School of Mines and Metallurgy, Kazi Nazrul University, Asansol, Burdwan, West Bengal, 713340, India. He was born in West Bengal, India in 1984. He received M.Tech. degree in Radio Physics and Electronics from University of Calcutta, India in 2010 and Ph.D. from NIT Durgapur in 2013. He was a Post-Doctoral Researcher at Pusan National University, South Korea with prestigious BK21PLUS Fellowship, Republic of Korea. He got Visiting Professor at Research Institute of Electronics, Shizouka University, Japan. He has been selected for IE(I) Young Engineer Award: 2019–2020 in Electronics and Telecommunication Engineering discipline, Institute of Engineers, India. Dr. Biswas has 10 years' of experience in teaching research and administration. Presently Dr. Biswas is working as an Assistant Professor in School of Mines and Metallurgy at Kazi Nazrul University, Asansol, West Bengal, India. He has 48 technical paper in different journals and 30 conference proceedings and six books, one edited volume and one book chapter with international repute. Dr. Biswas received research grant from Science and Engineering Research Board, Govt of India, under Early Career Research Scheme for research in Terahertz based GaN Source. He also received Research Grant from Centre of Biomedical Engineering, Tokoyo Medical and Dental University in association with RIE, Shizouka University, Japan for study of biomedical THz Imaging based on WBG semiconductor IMPATT Source. Presently Dr. Biswas is serving as an Associate Editor of Cluster Computing, Springer (SCI Indexed) and as a guest editor of Nanoscience and Nanotechnology-Asia (Scopus Indexed), Recent Patent in Material Science (Scopus Indexed), Benthamscience Publisher. Dr. Biswas has produced four Ph.D. students in different topics of applied optics and high frequency semiconductordevice. He has organized and chaired difference International Conferences in India and abroad. His research interest is in carrier transport in low dimensionalsystem and electronic device, non-linear optical communication, THz Semiconductor Source. Dr. Biswas acted as reviewer for reputed journals, and member of the Institute of Engineers (India) and Regular Fellow of Optical Society of India (India).

Dr. Hiroshi Inokawa Professor, Research Institute of Electronics, Shizuoka University, 3-5-1 Johoku, Naka-ku, Hamamatsu 432-8011, Japan. He received B.S., M.S., and Ph.D. degrees in electrical engineering from Kyoto University, Japan in 1980, 1982 and 1985, respectively. In 1985, he joined the Atsugi Electrical Communications Laboratories, Nippon Telegraph and Telephone Corporation (NTT), Kanagawa, Japan. Since then, he has been engaged in the research and development of scaled-down CMOS devices and silicon single-electron devices. During the course of his research, he invented the basic structure of FinFET in 1989 and single-electron multiple-valued logic in 2001, and received IEEE International Symposium on Multiple-Valued Logic (ISMVL) Outstanding Contributed Paper Awards in 2004 and 2006, Director's Award of NTT Basic Research Laboratories in 2004, 28th JSAP Award for the Best Original Paper in 2006, etc. In 2006, he became a professor of the Research Institute of Electronics, Shizuoka University, Hamamatsu, Japan, where he has been studying nanodevices for advanced circuits and systems. His recent work on SOI MOSFET single-photon detector was introduced by IEEE Photonics Journal in 2012 as a Breakthrough in Photonics. Prof. Inokawa is a member of the Institute of Electrical and Electronics Engineers (IEEE), the Japan Society of Applied Physics (JSAP), the Institute of Electronics, Information and Communication Engineers of Japan (IEICE), and the Institute of Electrical Engineers of Japan (IEEJ). He has served as a JSAP board member of representative in 2001–2003, an editor of JJAP in 2007–2013, the chair of the IEEJ survey committee of silicon nanosystem integration technology in 2009–2011, an advisory committee member of NICT Japan Trust International Research Cooperation Program in 2006–2009, a researcher of National Institute of Science and Technology Policy (NISTEP) in 2002–present, etc.

Contributors

Acharjee Pratik University of Engineering and Management, New Town, Kolkata, India

Acharyya Aritra Department of Electronics and Communication Engineering, Cooch Behar Government Engineering College, Harinchawra, Ghughumari, Cooch Behar, West Bengal, India

Banerjee J. P. Institute of Radio Physics and Electronics, University of Calcutta, Kolkata, West Bengal, India

Basak Arighna Department of Electronics and Communication Engineering, Brainware University, Barasat, India

Biswas Arindam Centre for Organic Spin-tronics and Optoelectronics Devices (COSOD) and Mining Engineering Department, Kazi Nazrul University, Asansol, Burdwan, West Bengal, India

Chakraborty P. K. Department of Electronics and Communication Engineering, Indian Institute of Technology, Kharagpur, West Bengal, India

Chattaopadhyay Rupanjana Techno Engineering College, Banipur, Habra, West Bengal, India

Chatterjee Aritrya University of Engineering and Management, New Town, Kolkata, India

Choudhury Kankana Department of Electronics and Communication Engineering, Siliguri Institute of Technology, Siliguri, West Bengal, India

Debbarma N. Department of Computer Science and Engineering, National Institute of Technology, Agartala, Tripura, India

Debbarma S. Department of Computer Science and Engineering, National Institute of Technology, Agartala, Tripura, India

Debnath Pampa Department of Electronics and Communication Engineering, RCC Institute of Information Technology, Kolkata, India

Dey Ayan Department of Physics, The University of Burdwan, Golapbag, Burdwan, West Bengal, India

Deyasi Arpan Department of Electronics and Communication Engineering, RCC Institute of Information Technology, Kolkata, India

Dhar R. Department of Electronics Engineering, IIT (BHU), Varanasi, Uttar Pradesh, India

Ganguly Anuva Department of Electronics and Communication Engineering, Dr. Sudhir Chandra Sur Institute of Technology and Sports Complex, Dum Dum,

Kolkata, West Bengal, India;
Institute of Radio Physics and Electronics, University of Calcutta, Kolkata, India

Gayen Dilip Kumar Department of Computer Science & Engineering, College of Engineering and Management, Kolaghat, KTPP Township, Purba Medinipur, West Bengal, India

Ghatak K. P. Department of Basic Science and Humanities, Institute of Engineering and Management, Kolkata, West Bengal, India

Ghosal Anirudhha Institute of Radio Physics and Electronics, University of Calcutta, Kolkata, West Bengal, India

Ghosh Dia Department of Electronics and Communication Engineering, Siliguri Institute of Technology, Siliguri, West Bengal, India

Ghosh Shankar K. Department of Computer Science and Engineering, Presidency University, Bangalore, India

Goswami Jayabrata Netaji Subhas Open University, Bidhannagar, Kolkata, West Bengal, India

Hazra Snigdha Department of Physics, The University of Burdwan, Burdwan, West Bengal, India

Inokawa Hiroshi Research Institute of Electronics, Shizuoka University, Hamamatsu, Japan

Kar Subal Institute of Radio Physics and Electronics, University of Calcutta, Kolkata, India

Majumder Avirup University of Engineering and Management, New Town, Kolkata, India

Mistri Hiranmay Department of Electronics and Communication Engineering, Ramkrishna Mahato Government Engineering College, Purulia, West Bengal, India

Mondal Ujjwal Department of Applied Physics, University of Calcutta, Kolkata, India

Mukherjee Arindum Department of Electronics and Communication Engineering, Central Institute of Technology, Kokrajhar, Assam, India

Mukhopadhyay S. J. Department of Electronics and Communication Engineering, Dr. Sudhir Chandra Sur Institute of Technology & Sports Complex, Kolkata, West Bengal, India

Mukhopadhyay Sourangshu Department of Physics, The University of Burdwan, Golapbag, Burdwan, West Bengal, India

Paitya Nitai Department of Computer Science and Engineering, Sikkim Manipal Institute of Technology, East Sikkim, India

Pal J. Department of Physics, Meghnad Saha Institute of Technology, Kolkata, West Bengal, India

Pal Srishti Department of Electronics and Communication Engineering, Siliguri Institute of Technology, Siliguri, West Bengal, India

Roy Shayantan Kr Department of Electronics and Communication Engineering, Siliguri Institute of Technology, Siliguri, West Bengal, India

Saha Tanushree Techno Engineering College, Banipur, Habra, West Bengal, India

Sarkar Angsuman Department of Electronics and Communication Engineering, Kalyani Government Engineering College, Kalyani, India

Satoh Hiroaki Research Institute of Electronics, Shizuoka University, Hamamatsu, Japan

Tewari Babul P. Department of Computer Science and Engineering, Indian Institute of Information Technology, Bhagalpur, India

Introduction to Millimeter-Wave, Infrared and Terahertz Technologies

Aritra Acharyya, Arindam Biswas, and Hiroshi Inokawa

Abstract In this preparatory chapter, brief introductions to the state-of-the-art millimeter-wave (mm-wave), infrared (IR) and terahertz (THz) technologies are given. Short descriptions of prospective applications of mm-wave, IR and THz signals have also been included in this chapter. A chapter-wise overview of the entire book has been incorporated at the end of this introductory chapter.

1 Introduction

The subject matter of this book covers three major frequency bands of the electromagnetic spectrum, such as millimeter-wave (mm-wave), infrared (IR) and terahertz (THz) spectrums. The mm-wave spectrum begins at 30 GHz and it is extended up to 300 GHz; the wavelength range of 1–10 mm falls within this spectrum. On the other hand, the IR spectrum starts from 0.3 THz and ends roughly at 430 THz. As a whole, the IR spectrum is a very wide frequency regime (wavelength range is 0.7–1000 μm). The IR spectrum is conventionally divided into three separate sub-spectrums, such as (i) near-IR spectrum having the wavelength range of 2.5–25 μm (i.e. frequency range of 120–428.57 THz), (ii) mid-IR spectrum having the wavelength range of 0.7–2.5 μm (i.e. frequency range of 12–120 THz), and (iii) far-IR spectrum having the wavelength range of 25–1000 μm (i.e. frequency range of 0.3–12 THz). These sub-spectrums like near-, mid- and far-IR regions are named with respect to their

A. Acharyya (✉)
Department of Electronics and Communication Engineering, Cooch Behar Government Engineering College, Harinchawra, Ghughumari, Cooch Behar, West Bengal 736170, India
e-mail: ari_besu@yahoo.co.in

A. Biswas
Centre for Organic Spin-tronics and Optoelectronics Devices (COSOD) and Mining Engineering Department, Kazi Nazrul University, Asansol, Burdwan, West Bengal 713340, India

H. Inokawa
Research Institute of Electronics, Shizuoka University, Hamamatsu 4328011, Japan
e-mail: inokawa.hiroshi@shizuoka.ac.jp
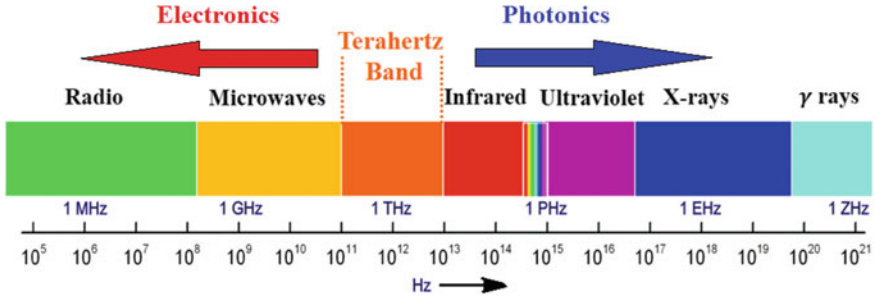
Fig. 1 Electromagnetic spectrum showing the position of the THz band [1]

close proximity to the visible spectrum of light (i.e. 0.39–0.7 µm). Now, the THz region is the portion of the electromagnetic spectrum (0.3–10 THz), which begins at the end of the mm-wave spectrum and extends up to far-IR regime. The left side of the THz spectrum belongs to the world of 'Electronics' and the world of 'Photonics' starts from the right edge of this spectrum. Figure 1 depicts an elaborate illustration of the electromagnetic spectrum [1]. In Fig. 1, the entire broad frequency band 1–300 GHz is denoted as microwaves; however, the spectrum 1–30 GHz is specifically known as microwaves and the spectrum 30–300 GHz is known as mm-waves.

The mm-wave spectrum is highly demanding for future wireless communication technologies [2]. Presence of three low absorption window frequencies, such as 94, 140 and 220 GHz (Fig. 2) makes it a highly attractive spectrum for wideband, long-haul wireless communication applications. In order to support ultra-high data rates, 5th generation (5G) technology is currently utilizing the mm-wave band of 24–86 GHz. Less costly mm-wave links may also replace comparatively costlier fibre optic links between mobile base stations. In future, mm-wave spectrum will be utilized in ultra high definition (UHD) video transmission, IEEE 802.11ad WiGig technology, next generation satellite communication links, wideband and high definition and high fidelity video and audio transmission in virtual reality devices, etc. However, despite having several advantages of this spectrum, one major hurdle is still obstructing the rapid progress of this technology. Considerable amount of atmospheric absorption of the mm-wave frequencies, especially in fog, dust particles, clouds, etc. is limiting the mm-wave communication range.

The IR spectrum is already in use in several existing technologies. Infrared heating technologies are used in safe heat therapy methods of natural health care and physiotherapy, cooking, industrial manufacturing processes, etc. Infrared imaging technology is very popular in military applications like passive night vision goggles, astronomy, etc. Most popular application of this spectrum is the use of it in high speed, wideband, short or medium or long range fibre optic communication technology. This technology utilizes three low absorption window wavelengths, such as (i) 1st window centred at 0.85 µm, (ii) 2nd window centred at 1.35 µm and (iii) 3rd window centred at 1.55 µm; Fig. 3 shows the positions of those windows [3].
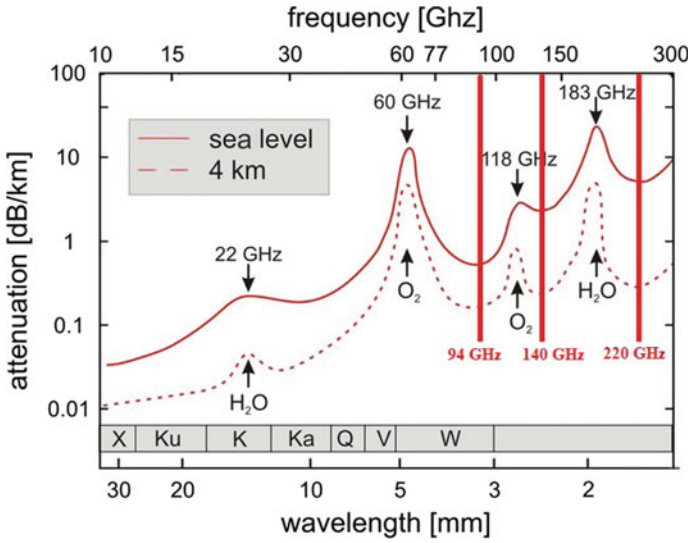
Fig. 2 Atmospheric absorption versus frequency/wavelength plot at sea level and at 4000 m altitude [2]
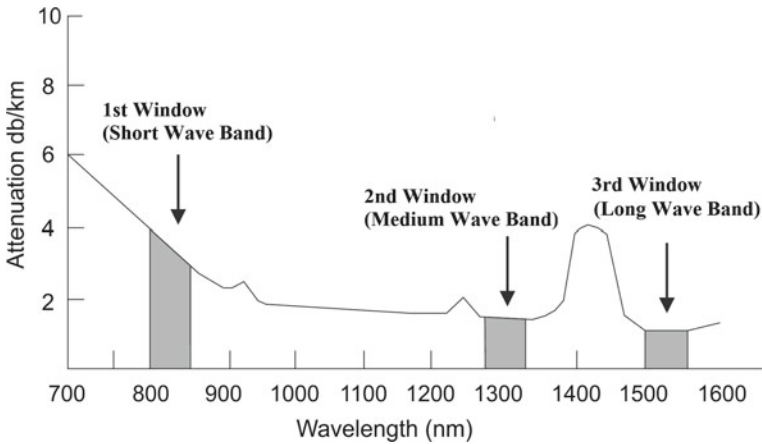
Fig. 3 Attenuation versus optical wavelength plot in glass; three optical transmission windows are shown in this plot [3]

The THz spectrum or THz band is also known as 'THz-gap', since it is the most technologically unexplored portion of the electromagnetic spectrum. As mentioned earlier, the 'THz-gap is an almost untouched frequency band (0.3–10 THz) lying between well explored mm-wave and IR spectrums. Higher data rate can be achieved in THz communication systems as compared to their equivalent mm-wave counterparts. On the other hand, better penetration capability of THz waves as compared to IR

frequencies makes the THz band superior to the IR spectrum in some specific applications. Currently, the THz spectrum has massive requirements in various scientific, security, medical and astronomical sectors. Some examples are bio-sensing, bio-imaging, remote sensing, spectroscopy, industrial quality inspection, medical and pharmaceutical sectors, food diagnostics, astronomy, etc. [4–24]. Significantly, the lower energy of THz photons makes those more convenient as compared to the high energy X-ray photons for remote inspection of some highly delicate substances like historical artefacts, historical structures, historical paintings, etc. [25].

2   Brief Overview of the Book

The scope of this book includes a significantly long portion of the electromagnetic spectrum, starting from the mm-waves (i.e. 30 GHz) and extended up to the end of the near-IR spectrum (i.e. 450 THz). Most significant aspect of this portion of the electromagnetic spectrum is that it includes a frequency regime where the gradual transition from electronics to photonics occurs; this frequency regime is nothing but the THz frequency spectrum. This book provides a detailed analysis, description and discussion of some recently developed technologies under this extended frequency spectrum. Especially, the emphasis is given on the state-of-the-art and upcoming research going on at various parts of the globe on THz science and technology [26–36]. This book can be considered as a textbook for undergraduate, post graduate, doctoral students and also for scientists due to the ultra-broad coverage of it.

Chapter-wise organization of the entire book is provided in this section. Sensitivity analysis of Ku-band substrate integrated waveguide has been presented in Chap. 2 for photonic circuit integration. The possibilities of realizing Gallium Nitride integrated power module for terahertz wave generation are discussed in Chap. 3. Design methodologies of SiSnC/Si heterostructure electro-optic modulator (EOM) for optical signal processing applications have been included in Chap. 4. Design and optimization techniques of graphene nanoribbon tunnel field effect transistors (TFETs) for low power digital applications are described in Chap. 5. Chapter 6 describes a very interesting topic of optoelectronics, i.e. birhythmic behaviour in dual loop optielectronic oscillators. Performance analysis of optical arithmetic circuits using artificial neural networks has been presented in Chap. 7. Chapter 8 demonstrates the design and modelling of an infrared sensor-based object detection circuit for computer vision applications. A comparative analysis on bandwidth management techniques in 6th generation mobile communication has been presented in Chap. 9. Noise performance of millimeter-wave impact avalanche transist time (IMPATT) oscillators has been summarized in Chap. 10. Chapter 11 deals with a brief introduction of high frequency passive circuits. Impact of negative bottom gate voltage for improvement of RF/analog performance in asymmetric junctionless dual material double gate MOSFET has been discussed in detail in Chap. 12. Chapter 13 presents a DC and RF analysis of gate all round tunneling field-effect transistor (GAA-TFET) based on graphene nanoribbon (GNR). Generalized distribution functions in heavily doped nano materials have been studied at terahertz frequency and the results are

summarized in Chap. 14. Chapter 15 deals with the influence of THz frequency on the gate capacitance in two-dimensional quantum-well field effect transistors (QWFETs). Chapter 16 reveals an alternative scheme of quantum optical superfast tristate controlled-NOT gate using frequency encoding principle of light with semi-conductor optical amplifier. Finally, the Chap. 16 deals with the detailed discussion regarding the use of frequency encoding principle for implementing nano-photonic ultrafast tristate Pauli X gate.

References

1. Zhang R, Liu S, Jin H, Luo Y, Zheng Z, Gao F, Zheng Y (2019) Noninvasive electromagnetic wave sensing of glucose. Sensors 19:1151–1170
2. Yang SS, Lim JH, Na YJ (2012) Design and fabrication of ka-band active PIN diode limiter for a millimeter wave seeker. J Korean Inst Electromagn Eng Sci 23(2):220–228
3. White JS (2008) The missing pieces: physical layer optical network security. Graduate Thesis submitted at The State University of New York Institute of Technology U#: U00099492, pp 1–140
4. Siegel PH (2002) Terahertz technology. IEEE Trans Microwave Theory Tech 50(3):910–928
5. Martyniuk P, Antoszewski J, Martyniuk M, Faraone L, Rogalski A (2014) New concepts in infrared photodeector designs. Appl Phys Rev 1:041102–1–35
6. Woodward RM, Cole BE, Wallace VP, Pye RJ, Arnone DD, Linfield EH, Pepper M (2002) Terahertz pulse imaging in reflection geometry of human skin cancer and skin tissue. Phys Med Biol 47:3853–3863
7. Nagel M, Bolivar PH, Brucherseifer M, Kurz H, Bosserhoff A, Buttner R (2002) Integrated THz technology for label-free genetic diagnostics. Appl Phys Lett 80(1):154–156
8. Karpowicz N, Zhong H, Zhang C, Lin KI, Hwang JS, Xu J, Zhang XC (2005) Compact continuous-wave subterahertz system for inspection applications. Appl Phys Lett 86(5):054105–1–3
9. Yamamoto K, Yamaguchi M, Miyamaru F, Tani M, Hangyo M (2004) Non-invasive inspection of c-4 explosive in mails by terahertz time-domain spectroscopy. J Appl Phys 43(3B):L414–L417
10. Kawase K, Ogawa Y, Watanabe Y, Inoue H (2003) Non-destructive terahertz imaging of illicit drugs using spectral fingerprints. Opt Express 11(20):2549–2054
11. Joerdens C, Koch M (2008) Detection of foreign bodies in chocolate with pulsed terahertz spectroscopy. Opt Eng 47(3):037003–1–5
12. Tonouchi M (2007) Cutting-edge terahertz technology. Nat Photonics 1:97–105
13. Prince JL, Links J (2006) Medical imaging signals and systems. 2nd Edition, Pearson Prentice Hall, Upper Saddle River
14. Chen S-L, Chang Y-C, Zhang C, Ok JG, Ling T, Mihnev MT, Guo TBNLJ (2014) Efficient real-time detection of terahertz pulse radiation based on photoacoustic conversion by carbon nanotube nanocomposite. Nat Photonics 8:537–542
15. Sirtori C (2002) Bridge for the terahertz gap. Nature 417:132–133
16. Saleh BEA, Teich MC (2007) Fundamentals of photonics, 2nd edn. Wiley, New York, p 1200
17. Biswas A, Sinha S, Acharyya A, Banerjee A, Pal S, Satoh H, Inokawa H (2018) 1.0 THz GaN IMPATT source: effect of parasitic series resistance. J Infrared Millim Terahertz Waves 39(10):954–974
18. Acharyya A, Banerjee JP (2014) Prospects of IMPATT devices based on wide bandgap semiconductors as potential terahertz sources. Appl Nanosci 4:1–14
19. Acharyya A, Banerjee S, Banerjee JP (2013) Potentiality of semiconducting diamond as base material of millimeter-wave and terahertz IMPATT devices. J Semiconduct 35(3):034005–1–11

20. Acharyya A (2019) Three-terminal graphene nanoribbon tunable avalanche transit time sources for terahertz power generation. physica status solidi (a) 216(18):1900277
21. Acharyya A (2019) 1.0 – 10.0 THz radiation from graphene nanoribbon based avalanche transit time sources. physica status solidi (a) 216(7):1800730 (2019)
22. Yeh KL, Hoffmann MC, Hebling J, Nelson KA (2007) Generation of 10 μJ ultrashort terahertz pulses by optical rectification. Appl Phys Lett 90:171121
23. Hauri CP, Ruchert C, Vicario C, Ardana F (2011) Strong-field single-cycle THz pulses generated in an organic crystal. Appl Phys Lett 99:161116
24. Kirley MP, Booske JH (2015) Terahertz conductivity of copper surfaces. IEEE Trans Terahertz Sci Technol 5:1012–1020
25. Dandolo CLK, Jepsen PU (2016) Wall painting investigation by means of non-invasive terahertz time-domain imaging (THz-TDI): inspection of subsurface structures buried in historical plasters. J Infrared Millime Terahertz Waves 37:198–208
26. Booske JH (2008) Plasma physics and related challenges of millimeter-wave-to-terahertz and high power microwave generation. Phys Plasmas 15:16–20
27. Barker RJ, Booske JH, Luhmann NC, Nusinovich GS (2005) (editors) Modern microwave and millimeter wave power electronics. Wiley, New York
28. Booske JH, Dobbs RJ, Joye CD, Kory CL, Neil GR, Park GS, Park J, Temkin RJ (2011) Vacuum electronic high power terahertz sources. IEEE Trans Terahertz Sci Technol 1:52–75
29. He W et al (2015) Generation of broadband terahertz radiation using a backward wave oscillator and pseudospark-sourced electron beam. Appl Phys Lett 107:133501
30. Gavrilov NG, Knyazev BA, Kolobanov EI, Kotenkov VV, Kubarev VV, Kulipanov GN, Matveenko AN, Medvedev LE, Miginsky SV, Mironenko LA, Oreshkov AD, Ovchar VK, Popik VM, Salikova TV, Scheglov MA, Serednyakov SS, Shevchenko OA, Skrinsky AN, Tcheskidov VG, Vinokurov NA (2007) Status of the Novosibirsk highpower terahertz FEL Nucl. Instrum Methods Phys Res A 575(1–2):54–57
31. Virginia Diodes Inc Virginia Diodes, Inc—Frequency Multipliers. Accessed April 2021. http://vadiodes.com/en/frequency-multipliers
32. Han R et al (2013) Active terahertz imaging using Schottky diodes in CMOS: array and 860-GHz pixel. IEEE J Solid-State Circuits 48:2296–2308
33. Grant JP et al (2013) A monolithic resonant terahertz sensor element comprising a metamaterial absorber and micro-bolometer. Laser Photon Rev 7(6):1043–1048
34. Carranza IE, Grant JP, Gough J, Cumming D (2017) Terahertz metamaterial absorbers implemented in CMOS technology for imaging applications: scaling to large format focal plane arrays. IEEE J Sel Top Quantum Electron 23(4):4700508
35. Dobrovolsky V, Sizov F (2007) Room temperature, or moderately cooled, fast THz semiconductor hot electron bolometer. Semicond Sci Technol 22:103–106
36. Sarieddeen H, Alouini MS, Al-Naffouri TY (2020) An overview of signal processing techniques for terahertz communications. TechRxiv. Preprint. https://doi.org/10.36227/techrxiv.12363359.v1

Sensitivity Analysis of Substrate Integrated Waveguide at Ku Band for Photonic Circuit Integration

Pampa Debnath, Arpan Deyasi, and Ujjwal Mondal

Abstract Electromagnetic bandgap structure has remained the backbone of photonic circuit design and fabrication, precisely after the invention of photonic crystal structure. However, another interesting field has also progressed in parallel with EBG is transmission line design, both in unbounded and bounded forms. Therefore, it becomes compatible to invoke waveguide and 2D planar antenna in the photonic circuit, as far as from a material science point of view, and here lies the need for research in estimating the performance parameters of those structures for successful integration. The two fundamental parameters, that need to be evaluated in this context, are cut-off frequency and impedance sensitivity for any bounded transmission line; which shapes the propagation of electromagnetic field inside the guided medium. In this present chapter, analysis has been carried out for substrate integrated waveguide at microwave frequency spectrum for performance evaluation, which speaks about its candidature for photonic circuit integration.

1 Introduction

Modern communication systems have the operating spectrum in microwave and millimeter wave spectra, and therefore, all the corresponding trans-receiver sections including antennas and channel needs to be designed considering the region of operation. Though conventional optical communication systems have exhibited improved characteristics in the last two decades in terms of lower loss and reduced cost, but the requirement has shifted in a new paradigm since the development of all-optical integrated circuit. More precisely, research on photonic crystal (PhC) structure has ushered an emerging communication system which requires the invention of secured

P. Debnath · A. Deyasi (✉)
Department of Electronics and Communication Engineering, RCC Institute of Information Technology, Kolkata 700015, India
e-mail: deyasi_arpan@yahoo.co.in

U. Mondal
Department of Applied Physics, University of Calcutta, Kolkata 700009, India

7

channel transmission having compatible electromagnetic characteristics. Substrate integrated waveguide (SIW) is probably the promising candidate in this regard till date where electromagnetic waves can be transmitted in those desired narrow EBG regions as offered by PhC based filters and isolators.

Conventional transmission lines such as coaxial cables or two wire transmission lines are generally used for the propagation of electromagnetic energy, as evident from day-to-day utilization. However, for application point-of-view, these non-planar structures are difficult to integrate with planar structures. Conventional waveguides are improved versions of the traditional transmission line. But they are bulky and non-planar also. A well-accepted recent technological solution to this long-standing problem comes with the invention of the Substrate Integrated waveguide, which is an advanced module of conventional metallic counterpart. In this modern high-frequency device, two rows of metallic vias have been embedded in a dielectric substrate between two conductors. It can alternatively be looked at as a rectangular waveguide filled with dielectric substrate. Similar configurations were developed previously under several terminologies such as post wall [1–3] and laminated [4–7] waveguide.

Rapid improvement of high frequency communication systems has forced an ever-rising demand for low cost, high power, high efficiency and easy to integrate compact devices. Microstrip line and conventional hollow waveguide have been used extensively for the recognition of high frequency devices [8–10]. These conventional technologies reveal certain disadvantages. Rectangular waveguide suffers from high cost, massive in size and complex developing process, whereas dielectric loss is the main drawback of microstrip technology at high frequency. A new technology known as gap waveguide [11] has been recently developed that overcomes the disadvantages of traditional technologies like a rectangular waveguide. Several transitions have been found in different literature. A simple transition of coaxial port to Ridge Gap waveguide (RGW) has been made by feeding the port in the top plate of RGW [12]. A bandwidth of 4 GHz with 10 dB return loss has been found in this transition. Ina waveguide [13] to RGW transition using excitation of the coaxial port has been done where a bandwidth of 20% at −15 dB matching level has been observed. A transition of microstrip to RGW has been designed in [14] with 25.4% bandwidth at better than 15 dB return loss and 0.85 dB insertion loss. A transition of inverted microstrip gap waveguide to rectangular waveguide using a planar probe to feed a horn antenna array has been presented in [15]. This transition has been done in two configurations in which a bandwidth of 45% at −15 dB return loss and 0.5 dB insertion loss has been found.

Most of the benefits like high quality factor and electrical–mechanical shielding are preserved by these SIW structures. Press worthy characteristic is that by using the same technology complete balance integration can be accomplished concerning active–passive circuits [16–20] and antenna [21] on the same substrate. For mm wave applications, circuits and antennas cannot be independently manufactured at very high frequency bands. Different processing technique such as LTCC and PCB has been used for the integration of several circuits and antenna using single or multi-layered SIW.

Role of material parameters in this system design plays a pivotal role as the compatibility of channel and circuit components augments the integration process. Henceforth, circuit components should be made by the materials of the channel. This is possible for SIW as channel and PhC based devices as transmitter and receiver circuits. The next section of the chapter depicts the pioneering works carried out in these fields individually without visualizing the system integration perspective.

2 Literature Review

An increased demand has been observed in wireless communication systems as several applications have been developed in micro and millimeter wave range of frequencies. Diverse applications [22–25] in the area of automotive RADARs, Biomedical devices and wireless sensors in millimeter wave frequency range have been anticipated in millimeter frequency range. The success of any system depends on cost effective equipments, appropriate for the mass production of systems. The heart of any system depends on the active components such as filters, mixers, local oscillators and low noise amplifiers (LNA). The most talented technology to build this stage is Substrate Integrated waveguide (SIW) [16–18, 26, 27]. It is similar to the structure of a conventional waveguide fabricated by two rows of metallic vias in a dielectric substrate. Its propagation characteristics, field configuration and dispersion characteristics are similar to the conventional waveguide. Most reliable and interesting features of SIW are high power handling capability in addition to high quality factors. Also, all active and passive components and antennas are implemented on the same substrate. SIW was initially invented as a post wall or laminated waveguide [6, 7] in an array of antennae. SIW technology has been employed in different applications [16–20, 28, 29] like filters, couplers, circulators, slot and leaky wave antennas. Several waveguide components have already been employed using SIW. For analysis of dispersion characteristics of SIW, either commercial software or electromagnetic simulators based on finite difference time domain or frequency domain technique [30], transverse resonance method [27], boundary integral-resonant mode expansion technique [31] have been used. Critical issue in the design of SIW when operated in mm wave frequency range is the minimization of loss. Conductor loss, dielectric loss and radiation losses are the major three losses [32, 33] that have to be taken into account in the design of SIW.

For practical application, electromagnetic wave transmitted inside SIW has to be transferred inside the confined channel, and for secure transmission with minimum data loss, photonic crystal based fibre has paved the way for replacing the age-old Cu cable. Ever since the conceptual formation of all-optical integrated circuit [18, 19], the requirement of photonic components [34–37] is emerging day-by-day in order to replace the existing electronic counterparts for better SNR, reliability, efficiency or compatible integration. This eventually leads to search of novel materials [38–40] from a performance improvement point-of-view. Here comes the importance of

photonic crystal, which makes a major breakthrough for the design of photonic integrated circuits by enabling the possible realization of different optical components [41, 42] considering the inherent feature of restricting electromagnetic waves of a few selected wavelengths and allowing others in the direction of propagation; and negative refractive index-based materials are the new class added to enhance the selective feature for ultra-narrowband spectrum [43]. However, low-K dielectrics are also investigated in the recent past for PhC based filter design, which also helps to integrate with SIW structure. In this context, design frequency and sensitivity become two extremely critical parameters for future circuit design.

In the present chapter, both cut-off frequency and sensitivity of SIW structure are analytically computed as a function of dimensions and operating spectrum (Ku band). The total manuscript is subdivided in the following sections: Sect. 3 exhibits design rule, Sects. 4 and 5 respectively describe cut-off frequency and sensitivity respectively, and chapter is ended with conclusion.

3   Design Rule

The main parameters of SIW are the thickness of substrate 'h', relative permittivity 'ε_r', 'a' (width of SIW), 'd' (diameter of vias) and 's' (separation between adjacent viases). The cut off frequency has been determined by taking into consideration the separation between the rows of metalized vias and the permittivity of dielectric material. As the current flow does not present through the two side walls of SIW, therefore transverse magnetic mode has not been supported by SIW instead propagation of transverse electric mode is only possible in this waveguide (Fig. 1).

Dispersion characteristics of [44] an SIW were meticulously examined and acknowledged with the combined method of BI-RME and Floquet theorem. The study of this characteristic reveals that both SIW and conventional rectangular waveguide has similar transmission characteristic provided both waveguides are filled with the same type of dielectric material using the equivalent width 'w' of SIW. It can be obtained by

$$w = a - \frac{d^2}{0.95s} \tag{1}$$

Diameter to width ratio has not been included in the above Eq. (1) and error comes into view when diameter 'd' increases.

To defeat this flaw, a numerical formulation was suggested in [26] based on the finite element method for finding the propagation constant of SIW in complex form. A precise empirical equation can be presented as:

(a)

(b)
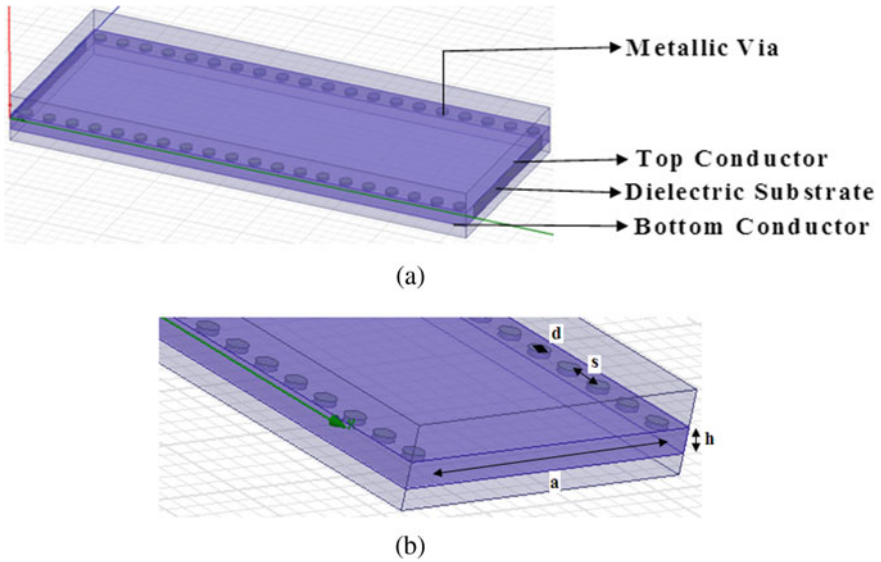
Fig. 1 Substrate Integrated Waveguide **a** side view; **b** top view

$$w|_{TE_{10}} = a - \frac{1.08d^2}{s} + \frac{0.1d^2}{a} \qquad (2)$$

$$w|_{TE_{20}} = a - \frac{d^2}{1.1s} + \frac{d^3}{6.6s^2} \qquad (3)$$

An additional accurate full-wave approach based on the method of lines (MoL) is mentioned in [44] where an eigenvalue equation has been formulated to enhance the computational efficiency to represent the transmission characteristics of SIW. The proposed method helped to formulate valuable empirical equations to construct different components of SIW.

A high frequency software simulator has been chosen for analysis of SIW modes because the S matrix formed by this software is appropriate for integration with mathematical calibration technique. Both SIW and conventional rectangular waveguides have identical properties but few differences still exist. Periodic structure exists in the configuration of SIW which may produce electromagnetic band-stop circumstances. SIW structure suffers a leakage difficulty owing to periodic gaps. Therefore, a leakage wave has been found in the analysis of SIW.

3.1 SIW Modes

Only TE_{x0} modes exist in SIW configurations. This is a very significant characteristic of SIW. In a guided structure, the establishment of mode refers that there should be the existence of surface currents. SIW can be considered as a rectangular waveguide with periodic holes on side walls. A huge radiation may exist if the currents cross the holes. There will be a very negligible radiation if the holes are aligned along the direction of movement of current.

The surface current has not been disturbed by periodic holes; therefore, the mode can be conserved in SIW. Identical surface currents have been found on the side walls in all TE_{x0} modes which is the reason for existing modes in SIW. Consider TM mode is propagating with holes of the side walls of SIW; a surface current with longitudinal feature has been generated by a transverse magnetic field. A high radiation occurred as transverse holes cut the surface current. These holes will also generate high radiation if TE_{xy} modes propagate in SIW with holes on side walls. So only TE_{x0} modes should be endorsed in SIW as suggested by holes radiation. The basic mode of SIW is TE_{10} mode as shown in Fig. 2. Similar field configuration has been observed in SIW as well as rectangular waveguide.

4   Cut-Off Frequency of SIW

Figure 1 demonstrates a distinctive SIW structure that is amalgamated with metallic holes. A substrate with low loss has been used here. Dimensions of SIW structure are optimized as mentioned in the figures, where ranges are considered within a practical framework. The dispersion features of SIW are equivalent to a conventional rectangular waveguide with equal width. As we assumed that the distance between two rows of metallic holes of SIW is 'a', diameter of hole is 'd', distance between adjacent hole 's', therefore the effective width can be given as mentioned by Eq. 2.

The propagation constant of SIW may be written as

$$\beta(w) = \sqrt{\omega^2 \mu \varepsilon - \left(\frac{\pi}{w_{eff}}\right)^2} \tag{4}$$

From Eqs. 2 and 4, propagation constant 'β' is calculated by the distance between two rows of metallic holes of SIW entirely for known values of dimensional as well as material parameters.

From Fig. 3, it has been observed that cut-off frequency varies monotonically with all the dimensional variations. However, it decreases with increasing both 'a/h' and 'a/d', whereas slowly increases with 'd/s'.

(a)

(b)

(c)
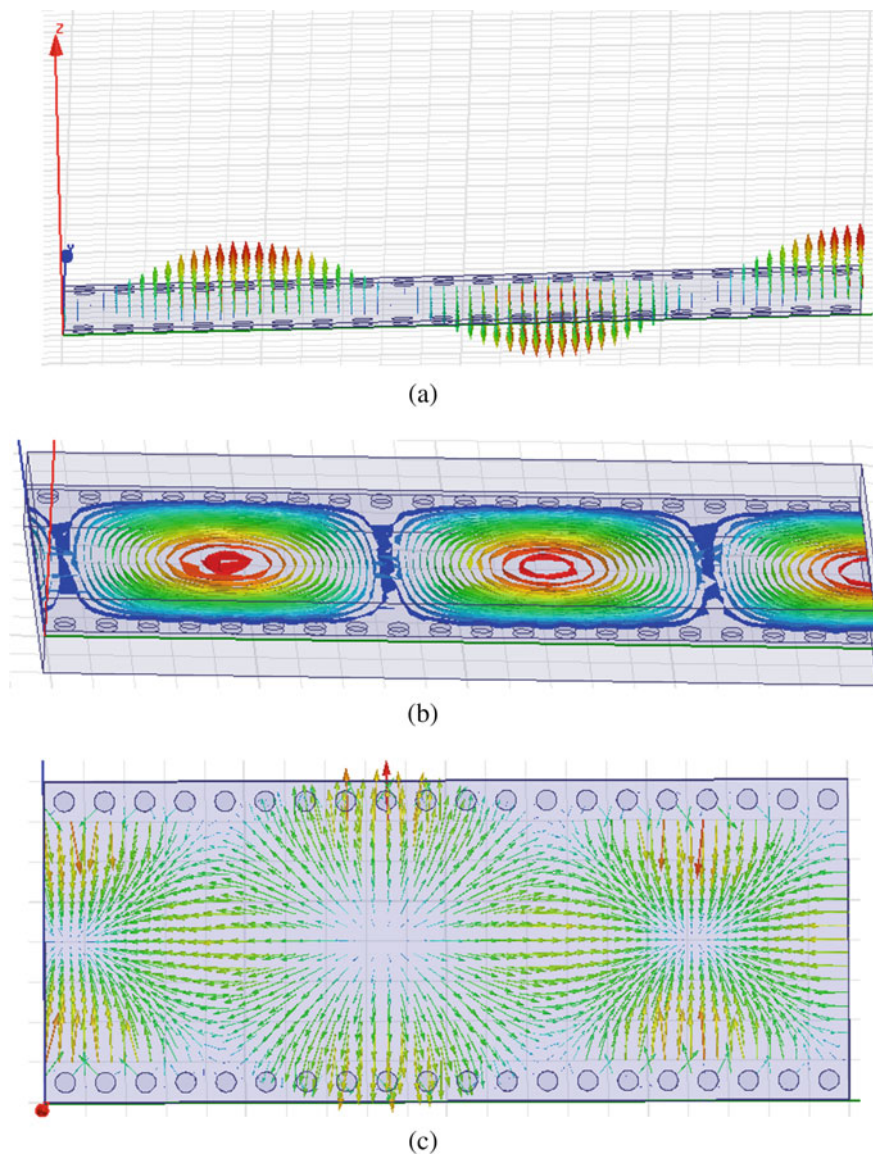
Fig. 2 Field & current distribution of Substrate Integrated Waveguide: **a** TE$_{10}$ Electric field vector distribution; **b** Magnitude of Electric field distribution; **c** Surface current distribution

SIW has cutoff frequency for basic mode TE_{10} alike rectangular waveguide. The cutoff frequency for TE10 mode and TE20 mode [22] are given by Eqs. 5, 6 and 7, 8 respectively. Frequency of operation of SIW should satisfy the criteria $f_{cTE10} < f < f_{cTE20}$

$$f_c|_{TE_{10}} = \frac{c}{2\sqrt{\varepsilon_r}} \left(a - \frac{d^2}{0.95s} \right)^{-1} \tag{5}$$

$$f_c|_{TE_{10}} = \frac{c}{2w_{eff}\sqrt{\varepsilon_r}} \tag{6}$$

$$f_c|_{TE_{20}} = \frac{c}{\sqrt{\varepsilon_r}} \left(a - \frac{d^2}{1.1s} + \frac{d^3}{6.6s^2} \right)^{-1} \tag{7}$$

$$f_c|_{TE_{20}} = \frac{c}{w_{eff}\sqrt{\varepsilon_r}} \tag{8}$$

It has been observed that with increasing 'a/h' and 'a/d' ratio cut-off frequencies for TE_{10} and TE_{20} mode are exponentially decreasing whereas cut-off frequencies increase with increasing d/s ratio. Using the combined method of BI-RME and Floquet's theorem, cut-off frequencies of TE_{10} and TE_{20} for SIW as shown in Eqs. 5 and 7 respectively, have been found out.

5   Sensitivity

Good performance SIW can be designed and its achievability can be obtained by using a commercial software HFSS. But surplus alternation in measurement can cause a change in electrical properties. Due to a small change in the electrical dimension of SIW, change in relative permittivity of substrate material, or inaccuracy of substrate thickness, this type of divergence may occur.

Reduction of tolerance can be possible by using more accurate fabrication as well as using a very good dielectric substrate. Other way to design a tolerance insensible SIW, is depending on the tolerance effect of the structure.

Sensitivity can be defined as

$$S_Y^X = \frac{\Delta X}{\Delta Y} \tag{9}$$

The above equation can be employed to establish the divergence in circuit features for a particular tolerance. Sensitivity investigation for Z_0 is presented here.

The impedance of SIW can be calculated using the given formula
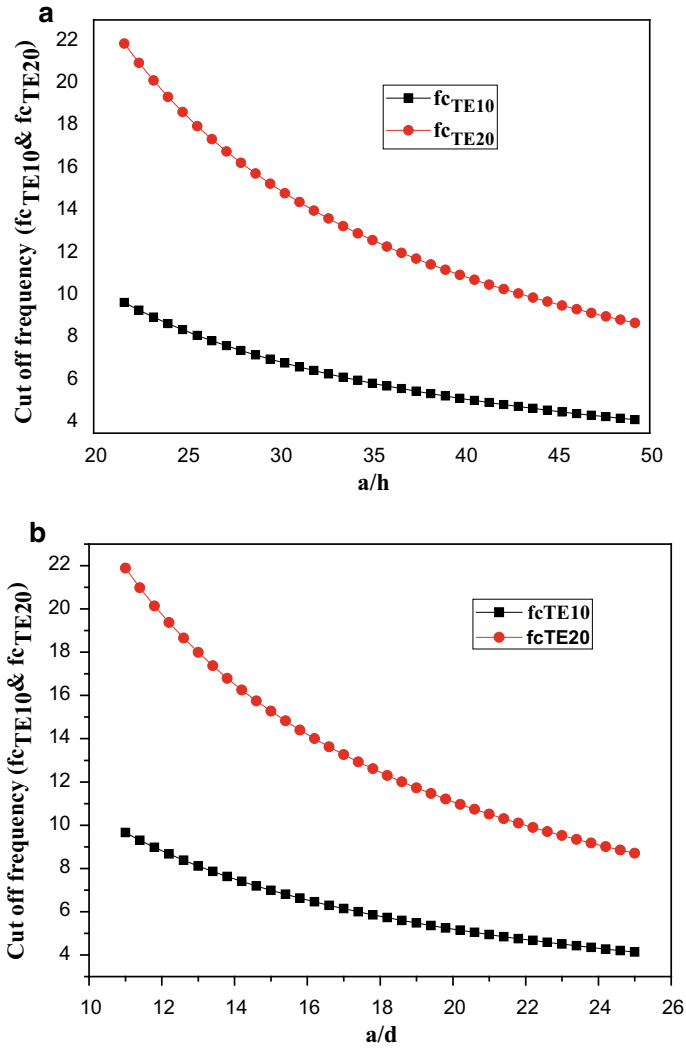
Fig. 3 a: Cut off frequencies for TE_{10} and TE_{20} modes for varying 'a/h'. **b**: Cut-off frequencies for TE_{10} and TE_{20} modes for varying 'a/d'. **c**: Cut-off frequencies for TE_{10} and TE_{20} modes for varying 'd/s'

$$Z_0 = \frac{h}{w} \cdot \frac{\eta}{\sqrt{1 - \left(\frac{\lambda}{\lambda_c}\right)^2}} \tag{10}$$

$$\eta = \frac{120}{\sqrt{\varepsilon_r}} \tag{11}$$
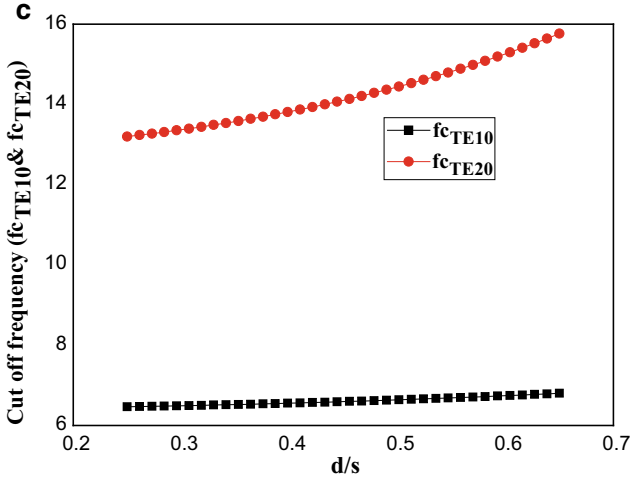
Fig. 3 (continued)

Sensitivity tolerance with respect to 'a/h', 'a/d', 'd/s', and λ are presented in Fig. 4. It has been observed that all sensitivity curves are monotonically changing without any abrupt fluctuation. The tolerance consequence of each parameter is approximately identical but the changing limit is dissimilar. It has been also observed that SIW impedance decreases with increase of 'a/h' and 'a/d' whereas sensitivity increases with increase of 'd/s' and λ.

6 Summary

The present analysis deals with the impedance sensitivity of high-frequency communication channel at Ku band when integrated in an optical integrated circuit. Results exhibit variation of sensitivity with structural parameters which helps the design engineer to set the operating point as per the practical limit. For integrated design, the range of channel dimension becomes extremely important as far as wired communication is concerned, and the present work throws light on that factor. This work may further be extended when a proper EBG structure with pre-defined bandgap can be designed, and then only the composite system may function successfully.
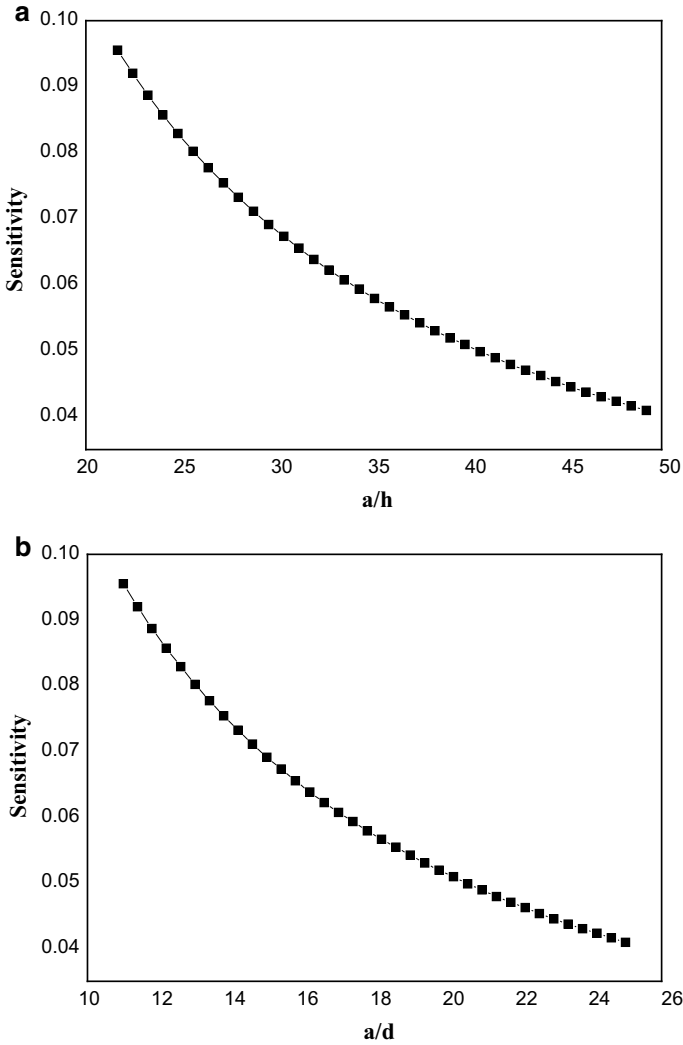
Fig. 4　a: Impedance sensitivity w.r.t 'a/h' at 15 GHz. **b**: Impedance sensitivity w.r.t 'a/d' at 15 GHz. **c**: Impedance sensitivity w.r.t 'd/s' at 15 GHz. **d**: Impedance sensitivity w.r.t wavelength. The characteristic impedance, phase constant of SIW is the function of width, substrate dielectric constant, height, the distance between metallized holes and diameter of holes. There are some significant factors that consist in fabrication for example location and dimension of via holes. Most of these parameters affect the variations of characteristic impedance and phase constant
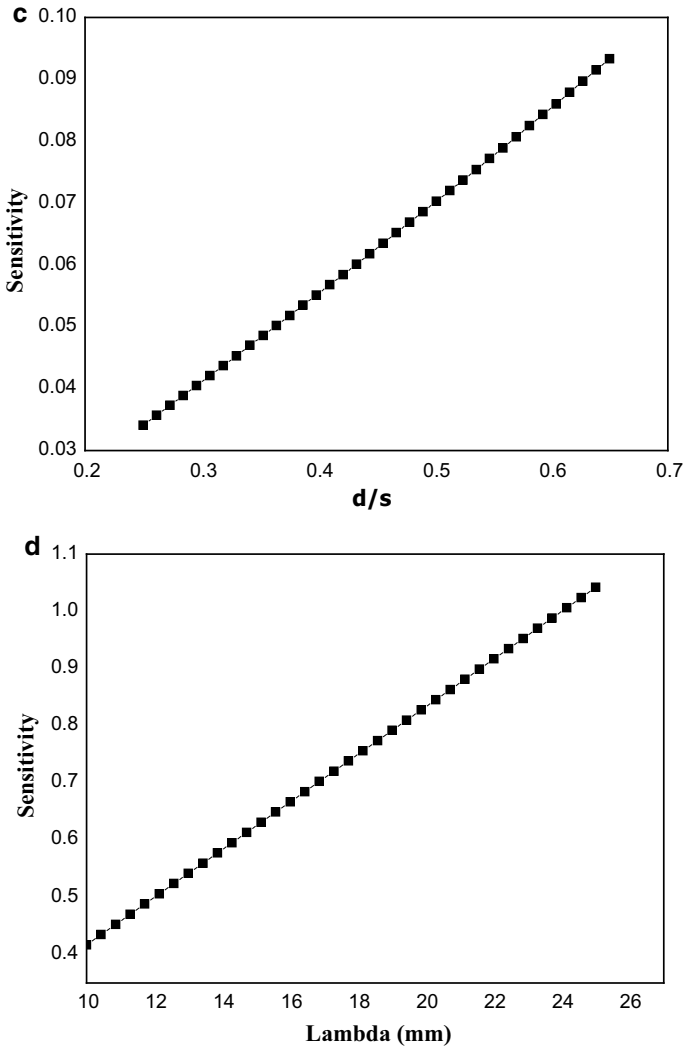
Fig. 4 (continued)

References

1. Hirokawa J, Ando M (2000) Efficiency of 76-GHz post-wall waveguide-fed parallel-plate slot arrays. IEEE Trans Antennas Propag 48(11):1742–1745
2. Hirokawa J, Ando M (2000) 45° linearly polarised post-wall waveguide-fed parallel-plate slot arrays. IEE Proceed Microwaves Antennas Propagat 147(6):515–519
3. Kai T, Hirokawa J, Ando M (2003) Analysis of a feeding structure for TEM wave excitation in an oversized rectangular waveguide. IEEE Antennas Propagat Soc Int Symposium, 1177–1180
4. Uchimura H, Takenoshita T, Fujii M (1998) Development of a laminated waveguide. IEEE Trans Microw Theory Tech 46(12):2438–2443

5. Yong H, Wu KL (2003) A broad-band LTCC integrated transition of laminated waveguide to air-filled waveguide for millimeter-wave applications. IEEE Trans Microw Theory Tech 51(5):1613–1617

6. Yong H, Wu KL, Ehlert M (2003) An integrated LTCC laminated waveguide to microstrip line T-junction. IEEE Microwave Wirel Compon Lett 13(8):338–339

7. Cruz JA, Zaki KA (2005) Canonical ridge waveguide filters in LTCC or metallic resonators. IEEE Trans Microw Theory Tech 53(1):174–182

8. Chakravorty P (2014) Analysis of rectangular waveguides–an intuitive approach. IETE J Educ 55(2):76–80

9. Benkraouda M, Ghamlouche H, Hussein MI, Badarneh TM (2010) Numerical modelling of high–Tc superconducting microstrip line using fdtdtechnique. Int J Model Simul 30(1):67–72

10. Bichurin MI, Petrov VM, Petrov RV, Bukashev FI, Smirnov AY (2002) Electrodynamic analysis of strip line on magnetoelectric substrate. Ferroelectrics 280(1):203–209

11. Kildal PS (2011) Waveguides and transmission lines in gaps between parallel conducting surfaces. U.S. Patent 2011 0 181 373 A1

12. Al Sharkawy M, Kishk AA (2014) Design of waveguide to ridge gap waveguide transition using probe excitation. In: Proceedings of the 8th European conference on antennas and propagation (EuCAP), Hague, The Netherlands, 946–949

13. Brazález AA, Zaman AU, Kildal PS (2012) Investigation of a microstrip-to-ridge gap waveguide transition by electromagnetic coupling. Proc Antennas Propag Soc Int Symp, Chicago, IL, USA, pp 1–2

14. Brazález AA, Iglesias ER, Kildal PS (2014) Investigation of transitions for use in inverted microstrip gap waveguide antenna arrays. In: Proceedings of the 8th European conference on antennas and propagation (EuCAP), Hague, The Netherlands, 995–999

15. Raza H, Yang J, Kildal PS, Alós E (2014) Microstrip-ridge gap waveguide-study of losses, bends, and transition to WR-15. IEEE Trans Microw Theory Techniq 62(9):1943–1952

16. Wu K (2006) Towards system-on-substrate approach for future millimeter-wave and photonic wireless applications. Proceedings of the Asia-Pacific Microwave Conference

17. Tang HJ, Hong W, Hao ZC, Chen JX, Wu K (2005) Optimal design of compact millimetre-wave SIW circular cavity filters. Electron Lett 41(19):1068–1069

18. Chen JX, Hong W, Hao ZC, Li H, Wu K (2006) Development of a low cost microwave mixer using a broad-band substrate integrated waveguide (SIW) coupler. IEEE Microw Wirel Component Lett 16(2):84–86

19. Zhong C, Xu J, Yu Z, Zhu Y (2008) Ka-band substrate integrated waveguide Gunn oscillator. IEEE Microw Wirel Component Lett 18(7):461–463

20. Jin H, Wen G (2008) A novel four-way Ka-band spatial power combiner based on HMSIW. IEEE Microw Wirel Component Lett 18(8):515–517

21. Debnath P, Chatterjee S (2017) Substrate integrated waveguide antennas and arrays. In: IEEE 1st International conference on electronics, materials engineering and nano-technology, 1–6, Kolkata, India

22. Daniels RC, Heath RW (2007) 60 GHz wireless communications: emerging requirements and design recommendations. IEEE Veh Technol Mag 2(3):41–50

23. Fleming WJ (2008) New automotive sensors–a review. IEEE Sensor J 8(11):1900–1921

24. Yujiri L, Shoucri M, Moffa P (2003) Passive millimeter wave imaging. IEEE Microw Mag 4(3):39–50

25. Mizuno K, Wagatsuma Y, Warashina H, Sawaya K, Sato H, Miyanaga S, Yamanaka Y (2007) Millimeter-wave imaging technologies and their applications. In: IEEE international vacuum electronics conference, 15–17 May, Kitakyushu, Japan

26. Xu F, Wu K (2005) Guided-wave and leakage characteristics of substrate integrated waveguide. IEEE Trans Microw Theory Tech 53(1):66–73

27. Deslandes D, Wu K (2006) Accurate modelling, wave mechanisms, and design considerations of a substrate integrated waveguide. IEEE Trans Microw Theory Tech 54(6):2516–2526

28. Deslandes D, Wu K (2005) Substrate integrated waveguide leaky-wave antenna: concept and design considerations. In: Proceeding of Asia-pacific microwave conference (APMC'05), Suzhou, China

29. D'Orazio W, Wu K (2006) Substrate-integrated-waveguide circulators suitable for millimeter-wave integration. IEEE Trans Microw Theory Tech 54(10):3675–3680

30. Xu F, Zhang Y, Hong W, Wu K, Cui TJ (2003) Finite-difference frequency-domain algorithm for modelling guided-wave properties of substrate integrated waveguide. IEEE Trans Microw Theory Tech 51(11):2221–2227

31. Cassivi Y, Perregrini L, Arcioni P, Bressan M, Wu K, Conciauro G (2002) Dispersion characteristics of substrate integrated rectangular waveguide. IEEE Microw Wirel Component Lett 12(9):333–335

32. Bozzi M, Perregrini L, Wu K (2008) Modelling of conductor, dielectric and radiation losses in substrate integrated waveguide by the boundary integral-resonant mode expansion method. IEEE Trans Microw Theory Tech 56(12):3153–3161

33. Bozzi M, Pasian M, Perregrini L, Wu K (2009) On the losses in substrate integrated waveguides and cavities. Int J Microw Wirel Technol 1(5):395–401

34. Karmakar A, Roy I, Deyasi A, Deb A, Kundu A (2013) Suitability of semiconductor heterostructure over SiO_2-Air composition for one-dimensional photonic crystal based bandpass filter. Int J Electron Commun Comput Technol 3(3):403–406

35. Biswas P, Deyasi A (2015) Computing transmissivity of one-dimensional defected photonic crystal under polarized incidence for band-pass filter applications. J Electron Dev 21:1816–1822

36. Deyasi A, Sarkar A (2019) Computing optical bandwidth of bandpass filter using metamaterial-based defected 1D PhC. In: AIP conference proceedings, 2072:1, 020003

37. Chakraborty P, Ghosh R, Adhikary A, Deyasi A, Sarkar A (2019) Electromagnetic bandgap formation in two-dimensional photonic crystal structure with DNG materials under TE mode. In: IEEE 3rd International conference on devices for integrated circuit, 26–29, Kalyani, India

38. Gharaati A, Azarshab H (2012) Characterization of defect modes in onedimensional ternary metallo-dielectric nanolayered photonic crystal. Progress Electromagnet Res B 37:125–141

39. El-Amassi DM, Taya SA, Vigneswaran D (2018) Temperature sensor utilizing a ternary photonic crystal with a polymer layer sandwiched between Si and SiO_2 layers. J Theoret Appl Phys 12(4):293–298

40. Mukherjee S, Roy A, Deyasi A, Ghosal S (2016) Dependence of photonic bandgap on material composition for two-dimensional photonic crystal with triangular geometry. Foundations and Frontiers in Computer, Communication and Electrical Engineering, 259–263

41. Banerjee M, Dey R, Deyasi A, Dey S, Das A (2017) Butterworth filter design using ternary photonic crystal structure under polarized incidence of EM Wave. Springer Proceed Phys Adv Optical Sci Eng 194:205–210

42. Deyasi A, Banerji S, Halder A, Bose S (2014) Theoretical investigation on photonic bandgap tailoring in one-dimensional photonic crystal using different numerical methods. In: IEEE international conference on devices, circuits and communications, 1–6, Durgapur, India

43. Deyasi A, Ghosh R, Chakraborty P, Adhikary A, Sarkar A (2021) Investigating fill factor effect on brillouin zone of metamaterial-based 2D photonic crystal. Micro Nanosyst 13(4):433–441

44. Yan L, Hong W, Wu K, Cui TJ (2005) Investigations on the propagation characteristics of the substrate integrated wave-guide based on the method of lines. IEE Proceed Microw Antennas Propagat 152(1):35–42

Possibilities of Realizing an Integrated Power Module for Terahertz Wave Generation

Aritra Acharyya, Arindam Biswas, Subal Kar, Hiroaki Satoh, and Hiroshi Inokawa

Abstract Gallium nitride (GaN) has been emerged as a potential semiconductor material for realizing terahertz (THz) solid-state sources. In this chapter, possibilities of realizing two GaN avalanche transit time (ATT) diode based integrated THz power module structures have been discussed. Design and simulation of the GaN ATT diode have been carried out by using an indigenously developed large-signal simulation tool; diode structure and its detailed simulation results are already reported elsewhere. In this work, two integrated power module structures consisting of (i) a disk-cap circular microstrip patch antenna for narrowband operation and (ii) a slotted-disk circular microstrip antenna for the broadband operation to be fabricated on the diode-head are proposed and analyzed. High Frequency Structure Simulator (HFSS) is used to simulate the frequency response of the proposed structures.

A. Acharyya (✉)
Department of Electronics and Communication Engineering, Cooch Behar Government Engineering College, West Bengal 736170, India
e-mail: ari_besu@yahoo.co.in

A. Biswas
Department of Mining Engineering, Kazi Nazrul University, West Bengal 713340, India

S. Kar
Institute of Radio Physics and Electronics, University of Calcutta, Kolkata 700009, India
e-mail: subal.kar@fulbrightmail.org

H. Satoh · H. Inokawa
Research Institute of Electronics, Shizuoka University, Hamamatsu 4328011, Japan
e-mail: satoh.hiroaki@shizuoka.ac.jp

H. Inokawa
e-mail: inokawa.hiroshi@shizuoka.ac.jp

1   Introduction

It is already well known fact that gallium nitride (GaN) is a potential material for realizing micro- and nano-scale devices which are capable of radiating high power terahertz (THz) waves [1–10]. Out of various solid-state THz radiators like resonant tunneling diodes, heterojunction bipolar transistors (HBTs), high electron mobility field effect transistors (HEMTs), quantum cascade lasers (QCLs), etc. [11– 37] avalanche transit time (ATT) devices, more specifically impact avalanche transit time sources (IMPATT) diodes have more capabilities of generating high-power, high-efficient THz waves [38, 39]. Theoretical studies predict that the GaN based IMPATT oscillators are capable of THz power of the order of milli-watt (mW) up to 5 THz. In this chapter, the authors have presented an elaborated discussion on the possibilities of realizing a novel integrated power module by integrating the passive radiating element (i.e. the antenna) with the active source (i.e. the IMPATT structure).

Initially, the chapter can be organized into six sections which provided brief discussions on the primary developmental steps of the proposed integrated power module. Those are given by.

 (i)   Design and Fabrication of the Seed IMPATT diode Structure,
(ii)   Bonding and Packaging,
(iii) Resonant-Cap Cavity for THz IMPATT Source,
(iv)   Broadband Oscillator Realization,
 (v)   Source-Antenna Integration, and
(vi)   Power Combining.

Finally, in the final section device structure, material properties, simulation technique and simulation results are presented.

2   Design and Fabrication of the Seed IMPATT Diode Structure

Design and simulation of GaN based DDR IMPATT seed structure shown in Fig. 1 for 1.0 THz frequency generation has already been carried out [39]. Doping and thickness of different layers of the DDR structure are already chosen subject to obtain maximum DC to RF conversion efficiency [39]. The metal contacts for both anode and cathode have been confirmed by acquiring knowledge from the published literature. All details regarding the proposed DDR structure and its large-signal performance have been already published elsewhere [39]. However, after several close investigations, some issues have been raised regarding the proposed structure; those are point-wise briefed below.

1. Instead of using Sapphire [c(1000)-Al_2O_3] as the substrate for growing the entire DDR structure, it can be grown on GaN substrate. Primary advantage of homo-epitaxial growth over hetero-epitaxial growth is the reduction of dislocation at the

Anode

Au
Ni
Al
Ti
$p+$, p and n-layers of made of GaN
Mesa etched $n+$-layer made of GaN
$n+$-buffer layer made of GaN
Sapphire

$W_{Au(p)} = 150$ nm
$W_{Ni(p)} = 20$ nm
$W_{p+} = 200$ nm — $p^+ (N_{A+} = 2.0 \times 10^{24}$ m$^{-3})$
$W_p = 185$ nm — $p (N_A = 7.0 \times 10^{23}$ m$^{-3})$
$W_n = 185$ nm — $n (N_D = 6.8 \times 10^{23}$ m$^{-3})$
$W_{n+} = 300$ nm — $n^+ (N_{D+} = 2.0 \times 10^{24}$ m$^{-3})$

Cathode

Au
Ni
Al
Ti

$W_{buff} = 30$–50 μm — n^+-Buffer $(N_{buff} = 1.0 \times 10^{24}$ m$^{-3})$

$W_{sub} = 300$ μm — Sapphire [$c(1000) - Al_2O_3$]

Ti $(W_{Ti(n)1})$/Al $(W_{Al(n)})$/Ti $(W_{Ti(n)2})$/Au $(W_{Au(n)})$

$W_{Ti(n)1} = 30$ nm
$W_{Al(n)} = 100$ nm
$W_{Ti(n)2} = 20$ nm
$W_{Au(n)} = 150$ nm

$r_0 = 2.5$ μm
$r_{S-1} = 10$ μm
$r_{E1} = 40$ μm
$r_{E2} = 70$ μm
$r_{buff} = 100$ μm

Fig. 1 Schematic diagram showing the vertical section of the 1.0-THz GaN DDR IMPATT structure grown on sapphire substrate [39]

interface of the substrate and grown layer. Moreover, better thermal conductivity of GaN than Sapphire enables the GaN substrate to act as an internal heat sink.

2. Since the efficiency of the THz diode is expected to be smaller than 10%; therefore a large amount of heat energy is supposed to be dissipated within the diode during its continuous wave steady-state operation. This will lead to a thermal runway of the diode. In order to avoid this thermal issue, an external heat sink (having cylindrical shape) preferably made of type-IIa diamond (thermal conductivity ~ 1200 W m^{-1} K^{-1}) has to be attached below the substrate layer (Fig. 2a) of the diode chip by using an appropriate adhesive substance (having high thermal conductivity) [40–42]. The temperature distribution inside the type-IIa diamond heat sink is shown in Fig. 2b.

3. Proposed structure may face an electric field crowding effect which may lead to the edge (local) a breakdown or premature breakdown. Necessary structural modification has to be incorporated into the device structure in order to avoid such premature breakdown.

After finding the appropriate solutions for the abovementioned three issues, the bonding and packaging issues will have to be taken into consideration.
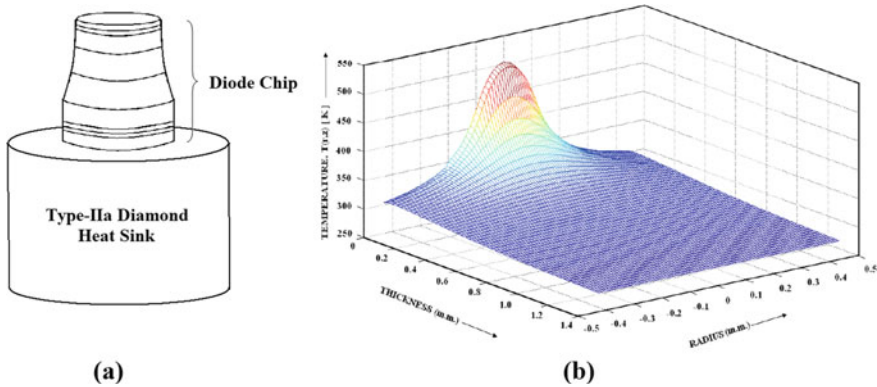
Fig. 2 **a** Diode chip attached on a cylindrical shaped type-IIa diamond heat sink, and **b** temperature distribution inside the heat sink for steady-state thermal operation at 500 K [40]

3 Bonding and Packaging

Wire bonding of anode and cathode terminals of the diode has to be done with the S4 package. Wire bonding of the anode can be done by following the conventional wire edge boding technique. Middle portion of a 5–10 μm diameter gold wire can be bonded on the top of the diode chip (anode) by the thermal sonic compressor and both ends of the gold wire can be connected with gold coated ring-cap (package anode) of the S4 package by using silver epoxy baked at 150 °C for half an hour. The diode chip attached with the external type-IIa diamond heat sink has to be die-bonded to gold coated copper cylinder at the lower surface of the S4 package; it will act as an integral heat sink along with the diamond heat sink. However, the bonding of the cathode with the gold coated copper cylinder (package cathode) is a tricky job. Figure 3 shows the bonding and packaging of the diode chip in an S4 package. Both anode and cathode of the diode chip have to be bonded with gold coated cap and gold plated copper cylinder respectively by using multiple numbers of gold wires in order to reduce effective parasitic series resistance; however, only single wire bonding is shown in Fig. 3. After packaging, the overall equivalent circuit of the packaged diode is shown in Fig. 4. Here, L_p and C_p are the package inductance and capacitance, -R_D, C_D and R_S are the diodes negative resistance, capacitance and parasitic series resistance (all are functions of frequency). At THz regime, stud-type package may be the better option as compared to the S4 package [43].

4 Resonant-Cap Cavity for THz IMPATT Source

The packaged diode has to be embedded in an appropriately designed rectangular waveguide cavity resonator as shown in Fig. 5. The diode has to be reverse-biased and may be embedded inside the cavity via a bias post as shown in Fig. 5. The
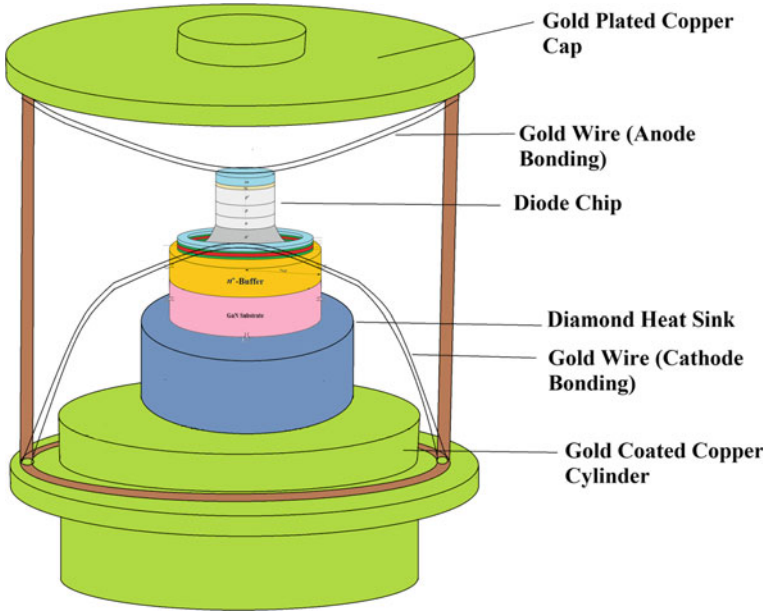
Fig. 3 Schematic illustrating the bonding and S4 packaging of the diode chip

Fig. 4 Equivalent circuit of the S4 packaged IMPATT chip
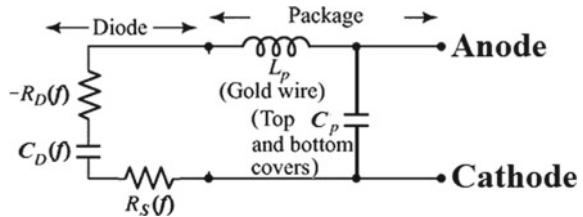
packaged diode mounted inside the suitable cavity resonator (circuit) leads to device-circuit interaction which results in oscillation. The magnitude of the overall negative resistance of the packaged diode designed to operate at 1.0 THz is very small, in the orders of 0.1–1.0 Ω [39]. On the other hand, the real part of the circuit impedance of the cavity resonator (resonant frequency $f_r = 1.0$ THz) remains in the order of 100 Ω. Therefore, a huge impedance mismatch is expected at this point and very inefficient power transfer can occur from the diode to the resonator. The impedance matching between the device and circuit can be achieved by using two possible methods. Those are.

(i) By using reduced height waveguide cavity, and.
(ii) By using resonant-cap cavity.

First method may be suitable for microwave/millimetre frequency range up to even 94 GHz. However, to match impedance from the reduced height waveguide in which
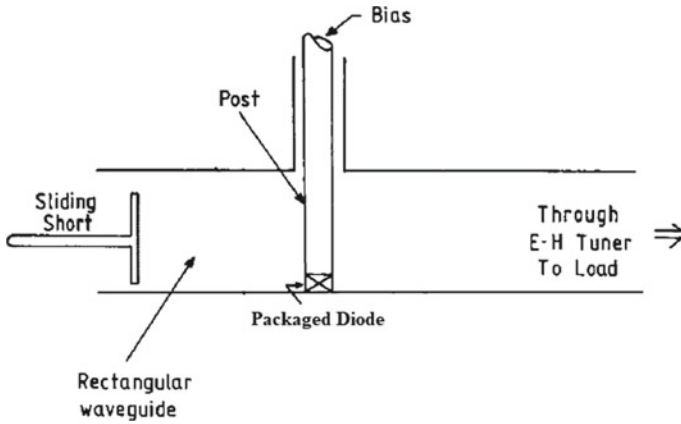
Fig. 5 Schematic of the packaged diode embedded inside a rectangular waveguide cavity resonator via a bias post

the diode is mounted needs to be matched with the full-height waveguide system either with stub matching or stepped impedance/exponential taper transformer. But for higher millimetre-wave frequencies and THz (0.3–10 THz) range it is impractical to use the post-mounting technique. Thus at the THz frequency range, resonant-cap cavity using a disk-cap resonator circuit is the best choice for impedance matching at THz regime [44, 45].

In a resonant-cap cavity type source, the packaged diode is embedded in a high-Q resonant-cap cavity and two together are mounted in a rectangular waveguide through which the source is connected to the load as shown in Fig. 6 [44]. The disk of the resonant-cap and the bottom broad-wall of the rectangular waveguide form the cap cavity, which is equivalent to a radial transmission line causing efficient power transfer from the device to the load [46]. The diameter of the disk must have the dimension $D = (\lambda_r/4 + m \lambda_r/2)$, where λ_r is the resonant wavelength and $m = 0$, 1, 2, 3, …… [46]. By choosing the suitable value of m, an appropriate cap-cavity structure can be designed.

5 Broadband Oscillation

The disk can be made slotted (Fig. 7) in order to increase the bandwidth of the cap-cavity oscillator [47–50].
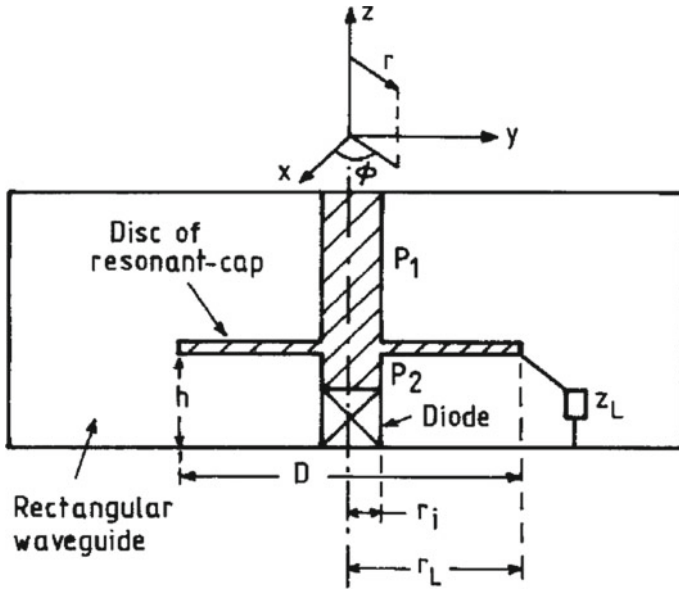
Fig. 6 Schematic of a resonant-cap based source with the devices embedded in the resonant-cap cavity [6]

f_{rH} is associated with R_1
f_{rL} is associated with R_2

(a)   (b)
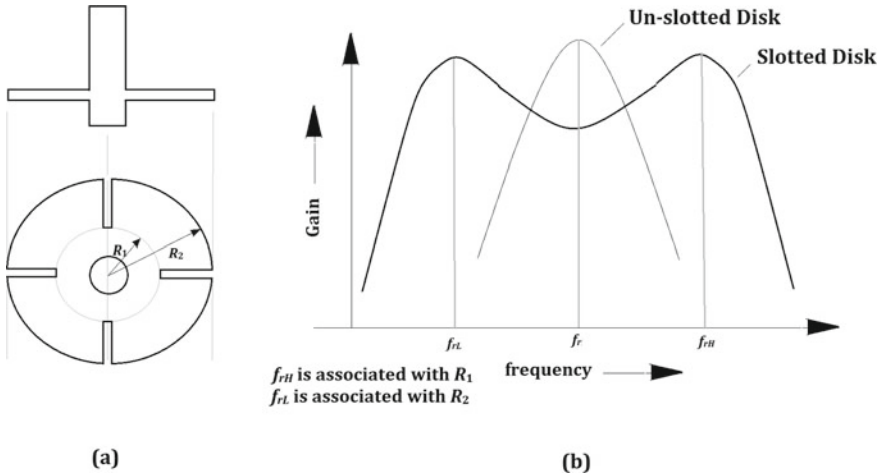
Fig. 7 **a** Side and top views of slotted disk structure, and **b** frequency response of slotted and un-slotted disk structure together with the bottom broad-wall of the waveguide
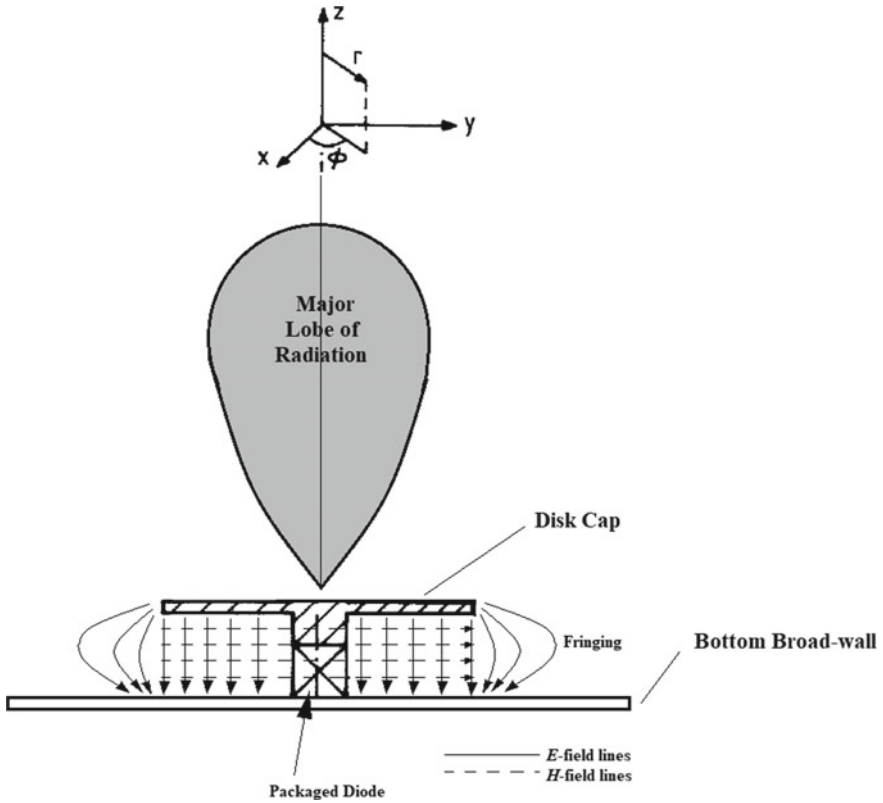
Fig. 8 Radial transmission line structure for source-antenna integration

6 Source-Antenna Integration

The radial transmission line structure itself can behave like an integral antenna for the THz IMPATT source. Its principle of working may be understood in terms of modelling it like a microstrip antenna. Its major radiation lobe will be along the direction of z-axis as shown in Fig. 8. However, the bias feeding point to the packaged IMPATT will have to be decided (bias post should not interfere with the major lobe) in order to obtain the best radiation efficiency.

7 Power Combining

THz power output from a single source may be very small (practically < 10 mW). Therefore, suitable power combining multiple sources must be implemented in order to enhance the radiated THz power. Twin-cap IMPATT power combining technique
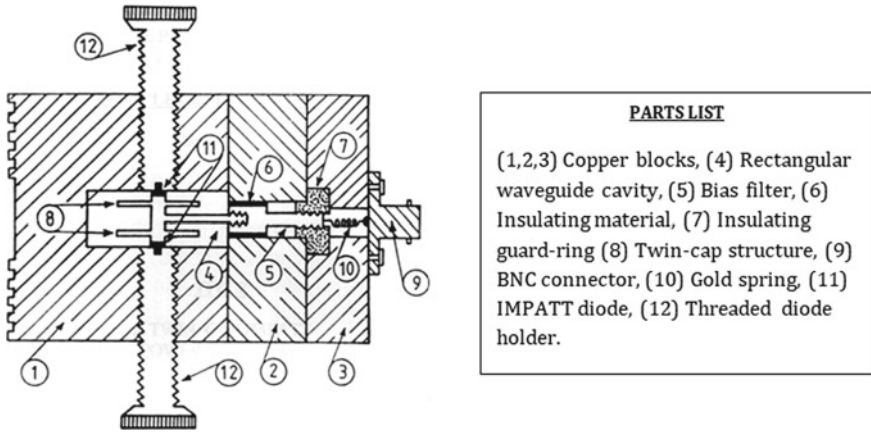
Fig. 9 Twin-cap IMPATT power combiner [50]

PARTS LIST

(1,2,3) Copper blocks, (4) Rectangular waveguide cavity, (5) Bias filter, (6) Insulating material, (7) Insulating guard-ring (8) Twin-cap structure, (9) BNC connector, (10) Gold spring, (11) IMPATT diode, (12) Threaded diode holder.

[50], vide Fig. 9, may be used that may be optimized for phase coherence using some form of Meta-surface too.

8 Proposed Device Structures and Simulation Results

Design and simulation of the GaN ATT diode have been carried out by using an indigenously developed large-signal simulation tool [39]; diode structure and its detailed simulation results are already reported elsewhere [39]. The important material parameters used in the simulation are tabulated in Table 1 [51–54]. In this work, two integrated power module structures consisting of (i) a disk-cap circular microstrip patch antenna for narrowband operation and (ii) a slotted-disk circular microstrip antenna for the broadband operation to be fabricated on the diode-head are proposed and analyzed. High Frequency Structure Simulator (HFSS) is used to simulate the frequency response of the proposed structures. Figures 10 and 11 show the device structures and Figs. 12 and 13 show corresponding HFSS layouts. The two-dimensional (2D) electric field and carrier concentrations plot for the centre voltage 30 V are shown in Figs. 16 and 17 respectively. Maximum electric field at the metallurgical junction is found to be $\xi_{max} = 22.5476 \times 10^7$ V m^{-1}. The electric field crowding effect was not considered for our simulation; however, it is better to study its impact while simulation its actual structure. The real and imaginary parts of the device ($Z_d(f) = R_d(f) + jX_d(f)$) and antenna ($Z_c(f) = R_c(f) + jX_c(f)$) impedances are plotted against frequency in Fig. 18. Antenna part is designed such a way that perfect impedance match between the device and circuit is achieved (i.e. $|R_d(f)||_{f=1\,\text{THz}} = |R_c(f)||_{f=1\,\text{THz}}$ and $|X_d(f)||_{f=1\,\text{THz}} = |X_c(f)||_{f=1\,\text{THz}}$) at $f = 1$ THz (Figs. 14 and 15).

Table 1 Important material parameters of GaN at room temperature

Material parameter	Value	Electric Field range, ξ ($\times 10^7$ V m^{-1})	Corresponding equation	Citation
Bandgap, E_g (eV)	3.4691	–		[51, 52]
Density of state effective mass, m_d^* ($\times m_0$)	1.5000	–		[51, 52]
Effective mass of electrons, m_n^* ($\times m_0$)	0.2000			[51, 52]
Effective mass of holes, m_p^* ($\times m_0$)	0.8000			[51, 52]
Permittivity, ε_r	10.4000	–		[51, 52]
Electron mobility, μ_n (m^2 V^{-1} s^{-1})	0.1000	–		[51, 52]
Hole mobility, μ_p (m^2 V^{-1} s^{-1})	0.0034	–		[51, 52]
Electron diffusivity, D_n ($\times 10^{-4}$ m^2 s^{-1})	2.6000	–		[51, 52]
Hole diffusivity, D_p ($\times 10^{-4}$ m^2 s^{-1})	0.8798	–		[51, 52]
Electron diffusion length, L_n ($\times 10^{-6}$ m)	6.5000	–		[51, 52]
Hole diffusion length, L_p ($\times 10^{-6}$ m)	2.1000	–		[51, 52]
Critical field, ξ_c ($\times 10^5$ V m^{-1})	0.5000	–		[51, 52]
Saturation drift velocity of electrons, v_{sn} ($\times 10^5$ m s^{-1})	3.0000	–	$v_n(\xi) =$ $\dfrac{\mu_n\xi + v_{sn}(\xi/\xi_c)^4}{1+(\xi/\xi_c)^4}$	[53]
Saturation drift velocity of holes, v_{sp} ($\times 10^5$ m s^{-1})	0.7500	–	$v_p(\xi) =$ $v_{sp}\left[1 - \exp\left(\dfrac{-\mu_p\xi}{v_{sp}}\right)\right]$	[53]
First ionization coefficient of electrons, A_n ($\times 10^9$ m^{-1})	13.8000	4.00–10.00	$\alpha_n(\xi) =$ $A_n \exp\left[\dfrac{-B_n}{\xi}\right]$	[54]
	12.2700	>10.00		
Second ionization coefficient of electrons, B_n ($\times 10^9$ V m^{-1})	1.4280	4.00–10.00		
	1.3630	>10.00		

(continued)

Table 1 (continued)

Material parameter	Value	Electric Field range, ξ ($\times 10^7$ V m^{-1})	Corresponding equation	Citation
First ionization coefficient of holes, A_p ($\times 10^9$ m^{-1})	0.6867	4.00–10.00	$\alpha_p(\xi) =$ $A_p \exp\left[\dfrac{-B_p}{\xi}\right]$	[54]
	0.3840	>10.00		
Second ionization coefficient of holes, B_p ($\times 10^9$ V m^{-1})	0.8720	4.00–10.00		
	0.7950	>10.00		

$m_0 = 9.1 \times 10^{-31}$ kg is the rest mass of an electron

$\varepsilon_s = \varepsilon_r\,\varepsilon_0$ is the permittivity of the semiconductor material; where $\varepsilon_0 = 8.85 \times 10^{-12}$ F m^{-1} is the permittivity of vacuum
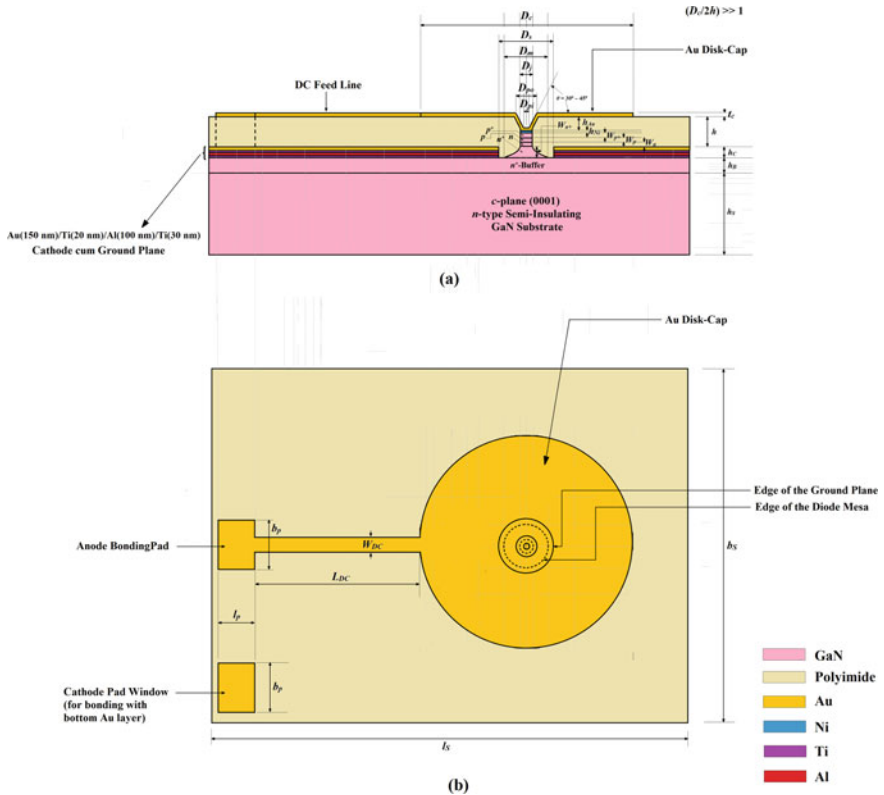
Fig. 10 Schematic diagrams of the **a** front-view and **b** top-view of the GaN integrated power module
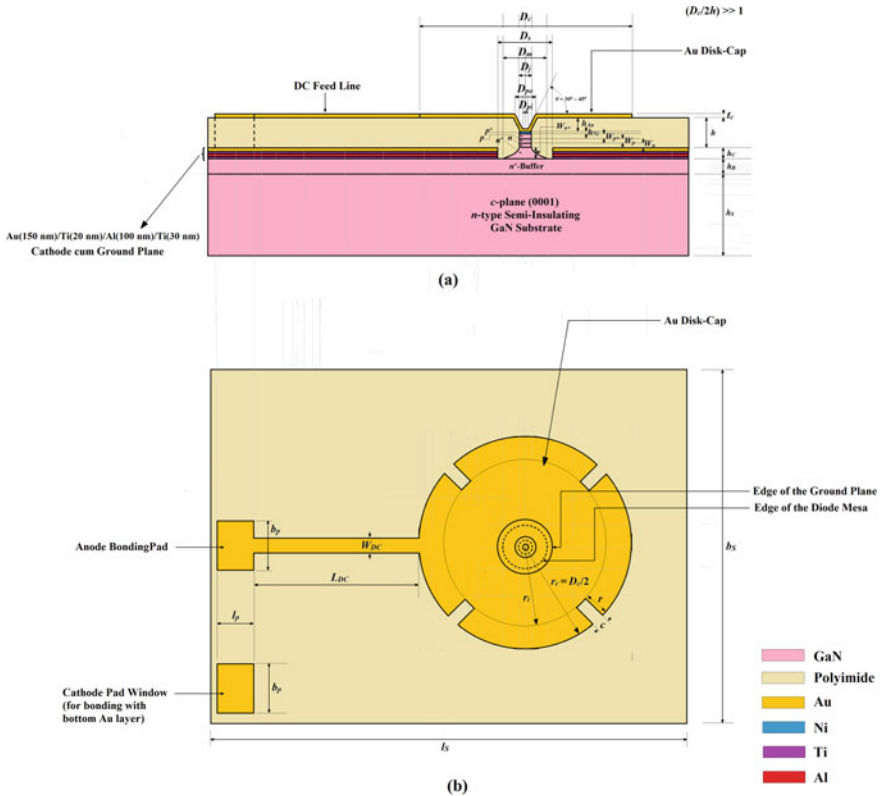
Fig. 11 Schematic diagrams of the **a** front-view and **b** top-view of the slotted-disk GaN integrated power module

Figures 17 and 18 show the variations of S_{11} parameter and VSWR of the disk-cap and slotted-disk GaN integrated power modules respectively. Narrowband operation of the disk-cap structure and broadband operation of the slotted-disk structure can be confirmed from Figs. 17 and 18. Two-dimensional field plots, 3D Gain and directivity plots of those structures shown in Figs. 19 and 20 depict the antenna performance at 1.0 THz (Table 2).

Fig. 17. Variation of S11 parameter of the disk-cap and slotted-disk GaN integrated power modules with frequency

9   Summary

In this chapter, possibilities of realizing two GaN ATT diode based integrated THz power module structures have been discussed. Design and simulation of the GaN ATT diode have been carried out by using an indigenously developed large-signal
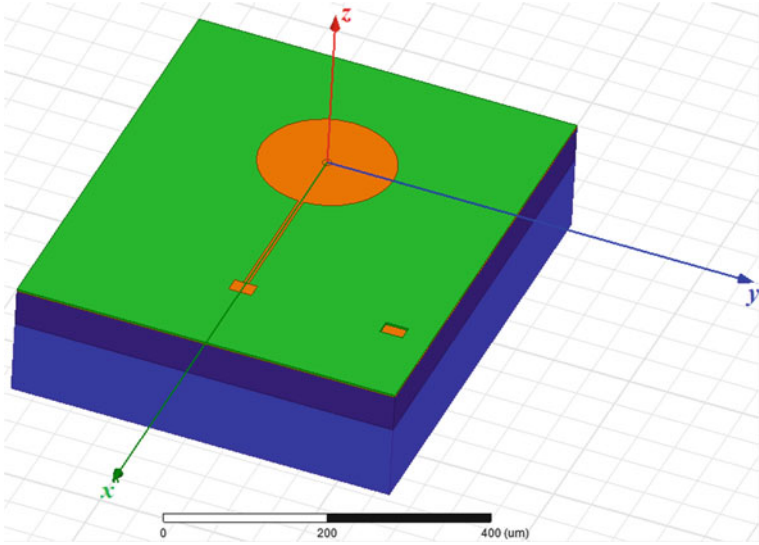
Fig. 12 HFSS layout of the GaN integrated power module
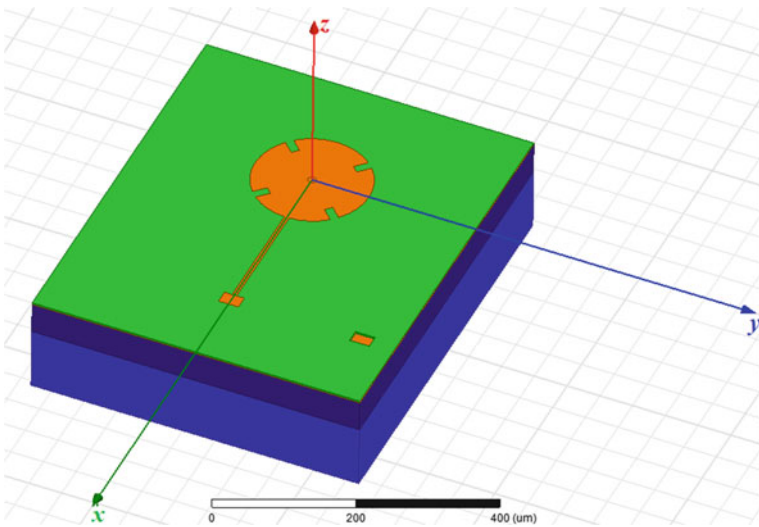
Fig. 13 HFSS layout of the slotted-disk GaN integrated power module

simulation tool; diode structure and its detailed simulation results are already reported elsewhere. In this work, two integrated power module structures consisting of a disk-cap circular microstrip patch antenna for narrowband operation and a slotted-disk circular microstrip antenna for the broadband operation to be fabricated on the diode-head are proposed and analyzed. High Frequency Structure Simulator
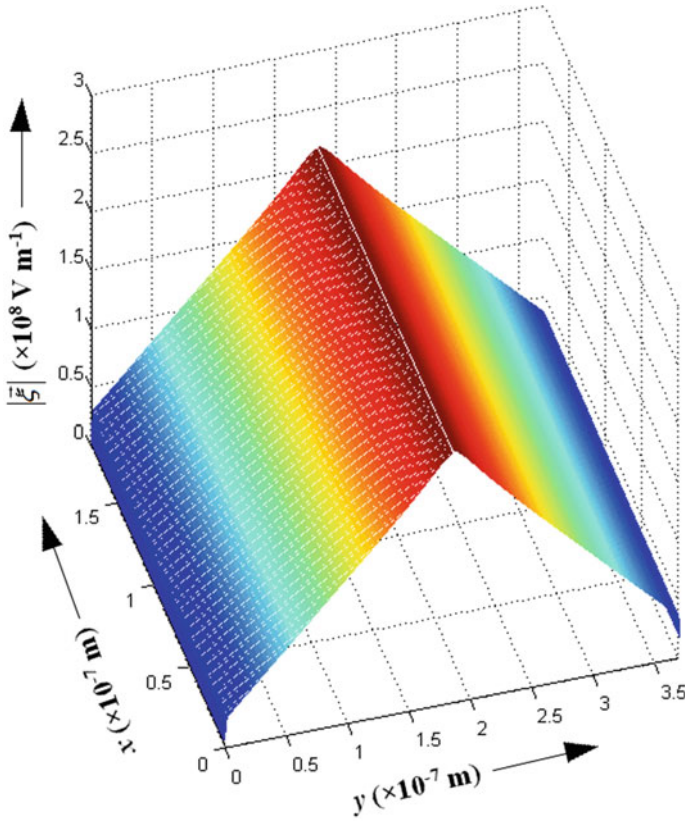
Fig. 14 2-D Electric field profile
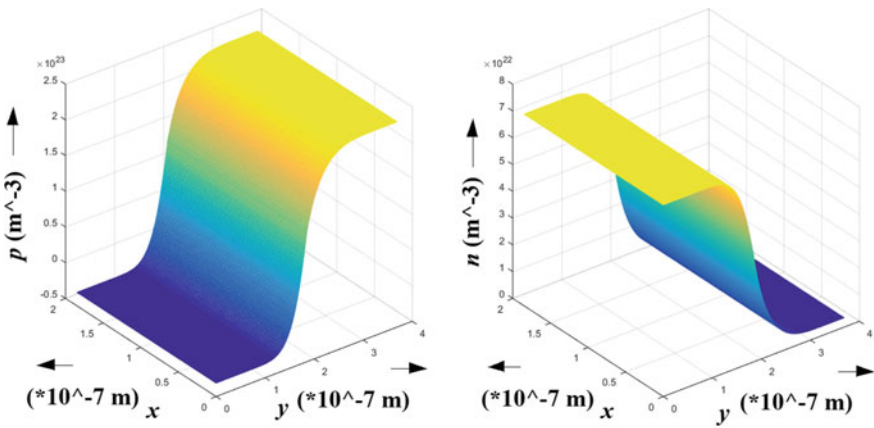
Fig. 15 2-D carrier density profiles
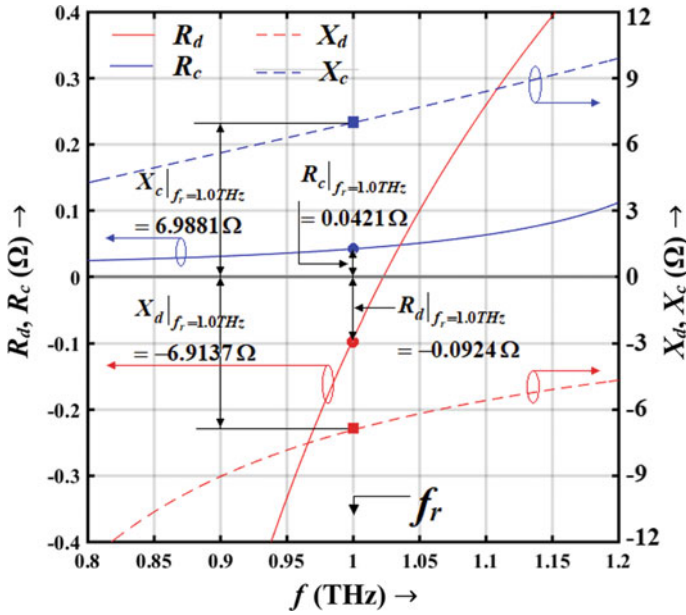
Fig. 16 Variations of real (R_d) and imaginary (X_d) parts of the large-signal diode impedance as well as real (R_c) and imaginary (X_c) parts of the cap-circuit impedance at the diode plane (i.e. at r = $D_j/2$)

Fig. 17 Variation of S11 parameter of the disk-cap and slotted-disk GaN integrated power modules with frequency
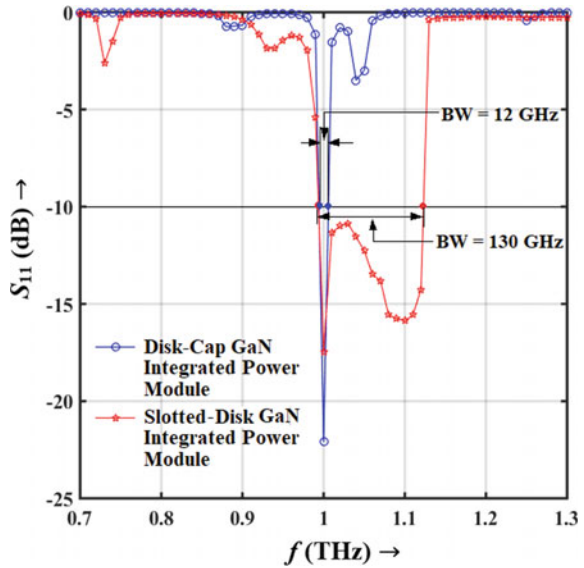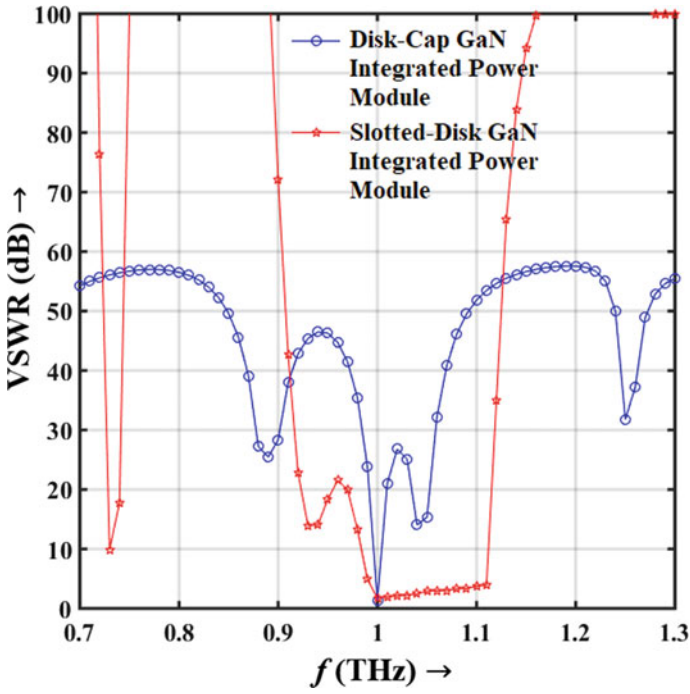
Fig. 18 Variation of VSWR of the disk-cap and slotted-disk GaN integrated power modules with frequency
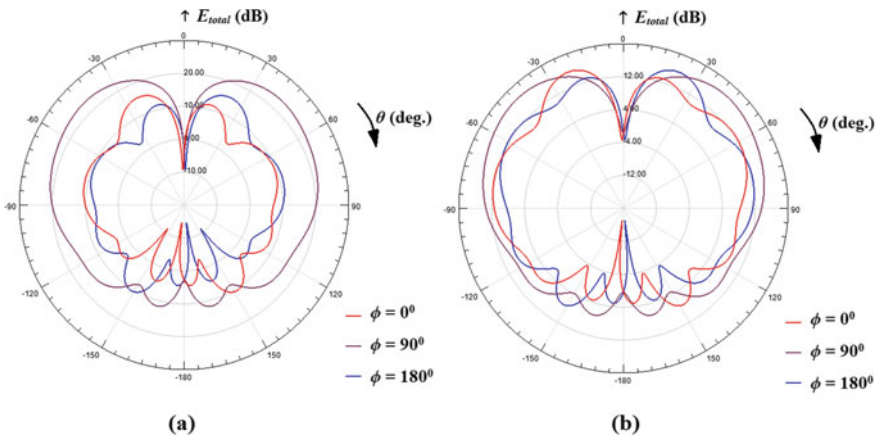
Fig. 19 2-D field patterns of **a** disk-cap and **b** slotted-disk GaN integrated power module for ϕ values of 00, 900 and 1800 at 1.0 THz
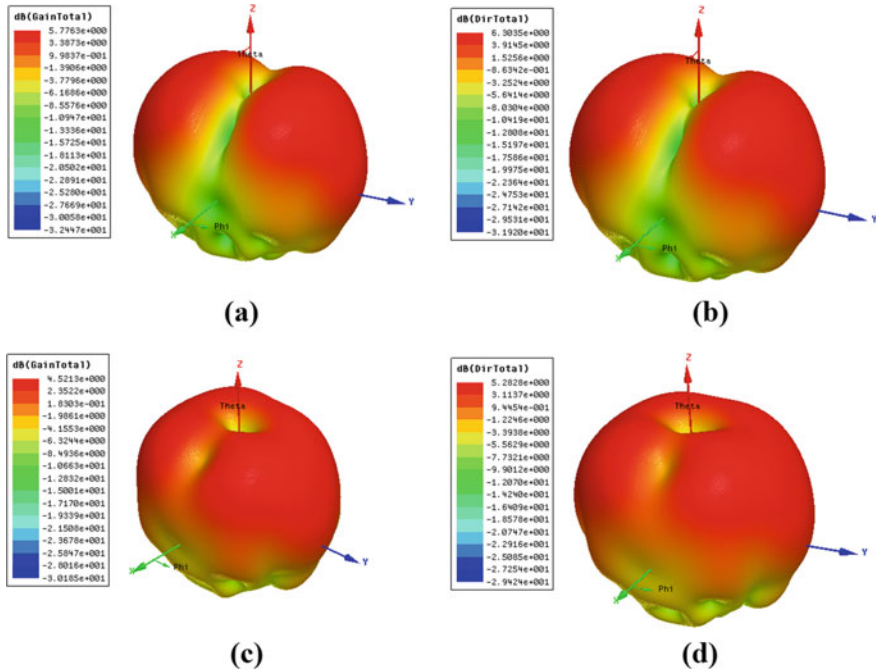
Fig. 20 3-D **a** gain and **b** directivity plots (3-D radiation patterns) of disk-cap GaN integrated power module at 1.0 THz; 3-D **c** gain and **d** directivity plots (3-D radiation patterns) of slotted-disk GaN integrated power module at 1.0 THz

(HFSS) is used to simulate the frequency response of the proposed structures. The proposed integrated power module structures have immense potentialities to be used as powerful and efficient THz source in various THz biomedical applications.

Table 2 Design parameters of the 1.0 THz GaN integrated power module considering the effect of fringing field

Length/breadth/thickness	Value (μm)	Doping concentration	Value (m^{-3})
W_n	0.185	N_{A+}	2.0×10^{24}
W_p	0.185	N_{D+}	2.0×10^{24}
W_{n+}	0.300	N_A	7.0×10^{23}
W_{p+}	0.200	N_D	6.8×10^{23}
h_{Au}	2.410	N_{buff}	1.0×10^{24}
h_{Ni}	0.020		
h_C	0.300		
t_c	0.100		
$h = (h_{Au} + h_{Ni} + W_{p+} + W_p + W_n - h_c)$	3.000		
D_c	174.000		
D_j	11.900		
D_m	20.000		
D_s	30.000		
$D_{po} = (D_j + 2h_{Au} \cot\theta - 2t_c)$	16.720 – 20.250 (for $\theta = 30°–45°$)		
$D_{pi} = (D_j - 2t_c)$	11.700		
b_S	500.000		
l_S	600.000		
L_{DC}	180.000		
W_{DC}	10.000		
b_p	30.000		
l_p	20.000		
r	24.990		
c	12.490		
$r_i = (D_c/2 - r)$	74.510		
$r_c = D_c/2$	87.000		

References

1. Shur MS (2014) AlGaN/GaN plasmonic terahertz electronic devices. J Phys 486:012025–1–6
2. Dyakonov MI, Shur MS (1996) Plasma wave electronics: novel terahertz devices using two dimensional electron fluid. IEEE Trans Electron Devices 43(10):1640–1645
3. Hocker LO (1967) Absolute frequency measurement and spectroscopy of gas laser transitions in the far infrared. Appl Phys Lett 10:147–149
4. Duguay M, Hansen J (1967) Optical frequency shifting of a modelocked laser beam. Int Electron Devices Meeting 13:34–38
5. Lu J-Q et al (1997) Detection of microwave radiation by electronic fluid in AlGaN/GaN heterostructure field effect transistors. In Proceedings of IEEE/ cornell conference on advanced concepts in high speed semiconductor devices and circuits, pp 211–217

6. Knap W et al (2002) Nonresonant detection of terahertz radiation in field effect transistors. J Appl Phys 91:9346–9353
7. Dyakonov M, Shur MS (1996) Detection, mixing, and frequency multiplication of terahertz radiation by two-dimensional electronic fluid. IEEE Trans Electron Devices 43(3):380–387
8. Shur MS, Lu JQ (2000) Terahertz sources and detectors using two-dimensional electronic fluid in high electron-mobility transistors. IEEE Trans Microwave Theory Tech 48(4):750–756
9. Allen SJ, Tsui DC, Logan RA (1977) Observation of the two-dimensional plasmon in silicon inversion layers. Phys Rev Lett 38(17):980–983
10. Tsui DC, Gornik E, Logan RA (1980) Far infrared emission from plasma oscillations of Si inversion layers. Solid State Commun 35(11):875–877
11. El Fatimy A et al (2006) Terahertz detection by GaN/AlGaN transistors. Electron Lett 42(23):1342–1343
12. Faist J et al (1994) Quantum cascade laser. Science 264:553–556
13. Köhler R et al (2002) Terahertz semiconductor-heterostructure laser. Nature 417:156–159
14. Williams BS et al (2005) Operation of terahertz quantum-cascade lasers at 164 K in pulsed mode and at 117 K in continuous-wave mode. Opt Express 13(9):3331–3339
15. Bellotti E et al (2009) Monte Carlo simulation of terahertz quantum cascade laser structures based on wide-bandgap semiconductors. J Appl Phys 105:113103–1–9
16. Bellotti E et al (2008) Monte Carlo study of GaN versus GaAs terahertz quantum cascade structures. Appl Phys Lett 92:1011121–1011123
17. Sudradjat F et al (2010) Sequential tunneling transport characteristics of GaN/AlGaN coupled-quantum-well structures. J Appl Phys 108:103704–1–5
18. Turchinovich D et al (2003) Ultrafast polarization dynamics in biased quantum wells under strong femtosecond optical excitation. Phys Rev B 68:241307–1–8
19. Turchinovich D, Monozon BS, Jepsen PU (2006) Role of dynamical screening in excitation kinetics of biased quantum wells: nonlinear absorption and ultrabroadband terahertz emission. J Appl Phys 99:013510–1–8
20. Hirayama H et al (2015) Recent progress and future prospects of THz quantum-cascade lasers. Proceedings of SPIE - the international society for optical engineering 9382:938217–1–11
21. Terashima W, Hirayama H (2015) Terahertz frequency emission with novel quantum cascade laser designs. Proc SPIE 6958:11–13
22. Miho S, Lin T-T, Hirayama H (2013) 1.9 THz selective injection design quantum cascade laser operating at extreme higher temperature above the $k_B T$ line. Phys Status Solidi C 10(1):1448–1451
23. Lin T-T, Hirayama H (2013) Improvement of operation temperature in GaAs/AlGaAs THz-QCLs by utilizing high Al composition barrier. Phys Status Solidi C 10(11):1430–1433
24. Lin T-T, Ying L, Hirayama H (2012) Threshold current density reduction by utilizing high-al-composition barriers in 3.7 THz GaAs/$Al_x Ga_{1-x}$As quantum cascade lasers. Appl Phys Express 5:012101
25. Edmunds C et al (2014) Terahertz intersubband absorption in non-polar m-plane AlGaN/GaN quantum wells. Appl Phys Lett 105:021109–1–3
26. Beeler M, Trichas E, Monroy E (2013) III-nitride semiconductors for intersubband optoelectronics: a review. Semicond Sci Technol 28(7):074022
27. Beeler M et al. (2014) Pseudo-square AlGaN/GaN quantum wells for terahertz absorption. Appl Phys Lett 105:131106–1–3
28. Durmaz H et al (2016) Terahertz intersubband photodetectors based on semi-polar GaN/AlGaN heterostructures. Appl Phys Lett 108:201102–1–3
29. Krishnamurthy S et al (1997) Bandstructure effect on high-field transport in GaN and GaAl. Appl Phys Lett 71(14):1999–2001
30. Foutz BE et al (1997) Comparison of high field electron transport in GaN and GaAs. Appl Phys Lett 70(21):2849–2851
31. Alekseev E, Pavlidis D (2000) GaN Gunn diodes for THz signal generation. IEEE MTT-S Int Microwave Symp Digest 3:1905–1908

32. Alekseev E et al (2000) GaN-based NDR devices for THz generation. In Proceedings of the Eleventh International Symposium on Space Terahertz Technology, pp 162
33. Veksler D et al (2006) GaN heterodimensional Schottky diode for THz detection. In 5th IEEE conference sensors, pp 323–326
34. Peatman WCB, Crowe TW, Shur MS (1992) A novel Schottky/2-DEG diode for millimeter- and submillimeter-wave multiplier applications. IEEE Electron Device Lett 13(1):11–13
35. Reklaitis A (2004) Monte Carlo study of hot-carrier transport in bulk wurtzite GaN and modeling of a near-terahertz impact avalanche transit time diode. J Appl Phys 95(12):7925–7935
36. Reklaitis A, Reggiani L (2005) Giant suppression of avalanche noise in GaN double-drift impact diodes. Solid State Electron 49:405–408
37. Wang Y et al (2016) Modulation of the domain mode in GaN-based planar Gunn diode for terahertz applications. Phys Status Solidi (c) 13(5–6):382–385
38. Acharyya A, Banerjee JP (2014) Prospects of IMPATT devices based on wide bandgap semiconductors as potential terahertz sources. Appl Nanosci 4:1–14
39. Biswas A, Sinha S, Acharyya A, Banerjee A, Pal S, Satoh H, Inokawa H (2018) 1.0 THz GaN IMPATT source: effect of parasitic series resistance. J Infrared Millim Terahertz Waves 39(10):954–974
40. Acharyya A, Banerjee JP (2011) Heat sink design and temperature distribution analysis for millimeter wave IMPATT oscillators using finite difference method. Archives Appl Sci Res 3(2):107–120
41. Acharyya A, Chakraborty J, Das K, Datta S, De P, Banerjee S, Banerjee JP (2013) Large-signal characterization of DDR silicon IMPATTs operating up to 0.5 THz. Int J Microw Wirel Technol 5(5):567–578
42. Kar S (2016) Microwave engineering: fundamentals, design and applications. Universities Press. ISBN: 9788173719899, 8173719896
43. Kar S (1997) Modelling and characterization of microwave resonant-cap circuits. Microw Opt Technol Lett 16(6):400–403
44. Kar S (1998) An experimental technique for the design of optimized resonant-cap circuits for microwave IMPATT oscillators and amplifiers. Microw Opt Technol Lett 19(2):81–84
45. Kar S (1989) Microwave properties of IMPATT oscillators and amplifiers with the device embedded in normal and modified resonant-cap cavities. Ph.D. dissertation, University of Calcutta, Chap. 2, pp 8–68
46. Kar S, Roy SK (1983) A modified resonant-cap microwave IMPATT oscillator. Indian Patent 157098, March 9. [Issued on 18.1.86]
47. Kar S, Roy SK (1984) A modified resonant-cap microwave IMPATT amplifier. Indian Patent 161758, August 24. [Issued on 30.1.88]
48. Kar S, Roy SK (1993) Experimental studies on the improvement of the performance of resonant-cap type microwave IMPATT oscillators through appropriate modification of the resonant-cap cavity. Int J Electron 75:941–950
49. Kar S (1997) Experimental studies on a modified resonant-cap microwave IMPATT amplifier with improved performance. Int J Electron 82:555–566
50. Kar S A twin-cap IMPATT power combiner. Indian Patent No.: 18414, [Issued on 04.07.1996]
51. Kar S Electronic archive: new semiconductor materials, characteristics and properties. http://www.ioffe.ru/SVA/NSM/Semicond/index.html. Accessed June 2014
52. Zeghbroeck BV (2011) Principles of semiconductor devices. Colorado Press, USA
53. Shiyu SC, Wang G (2008) High-field properties of carrier transport in bulk wurtzite GaN: monte carlo perspective. J Appl Phys 103:703–708
54. Kunihiro K, Kasahara K, Takahashi Y, Ohno Y (1999) Experimental evaluation of impact ionization coefficients in GaN. IEEE Electron Device Letter 20(12):608–610

Design of Si$_{(1-x-y)}$ Sn$_{(x)}$ C$_{(y)}$/Si Hetrostructure EOM for Optical Signal Processing Applications

Jayabrata Goswami, Rupanjana Chattaopadhyay, and Tanushree Saha

Abstract Design and Simulation are carried out to achieve Si$_{(1-x-y)}$ Sn$_{(x)}$ C$_{(y)}$ /Si hetrostructure Electro-Optic Modulator (EOM) for optimum performance. The absorption coefficient, current and turn on time are calculated by solving the equations by utilizing an indigenously created program for simulation of the device properties. Therefore the come about shows that the on-current and switching speed of operation of the modulator is found better at 20 µm design length. Thus Si$_{(1-x-y)}$ Sn$_{(x)}$ C$_{(y)}$ /Si hetrostructure broadband Electro-Optic Modulator (EOM) are promising next generation devices for optical signal processing applications.

1 Introduction

Si is the material that has overwhelmed the semiconductor business for over the previous couple of decades as a result Si is the least expensive electronics innovation for integrated circuits. The foremost necessary reason for the dominance of Si is that the accessibility of its 2 insulators, silicon oxide and chemical element compound. The chemistry of Si and Si insulators enables statement on any particular etching forms to be created with outstandingly high consistency. The chemical element material system has a beautiful target for photonic system applications currently on a daily basis. In recent years, work on Si primarily based hetrostructure and quantum wells have been extended to hide different opto-electronic devices, still as Si primarily based opto-physics has been gaining additional and additional importance day by day. Each all-silicon and silicon–germanium electro-optic modulators are incontestable [1]. Most of the arranged electro-optic devices misuse the free carrier dispersion result to differ each real index of refraction and optical coefficient of absorption. Typically

J. Goswami (✉)
Netaji Subhas Open University, DD 26, DD Block, Sector 1, Bidhannagar, Kolkata 700064, West Bengal, India
e-mail: goswamijayabrata@gmail.com

R. Chattaopadhyay · T. Saha
Techno Engineering College, Banipur College Road, Banipur, Habra 743233, West Bengal, India

regularly as a result of the unstrained unadulterated crystalline Si doesn't show direct electro-optic (Pockels) result, and thus the refractive-index changes much appreciated to the Franz-Keldysh result and Kerr result is fantastically powerless PM in a really specific region of optical devices, like Mach–Zehnder modulators, total-internal-reflection (TIR)-based structures, cross switches, Y switches, and Fabry–Pérot (F-P) resonators, to boot usual tweak the yield concentrated. So, the modulators essentially based upon the plasma scattering result require a conventional cover of the optical mode with the locale wherever there'll be larger than usual concentrations square measure injected [2–5].

In SiGe/Si heterostructures, there'll be an oversized lattice match between Ge and chemical element ends up in terribly little values for the vital thickness of epitaxial layers [6–8]. Recently, it had been shown that Si1-yCy & Si1-x-yGexCy layers will be adult pseudomorphically on Si (001) victimization MBE or completely different chemical vapour deposition technique [9]. This new material would possibly overcome a number of the constraints of SiGe on Si (001). Inquire about greatly super saturated, carbon containing combinations on Si substrate begun exclusively numerous years past. In the interim, information has been collected on growth, strain, control, thermal stability, carbon effects on band structure and charge transport. Low carbon concentrations will indeed be accustomed smother diffusion of dopants. Thus SiGeC/Si Electro-Optic Modulator has been reported [10] at 30 μm length.

In this analysis work, the authors will examine that silicon-tin-carbon (SiSnC) alloy heterostructures will be accustomed style optical wave guides which will confine each of the injected carriers and therefore the optical mode to the waveguide core, in this manner giving openings for realizing predominant compact broadband electro-optic phase/intensity modulators on the chemical component. SiSnC alloys are around for over ten a long time and are accustomed create numerous electronic devices like hetrojunction bipolar transistors and thermo-electrical coolers, though SiSnC/Si hetrostructures have additionally been utilized in wave guide picture detectors. Throughout this analysis work, authors will examine SiSnC because of the active region material p-i-n hetrostructure electro-optic modulator. In this way, it'll appear that the modulators with lengths around 20 μm and turn on times underneath 0.1 ns are feasible with optimized styles.

2   Device Band Diagram and Analysis

In SiSnC/Si electro-optic modulator wave guide, there'll be 2 bands offset shown in Fig. 1 during this 2 band profile i.e. the physical phenomenon and valence band profile, the physical phenomenon band offset between Si and Si $_{1-x-y}$ Sn$_x$ C$_y$ for tiny carbon fraction and therefore the serious hole valence band offset is shown within the figure.

The physical phenomenon band offset is going to increase between Si and SiSnC compared thereto between Si and SiGe for the addition of carbon. Thus for big band offset values square measure decent to restrict the injected electrons and holes within the wave guide active region.
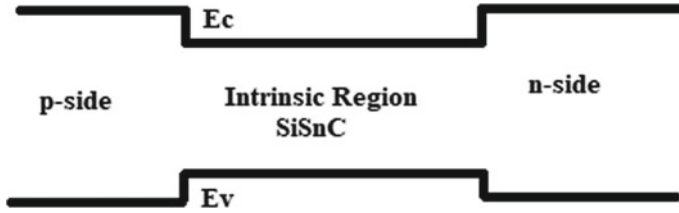
Fig. 1 Band diagram for a SiSnC p-i-n hetrostructure device

3 Device Absorption Coefficient Model and Refractive Index Model

In SiSnC alloys, the refractive model depends solely on the band gap of the alloy and therefore the indexes of bulk chemical elements and tin. Therefore during this work, the author's square measure studied the index of refraction of a SiSnC layer is assumed to be a twin of that of a SiGe layer with an identical band gap [11].

$$n_{Si1-x-ySnxCy} = n_{Si} + (n_{Sn} - n_{Si})(x - \frac{2.1}{0.9}y) \tag{1}$$

It is attention-grabbing to match a straightforward free-carrier or Drude model of c-Si Δn results and to experimental $\Delta\alpha$ information [12]. The well-known equations refraction and absorption are much appreciated to free electrons and free holes unit of measurement as takes after:

$$\Delta n = -\left(\frac{e^2\lambda^2}{8\pi^2 c^2 \varepsilon_0 n}\right)\left[\frac{\Delta N_e}{m_{ce}^*} + \frac{\Delta N_h}{m_{ch}^*}\right] \tag{2}$$

$$And\ \Delta\alpha = \left(\frac{e^2\lambda^2}{4\pi^2 c^3 \varepsilon_0 n}\right)\left[\frac{\Delta N_e}{m_{ce}^{*2}\mu_e} + \frac{\Delta N_h}{m_{ch}^{*2}\mu_h}\right], \tag{3}$$

where ε_0 is the permittivity of free house, e is the electronic charge, n is the index of refraction of unflurried c-Si, m_{ce}^* is the conduction effective mass of electrons, m_{ch}^* is the conduction effective mass of holes, μ_e is that the lepton quality and μ_h is that the hole quality.

The external potency is powerfully enthusiastic about the fabric coefficient of absorption, A, associate degree estimate of A as an operation of gauge boson energy (or wavelength) and tin content of the alloy is critical. During this work, material absorption was calculated employing a show for phonon-assisted indirect optical moves. Therefore the absorption coefficient is given by

$$A = 0\hbar\omega \leq E_g - K\theta \tag{4}$$

$$= B_a \frac{[\hbar\omega - \mathrm{E_g} + K\theta]^2}{\exp\left(\frac{\theta}{T}\right) - 1} \mathrm{E}_g - K\theta < \hbar\omega < \mathrm{E_g} + K\theta \tag{5}$$

$$= B_a \frac{[\hbar\omega - \mathrm{E_g} + K\theta]^2}{\exp\left(\frac{\theta}{T}\right) - 1} + B_e \frac{[\hbar\omega - \mathrm{E_g} - K\theta]^2}{1 - \exp(-\frac{\theta}{T})} \hbar\omega \geq \mathrm{E_g} + K\theta, \tag{6}$$

where $\mathrm{E_g}$ is the indirect-bandgap, T is the temperature, and K is the Boltzman constant, and θ is the phonon equivalent temperature. The parameters Ba and Be square measure quotient factors for the method of phonon absorption and phonon emission, severally. From the higher than expression, the primary term, $\hbar\omega \geq \mathrm{E_g} + K\theta$, whereas within the second, $\hbar\omega \leq \mathrm{E_g} - K\theta$. This expression depicts the absorption of indirect electronic moves including the creation additionally the destruction of phonons of given energy $(K\theta)$.

On the off chance that the phonons handiest in supporting the indirect transitions truly have a place to one branch of the undulation range, the higher than expression suffices to give up their vitality appropriately. That the result of carbon and strain is ignored with the special case of the adjustment to the band gap.

4 Modulator Design Model

In Fig. 2 a pair shows the actual cross-sectional read of the p-i-n diode a broadband electro-optic modulator with SiSnC /Si Hetero Structure materials. The most attention of the Mach–Zehnder measuring instrument style is to convert modulation in one arm of the measuring instrument to amplitude/intensity modulation at the output [10]. The section shift is sort of near to require in one arm of the measuring instrument with relevance to the opposite arm. The dynamic region of the SiSnC is sandwiched between n- and p-doped Si protection layers that's why the core layer makes a difference to restrict each of the injected carriers moreover since the optical mode. That the execution of the modulator is characterized by the length additionally the altered current required to achieve to accomplish segment move. The modulator current (I_m) can be calculated as

$$\frac{\partial l}{\partial t} = \frac{Im}{qV} - \frac{l}{\tau_{SRH}} - R_{Auger}(l) - \frac{l}{\tau_{on(l)}} \tag{7}$$

where V is the overall core region volume, τ_{SRH} is the Schockley-Read-Hall carrier recombination time period, R_{Auger} is the Auger recombination rate that is given by

$$R_{Auger} = C_n n^2 p + C_p n p^2 \tag{8}$$
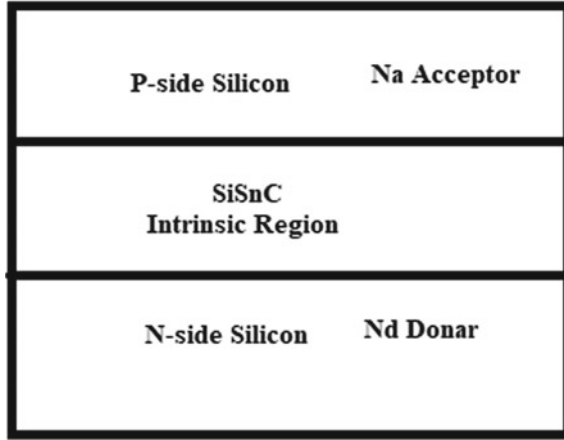
Fig. 2 Particular cross-sectional read of the p-i-n diode electro-optic modulator
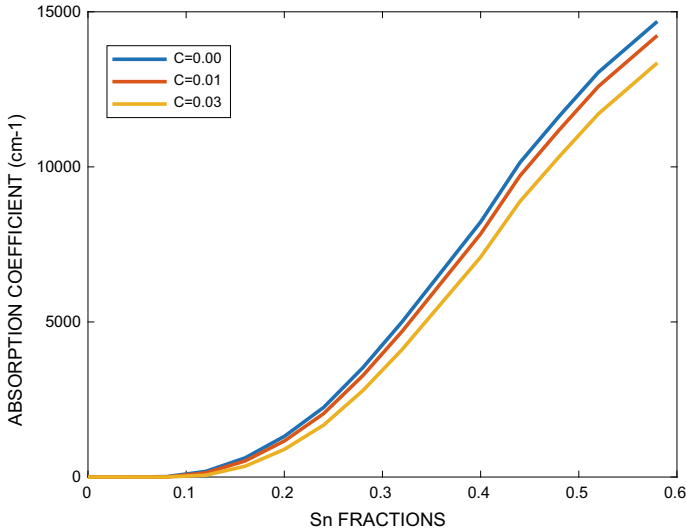
Fig. 3 Absorption coefficient of Si$_{1-x-y}$Sn$_x$C$_y$ as a function of Sn content for the carbon fraction 0.01, 0.02, and 0.03

From that by the higher than Eq. 8 the common relationship for the Auger time period in n-type and p-type material beneath low injection(τli) and high injection conditions(τhi) will be determined.

$$\text{For } n - \text{type } \tau_{li} = \frac{1}{C_n N_D^2} \quad and \quad \tau_{hi} = \frac{1}{(C_n + C_p)\Delta p^2} \tag{9}$$

$$\text{and for } p - \text{type } \tau_{li} = \frac{1}{C_n N_A^2} \quad and \quad \tau_{hi} = \frac{1}{(C_n + C_p)\Delta n^2} \qquad (10)$$

where N_D and metallic element square measure the density of donor and acceptor atoms, Δn and Δp square measure the surplus carrier densities and $Ca = Cn + Cp$ is ambipolar constant from Eqs. (9) and (10). Therefore it will be seen that the Auger time period ideally depends on the inverse of the carrier density square. Therefore the calculation of turn on time of the modulator is written as

$$\tau_{on}(l) = \frac{qhl}{P_{leak}} \qquad (11)$$

Subsequently, the total minority carrier current thickness is a pleasant estimate of this that leaks out of the dynamic region Pleak. The lepton and hole density going absent the dynamic locale unit of measurement each given by P leak/qh, wherever h is the height of the designed modulator.

5 Simulations Results

The material interband absorption coefficient is calculated from the Eqs. (4)–(6), and once the calculation the corresponding simulation results are shown in Fig. 3. The plotting curve provides a concept of absorption coefficient results for SiSnC alloys. The character of the curve is precisely the same as the SiGeC alloys [10]. Because of the result of carbon fraction are the values of (0, 0.01, 0.02, 0.03,) and strain is neglected within the SiSnC, and with the exception of the modification to the bandgap. Therefore in application, it's found that the range for each test considered may perhaps be fitted very pleasantly by these equations.

The turn on time will be calculated just by the condition (7). This turn on time is expected to be the constraining portion of choosing the altered speed of SiSnC modulators. Figure 4 appears to turn on time as a work of the current infusion level.

Figure 5 appears that the altered time for modulators with a total injected current is a work of the modulator length for the optimized modulators, once carbon divisions are bigger than zero.02, sub-100 µm modulator gadget lengths unit of measurement doable with alter times around 1 ns. Therefore for bigger carbon fractions, lengths unit drawing nearer 20 µm unit pertinent. So the small device lengths unit suitable for each optical mode confinement conjointly with the charge confinement given by the SiSnC/Si heterostructures,
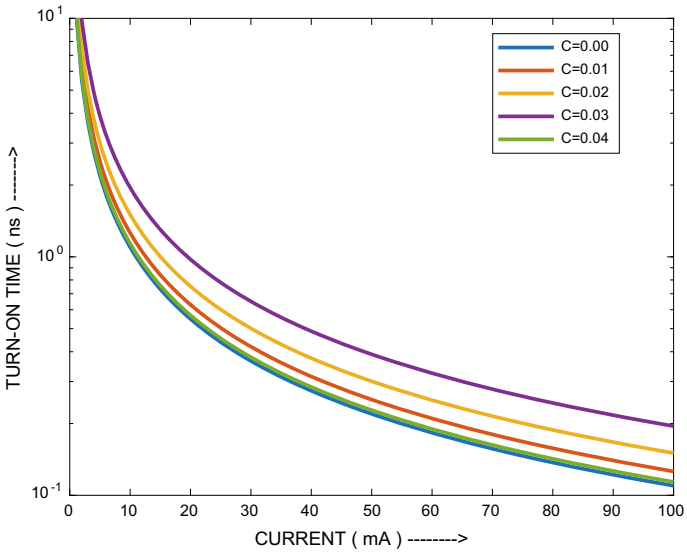
Fig. 4 Turn-on time of 20 µm modulators with carbon fractions of 0.01, 0.02, 0.03, 0.04
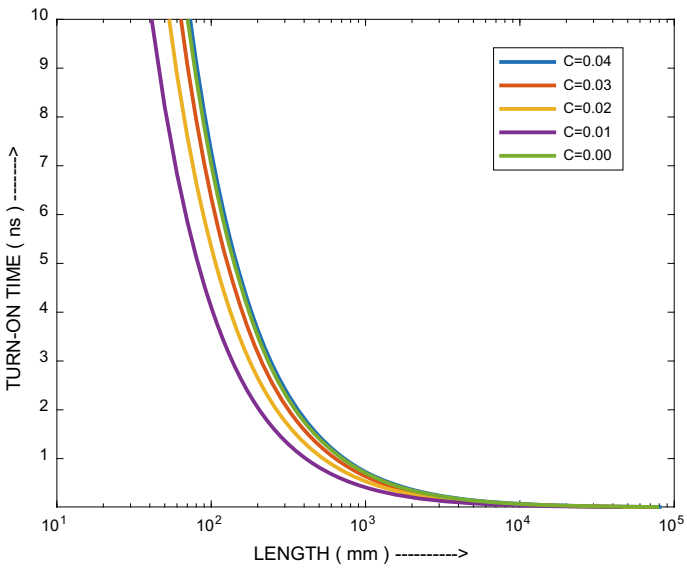
Fig. 5 Turn-on time of optimized modulators for a 20 µm length with carbon fractions of 0.04, 0.03, 0.02, 0.01 and 0

6   Summary

Design and Simulation square measure dole out to attain $Si_{(1-x-y)}Sn_{(x)}C_{(y)}$/Si hetrostructure Electro-Optic Modulator (EOM) for optimum performance. The absorption coefficient, on current and turn on time are calculated by finding the equations by device property analysis. So the authors indigenously created a software system for simulation of the device properties. In this manner to boot, since the band counterbalanced between Si and SiSnC capably limits carriers to the wave direct center, in this manner as a result which supplies in durable cover between massive infused carrier concentration conjointly the optical mode, and authors can indeed think about that SiSnC/Si modulators with lengths around 20 µm and turn on time are found 0.1 ns. Therefore this new style model is beneficial for coming optical signal process applications.

References

1. Barrios CA, Almeida VR, Lipson M (2003) Low-power-consumption Short-length and high-modulation-depth silicon electro-optic modulator. J Lightw Technol 21(4):1089–1098
2. Yang M, Chang C, Sturm JC, Pantellides ST, (2002) Band alignments and band gaps in SiGeC/Si structures. In: Zollner S (ed) Silicon-germanium-carbon alloys. Taylor and Francis, New York
3. Naval L, Jalali B, Gomelski L, Liu JM (1996) Optimization of SiGe/Si waveguide photo detectors operating at 1.3 µm. J Lightw Technol 14(4):787–797 (1996)
4. Soref RA, Bennett BR (1987) Electrooptical effects in silicon. IEEE J Quantum Electron 23(1):123–129
5. Braunstein R, Moore A, Herman F (1958) Intrinsic optical absorption in germanium-silicon alloys. Phys Rev 109(3):695–710
6. Qasaimeh O, Singh J, Bhattacharya P (1997) Electro absorption and electro optic effect in SiGe-Si quantum wells: Realization of low voltage optical modulators. IEEE J Quantum Electron 33(9):1532–1536
7. Soref RA (1996) Silicon based group IV heterostructures for optoelectronic applications. J Vac Sci Technol A Vac Surf Films 14(3):913–918
8. Zollner S, Pantellides ST (2002) Optical properties and band structure of unstrained and strained $Si_{1-x}Ge_x$ and $Si_{1-x-y}Ge_xC_y$ alloys. In: Zollner S (ed) Silicon-germanium-carbon alloys. Taylor and Francis, New York
9. Li B, Jiang Z, Zhang X, Wang X, Wan J, Li G, Liu E (1999) SiGe/Si Mach-Zehnder interferometer modulator based on the plasma dispersion effect. Appl Phys Lett 74(15):2108–2109
10. Schubert MF, Rana F (2007) SiGeC/Si electrooptic modulators. J Lightwave Technol 25(3):866–874
11. Naval L, Jalali B, Gomelski L, Liu JM (1996) Optimization of SiGe/Si waveguide photodetectors operating at 1.3 µm. J Lightw Technol 14(4):787–797
12. Soref RA, Bennett BR (1987) Electrooptical effects in silicon. J Quantum Electron 23(1):123–129

Design and Optimization of Graphene Nanoribbon TFETs for Low Power Digital Applications

Jayabrata Goswami, Anuva Ganguly, Anirudhha Ghosal, and J. P. Banerjee

Abstract Plan and optimization of a P-channel Tunnel Field Effect Transistor (TFET) with Graphene Nanoribbon (GNR) as channel material are carried out in this paper to attain high performance in low power advanced circuits. A self-consistent iterative strategy is utilized to illuminate numerically 1-D Poisson's condition subject to suitable boundary conditions at the source and drain closes of the device. The energy band diagram is gotten from which surface potential and boundary heights are extracted. The structural parameters are appropriately designed to optimize the performance of the device for future application in low power digital circuits.

1 Introduction

The sub-threshold slope of Silicon Metal Oxide Semiconductor Field Effect Transistors (MOSFETs) cannot be diminished underneath 60 mV/decade at room temperature due to thermionic limitation. This is a fundamental limitation of Si MOSFETs in ULSI (Ultra Large Scale Integration) chips. However, this limitation does not arise if Si MOSFETs are replaced by Tunnel Field Effect Transistors (TFETs). Theoretical and experimental studies reported so far [1, 2] show that the subthreshold slope of TFETs can be decreased below 60 mV/decade at room temperature. It is also reported [3, 4] that TFETs provide a higher on–off current ratio than MOSFETs.

Heterojunction TFETs based on Si/Si_xGe_{1-x} and III–V semiconductors as channel material are reported [5, 6] to have a steep sub-threshold swing of about 15 mV/decade, suitable for application in low power, energy efficient digital circuits. Double gate TFETs based on strained Ge heterostructure as channel material with

---

J. Goswami (✉)
Netaji Subhas Open University, Saltlake, Kolkata, India
e-mail: goswamijayabrata@gmail.com

A. Ganguly · A. Ghosal · J. P. Banerjee
Institute of Radio Physics and Electronics, University of Calcutta, Kolkata, India

a high current density of 300μA/μm are also reported in the literature [7]. In these devices, the on-current is high while off-current remains almost constant leading to a significant increase in on–off current ratio.

Tunnel field effect transistors (TFETs) using Graphene Nanoribbon (GNR) as channel material are attracting considerable attention due to the favourable electronic properties of Graphene which lead to high performance from the device in low power digital circuits. GNR FETs with channel lengths less than 10 nm are reported to provide a high On–Off current ratio ($\sim 10^6$) [8].

The room temperature mobility of Graphene is significantly higher than the conventional semiconductors [9, 10]. GNR possesses the unique property of tunable band gap with respect to its ribbon width. Graphene possesses robust mechanical strength and high thermal conductivity. The scattering relations for electrons and holes in Graphene are symmetric which is insensitive to doping fluctuation. Further TFETs based on GNR as channel material have distinct advantages so far as planar processing in ULSI is concerned.

Zhang et al. [11] used a semi classical analytical model with a triangular good approximation at the source-channel interface to evaluate various key performance parameters of GNR TFET. They observed a high On–Off current ratio of the order of 10^7 and a very low subthreshold slope below 3 mV/decade from a GNR TFET whose channel length is 20 nm and ribbon width is 5 nm. These results were however not verified from experiments or numerical simulations. Zhao et al. [12] reported a much higher On–Off current ratio of the order of 10^{11} from a p-i-n type GNR TFET.

The main objective of the present work is to design the structural parameters of a GNR PTFET inconsistent with the current ITRS requirement [13] and optimize the On–Off current ratio and subthreshold swing of the device. The intrinsic gate delay (τ_{int}), gate capacitance (C_G) and quantum capacitance (C_Q) of the device are also studied to test the suitability of the optimized device in low power digital circuits.

2 Device Structure and Analysis

The quasi 1-D geometry of GNR PTFET structure is appeared in Fig. 1. The n^+source and p^+drain regions are intensely doped with doping concentrations of 3.4×10^{20} cm^{-3} and 1.1×10^{20} cm^{-3} respectively. The channel is formed with a 1-D channel layer of GNR, uniformly deposited over Si substrate. The thickness of monolayer graphene (t_{GNR}) is in the range of 0.3–0.4 nm [14]. GNR is intensely doped to make a p + n + tunnel junction and the gate is put over the channel which is totally depleted at zero gate bias. Chemical and electrostatic doping are reported [15, 16] to form good $p^+ n^+$ tunnel junction in Carbon Nanotube (CNT) FET and this type of doping can also be used in GNR. A high-k dielectric material like Y_2O_3 ($\varepsilon_{OX} = 10\varepsilon_0$) is used as gate oxide having a thickness (t_{ox}) of 2 nm.

In the on state the applied gate-source and drain-source voltages are V_{gs} and V_{ds} respectively. The length of the channel is L_{CH} as shown in Fig. 1.
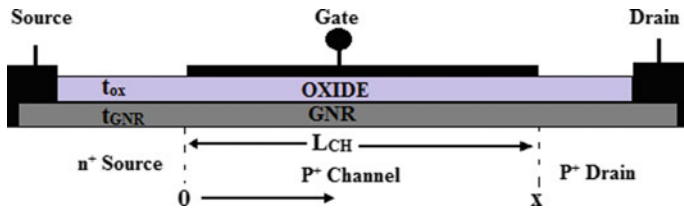
Fig. 1 The quasi 1-D structure of a p-channel GNR TFET

The surface potential method in the channel region is calculated from the numerical solution of the following 1-D Poisson's equation

$$\frac{d^2\varphi_s(x)}{dx^2} - \frac{\varphi_s(x) - V_{gs} - V_{BI}}{\lambda^2} = -\frac{\rho(x)}{\varepsilon_{GNR}} \tag{1}$$

In Eq. (1), $\varphi_s(x)$ is the surface potential at the interface of gate oxide and channel material, V_{gs} is the gate to source voltage, V_{BI} is the built-in potential, $\rho(x)$ is the total charge density, λ is the screening length [17] for the particular device structure and V_{GNR} is the permittivity of GNR. Assuming the channel region to be completely drained within the off state as well as in the on state with low V_{gs}, the total charge density is taken to be approximately equal to the impurity charge density. The bandgap of GNR arises from lateral confinement of charge carriers and is dependent on the ribbon width. The dispersion relation of a mobile electron in graphene is given by [18]

$$E(k) = s\eta V_F|k| \tag{2}$$

In Eq. (2), V_F is the Fermi velocity of the carrier in graphene, taken to be 10^6 m/s, the wave vector is $|k| = \sqrt{k_x^2 + k_y^2}$, $\hbar$ is the reduced Planck's constant and the value of s is $+1$ for the conduction band and -1 for the valence band.

The electron wave vector k_y in y direction can be expressed as

$$k_y = \frac{m\pi}{W_{GNR}} \tag{3}$$

In Eq. (3), m is an integer both positive and negative and W_{GNR} is the ribbon width.

Using Eq. (3) in Eq. (2), the energy dispersion relation can be communicated as

$$E(m, k_x) = s\eta V_F \sqrt{k_x^2 + \left(\frac{m\pi}{W_{GNR}}\right)^2} \tag{4}$$

The band gap energy of GNR is obtained as

$$E_G = E_C - E_V = E(1,0)_{S=+1} - E(1,0)_{S=-1} = \frac{2\pi \eta V_F}{W_{GNR}} \tag{5}$$

Therefore the bandgap of GNR depends inversely on the ribbon width W_{GNR} and directly on Fermi velocity (V_F). The screening length λ is written as [17]

$$\lambda = \sqrt{\frac{\varepsilon_{GNR}}{\varepsilon_{OX}} t_{GNR} t_{OX}} = \sqrt{t_{GNR} t_{OX}} \tag{6}$$

In Eq. (6), t_{ox} and t_{GNR} are the gate oxide and GNR thicknesses respectively. High–k dielectric material Y_2O_3 is chosen as gate oxide so that the gate leakage is minimised. The screening length expressed in Eq. (6) depends only on the thicknesses of the gate oxide and GNR since $\varepsilon_{GNR} = \varepsilon_{OX}$.

The drain current arises from the tunnelling of charge carriers from source to drain which can be found by using Landauer's expression.

The energy dependent tunnelling probability $T_S(E)$ is written as

$$T_S(E) = exp\left(-2 \int |k_x| dx\right) \tag{7}$$

In a highly-doped GNR p + n + structure, the primary sub-band is only considered for tunnelling and the wave vector in x-direction is expressed as

$$k_x \frac{1}{\eta V_F} \sqrt{\left[E_C(x) - E - \frac{E_G}{2}\right]^2 - \left(\frac{E_G}{2}\right)^2} \tag{8}$$

The wave vector, k_x in Eq. (8) is necessarily an imaginary quantity for the exponential decay of tunnelling current to take place in the channel region.

Using Eq. (8) in Eq. (7), we obtain

$$T_S(E) = exp\left(-\frac{2}{\eta V_F} \int_{x_i}^{x_f} \sqrt{\left(\frac{E_G}{2}\right)^2 - \left[E_C(x) - \left(E + \frac{E_G}{2}\right)^2\right]} dx\right) \tag{9}$$

In Eq. (9), $E_C(x)$ is the energy at the bottom of the conduction band and x_i and x_f are the initial and final positions of tunnelling respectively. The tunnel injected charges from source to channel (Q_{CS}) and drain to channel (Q_{CD}) are expressed as

$$Q_{CS} = q \int \rho_{GNR}(E)(1 - f_S(E))T_S(E) dE \tag{10}$$

$$Q_{CD} = q \int \rho_{GNR}(E)[(f_D(E) - 1)T_S(E) + 2(1 - f_D(E))] dE \tag{11}$$

In Eqs. (10) and (11), $f_S(E)$ and $f_D(E)$ denote the Fermi–Dirac distribution function at the source and drain regions individually. The density of states function of 1-D GNR for mth subband is expressed as

$$\rho_{GNR}(m, E) = \frac{4}{\pi \eta V_F} \frac{E}{\sqrt{E^2 - E_m^2}} \Theta(E - E_m) \qquad (12)$$

In Eq. (12), V_F is the Fermi velocity (10^6 m/s), Θ is the Heaviside unit step function, $E_m = m\pi\eta V_F / W_{GNR} = mE_G/2$.

The total density of state function is

$$\rho_{GNR}(E) = \sum_m \rho_{GNR}(m, E) \qquad (13)$$

Now substituting the expressions for $\rho_{GNR}(E)$ and $T_S(E)$ from Eqs. (13) and (9) respectively into Eqs. (10) and (11), numerical integration is carried out to find out Q_{CS} and Q_{CD}.

The overall channel charge of the device ($Q_C = Q_{CS} + Q_{CD}$) is included and the surface potential is evaluated from Eq. (1). The drain current is calculated from Landauer's expression

$$I_D = \int (f_S(E) - f_D(E)) P(E) dE \qquad (14)$$

where $P(E) = (2q^2/\eta) H(E) T_S(E)$, and $H(E) = W_{GNR}(2|\xi|/\pi\eta V_F)$, W_{GNR} is the ribbon width, is η the reduce Plank's constant, $|\xi|$ is the transverse mode energy and the expression of $H(E)$ is specific to graphene [19].

The following boundary conditions are used to solve Eq. (1) numerically.

(i) Electric fields at the heavily doped source and drain terminals of the channel are taken to be zero.
(ii) Both the electric field and potential functions at the source-channel and drain–channel interfaces are continuous.
(iii) The Fermi level at the source terminal is aligned with that at the channel region for $V_{GS} = 0$ and
(iv) $E_F - E_c = E_v - E_F = kT$ at the source and drain ends, kT is the thermal energy.

A MATLAB based program is developed to obtain the energy band profile. The surface potential and barrier height can be extracted from the simulated band diagram.

With expanding current thickness, increasingly carriers will be infused into the channel and accordingly the energy band profile in the channel region is adjusted with new surface potential. The self-consistent iterative method is used for the said adjustment. The steps to achieve self-consistency are.

Step1: The energy band is computed first from the solution of Poisson's equation by the solution of boundary conditions as described earlier.

Step2: The energy-dependent tunneling probability, $T_S(E)$ is at that point calculated from the band diagram. The charges infused from the source and the deplete (Q_S and Q_D) are at that point calculated.

Step3: The total injected charge $Q = Q_S + Q_D$ in the channel is obtained and substituted in Poisson's equation to adjust the band diagram.

The aforementioned steps are repeated till the condition, $\phi_S^{n+1} - \phi_S^n < 0.0001$ eV is fulfilled where ϕ_S^n is the surface potential of the channel at nth iteration. The energy band diagram is then obtained as appeared in Fig. 5.

3 Simulation Results

Figure 2a shows on-current with gate-source voltage for ribbon widths of 2, 3, 4 and 5 nm with a fixed channel length of 20 nm and oxide thickness of 2 nm while Fig. 2b shows on-current versus gate-source voltage for channel lengths of 20, 25, 28 and 30 nm with a settled ribbon width of 4 nm and oxide thickness of 2 nm at a fixed drain to source bias, V_{ds} of –0.1 V.

It is observed from Fig. 2a that the drain current is higher for larger ribbon width at a particular V_{gs}. As ribbon width increases, the band gap (E_G) decreases and therefore tunnelling current or on-current increases. Figure 2b shows that on current diminishes with the increment of channel length at a particular V_{gs}. The on-current is therefore optimized for a channel length of 20 nm.

Neglecting gate leakage and considering thermionic emission across the potential barrier, the off state current is obtained from the following equation [20]
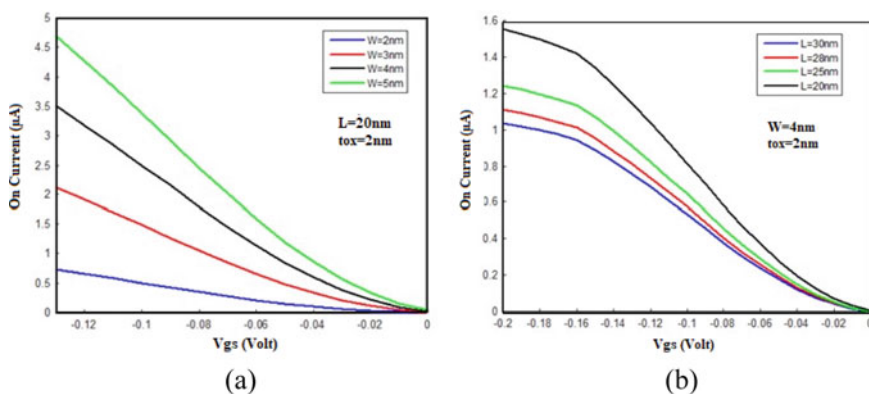
Fig. 2 a On-current versus V_{gs} for different ribbon widths **b** On-current versus V_{gs} for different channel lengths

$$I_{OFF} = \left(\frac{q^2 v_T}{\eta \pi}\right) exp\left(\frac{-\varphi_B}{q v_T}\right) \qquad (15)$$

In Eq. (15), $q v_T$ is the thermal energy and φ_B is the barrier height.

Figure 3 shows the plot of Off-state current versus ribbon width for $L_{CH} = 20$ nm and $t_{ox} = 2$ nm. The Off-state current is 0.15pA for ribbon width of 4 nm and channel length of GNR 20 nm which is lower than that reported in [8]. The increase of Off-state current with the increase of ribbon width is inconsistent with that reported in [21].

Figure 4 shows the On–Off current ratio versus gate-source voltage (V_{gs}) for three different gate oxide thicknesses (t_{ox}). It is watched that On–Off current proportion is higher for more slender gate oxide at a specific value of Vgs. Further On-current increases more rapidly than Off-current leading to an increase of On–Off current ratio with the decrease of gate oxide thickness. Figure 4 shows that On–Off current ratio attains a value of 2.71×10^3 at $V_{gs} = -0.1$ V and $t_{ox} = 2$ nm and $L_{CH} = 20$ nm.

With the application of $V_{gs} = -0.1$ V and $V_{ds} = -0.1$ V, the drain current starts to flow and the device goes to On-state. Figure 5a shows the On-state energy band profile of the designed device structure at $V_{gs} = -0.1$ V and $V_{ds} = -0.1$ V while Fig. 5b shows the Off-state band profile at $V_{gs} = 0$ V, $V_{ds} = -0.1$ V.

The aforementioned studies indicate that the optimum performance is obtained from appropriately designed GNR TFET. The design values of ribbon width is $W_{GNR} = 4$ nm and channel length is $L_{CH} = 20$ nm.

Figure 6a shows the On-state current density versus gate-source voltage, V_{gs} of the device at channel length (L_{CH}) = 20 nm, ribbon width (W) = 4 nm and t_{ox} = 2 nm. The On-state current density of the device is 406 μA/μm at $V_{gs} = -0.1$ V. The sub-threshold swing (SS) of a TFET [22] is calculated from

$$SS = ln_{10}\left(\frac{I_D}{g_m}\right) \qquad (16)$$

Fig. 3 Off state current versus ribbon width of GNR PTFET
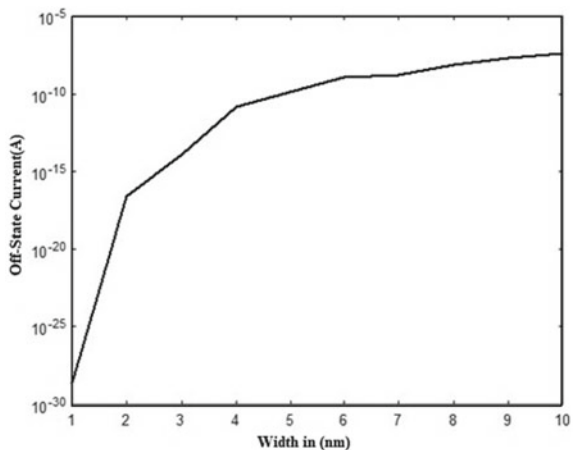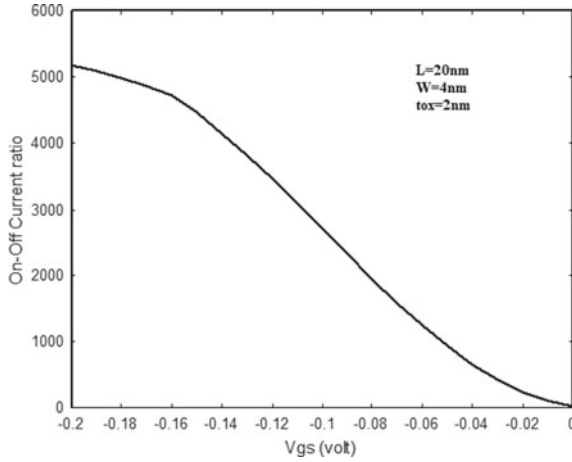
Fig. 4 On–Off current ratio versus V_{gs} of GNR PTFET
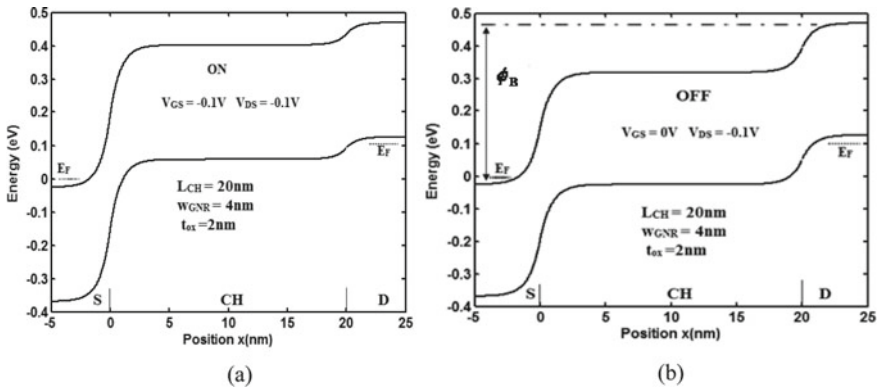
Fig. 5 Energy band diagrams for a GNR PTFET in the **a** ON-state and **b** OFF-state

In Eq. (16), g_m is the transconductance of the device. The sub-threshold swing (SS) of the device is found to be 8 mV/decade at $V_{gs} = -0.1$ V. The variation of drain current density with temperature is shown in Fig. 6b. It is observed that the drain current density decreases sharply when the temperature is increased from 200 to 400 K. The sharp decrease of drain current density in the temperature range of 200 to 400 K agrees with that reported in [9]. This is due to a sharp increase of the resistivity of GNR above 200 K caused by the scattering of intra-ripple flexural phonons. The increase of channel resistance leads to a decrease of drain current at temperatures exceeding 200 K. The intrinsic gate delay (τ_{int}), characterized as the proportion of the gate initiated channel charge to the limit current to make the device on is an important parameter which controls the performance of the device in digital circuits. The gate delay is given by
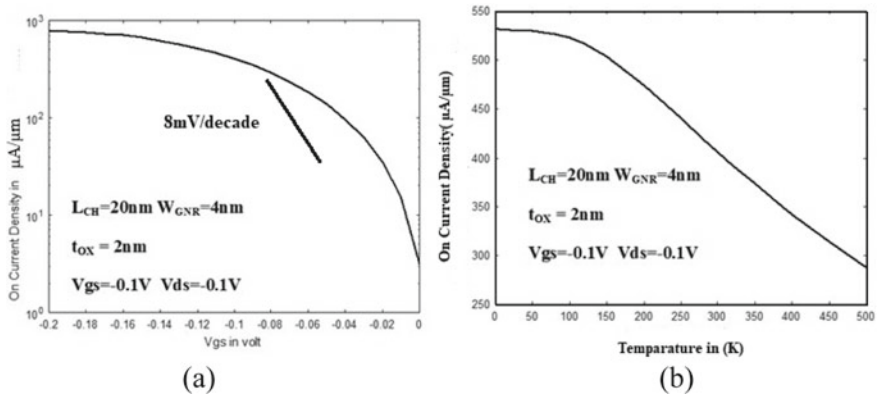
Fig. 6 a On current density versus V_{gs}, **b** On current density versus temperature

$$\tau_{int} = \frac{Q_{C(ON)} - Q_{C(OFF)}}{I_D} \tag{17}$$

In Eq. (17), I_D is the threshold or on-state drain current, $Q_{C(ON)}$ and $Q_{C(OFF)}$ are the channel charges in the off and on-states respectively. In the present work, the supply voltages are taken to be $V_{gs} = -0.1$ V and $V_{ds} = -0.1$ V. The intrinsic gate delay of the optimized GNR PTFET is found to be $2f_S$ which satisfies the current ITRS requirement. The gate capacitance (C_G) is the rate of alter of add up to channel charge (Q_C) with gate to source voltage (V_{gs}) given by

$$C_G = \frac{dQ_C}{dV_{gs}} \tag{18}$$

The sizes of C_G for different values of the gate-source voltages (V_{gs}) are gotten from the entirety of gate to source and gate to drain capacitances i.e.,

$$C_G = C_{GS} + C_{GD} \tag{19}$$

Figure 7a shows the plots of C_{GS}, C_{GD} and C_G versus V_{gs} of the optimized device whose channel length, ribbon width and oxide thickness are 20 nm, 4 nm and 2 nm respectively. The values of C_{GS}, C_{GD} and C_G at $V_{GS} = -0.1$ V and $V_{DS} = -0.1$ V are found to be 27.66 aF/μm, 23.06 aF/ μm and 50.72 aF/μm respectively. In the ON-state the gate capacitance C_G is usually equal to the gate oxide capacitance C_{OX}. In the OFF state i.e., at zero gate to source voltage, the surface potential is zero. In the ON-state, the surface potential, φ_S is less than gate to source voltage by Q_C/C_{OX}, i.e.,
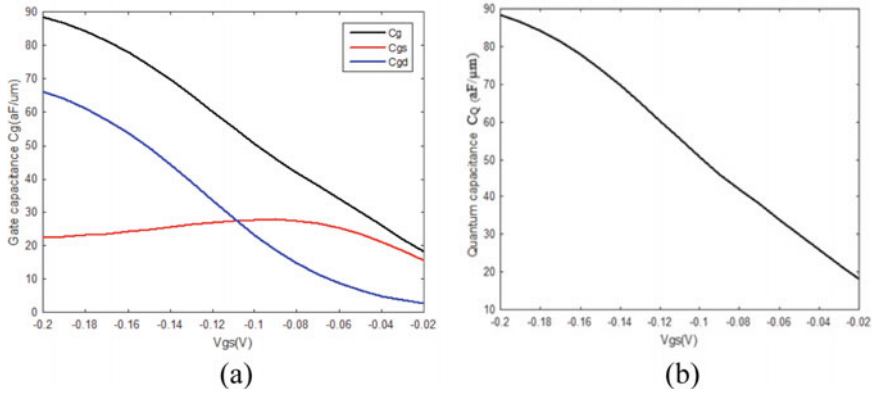
Fig. 7 **a** Gate capacitance versus V_{gs} of GNR PTFET and **b** Quantum capacitance versus V_{gs} of GNR PTFET

$$\varphi_S = V_{gs} - \frac{Q_C}{Q_{OX}} \tag{20}$$

The rate of alter of channel charge with gate to source voltage is written as

$$\frac{dQ_C}{dV_{gs}} = \frac{dQ_C}{d\varphi_S} \frac{d\varphi_S}{dV_{gs}} \tag{21}$$

Now substituting Eq. (20) into Eq. (21) we obtain

$$\frac{dQ_C}{dV_{gs}} = \frac{C_{OX}\left[\frac{dQ_C}{d\varphi_S}\right]}{C_{OX} + \left[\frac{dQ_C}{d\varphi_S}\right]} \tag{22}$$

In Eq. (22), dQ_C/dV_{gs} has the unit of capacitance known as quantum capacitance, C_Q which is the characteristic property of a 1-D wire structure like GNR [23]. The quantum capacitance of GNR is proportional to the density of states function of one-dimensional wire. In terms of quantum capacitance, Eq. (22) can be rewritten as

$$\frac{dQ_C}{dV_{gs}} = \frac{C_{OX}C_Q}{C_{OX} + C_Q} \tag{23}$$

Figure 7b shows the variation of quantum capacitance of the optimized GNR PTFET as a function of gate to source voltage. It is watched that the values of C_G and C_Q are 50.72 and 51.72 aF/μm respectively at $V_{gs} = -0.1$ V and $V_{ds} = -0.1$ V. The ratio of C_G/C_Q is 0.98, close to the quantum limit of unity. This study reveals that both gate capacitance and quantum capacitance play a significant role to determine the high performance of the device in low power digital circuits.

From Table 1, it appears that both on–off current ratio and subthreshold swing (SS) are better for the proposed GNR PTFET structure as compared to those reported

Table 1 Comparison of the performance parameters of the proposed GNR TFET with those of GNR FET reported in [8]

Performance parameters	Proposed GNR TFET	Reported GNR FET
On –state current density	406 (μA/μm)	2000 (μA/μm)
Off-state current	0.15 (pA)	1 pA
On–Off current ratio	2.71×10^3	10^6
SS	8 (mV/decade)	Not available

in [8]. Thus the proposed GNR PTFET device can be used in future low power digital ULSI chips.

4 Summary

The design and analysis of a GNR PTFET are carried out to achieve various performance parameters such as on–off current ratio, subthreshold swing, intrinsic gate delay, gate capacitance and quantum capacitance. Different structural parameters of the device such as the ribbon width, channel length and gate oxide thickness are suitable designed for high performance in low power digital circuits. Simulation is based on a self-consistent iterative strategy to carry out numerical arrangement of 1-D Poisson's condition subject to suitable boundary conditions at the source and drain ends. The energy band diagram of the device is also simulated to obtain the surface potential and barrier height. The source and drain currents of the device are found from the tunneling probability and Fermi functions. The study provides the key performance parameters of the optimized device such as on–off current ratio, sub-threshold swing, intrinsic gate delay, gate capacitance and quantum capacitance which show that the optimized device is highly suitable for low power digital applications.

References

1. Zhang Q, Zhao W, Seabaugh AC (2006) Low subthreshold swing tunnel transistors, IEEE Device Lett 27(4):297–300
2. Bhuwalka KK, Schulze J, Eisele I (2004) Performance enhancement of vertical tunnel field-effect transistor with SiGe in the δp+ layer. Jpn J Appl Phys 43(7A):4073–4078
3. Brahma M, Kabiraj A, Saha D, Mahapatra S (2018) Scalability assessment of group-IV mono-chalcogenide based tunnel FET. Sci Rep 8:5993
4. Uygar Avci E, Rios R, Kelin Kuhn J, Ian Young A (2011) Comparison of power and performance for the TFET and MOSFET and considerations for P-TFET. In: 2011 11th IEEE international conference on nanotechnology, pp 869–872. https://doi.org/10.1109/NANO.2011.6144631

5. Khatami Y, Banerjee K (2009) Steep subthreshold slope n- and p-type tunnel-FET devices for low-power and energy-efficient digital circuits. IEEE Trans Electr Dev 56(11):1–12

6. Dewey G, Chu-Kung B, Boardman J, Fastenau JM, Kavalieros J, Kotlyar R, Liu KW, Lubyshev D, Metz M, Mukherjee N, Oakey P, Pillarisetty R, Radosavl M, Then, Chau R (2011) Fabrication, characterization, and physics of III-V heterojunction tunneling field effect transistors (H-TFET) for steep sub-threshold swing. In: 2011 international electron devices meeting, pp 785–788. https://doi.org/10.1109/IEDM.2011.6131666.

7. Krishnamohan T, Kim D, Raghunathan S, Saraswat K (2008) Double-gate strained-Ge heterostructure tunneling FET (TFET) with record high drive currents and 60 mV/decade subthreshold slope. In: Proceedings of the international electron devices meeting, pp 947–949

8. Wang X, Ouyang Y, Li X, Wang H, Guo J, Dai H (2008) Room temperature all-semiconducting sub-10-nm graphene nanoribbon field effect transistors. Phys Rev Lett 100(20):206–212

9. Morozov SV, Novoselov KS, Katsnelson MI, Schedin F, Elias DC, Jaszczak JA, Geim AK (2008) Giant intrinsic carrier mobilities in graphene and its bilayer. Phys Rev Lett 100:016602–1–8

10. Hirai H, Tsuchiya H, Kamakura Y, Mori N, Ogawa M (2014) Electron mobility calculation for graphene on substrates. J Appl Phys 116:083703–1–12

11. Zhang Q, Fang T, Xing H, Seabaugh A, Jena D (2008) Graphene nanoribbon tunnel transistors. IEEE Electron Dev Lett 29(12):1344–1346

12. Zhao P, Chauhan J, Guo J (2009) Computational study of tunneling transistor based on graphene nanoribbon. Nano Lett 9(2):684–688

13. http://www.itrs.net/ (2016)

14. Fahad Shamiul M, Srivastava A, Ashwani Sharma K, Mayberry C (2016) Analytical current transport modeling of graphene nanoribbon tunnel field-effect transistors for digital circuit design. IEEE Trans Nanotechnol 15(1):39–50

15. Lin YM, Farmer DM, Tulevski GS, Xu S, Gordon RG, Avouris P (2008) Chemical doping of graphene nanoribbon field-effect devices. In: 66th DRC, pp 27–28

16. Knoch J, Appenzeller J (2008) Tunnelling phenomena in carbon nanotube field-effect transistors. Phys Stat Sol 205(4):679–694

17. Yan R-H, Ourmazd A, Kwing Lee F (1992) Scaling the Si MOSFET: from bulk to SOI to bulk. IEEE Electron Dev 39(7):1704–1710

18. Fang T, Konar A, Xing H, Jena D (2007) Carrier statistics and quatum capacitance of graphene sheets and ribbons. Appl Phys Lett 91:092109–1–3

19. Lundstrom M, Jeong C (2012) Lessons from nanoscience: a lecture note series near-equilibrium transport, vol 2. World Scientific, New York, pp 20–31

20. Sze SM (1981) Physics of semiconductor devices, 2nd ed. Wiley, New York, p 255

21. Lu Y, Guo J (2010) Local strain in tunneling transistors based on graphene nanoribbons. Appl Phys Lett 97:073105–1–2

22. Barboni L, Siniscalchi M, Rodriguez BS (2015) TFET based circuit design using the transconductance generation efficiency g_m/I_d method. J Electron Devic Soc 3(3):10–22

23. John DL, Castro LC, Pulfrey DL (2004) Quantum capacitance in nanoscale device modeling. J Appl Phys 96(9):5180–5184

Birhythmic Behavior in a New Dual Loop Optoelectronic Oscillator

Srishti Pal, Kankana Choudhury, Shayantan Kr Roy, Arindum Mukherjee, and Dia Ghosh

Abstract In the present paper, we report the birhythmic behavior of a time delayed Optoelectronic Oscillator (OEO) with two delays, popularly known as the Dual Loop Optoelectronic Oscillator (DLOEO). The present DLOEO contains a van der Pol Oscillator (VDPO) in its feedback loop, in place of the RF Band Pass Filter (BPF). We derive the system equation of the oscillator using weak nonlinear analysis. Coexistence of the two limit cycle oscillation is known as birhythmicity. Birhythmicity in an oscillator is an intriguing phenomenon. Often, birhythmicity is desirable as it presents us with two possible coexisting stable oscillatory states for common values of system parameters. It can also be a nuisance because a random perturbation may make the system settle onto an unwanted stable state. Therefore, identifying birhythmic behavior in an oscillator is an important task. Through detail analytical and numerical bifurcation analysis, for the first time, our study reveals birhythmic behavior in a DLOEO.

1   Introduction

Nonlinear dynamics of time delayed systems has been a fascinating area of research during the last few decades. A delay appears in any physical or engineering system because time is needed to sense information and react to it. This time lag may often introduce oscillatory instabilities in the system. These instabilities, generated by the delay, arise in all areas of science and engineering such as mechanical, chemical, electrical, optical etc. In optical and photonic nonlinear time delayed systems, different

S. Pal · K. Choudhury · S. K. Roy · D. Ghosh (✉)
Department of Electronics and Communication Engineering, Siliguri Institute of Technology, Siliguri, West Bengal 734009, India
e-mail: dia.slg42@gmail.com

A. Mukherjee
Department of Electronics and Communication Engineering, Central Institute of Technology, Kokrajhar, Assam 783370, India

stability problems have been extensively studied both analytically and experimentally [1]. These regular or irregular behaviors are either desirable or undesirable. They are desirable because they can be used to design a high frequency broadband chaotic photonic oscillator. However, they can limit the performance of the system, which makes them undesirable. The Optoelectronic Oscillators (OEOs) are classical examples of the time delayed photonic system. A lot of theoretical as well as experimental studies have been devoted to unveil the collective dynamical behavior of OEOs. For instance, ultrapure microwave signal generation [2–4], injection synchronization [5–8], chaotic dynamics [9–15], Chimera death state [16, 17], and amplitude death [18] both in single and dual loop OEO have been studied. While there is a substantial amount of work devoted to explore the single delayed feedback problems, little effort is made for the two delay problems. In the present work, we investigate the birhythmic behavior in a modified Dual Loop Optoelectronic Oscillator (DLOEO). Birhythmicity is a phenomena where two stable periodic oscillations of different amplitudes and frequencies coexist, with different initial conditions. Birhythmicity may produce major nuisance in engineering systems, because in a noisy environment the system may portray irregular dynamics. On the other hand, it may proffer good flexibility in the system performance, without altering major parameters. Lately, the multirhythmic behavior of a single loop OEO has been revealed by Weicker et al. [19]. They have demonstrated the emergence of coexisting multiple square-wave oscillations from successive Hopf bifurcation. In [20], the birhythmic behavior of a single loop OEO and its control has been recently reported by the present author. It is worthwhile to point out that bifurcation analysis of time delayed systems is a difficult task. The presence of delay in the feedback loop makes the system infinitely dimensional. Moreover, a DLOEO holds two sets of delay lines in its feedback loop [21, 22]. Due to the presence of two feedback delay lines, bifurcation analysis of the system becomes more complicated. So far our knowledge is concerned, bifurcation analysis to unveil the birhythmic behavior of a DLOEO has never been approached previously. The DLOEO contains two feedback delays of different lengths. Each loop contains its own individual sets of cavity modes. However, the closest oscillation modes from both loops will synchronize and eradicate the extra modes. In DLOEO, the phase noise is an average of noise in the two individual loops instead of the phase noise of the longer loop. Moreover, side modes from individual loops are not completely removed, but merely suppressed.

Here, we consider a new architecture of DLOEO [23]. The oscillator holds a VDPO in its feedback loop instead of the band pass filter. The photodetector output drives the VDPO. The VDPO output must be well-matched with one of the desirable oscillation modes, coming out from the photodetector. Consequently, these two signals are injection locked and a single mode of oscillation can be achieved at the output of the oscillator [24]. The driven VDPO serves the purpose of the RF BPF. Several studies report different architectures of OEO using VDPO in the feedback loop [13, 14], nevertheless, in these reports the VDPO is not used to replace the RF filter. Replacement of the RF filter using the injection synchronized VDPO is advantageous since in high frequency region designing of an RF filter is a quite difficult

task. In the present study, we aim to explore the birhythmic behavior of the modified DLOEO with the help of numerical and analytical bifurcation analysis, considering delay as a control parameter.

The chapter is organized in the following sequence: Sect. 2 reports the basic architecture of the proposed oscillator along with the derivation of nonlinear delay dynamical system equation of the oscillator. In Sect. 3, we produce the linear stability analysis. The bifurcation analysis of periodic motion using the Multiple Time Scale Method is described in Sect. 4. Finally, Sect. 5 summarizes the chapter.

2 The Dynamical Model

The basic architecture of the proposed DLOEO is depicted in Fig. 1. The oscillator includes a continuous wave (CW) laser source, where the output optical signal from the CW laser is applied to a Mach–Zehnder modulator (MZM). The MZM works as an intensity modulator. The oscillator consists of two delay lines in its feedback loop. The shorter loop delay is τ_{f1}, and the longer loop delay is τ_{f2}. The MZM produces an intensity modulated output signal which traverses through the delay lines. The combined feedback loop gain must be greater than unity in order to sustain oscillation. The cavity modes emerging out from each loop should add up in the same phase and finally be converted to the RF signal by the photodetectors. The RF combiner combines the output of the photodetectors. However, it is important to mention here that since both the loops carry side modes, they are not entirely removed, but only suppressed. To eliminate these side modes a VDPO is used in place of the BPF following the RF combiner. Consequently the two signals i.e., output of the VDPO and the oscillatory signal, sustained in the feedback loop, will be injected in a synchronized manner and the OEO generates a single RF oscillation mode. The usefulness of the injection locked VDPO as an RF BPF is reported in the appendix of [20]. Since injection synchronization improves spectral purity and reduces phase noise, it is expected that the spectral purity of the RF output signal will be improved compared to the conventional OEO. The optical output power of the MZM and the input voltage of the oscillator are related by Mukherjee et al. [5].

$$P_M(t) = \frac{1}{2}\sigma\, P_0\left[1 - \eta_e \mathrm{Sin}\,\pi\left(\frac{V_i(t) + V_B}{V_\pi}\right)\right], \tag{1}$$

where $V_i(t)$ is the input RF voltage and represented as $V_i(t) = V(t)e^{j(\omega_0 t + \theta(t))}$. The applied optical power is P_0, σ stands for the insertion loss of the MZM, the extinction ratio of the MZM is η_e, V_B and V_π correspond to the bias voltage and the half wave voltage of the MZM, respectively. For DLOEO, let us consider the output of the photodetector which after passing through the VDPO becomes [20, 21].

Fig. 1 Basic configuration of DLOEO
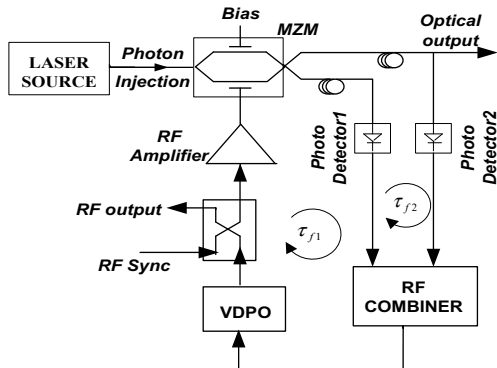
$$V_0(t) = V_{ph} \left[\begin{array}{l} 1 - \eta_e \, \sin\left(\dfrac{\pi V_B}{V_\pi}\right) \left\{ J_0\left(\dfrac{\pi V(t-\tau_f)}{V_\pi}\right) + 2 \sum_{m=1}^{\infty} J_{2m}\left(\dfrac{\pi V(t-\tau_f)}{V_\pi}\right) \, \cos\, [2m\omega(t-\tau_f)] \right\} \\ -2\eta_e \, \cos\left(\dfrac{\pi V_B}{V_\pi}\right) \times 2 \sum_{m=0}^{\infty} J_{2m+1}\left(\dfrac{\pi V(t-\tau_f)}{V_\pi}\right) \, \sin\, [(2m+1)\omega(t-\tau_f)] \end{array} \right]$$

$$(2)$$

Now this output signal $V_0(t)$ falls on the VDPO. The oscillation frequency of the VDPO is kept same as the highest spectrum component of $V_0(t)$. As the oscillation amplitude increases, the bandwidth of the tuned circuit becomes narrower; as a result, small components of the spectrum would be attenuated, whereas the highest component of the spectrum would prevail. After passing through the VDPO, the photodetector output will be reduced to the following form $V_0(t) = \left[\frac{N[V(t-\tau_{f1})]}{V(t)} e^{s\tau_{f1}} + \frac{N[V(t-\tau_{f2})]}{V(t)} e^{s\tau_{f2}} \right] V_i(t)$.

Where $N[V(t-\tau_f)] = -2\eta_e V_{ph} \cos\left(\frac{\pi V_B}{V_\pi}\right) J_1\left(\frac{\pi V(t-\tau_f)}{V_\pi}\right)$ and $V_{ph} = \frac{\sigma R_p \rho_p P_0}{2}$. Now for the ease of derivation, let us consider $\eta_e = 1$; $V_B = V_\pi$; $\pi V_{ph} = V_\pi$; $V_\pi = \pi$ and $N[V(t-\tau_f)] = 2J_1[V(t-\tau_f)]$; here J_1 represents the Bessel function of the first kind of order one. We consider the cubic nonlinearity of the VDPO as $N_1(V) = \alpha V(t) - \gamma V^3(t)$. Consequently the overall output voltage of the oscillator can be expressed as [20, 21].

$$\frac{V}{Z(s)} = g_m \left[2J_1[V(t-\tau_{f1})] \, e^{-s\tau_{f1}} + 2J_1[V(t-\tau_{f2})] \, e^{-s\tau_{f2}} + \left(\alpha V(t) - \frac{3}{4}\gamma V^3(t) \right) \right]$$

$$(3)$$

After some algebraic manipulation one can obtain the system equation of the oscillator as [20, 21].

$$\frac{d^2 v}{dt_n^2} = \mu \frac{d}{dt_n} \left\{ [v\,(t_n - \tau_{n1})] + [v\,(t_n - \tau_{n2})] + \left(\alpha\,v(t_n) - \frac{3}{4}\gamma\,v^3\,(t_n) \right) \right\} - \eta \frac{dv}{dt_n} - v \tag{4}$$

3 Linear Stability Analysis

Equation (4) has a single steady state at $v = 0$. When all the characteristic roots lie on the left half of the complex plane, the steady state remains stable. As soon as a pair of complex conjugate roots lie on the imaginary axis, i.e., $\lambda = \pm i\omega$, the system will be at the boundary of the stability; this is known as Hopf bifurcation [28]. To obtain the Hopf bifurcation points, we write Eq. (4) in the following linearized form

$$\frac{d^2 v}{dt_n^2} - \mu \frac{d}{dt_n} \{v\,(t_n - \tau_{n1}) + v\,(t_n - \tau_{n2}) + \alpha\,v(t_n)\} + \eta \frac{dv}{dt_n} + v = 0 \tag{5}$$

Now let us consider $v = e^{\lambda t_n}$ and the characteristic equation becomes

$$\lambda^2 - \mu \left(\lambda\,e^{-\lambda \tau_{n1}} + \lambda\,e^{-\lambda \tau_{n2}} + \alpha\lambda \right) + \eta\lambda + 1 = 0 \tag{6}$$

Further from (6) one can obtain the following equations

$$\tau_{n1} = \frac{1}{\omega} \left\{ \pm \mathrm{Cos}^{-1} \left[-\frac{p^2 + q^2}{2\mu\omega\sqrt{p^2 + q^2}} \right] - \tan^{-1} \left(\frac{q}{p} \right) + 2m\pi \right\} \tag{7}$$

In a similar way one can get

$$\tau_{n2} = \frac{1}{\omega} \left\{ \pm \mathrm{Cos}^{-1} \left[-\frac{p^2 + q^2}{2\mu\omega\sqrt{p^2 + q^2}} \right] - \tan^{-1} \left(\frac{q}{p} \right) + 2n\pi \right\} \tag{8}$$

where m and n are integers. Figure 2 depicts the Hopf bifurcation curve in μ and τ_{n1} parameter space. Birhythmic oscillation is expected at those values of μ and τ_{n1}, wherein, two Hopf bifurcation lines coexist. This is being further confirmed from the bifurcation of periodic solution in the next section.

4 Periodic Motion Using Multiple Time Scale Method

Here, using the weak nonlinear analysis, we derive the periodic solution of the system [25–28]. The solution of (4) can be achieved in the following form
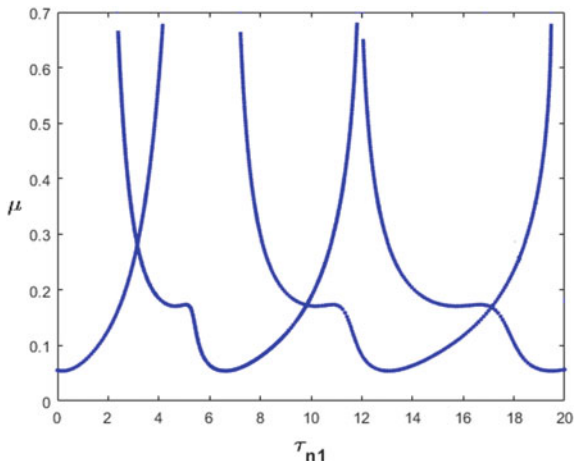
$$v(t_n) = v_0(T_0, T_1) + \varepsilon\, v_1(T_0, T_1) + O(\varepsilon^2) \tag{9}$$

where ε is a small parameter $(0 < \varepsilon << 1)$, $T_0 = t_n$ is the fast time scale and $T_1 = \varepsilon\, t_n$, is the slow time scale. We take $\mu = \varepsilon\, \mu_0$ and $\eta = \varepsilon\, \eta_0$. Using the chain rule, one can write the following differential operator

$$\frac{d}{dt_n} = \frac{\partial}{\partial T_0} + \varepsilon \frac{\partial}{\partial T_1} + O(\varepsilon^2) = D_0 + \varepsilon\, D_1 + O(\varepsilon^2)$$

$$\frac{d^2}{dt_n^2} = D_0^2 + 2\,\varepsilon\, D_0 D_1 + O(\varepsilon^2) \tag{10}$$

Substituting (9), and (10) in (4) and equating the same power of ε, the following equations can be achieved

$$D_0^2 v_0 (T_0, T_1) + v_0 (T_0, T_1) = 0 \tag{11}$$

$$D_0^2 v_1(T_0, T_1) + v(T_0, T_1) = -2\, D_0 D_1\, v_0(T_0, T_1) + \mu_0 D_0 v_0(T_0 - \tau_{n1}, T_1)$$
$$+ \mu_0 D_0 v_0(T_0 - \tau_{n2}, T_1)$$
$$+ \mu_0 \alpha\, D_0 v_0(T_0, T_1) - \frac{3}{4}\mu_0 \gamma\, D_0 v_0(T_0, T_1)^3 - \eta_0 D_0 v_0(T_0, T_1)$$

The solution of (11) can be considered as

$$v_0(T_0, T_1) = A(T_1)\, e^{i T_0} + c.c \tag{12}$$

A represents the amplitude of periodic oscillation. Substituting (12) into (11), eliminating the secular terms and introducing $A = R\, e^{i\phi}$ one can get the periodic motion of the oscillator as

$$2\omega = -\mu_0[\,\text{Sin}\,(\tau_{n1} + \omega\,\varepsilon\,\tau_{n1}) + \text{Sin}\,(\tau_{n2} + \omega\,\varepsilon\,\tau_{n2})] \tag{13}$$

$$\frac{9}{4}\,\gamma\,\mu_0\,R^2 = \mu_0\,\alpha + \mu_0[\,\text{Cos}\,(\tau_{n1} + \omega\,\varepsilon\,\tau_{n1}) + \text{Cos}\,(\tau_{n2} + \omega\,\varepsilon\,\tau_{n2})] - \eta_0 \tag{14}$$

The bifurcation diagram of the periodic solution is shown in Fig. 3. Figure 3a shows the analytical bifurcation diagram of the periodic motion, achieved using (13) and (14). Figure 3b is achieved by solving (4) using MATLAB continuation package DDEBIFTOOL [29, 30]. It is evident from the numerical diagram that in Fig. 3b, the periodic motions emerge from the supercritical Hopf bifurcation, since the stable periodic solution (blue dots) coexists with an unstable steady state (red line). It is apparent from Fig. 3 that two different branches of periodic oscillations are coexisting at different values of τ_{n1}. The hysteresis curve as a function of τ_{n1}, is shown in Fig. 4. With progressive increment of the delay τ_{n1} birhythmicity emerges through saddle node bifurcation. The critical value of τ_{n1}^* and τ_{n2}^* at which birhythmicity appears can be computed by differentiating (13) with respect to ω. Once differentiated, we obtain

$$2 = -\{\mu_0\varepsilon\tau_{n1}\,\text{Cos}(\tau_{n1} + \omega\varepsilon\tau_{n1}) + \mu_0\varepsilon\tau_{n2}\,\text{Cos}(\tau_{n2} + \omega\varepsilon\tau_{n2})\} \tag{15}$$

Differentiating again
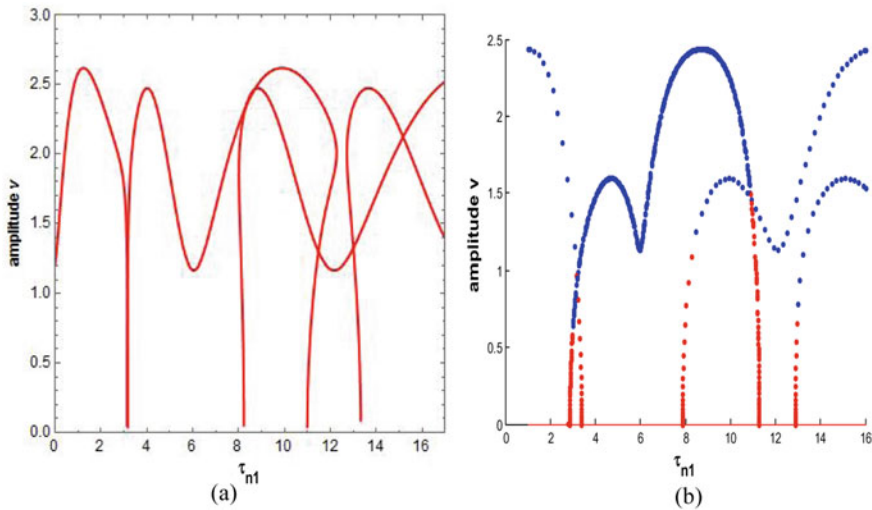
Fig. 3 Bifurcation diagram of periodic motion considering τ_{n1} as a control parameter: **a** Analytical bifurcation diagram (obtained using (13) and (14)) **b** Numerical bifurcation diagram. The parameter values are $\varepsilon = 0.1$, $\mu_0 = 3.56$, $\mu = 0.356$, $\eta_0 = 0.4$, $\eta = 0.04$, $\tau_{n2} = 9.2$, $\alpha = 0.5$, $\gamma = 0.5$

Fig. 4 Hysteresis curve:
time period $T = \frac{2\pi}{\omega}$ as a
function of τ_{n1}, the
parameter values are
$\varepsilon = 0.1, \mu_0 = 3.5, \mu = 0.35,$
$\tau_{n2} = 9.2.$
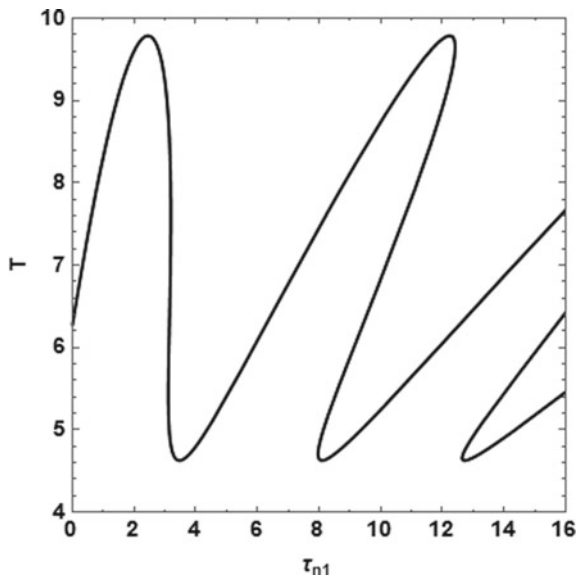
$$Sin\,(\tau_{n2} + \omega\varepsilon\tau_{n2}) = -\left(\frac{\tau_{n1}}{\tau_{n2}}\right)^2 Sin\,(\tau_{n1} + \omega\varepsilon\tau_{n1}) \tag{16}$$

Using (13) and (16) we achieve the solution for ω as a function of τ_{n1} considering a fixed value of τ_{n2} . Using (15) one can obtain the critical value of delay at which birhythmicity appears, as given below

$$\tau_{n1} = \frac{2n\pi}{1 + \omega\varepsilon} \tag{17}$$

and

$$\tau_{n2} = \frac{2m\pi}{1 + \omega\varepsilon} \tag{18}$$

here, m and n are integers. It is evident from Fig. (4) that for the parameters $\varepsilon = 0.1$, $\mu = 0.35, \tau_{n2} = 9.2$, birhythmicity appears close to $\tau_{n1}^* = 3$.

Next in Fig. 5, we demonstrate the birhythmic behavior of the system through the phase plane and time series plot obtained numerically using (4). Figure 5a reveals the coexistence of the two periodic oscillations with different amplitudes and frequencies defined using different initial conditions. The blue (small) limit cycle is obtained using the initial condition $v_0 = 7$, $\dot{v}_0 = 0$ and the red (large) limit cycle is achieved for the initial condition $v_0 = 1$ $\dot{v}_0 = 0$. The parameter values are $\mu = 0.35$, $\gamma = 0.5\,;\alpha = 0.5$, $\tau_{n1} = 3$, $\tau_{n2} = 9.2, \eta = 0.04$.
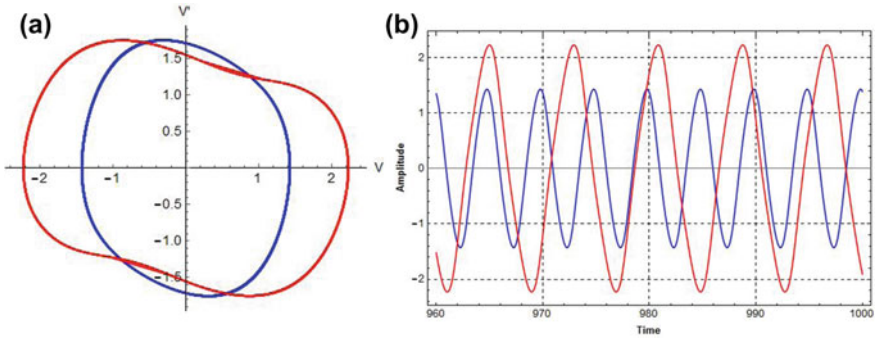
Fig. 5 Phase plane trajectories and Time series Plot: **a** Birhythmicity in the absence of the self feedback control. The red limit cycle is obtained using initial condition $v_0 = 1$, $\dot{v}_0 = 0$ and the blue limit cycle is obtained using initial condition $v_0 = 7$, $\dot{v}_0 = 0$. The parameter values are $\mu = 0.35$ $\tau_{n1} = 3$, $\tau_{n2} = 9.2$, $\eta = 0.04$, $\alpha = 0.5$, $\gamma = 0.5$

Figure 6 shows the numerically obtained RF output spectrum of the oscillator. The spectrum of $f_1 = 0.125$ is shown in Fig. 6a, the initial condition is $v_0 = 1$, $\dot{v}_0 = 0$, and the other signal f_2 is also visible in the figure at $f_2 = 0.198$. Similarly the spectrum of the limit cycle oscillation at $f_2 = 0.198$ is obtained with initial condition $v_0 = 7$ $\dot{v}_0 = 0$, (Fig. 6b), where the presence of $f_1 = 0.125$ can be previewed in this figure along with f_2.
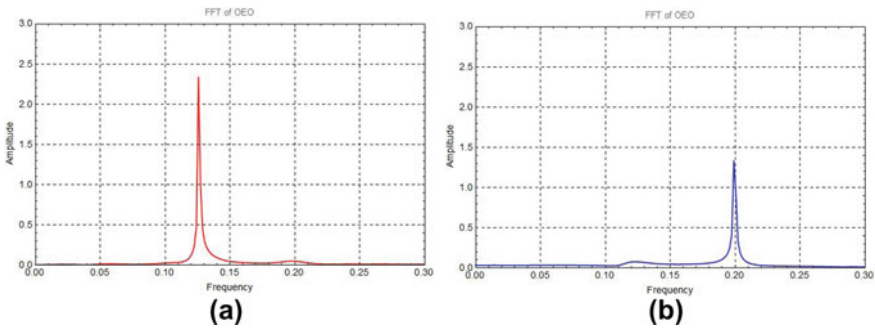
Fig. 6 RF output spectrum: **a** RF spectrum of $f_1 = 0.125$ when the initial condition is $v_0 = 1$, $\dot{v}_0 = 0$. **b** RF spectrum of $f_2 = 0.198$ when the initial condition is $v_0 = 7$, $\dot{v}_0 = 0$. The parameter values are $\mu = 0.35, \tau_{n1} = 3$, $\tau_{n2} = 9.2, \eta = 0.04, \alpha = 0.5$, $\gamma = 0.5$

5   Summary

In the present work, for the first time we have investigated the birhythmic behavior of a modified DLOEO. The basic configuration of the oscillator under study is different from the original DLOEO. Compared to the fundamental DLOEO, in the proposed model, we replace the RF BPF by a VDPO with cubic nonlinearity. The VDPO output signal is injection synchronized with the RF output from the photodetector. The injection locked VDPO is more helpful to reject unwanted signals compared to an RF BPF. We explore through a detail analytical and numerical study, how the interplay between feedback delay, feedback gain and overall nonlinearity of the oscillator generates bihythmicity in the system through the saddle node bifurcation. We obtain the periodic solution of the oscillator through perturbative calculations, using the multiple time scale method. The analytical findings are supplemented through numerical solutions using DDEBIFTOOL. We believe that this study is important in identifying the birhythmic behavior of the oscillator before using it in different applications, for instance, as a stable local oscillator in RADAR, and PLL for acquiring signals from a spacecraft in deep space missions and in optical communication. Also, an interesting future direction of this study is to investigate how to control the birhythmic oscillation and induce the monorhythmicity in the oscillator.

References

1. Erneux T, Glorieux P (2010) Laser dynamics. Cambridge University Press, Cambridge
2. Yao XS, Maleki L (1996) Converting light into spectrally pure microwave oscillation. Opt Lett 21:483–485
3. Yao XS, Maleki L (1996) Optoelectronic microwave oscillator. J Opt Soc Am B 13:1725–1735
4. Yao XS, Maleki L (1996) Opto-electronic oscillator for photonic systems. IEEE J Quantum Electron 32:1141–1149
5. Mukherjee A, Biswas BN, Das NR (2015) A study on the effect of synchronization by an angle modulated signal in a single loop optoelectronic oscillator. Opt Int J Light Electr Opt 126:1815–1820
6. Bishayee K, Mandal S, Mukherjee A, Biswas BN, Sarkar CK (2018) Study on synchronization capability enhancement of optoelectronic oscillator using dynamic control band pass filter, IET Optoelectron
7. Mukherjee A, Ghosh D, Biswas BN (2015) On the effect of combining an external synchronizing signal feeding the Mach-Zehnder modulator in an optoelectronic oscillator. Opt Int J Light Electr Opt 127:3576–3581
8. Mukherjee A, Mandal S, Ghosh D, Biswas BN (2021) Influence of additive white Gaussian noise on the OEO Output. IEEE J Quantum Electron 57:1–10
9. Chembo YK, Larger L, Colet P (2008) Nonlinear dynamics and spectral stability of optoelectronic microwave oscillator. IEEE J Quantum Electron 44:858–868

10. Callan KE, Illing L, Gauthier DJ, Scholl E (2010) Broad band chaos generated by an Optoelectronic Oscillator. Phys Rev Lett 104
11. Chembo Koumou Y, Colet P, Larger L, Gastaud N (2005) Chaotic breathers in delayed electro-optical systems. Phys Rev Lett 95
12. Peil M, Jacquot M, Chembo YK, Larger L, Erneux T (2009) Routes to chaos and multiple time scale dynamics in broadband bandpass nonlinear delay electro-optic oscillators. Phys Rev E 79
13. Talla AF, Martinenghi R, Woafo PO, Chembo Y () Breather and pulse-package dynamics in multinonlinear electrooptical Systems with Delayed Feedback. IEEE Photon J 8
14. Géraud R, Chengui G, Jimmi H, Talla M, Talla AF, Woafo P, Chembo Y (2018) Dynamics of optoelectronic oscillators with electronic and laser nonlinearities. IEEE J Quantum Electron 54
15. Ghosh D, Mukherjee A, Das NR, Biswas BN (2018) Generation and control of Chaos in an optoelectronic oscillator. Opt Int J Light Electr Opt 165:275–287
16. Brunner D, Penkovsky B, Levchenko R, Schöll E, Larger L, Maistrenko Y (2018) Two-dimensional spatiotemporal complexity in dual-delayed nonlinear feedback systems: chimeras and dissipative solitons. Chaos 28
17. Larger L, Penkovsky B, Maistrenko Y (2015) Laser chimeras as a paradigm for multistable patterns in complex systems. Nat Commun 6
18. Nguimdo RM (2018) Constructing Hopf bifurcation lines for the stability of nonlinear systems with two time delays. Phys Rev E 97
19. Weicker L, Erneux T, Rosin DP, Gauthier DJ (2015) Multi-rhythmicity in an optoelectronic oscillator with large delay. Phys Rev E 91
20. Ghosh D, Mukherjee A, Das NR, Biswas BN (2018) Control of coexisting periodic oscillations in an optoelectronic oscillator. Opt Eng 57
21. Ghosh D, Mukherjee A, Mandal S, Das NR, Biswas BN (2022) Controlling birhythmicity in a new Dual Loop Optoelectronic Oscillator with an injection locked van der Pol oscillator. Phys D Nonlinear Phenom. https://doi.org/10.1016/j.physd.2022.133324
22. Yao XS, Maleki L (1997) Dual microwave and optical oscillator. Opt Lett 22
23. Yao S, Maleki L (2000) Multi-loop optoelectronic oscillator. IEEE J Quantum Electron 36:79–84
24. Ghosh D, Mukherjee A, Chatterjee S, Biswas BN (2016) A comprehensive theoretical study of dual loop opto electronic oscillator. Opt Int J Light Electr Opt 127:3337–3342
25. Erneux T, Grasman J (2008) Limit cycle oscillator subject to a delayed feedback. Phys Rev Lett E 78:1–8
26. Nayfeh AH (1981) Introduction to perturbation techniques. Wiley-Interscience, New-York
27. Nayfeh AH (2011) The method of normal forms. Wiley-Vch, Verlag GmbH & Co, KGaA Germany
28. Erneux T (2009) Applied delay differential equations. Springer Science & Business Media, Berlin
29. Engelborghs K, Luzyanina T, Roose D (2002) Numerical bifurcationanalysis of delay differential equations using: DDEBIFTOOL. ACM Trans Math Softw 28:1–21
30. Sieber J, Engelborghs K, Luzyanina T, Samaey G, Roose D (2014) DDE-BIFTOOL v.3.1.1 Manual—Bifurcation analysis of delay differential equations. http://arxiv.org/abs/1406.7144

Performance Analysis of Optical Arithmetic Circuit Using Artificial Neural Network

Dilip Kumar Gayen

Abstract Modern communication technologies need huge operational speed. This will be achieved if a standard data service, i.e. electron, is substituted by photon for the devices which are mainly focused on switching and logic. Gates are the basic building blocks of any complex circuit. Different logic and arithmetic operations can be carried out using these. In high-speed communication networks, all-optical arithmetic and logic operations are highly anticipated. In this chapter, the author has designed a parallel model to perform addition of two binary digits based on terahertz optical asymetric demultiplexer (TOAD)/semiconductor optical amplifier (SOA)-assisted Sagnac gates. By using only two parally operating TOADs-based switches, a half adder has been designed. An equivalent model of this circuit has also been designed using artificial neural networks (ANN). This circuit design has been verified by using ANN. This optical circuit not only increases the speed of operation but also produces the desired output in the optical domain. The most significant advantage of this parallel circuit is that no synchronization is required for the inputs. Details of the performance analysis of this circuit, using the ANN model, have been presented.

1 Introduction

Today's optical networks depend heavily on high-speed all-optical logic gates because they perform critical signal processing functions like switching regeneration and identification processing on photonic switching nodes [1–3]. The system for optically processing data has undergone a revolution. The Sagnac Gate with a Terehartz Optical Asymmetric Demaltiplexer (TOAD)/Semiconductor Optical Amplifier (SOA) is one of the optical switches that successfully combines low power consumption, high repetition rate, and quick switching time [4–6]. The SOA-assisted Sagnac

D. K. Gayen (✉)

Department of Computer Science & Engineering, College of Engineering and Management, Kolaghat, KTPP Township, Purba Medinipur, West Bengal 721171, India
e-mail: dilipgayen@cemk.ac.in

interferometer has been used to implement the half-adder, as proposed and shown by various research teams [7–11]. Using the Mach–Zehnder interferometer, Ghosh et al. have developed a contemporary method of expanding SOA to use optical frequency encoded operations [12]. Recently, neural networks have evolved into incredibly encouraging elective computing stages. Neural networks are developing theories to remove barriers to increase computational efficiency. A potentially effective way to address the energy-cost issue raised by deep learning is provided by optical neural networks [13]. Optics, which are caused by the local impedance characteristics of light, have been applied to neural network applications or free-space optical circuits to understand an optical lattice duplication unit that is completely inactive [14]. With the assistance of Machine Learning (ML), all scientists working on light–matter collaboration have turned onto another level, helped by material science, physical science, and photonic innovations. The first is the rise of wise photonic frameworks, another is the reconciliation of ML into physical and substance sciences for top to bottom information securing and inventive principal experiences [15]. Wu et al. have presented a method for optical performance monitoring of quadrature phase-shift-keying (QPSK) data signals by training the artificial neural networks and the parameters extracted from asynchronous diagrams. They demonstrated that in a 100 Gb/s QPSK system, balanced detection produces asynchronous diagrams that perform better than single-ended detection. Also, the usefulness of the proposed technique has been experimentally demonstrated [16]. The author has proved that an atomic vapor cell can conduct a local, consequently, a nonlinear activation in two dimensions. It is possible to use fully optical ANN for picture recognition written in digits. A network of this kind may manage a huge number of concurrent data streams [17]. Large-area optical switches, which have the important advantages of short idle time and low power consumption, are essential for facilitating the ever-increasing information exchange between servers in both intra- and inter-datacenter environments. Because of the advantages of low imprint and quick reaction time, coordinated silicon photonics has recently shown remarkable potential for developing large-scale optical switch textures for applications in the cutting-edge all-optical network [18]. Authors propose a binaries lucid optical beneficiary. This optical neural network uses opto-electronics components. This network comprises of a number of layers. Here, it uses three layers. The first layer is the transmission layer, second layer is the optical neuron layer, and the third layer is the electronic neuron layer. The transmission layer, which is based on the Mach–Zehnder interferometer (MZI), copies and selects the information optical sign for transmission into the opto-electronic network. The optical layer, which can be implemented on silicon alongside the transmission layer, consists of specially developed designs for planning binarized loads into optical space [19]. In this chapter, the author has provided a parallel model that uses Sagnac gates supported by semiconductor optical amplifiers (SOA)/terahertz optical asymmetric demultiplexers (TOAD) to add two binary digits. Only two parallelly running TOADs-based switches have been used to design a half-adder. The author has also designed a comparable model of this circuit by utilizing the ANN.

This circuit configuration has been verified by using the said ANN model. The advantage of this parallel circuit is that no synchronization is needed for the inputs. An ANN model was used to analyze this circuit's performance in detail.

2 Architecture of Switch

Figure 1 depicts the fundamental design of a TOAD-based switch [20–25]. An amplifier component is arranged unevenly in a circle in this illustration. The semiconductor optical amplifier is used for the optical amplifier. The output from both the transmitting and reflecting modes of this switch have to be used.

The power of the transmitting (POW_{Up}) and reflecting (POW_{Low}) ports might be expressed as [20–25]

$$POW_{Up}(t) = \frac{POW_{in}(t)}{4} \cdot \{GAIN_{cw}(t) + GAIN_{ccw}(t)$$
$$- 2\sqrt{GAIN_{cw}(t) \cdot GAIN_{ccw}(t)} \cdot \cos(\Delta\varnothing)\} \qquad (1)$$

$$POW_{Low}(t) = \frac{POW_{in}(t)}{4} \cdot \{GAIN_{cw}(t) + GAIN_{ccw}(t)$$
$$+ 2\sqrt{GAIN_{cw}(t) \cdot GAIN_{ccw}(t)} \cdot \cos(\Delta\varnothing)\} \qquad (2)$$

Here, gain in clockwise direction is $GAIN_{cw}(t)$ and gain in counter clockwise direction is $GAIN_{ccw}(t)$. Phase difference between these two gains is $\Delta\varnothing = -\beta/2 \log_e (GAIN_{cw}(t)/GAIN_{ccw}(t))$. The line-width enhancement factor is β.

Incoming signal enters the circular system via the optical circulator in the absence of a control (CP). This signal is split into two halves and sent through the loop. One portion moves in a clockwise manner, while the other moves in the opposite way. Both signals have the same amount of unsaturated gain. When the two signals meet again at the input, they achieve the same gain, i.e. $GAIN_{ccw} \approx GAIN_{cw}$. The phase

Fig. 1 Basic structure of TOAD
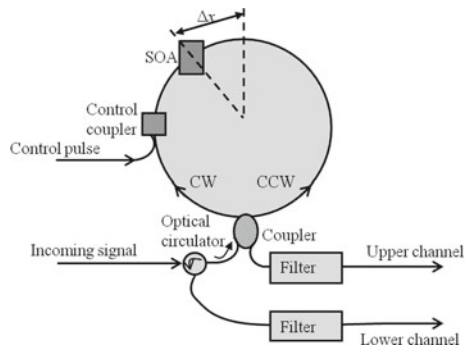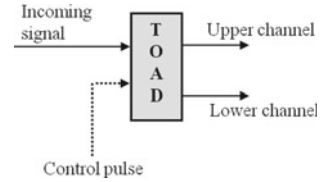
difference between them is nearly equal to zero at that point, i.e. $\Delta\emptyset \approx 0$. Then
the gain in the upper port is nearly equivalent to zero, i.e. $POW_{Up}(t) \approx 0$. The
gain in the lower port is hence $POW_{Low}(t) = POW_{in}(t) \cdot GAIN_{ss}$, where $GAIN_{ss}$
is the small signal gain. Information appears to be reflected back to the source.
After applying a CP, when it is fed into the system, it changes the properties of the
SOA. SOA's popularity is rapidly dwindling. Both signals have different amounts of
unsaturated gain. When the two signals meet again at the input, they achieve different
gains, i.e. $GAIN_{ccw} \neq GAIN_{cw}$. At that time, the phase difference between them is
roughly equivalent to -1, i.e. $\Delta\emptyset \approx -1$. The upper port gain is then almost equal
to $POW_{Up}(t)$, which is not zero. However, the power in the lower port is almost nil,
i.e. $POW_{Low}(t) \approx 0$. So the information appears only in the upper port at this point.
Equation (1) can be used to calculate the power at the upper port. Similarly, Eq. (2)
can be used to calculate the value of power at the lower port. At the output ports, a
band pass filter can be employed. The incoming signal will pass through this filter,
but the control signal will be blocked. The block diagram of a TOAD is shown in
Fig. 2.

3   Parallel Half Adder

Half-adder accepts two binary values as inputs, A and B, and provides a sum (S) and
a carry as outputs (Cout). The sum (S) and the carry (Cout) are each one bit. Figure 3
shows a circuit diagram for an optical parallel half adder. Only two TOAD-based
switches, TOAD1 and TOAD2, are used in this circuit.

By suitably adjusting the wavelength of the input signal through the wavelength
converter, the same input can be used both as a control and an incoming signal in
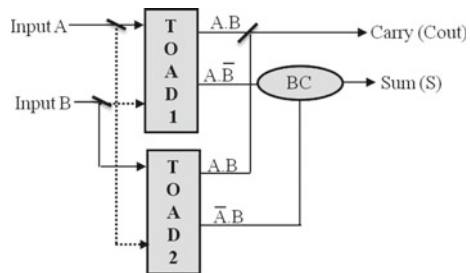
this circuit. By combining the lower channels of TOAD1 and TOAD2, the Sum (S) output is obtained, and similarly by combining the upper channels of TOAD1 and TOAD2, the Carry (C_{out}) output is obtained. These are depicted in Fig. 3.

4 Optical Neural Network

When necessary, optical neural networks (ONN) are developed. They have the qualities of high transmission capacity, high interconnection and interior equal handling, which can speed up the halfway activity of programming and electronic equipment, even up to the "light speed", is a promising strategy to supplant counterfeit neural network. Lattice increase can be done at the speed of light in the photonic structure, which can really settle the thick grid augmentation in the artificial neural network, to lessen the utilization of energy and time. In addition, the nonlinearity in ANN can likewise be acknowledged by nonlinear optical components. When the preparation of the optical brain network is finished, the whole construction can play out the optical sign computation without any additional energy input, at the speed of light.

Today, ANN vanquishes the requirements of ordinary techniques. A specific condition structure isn't used for setting up an ANN, but satisfactory input and output data are fundamental. After being trained, an ANN estimates output to new input data. When configured correctly, an ANN can examine the known data to learn any straight or nonlinear link. The fundamental step is to set up an ANN calculation with the aid of input and output data. As shown in Fig. 4, this neural network has three levels: the first level is the input level, the last level is the output level, and the intermediate level is the hidden level. This figure is represented by a single TOAD. In this plan, the input layer comprises of seven neurons, in particular, incoming pulse ($P_{in}(t)$), width of the incoming pulse (τ_0), recovery of gain time of the SOA (τ_e), T_{asym}, the loop eccentricity, CP as ($P_{cp}(t)$), control pulse energy (E_{cp}), and width of control pulse (σ) as indicated by the contributions of the framework. The resulting layer comprises of two neurons in particular, the upper channel (P_{Upper}) and the lower channel (P_{Lower}). Our dataset has been divided into three parts: the test dataset, the training dataset, and the validation dataset. For diverse objectives, multiple datasets are used. The arrangement of the neurons has been contrilled by using the training dataset.

To minimise error, the network adjusts its own weight capacity. Preparation is finished while network hypotheses are not outperforming, which is decided by the validation dataset. With the use of the testing dataset, the network performance both during and after training is evaluated. In this strategy, the training data use 85% of the total data collection, testing makes use of 10% of the data collection, and network validation is assessed using the remaining dataset.

For this method, 18 neurons are used in the hidden layer. Mean Square Error (MSE) is the common squared deviation between the results and targets. It is better to make it small. This value is closer to zero. Figure 5 displays the variation of MSE for training, validation, and testing datasets with many epochs. This figure shows
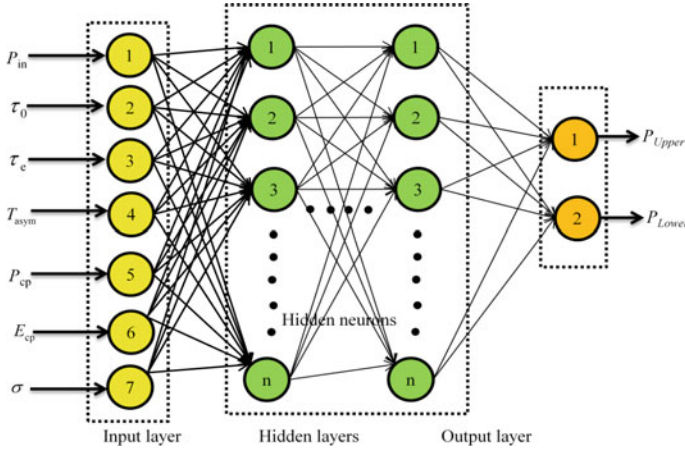
Fig. 4 An artificial neural network with a single TOAD has an input level with seven neurons and an output level with two neurons as its structural components

that the best result occurs at epoch number 22. The valuse of error is 0.099065. The training must be stoped after the epoch number 22.

The correlation between the results and goals determines the significance of a direct relapse. Close relationships always have a value between 1 and 0. Figure 6 displays the informative collection's relapse. As can be observed from the figure, the error factor is closer to 1, emphasising the close relationship between the input data and output data.

Connection among information sources and result focuses can be obtained by ANN in a direct or nonlinear relapse approach. Here, a straight relapse approach is applied for deciding the connection among the information sources and results. This ANN configuration acknowledges seven contributions as the incoming pulse ($P_{in}(t)$) [x_1], width of the incoming pulse (τ_0) [x_2], recovery time of gain of SOA (τ_e) [x_3], T_{asym} is the loop eccentricity as [x_4], control pulse ($P_{cp}(t)$) [x_5], control pulse energy (E_{cp}) [x_6], and width of the control pulse (σ) [x_7] and produce two outputs as the

Fig. 5 Change of MSE in respect to the number of epochs for the validation, training, and testing data sets
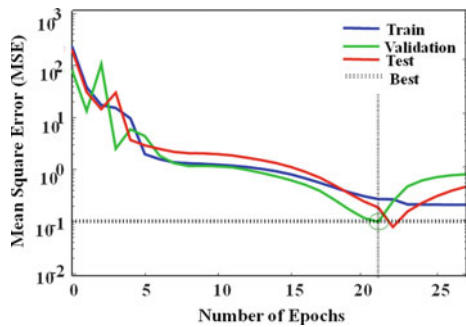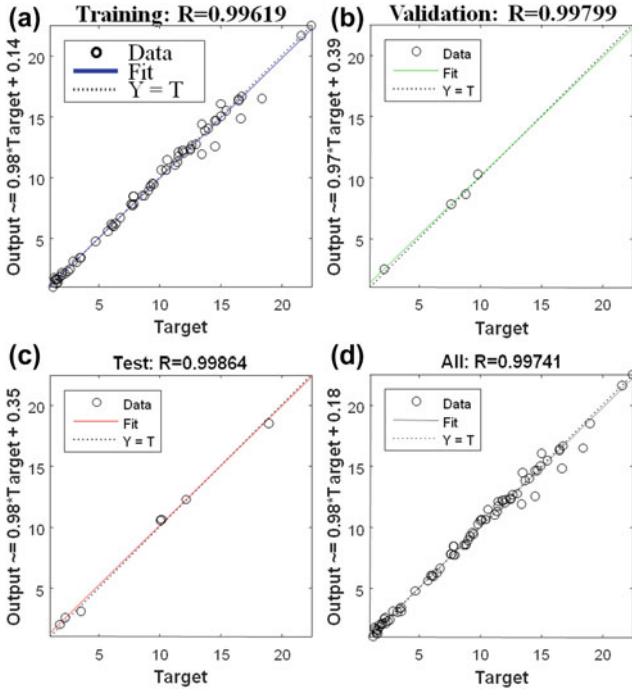
Fig. 6 Modeled data, training datasets, validation datasets, testing datasets, and the input dataset itself were used to fit regression to the input dataset

upper channel (P_{Upper}) [y_1] and lower channel (P_{Lower}) [y_2]. This capacity is for the most part eluded as actuation work. The author has endeavored to tackle a straight relapse issue with an essential direct condition as our enactment work. As far as a direct capacity, the straight relapse is characterized as

$$\hat{y_1} = b_1 + p'_1 x_1 + p'_2 x_2 + p'_3 x_3 + p'_4 x_4 + p'_5 x_5 + p'_6 x_6 + p'_7 x_7 \qquad (3)$$

$$\hat{y_2} = b_2 + p''_1 x_1 + p''_2 x_2 + p''_3 x_3 + p''_4 x_4 + p''_5 x_5 + p''_6 x_6 + p''_7 x_7 \qquad (4)$$

where $y_1{}^\wedge$ and $y_2{}^\wedge$ are the forecast for the result variables y_1 and y_2 and x_1, x_2,…, x_7 are the sources of info, p_1, p_2,…, p_7 are the loads and b_1 and b_2 indicate the predisposition terms. With this direct initiation work, the author has accomplished in general 99.74% precision of this ANN plan. Figure 6 shows the correlation between unique information with anticipated information and the relapse coefficient. From the figures (Figs. 5 and 6) it is seen that relapse factor is more like 1 depicting the power full relationship among the input informational index and demonstrated informational index in this neural network.

5   Results and Analysis

The writing guidelines for many research publications were used as the basis for the parameters used in this paper [5, 6, 15]. The values of several parameters are as follows: The SOA's unsaturated enhancer pickup (Gss) is 20 dB and 100 ps as τ_e is the pickup recuperation time of SOA. The others parameters are the E_{cp} as the exchanging beat vitality of 100 fJ, E_{sat} as the immersion vitality of the SOA of 1000 fJ, T_c as the bit period of 50 ps, σ as the full width at half greatest of the control beat of 12 ps, and T_{asym} as the unpredictability of the circle of 30 ps. These criteria were selected such that they must satisfy the operational requirement. Figures 7 and 8, respectively, show the adder circuit's corresponding input and output waveforms.

   To concentrate on the capacity of the circuit, increase in the proper width of the SOA short sign is observed for which the exchanging power is decreased. Therefore, the reliance of the turning power on the little sign increase is plotted in Fig. 9. From this figure it is seen that the power diminishes essentially with the increment of the little sign addition and arrives at least 100 fJ at 20 dB.

   ER is the extinction ratio. To evaluate our plan, considering the ER as [22],

$$E.R. = 10 \times \log\left(\frac{PO^1_{min}}{PO^0_{max}}\right) \qquad (5)$$

   In this Eq. (5), PO^1_{min} stands for the minimum power of the 1-state. Similarly PO^0_{max} stands for the maximum power of the 0-state. For better output, ER should ideally be more than 8.50 dB. 1- and 0-states can be distinguished from one another
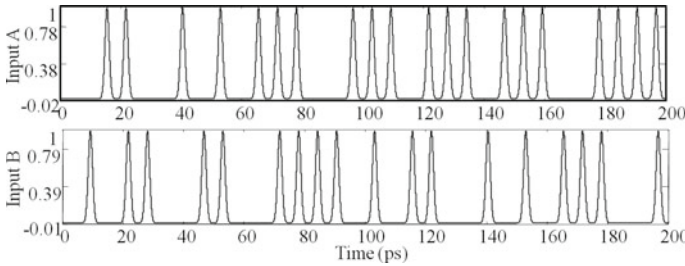
Fig. 7   Input waveforms of the Input A and Input B

Fig. 8   Output waveforms of the Carry (Cout) and Sum (S)
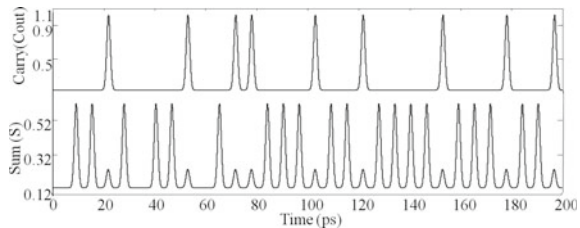
Fig. 9 Switching energy variation with respect to small signal gain
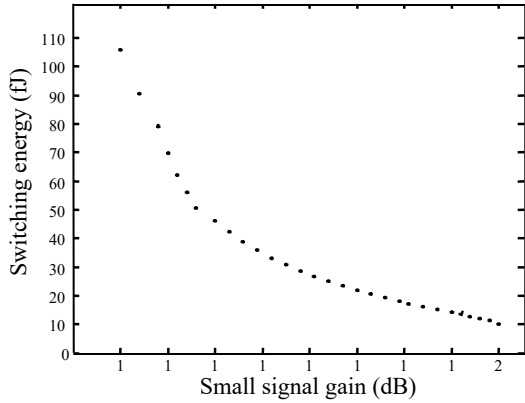
quite clearly based on the extinction ratio. Functionality of this design is dependent on CP energy and SOA recovery.

Figure 10 shows how the expansion, recovery, and energy of CP affect the ER. It is shown that ER grows with increasing CP energy and that ER decreases after a certain value (100 fJ and 100 ps). High expansion recovery times and CP energy also reduce ER, as can be observed in Fig. 10. This was protected by obtaining a dynamic SOA answer. Beat requires more opportunity to recover its fundamental increment for high expansion recovery times, which reduces ER. With a fixed inundation power, the submersion energy decreases as the gain recovery time increases. Less energy is anticipated to flood the SOA as a result, which is the rationale.

The optical bit rate component is a key restriction that affects the circuit display. Figure 11 shows how gain recovery time and information estimation affect the ER. It states that a lower ER results from a lower bit estimation and a longer recovery period. This happens as a result of an improper method; altogether, the SOA needs more in order to reclaim its advantage and supplies the required fragment adjustment. The ER demonstrates consistency once a bit and the recovery time cost of gain calculation has been completed. A specified ER will be reached with less energy and a more limited bit estimation.

Fig. 10 A variety of ER with increased CP recovery time and energy at the results, while maintaining fixed other boundaries
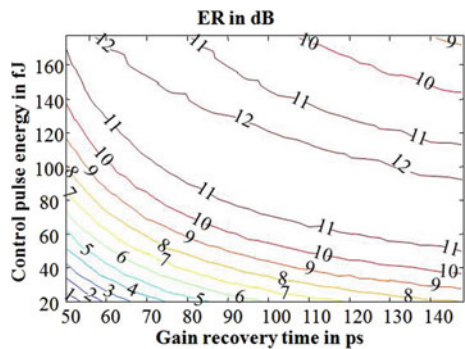
Fig. 11 Shows several ER types with pulse width and recovery duration at the outcomes
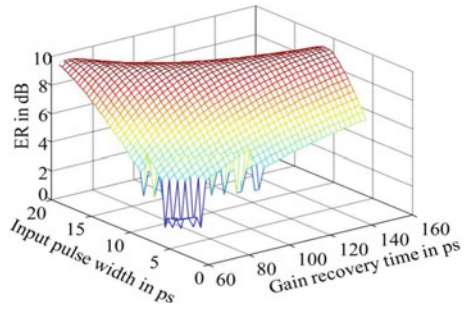
Fig. 12 Pseudo eye chart
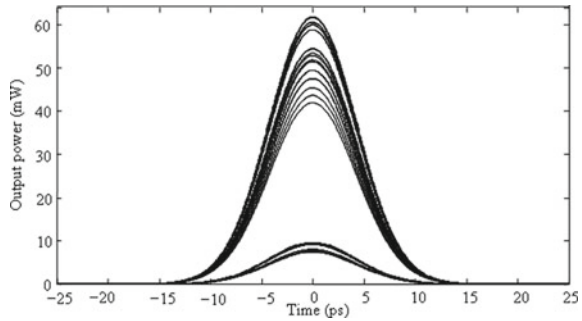
When information sources are used multiple times, such as when the inputs range from zero to one or one to one, etc., the results are superimposed to make an eye-chart [26]. Figure 12 is clearly not a typical eye-outline because the locator and optical strands provide connection links, such as clamor source, which are not as enlightening as in the deteriorating effects, which are often observed in the highlight point. This figure is known as a pseudo-eye-diagram[27].

The general eye opening (O) is characterized $O = (P^1_{min} - P^0_{max}) / P^1_{min}$, as P^0_{max} and P^1_{min} are the maximum and minimum powers at the outputs at 0-state and 1-state, respectively. Huge eyes on an eye-graph indicate a transmission that is unambiguous and has a low piece rate [28]. The value of eye opening (O) is found to be 87.5%. This value displays a fairly respectable response from the circuit's output terminals.

6 Summary

The author has designed an optical parallel half adder utilizing only two TOAD-based switches. The circuit has designed theoretically and verified through numerical simulations. Both the ports, reflected and transmitted, are used to perform the simulation of the circuit. This circuit gives the desired result at the outputs. The author has also

designed a comparable model of this circuit by utilizing ANN. This circuit configuration has been confirmed by utilizing ANN. This optical circuit not only increases the speed of the operation but also produces the desired output in the optical domain. The most notable advantage of this parallel circuit is that no synchronization is required for the inputs. This circuit can serve as a fundamental building block for more complicated circuit designs.

References

1. Suzuki M, Uenohara H (2009) Invesigation of all-optical error detection circuitusing SOA-MZI based XOR gates at 10 Gbit/s. Electron Lett 45(4):224–225
2. Gayen DK, Roy JN, Taraphdar C, Pal RK (2011) All-optical reconfigurable logic operations with the help of terahertz optical asymmetric demultiplexer. Int J Light Electron Opt 122(8):711–718
3. Minh HL, Ghassemlooy Z, Ng WP (2008) Characterization and performance analysis of a TOAD switch employing a dual control pulse scheme in high speed OTDM demultiplexer. IEEE Commun Lett 12(4):316–318
4. Bhattacharyya A, Gayen DK, Chattopadhyay T (2013) Alternative all-optical circuit of binary to BCD converter using terahertz asymmetric demultiplexer based interferometric switch. In: Proceedings of 1st international conference on computation and communication advancement (IC3A–2013)
5. Zoiros KE, Vardakas J, Houbavlis T, Moyssidis M (2005) Investigation of SOA-assisted Sagnac recirculating shift register switching characteristics. Int J Light Electron Opt 116(11):527–541
6. Zoiros KE, Avramidis P, Koukourlis CS (2008) Performance investigation of semiconductor optical amplifier based ultra-fast nonlinear interferometer in nontrivial switching mode. Opt Eng 47(11):115006–115011
7. Li P, Huang D, Zhang X, Zhu G (2006) Ultra-high speed all-optical half-adder based on four wave mixing in semiconductor optical amplifier. Opt Exp 14(24):11839–11847
8. Kim JH, Kim SH, Son CW, Ok SH, Kim SJ, Choi JW, Byun YT, Jhon YM, Lee S, Woo DH, Kim SH (2005) Realization of all-optical full-adder using cross-gain modulation. Proc Conf Semicond Lasers Appl, SPIE 5628:333–340
9. Poustie A, Blow KJ, Kelly AE, Manning RJ (1999) All-optical full-adder with bit differential delay. Opt Commun 168(1–4):89–93
10. Mukhopadhyay S, Chakraborty B (2009) A method of developing optical half- and full-adders using optical phase encoding technique. In: Proceedings of the conference on communications, photonics, and exhibition (ACP), TuX6, pp 1–2
11. Mukherjee K (2011) Method of implementation of frequency encoded all-optical half-adder, half-subtractor, and full-adder based on semiconductor optical amplifiers and add drop multiplexers. Int J Light Electron Opt 122(13):1188–1194
12. Ghosh P, Kumbhakar D, Mukherjee AK, Mukherjee K (2011) An all-optical method of implementing a wavelength encoded simultaneous binary full-adder-full-subtractor unit exploiting nonlinear polarization rotation in semiconductor optical amplifier. Int J Light Electron Opt 122(19):1757–1763
13. Wang T, Ma S-Y, Wright LG, Onodera T, Richard BC, McMahon PL (2022) An optical neural network using less than 1 photon per multiplication. Nat Commun 13(123):1–8
14. Lin X, Rivenson Y, Yardimci NT, Veli M, Luo Y, Jarrahi M, Ozcan A (2018) All-optical machine learning using diffractive deep neural networks. Science 361(6406):1004–1008
15. Zhou J, Huang B, Yan Z, Bünzli J-CG (2019) Emerging role of machine learning in light-matter interaction. Light Sci Appl 8:84. https://doi.org/10.1038/s41377-019-0192-4

16. Wu X, Jargon JA, Paraschis L, Willner AE (2011) ANN-based optical performance monitoring of QPSK signals using parameters derived from balanced-detected asynchronous diagrams. IEEE Photon Technol Lett 23(4):248–250

17. Ryou A, Whitehead J, Zhelyeznyakov M, Anderson P, Keskin C, Bajcsy M, Majumdar A (2021) Free-space optical neural network based on thermal atomic nonlinearity. Photon Res 9(4):B128–B134

18. Gao W, Lu L, Zhou L, Chen J (2020) Automatic calibration of silicon ring-based optical switch powered by machine learning. Opt Exp 28:10438–10455

19. Yu Z, Zhao X, Yang S, Chen H, Chen M (2020) Binarized coherent optical receiver based on opto-electronic neural network. IEEE J Sel Top Quantum Electron 26(1):1–9

20. Sokoloff JP, Prucnal PR, Glesk I, Kane M (1993) A terahertz optical asymmetric demultiplexer (TOAD). IEEE Photon Technol Lett 5(7):787–790

21. Wang B, Baby V, Tong W, Xu L, Friedman M, Runser R, Glesk I, Prucnal P (2002) A novel fast optical switch based on two cascaded terahertz optical asymmetric demultiplexers (TOAD). Opt Exp 10(1):15–23

22. Gayen DK, Chattopadhyay T, Das MK, Roy JN, Pal RK (2011) All-optical binary to gray code and gray to binary code conversion scheme with the help of semiconductor optical amplifier -assisted sagnac switch. IET Circ Dev Syst 5(2):123–131

23. Gayen DK (2016) Optical arithmetic operation using optical demultiplexer. Circ Syst 7(11):3485–3493

24. Gayen DK (2016) All-optical 3:8 decoder with the help of terahertz optical asymmetric demultiplexer. Opt Photon J 6(7):184–192

25. Gayen DK (2022) Optical parallel half adder using semiconductor optical amplifier-assisted Sagnac gates. J Mech Continua Math Sci 17(4):1–7

26. Gowar J (1993) Optical communication system, 2nd edn. Prentice Hall of International Limited, UK

27. Wang Q, Zhu G, Chen H, Jaques J, Leuthold J, Piccirilli AB, Dutta NK (2004) Study of all-optical XOR using Mach-Zehnder interferometer and differential scheme. IEEE J Quant Electron 40(6):703–710

28. Yariv A, Yeh P (2007) Photonics: optical electronics in modern communications, 6th edn. Oxford University Press, UK

Design and Modeling of an Infrared Sensor-Based Object Detection Circuit for Computer Vision Applications

Pratik Acharjee, Avirup Majumder, Aritrya Chatterjee, and Jayabrata Goswami

Abstract Infrared (IR) sensor utilizes the principle of selective light sensing by distinguishing a particular light wavelength within the entire infrared (IR) spectrum. Currently, the cutting-edge industries are utilizing infrared sensors in various applications. In this chapter, the authors have proposed a contemporary demonstration of Infrared Sensor-based object detection circuit (ODC) by using Multisim software. The proposed circuit will be useful for various computer vision applications.

1 Introduction

Theoretical analysis of object detection, by utilizing the infrared (IR) spectrum, has already shown various potential capabilities. The essential deep neural network for object detection is already over-feat. Object detection combines the tasks of object classification and localization. An object detector can be defined as a network separating the task of deciding the placement of objects and classification [1].

An IR device measures and recognizes infrared wavelength in its encompassing air medium. The infrared radiation from the semiconductor light emitting diode gets reflected by the object and that reflected IR's wavelength is sensed by the IR sensor [2]. Object detection is a crucial task that deals with various kinds of investigation on the instances of visual objects (such as humans, animals, or cars) in one or more digital pictures. The target of object detection is to develop procedural models and techniques. The IR sensing component may be a simple device that transmits IR radiation, senses the reflected wave and identifies the object from the reflected IR radiation in order to detect the bound obstacles [3]. Object detection is the process of finding and classifying a variety of objects on an image. The output of an object detector may be very complex in nature, since the quantity of the detected objects

P. Acharjee · A. Majumder · A. Chatterjee
University of Engineering and Management, New Town, Kolkata, India

J. Goswami (✉)
Netaji Subhas Open University, Saltlake, Kolkata, India
e-mail: goswamijayabrata@gmail.com

might change from image to image [4]. In order to overcome those drawbacks, the authors have used the associate degree IR sensing element [5] in their design.

The authors are aiming to modify and improve the model of the IR (infrared) sensor-based circuit of the existing object detection system for physically challenged persons, which is a part of computer vision application.

2 Circuit Design and Principle

Figure 1 shows the basic IR sensor-based circuit which was reported in Ref. [6]. The circuit is capable of detecting a single object at a time. But the major drawback of this circuit is that it cannot detect multiple-objects simultaneously, which is essential for the real-world scenario.

The circuit shown in Fig. 1 is implemented and analyzed using Multisim Software. An infrared sensor is an electronic device which can recognize the degree of the transmitted infrared radiation in its surrounding environment. As a result, when any obstacle or a body comes close to the sensor, the infrared light emitted from the circuit gets reflected by the obstacle or body and that the reflected light is recognized by the beneficiary IR sensor. Figure 2 shows the modified circuit designed by the authors using IR sensor, Zener diode, P–N Junction diode. It is capable of detecting multiple objects simultaneously. This circuit is also simulated by the Multisim software.

Table 1 provides the list of basic components which are used for the circuit implementation. Therefore, the above mentioned new design model is a very promising circuit for multiple signal detection circuit analysis for Computer Vision Applications.
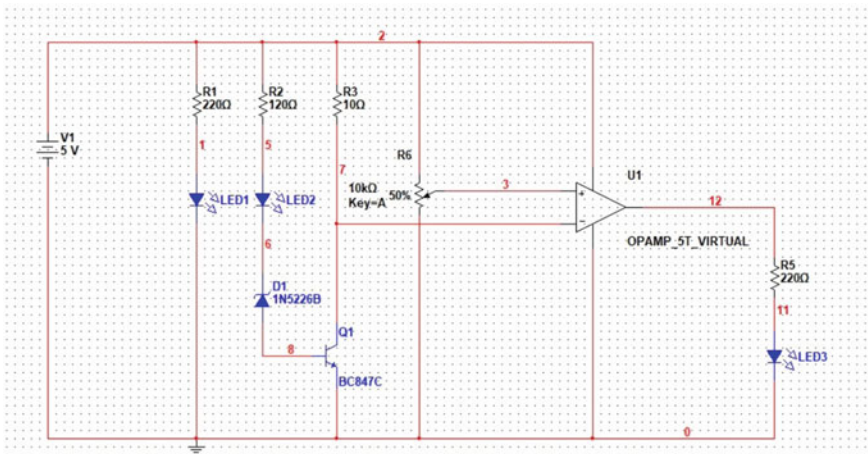
Fig. 1 IR sensor-based circuit for object detection [6]
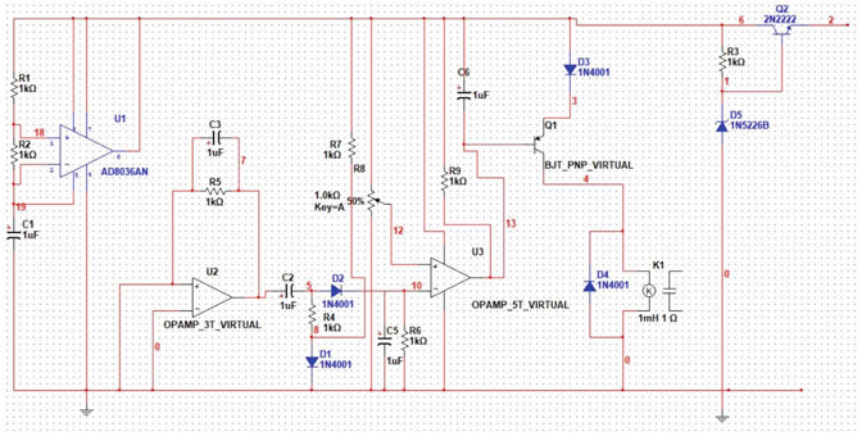
Fig. 2 Infrared sensor-based modified object detection circuit

Table 1 List of basic components

Serial number	Parts list	Values
01	Resistance R1	10 k (2 W)
02	Resistance R2, R5, R6, R9	1 k (2 W)
03	Resistance R3	33R (2 W)
04	Resistance R4, R8	1 M (2 W)
05	Trimmer Cermet R7	10 k
06	Resistance R10	22 k (2 W)
07	Capacitance C1, C4	1 uF
08	Capacitance C2	47 pF
09	Capacitance C3, C5, C6	100 uF
10	Diode D1	IR LED
11	Diode D2	IR photo-diode
12	Diode D3, D4	1N4148 (75 W/150 mA)
13	Diode D5	LED
14	Diode D6, D7	1 N 4002
15	PNP Transistor Q1	BC 558 (45v/800 mA)
16	Timer IC IC1	NE 555
17	PNP transistor	BC 558
18	NPN transistor	BC 548
19	Relay	SPDT (2A/220v)

3   Circuit Operation

The circuit uses a yield of IC1 555 IC implied for a prerequisite cycle of 0.8 ms, with a recurrence of 120 Hz and 300 mA top current. It is utilized to drive the ruddy intersection rectifier (D1) diode. From the connection, it is clear that the diodes D1 and D2 are in a straight-line and essentially a few centimeters separated on the board. Hence, the diode D2 gets the infra-red yield from the diode D1. The diode flag that is connected to the rearranging terminal of the op-amp IC LM358 gets intensified IR radiation and finally it is recognized by diode D4 and capacitor C4. The forward voltage developed across diode D4 is compensated by diode D3 and resistances R5 and R6. According to the separation between the infra-red transmitter and receiver, a relative DC voltage is applied to the modifying input of IC2. According to the yield of the comparator, the intersection rectifier is either turned ON or OFF. It is often regularly recognized by the semiconductor device Q1. Thus the hand-off is driven as per the output of Q1. This circuit is mainly utilized for discovering the fluid level location or its vicinity. A leading advantage of this circuit is that no physical contact is required from the distance measurement. Accurate remote distance measurement is possible.

4   Summary

In this chapter, the authors have presented a modified and improved design of IR sensor-based object detection circuit by using Multisim software simulation tools. This system can distinguish the infrared signal for detecting any object in its proximity and can be very useful for physically challenged people to identify obstacles.

References

1. _____, IR sensor circuit and its working principle. https://www.elprocus.com/infrared-ir-sensor-circuit-and-working/. Accessed June 2022
2. _____, Infrared sensors. http://www.engpaper.com/infrared-sensor.htm. Accessed June 2022
3. _____, Electrical & systems engineering. Report published by Washington University, St. Louis. https://ese.wustl.edu/ContentFiles/Research/UndergraduateResearch/Final%20Report.pdf. Accessed June 2022
4. Redmon J (2016) You only look once: unified, real-time object detection. In: Proceedings of the IEEE conference on computer vision and pattern recognition. arXiv: 1506.02640. Bibcode: 2015arXiv150602640R
5. Yi LT (2020) Focal loss for dense object detection. IEEE Trans Pattern Anal Mach Intell 42(2):318–327
6. Herbert L (1972) Berman, Altos Hills Los, and Calif, infrared intrusion detector. System 3:703–718

A Comprehensive Analysis on Bandwidth Management in 6G: Sharing, Reuse or Introducing New Bandwidth?

Babul P. Tewari and Shankar K. Ghosh

Abstract The performance of the traditional cellular network becomes restricted due to significant increase in the number of mobile users with high data rate applications. Nowadays, growing number of network connectivity creates a tremendous spectrum crisis on the usage of cellular licensed band. In this context, the sixth generation (6G) network system is envisioning the promise of very high data rate with increased network capacity. However, limitation in the availability of cellular licensed spectrum limits the performance of existing cellular systems. To increase the system capacity, a number of attempts have been initiated in the recent past. It may be noted that the upgradation to a higher generation network system is mainly concerned about (a) increasing the spectral efficiency by intelligently sharing the spectrum among the users (e.g., cognitive radio, device-to-device communication) (b) increasing the available bandwidth by introducing new frequency bands (e.g., unlicensed band, terahertz frequency, millimetre wave frequency etc.) and (c) increasing the reuse of the existing bandwidth (e.g., ultra-densification, reconfigurable intelligent surface, interference cancellation etc.). In this work, first we have analysed different solutions for bandwidth increment comprehensively, and then pointed out the challenges and opportunities associated with each particular paradigm.

B. P. Tewari (✉)
Department of Computer Science and Engineering, Indian Institute of Information Technology, Bhagalpur 813210, India
e-mail: bptewari.cse@iiitbh.ac.in

S. K. Ghosh (✉)
Department of Computer Science and Engineering, Presidency University, Bangalore 560064, India
e-mail: shankar.it46@gmail.com

1 Introduction

Future wireless communications will be driven by technology that promises Internet of Everything (IoE). It will revolutionize people's daily life by their rich technological features. The sixth-generation cellular system (6G) is expected to be a heterogeneous network (HetNet) consisting of different kinds of radio access technologies such as new radio (NR), long term evolution advanced (LTE-A) and 802.11 wireless local area networks (WLAN). In addition, 6G is expected to introduce several service classes requiring high reliability, low latency and high throughput. Ultra-dense connectivity, high data rate and low latency remain the basic requirements of 6G that are further extended to meet the demands of IoE. Such demanding requirements may include tera-hertz communications, large intelligent surface, orbital angular momentum (OAM), spectrum sharing using blockchain technology, quantum and molecular communications [1]. Network capacity becomes restricted due to the increasing load from the ongoing densification of the different networks. While roaming across such HetNet, the data rate received by the mobile terminals (MTs) may fall below the requested rate due to path loss, fading and increased interference. Such data rate reduction calls for frequent network switching between adjacent cells. Frequent network switching also has a significant influence on the interference relationship resulting in a gross degradation of network performance. Coexistence of such multiple networks calls for an efficient user association mechanism that would not only mitigates the interference but also helps to attain the desired quality of service (QoS) through achieving a high data rate. Hence, designing appropriate user association remains a praising research challenge in this direction. This requires detailed consideration of service requirement, network characteristics and communication technology used.

Since high data rate is the main concern in the forthcoming 6G systems, so far, there is no unified solution to provide the expected data rate and it is worthy to analyse the scope of bandwidth increment. We consider the well-known Shannon Capacity formulae as the starting point of our analysis: $B = \log_2(1 + S/(N + I))$, where B represents the communication bandwidth, S represents the signal strength and I represents the interference. It may be noted that the upgradation to a higher generation network system is mainly concerned about (a) increasing the bandwidth (B) by intelligently sharing the spectrum among the users (e.g., cognitive radio, device-to-device communication) (b) increasing the available bandwidth (B) by introducing new frequency bands (e.g., unlicensed band, terahertz frequency, millimetre wave frequency etc.) and (c) decreasing the interference (I) by increasing the reuse of the existing bandwidth (e.g., ultra-densification, reconfigurable intelligent surface, interference cancellation etc.).

Device-to-Device (D2D) communication helps to coordinate communication among two nearby devices without taking support from any existing infrastructure [2]. The main advantages of D2D communications are increased spectrum efficiency, high proximity gain and reuse gain. As D2D enables short range direct communication, it has a positive impact on energy efficiency and maintaining QoS [3]. Sharing

the uplink spectrum resource with the existing cellular network enables the D2D technology to achieve a higher spectrum efficiency [3, 4]. The potential data rate of D2D communication can be immensely higher with the help of millimetre-wave (mm-wave) technology. Therefore, mm-wave enabled D2D technology is an important technological feature for future wireless communications. Despite such advantages, mm-wave suffers from the drawback of high propagation loss and path loss from the obstacles [5, 6]. Hence, there is a continuous need for finding a suitable D2D user association technique that uses such high data rate enabling technology while avoiding the drawback of intermediate obstacles. Sharing an uplink spectrum resource leads spectrum efficiency, however, significant interferences are caused by simultaneous communications in the same band of a heterogeneous networks. Therefore, along with an intelligent user association scheme there is also a need for a suitable interference management policy.

Reconfigurable intelligent surface (RIS) has been introduced to eliminate the interference in ongoing D2D communications [3]. Using RIS, the interference can be cancelled with appropriate beamforming. Moreover, RIS can also help to avoid the loss from intermediate obstacles. To provide high throughput to the users, RIS has emerged as one of the promising solutions to improve the coverage and data rate in 6G systems. RIS is a holographic multiple input multiple output surface [3]. In RIS, a massive number of passive radiating elements are stacked to realize a continuous electromagnetically active surface. In an RIS assisted environment, data can be communicated to the users in *two ways*: firstly, through the *direct channel* from the serving base station (BS) to the user (namely channel A) and secondly, through the *indirect channel* via the RIS (namely channel B). Due to availability of an additional channel, throughput performance in the RIS assisted environment is greatly enhanced [7].

It may be noted that although RIS has been envisioned to reduce interference in D2D communication, it imposes a significant design complexity in the communication system. It has been shown that interference may become significantly higher depending on the beamwidth when D2D communication is integrated with RIS. Therefore, RIS deployment must be taken care with appropriate beamwidth selection [8].

To satisfy the requested bandwidth, appropriate associations between MTs access networks are very crucial. The traditional *user association problem* is known to be NP-hard [9, 10]. On top of that 6G introduces new challenges. For example, a user can be associated with the target network via RIS in the presence of dynamic obstacles even if the direct channel from the serving base station is not available. Since, the RIS assisted wireless environment involves a lot of stochastic components including intermittency of channel B, user preference, user mobility and type of requested service, the user association mechanisms designed so far cannot address the challenges associated with RIS enabled networks. Hence, designing user association algorithms in such context is still a challenging problem for the research community.

In this work, our *objective* is to provide a comprehensive review on different paradigms of increasing spectral efficiency and then analyse the challenges and

opportunities associated with each paradigm. Our *contributions* can be summarized as follows:

- First, we provide a brief discussion on the existing capacity improving paradigms such as D2D, millimeter wave communication, unlicensed band communication and RIS.
- Then we classify the existing approaches to improve spectral efficiency in the context of forthcoming 6G systems.
- Next, we analyse the advantages and drawbacks associated with each paradigm.

We organize the paper as follows: Sect. 2 describes a brief overview of the existing paradigms followed by a comprehensive analysis on the existing approaches in Sect. 3. Section 4 presents the challenges and opportunities associated with each paradigm. Finally, we conclude the paper in Sect. 5.

2   Brief Overview of Existing Approaches

D2D communications has been evolved as one of the important communication paradigms under 5G cellular communications. This allows two nearby devices to communicate directly without taking infrastructure support from the existing cellular base station (BS) or evolved NodeB. It is a key enabling technology that provides high speed QoS specific communication with suitable spectrum efficiency. In licensed band cellular communication, D2D carries opportunistic use of the spectrum band with the existing cellular communication and the approach is called the underlay D2D mode [11]. On the other hand, when it uses its reserved band other than the cellular users it is supposed to operate in the overlay mode. D2D communication may take place in the unlicensed spectrum without affecting the performance of the existing Wi-Fi communications [2]. D2D communication contributes high data rate, feasible spectrum efficiency and low energy consumption to the 5G and B5G communications.

RIS has been envisioned as a new type of relaying technology for future wireless communications [8]. RIS is a holographic multiple input multiple output surface [12]. In RIS, a massive number of passive radiating elements are stacked to realize a continuous electromagnetically active surface. In an RIS assisted environment, data can be communicated to the mobile terminal (MT) in *two ways*: firstly, through the *direct channel* from the serving BS to the MT (namely channel A) and secondly, through the *indirect channel* via the RIS (namely channel B). Due to the availability of an additional channel, throughput performance in the RIS assisted environment is greatly enhanced [7].

Millimeter wave communication has been exploited as one of the spectrum band solutions for 5G communications [11]. It is a promising solution for high-speed communications in a short range. In mm wave, a wide range of carrier frequencies operate over the 3–300 GHz band and include many feasible characteristics like

higher bandwidth and directional transmissions. Using mm wave the D2D communications can take place at a very high speed and thereby can achieve a high network performance.

3 Comprehensive Analysis on Existing Approaches

The performance of the traditional cellular network is limited by the availability of bandwidth. To increase the system capacity, a number of attempts have been initiated in the recent past. The upgradation to a higher generation network system is mainly concerned about (a) increasing the spectral efficiency by intelligently sharing the spectrum among the users (e.g., cognitive radio, D2D) (b) increasing the available bandwidth by introducing new frequency bands (e.g., unlicensed band, terahertz frequency, millimetre wave frequency etc.) and (c) increasing the reuse of the existing bandwidth (e.g., ultra-densification, RIS, interference cancellation etc.). With the introduction of different access technologies (e.g., OFDMA, BDMA) and various kinds of user demands, the future generation networks are moving towards heterogeneity. In this section, we will provide a brief description of the existing works in the *aforesaid directions* as long as the upgradation from 5 to 6G is concerned. The existing works can be summarized as follows (Table 1).

3.1 Intelligently Sharing the Spectrum

D2D communications is an emerging communication paradigm for B5G systems where closely located user equipment can directly communicate with each other without the involvement of any physical infrastructure support. In such communications, D2D users opportunistically use the cellular spectrum to satisfy their demands. D2D communication was proposed to increase the service coverage of the existing

Table 1 Summary of the existing works

Main concern	Technology used	Existing works
Intelligently sharing the spectrum	D2D	[4, 9, 13–17]
	Load balancing	[18, 19]
Introducing new frequency bands	Unlicensed band	[2, 10, 20]
	Millimetre wave frequency	[21, 22]
Reuse of existing bandwidth	Ultra-densification	[23, 24]
	RIS	[3, 25–29]
	Interference management	[4]

base stations by sending the data packets over multiple hops [4, 9]. In D2D communications, two closely located user equipment can directly communicate with each other without any infrastructure support [9]. Waqas et al have addressed the mobility management perspectives in D2D association mechanisms [13]. In Ref. [14], a user association mechanism has been proposed explicitly considering the delay and power constraints. In the D2D environment, user association is quite challenging because of the mobility of the users [9]. In Refs. [4, 15], user association mechanisms have been proposed to minimize interference and power allocation, respectively. Mukherjee and Ghosh [16] have proposed a game theoretic approach for the resource allocation among the 5G D2D users considering the issue of fairness between the legacy 4G users and 5G users. Ghosal et al. has proposed a near optimal solution for joint power and channel allocation problem for D2D users [17].

In Ref. [18], Zhou et al. have proposed a load balancing strategy with frequency partitioning scheme with an objective to maximize the logarithmic sum-rate. Load balancing in the context of D2D resource allocation from the perspective of orthogonal frequency division multiple access (OFDMA) has been addressed by Zhang et al [19]. In Ref. [13], Waqas et al have proposed a D2D association considering mobility perspective [13]. Here, an integrated approach of power control and user association has been taken with an objective to minimize the overall power consumption [14]. Here, the authors have framed the problem as a mixed linear integer programming problem. In Ref. [15], Liang et al. have proposed a D2D resource allocation mechanism through spectrum sharing and power allocation for vehicular communications. A review on resource allocation for D2D communications has been presented by Jayakumar and Nandankumar [30].

3.2   Introducing New Frequency Bands

The main reason of interference is that D2D users as well as the usual mobile terminals are sharing the same band of frequency among them [3]. So, the D2D association ensuring spectrum efficiency is of utmost importance. To alleviate the crisis of licensed spectrum, several efforts have been initiated to introduce an *unlicensed band* in D2D communication [2, 20]. The authors have analysed interference when both licensed and unlicensed spectrums are used for communication in D2D. Exploiting the frequency band having a higher frequency (e.g., millimetre wave) is also an option to improve data rates in the forthcoming wireless systems. In Ref. [22], Liu et al. have introduced the millimetre wave in D2D communications for enhanced capacity. However, it is important to note that due to the presence of obstacles, millimetre wave communication may suffer a high path loss. A detailed survey in this direction can be found in Ref. [31]. In Ref. [21], Basar et al. have addressed the importance of designing a new radio interface in order to communicate in 6G systems. User association in the context of 802.11 WLAN which is fully based on an unlicensed band has been addressed by Tewari and Ghosh [10].

High propagation and penetration losses from the obstacles are the major performance constraints in millimetre wave D2D communications as reported in Ref. [5]. To address this problem, Ganesan and Ghosh have introduced multiple hops in between the source and destination to avoid the obstacles [6]. Here, the authors have shown that introducing multiple hops is a better solution than that of the existing probabilistic models. Dutta et al. have addressed the resource allocation in the context of a relay-based D2D association [29].

3.3 Reuse of Existing Bandwidth

To improve spectral efficiency, ultra-densification has emerged as a promising solution. However, due to limited coverage regions of small cells in ultra-dense networks, frequent handover may occur which results in severe performance degradation [23]. Habbal et al. have proposed a context aware network selection mechanism for the ultra-dense network scenario [23]. In Ref. [24], an adaptive cell selection methodology has been proposed for ultra-dense heterogeneous networks considering load balancing.

In Ref. [3], Chen et al. have shown how RIS deployment can help to reduce interference in the heterogeneous network scenario. In Ref. [25], it has been shown that the reflecting surface of the RIS helps appropriate beamforming optimization leading to an enhanced data rate and interference cancellation. Zhang et al. have analysed the impact of phase shift on the obtained data rate [27]. A hybrid beamforming scheme for multiple users in the RIS deployed environment has been proposed by Di et al. [28]. Mao et al. [32] have addressed the use of an intelligent surface for the purpose of task offloading and simultaneous resource management. Here, different system parameters such as power management, bandwidth allocation and phase beamforming of the surface have been considered. Cao et al. [12] have addressed the challenges associated with RIS functioning in the medium access control (MAC) layer. It has been argued that AI-assisted MAC will result in less complexity in the RIS assisted environment. Cai et al. [26] proposed a time scale optimization technique for RIS assisted D2D communications in the underlay mode. It may be noted that the existing works either have considered the random deployment of the RIS or have assumed an existing deployment of the RIS.

Millimetre-wave can help to obtain a high data rate but they are obstacles prone. Dev et al. have shown that deployment of RIS can mitigate interference in millimetre wave D2D communications [29]. The authors have argued for deployment of minimum number of RISs. Dev and Ghosh have proposed a resource block allocation problem for the RIS assisted network environment considering both direct and indirect channels. In these works, the authors have assumed a random deployment of the RISs.

4 Challenges and Opportunities

4.1 User Association in RIS Assisted Environment

In recent past, a number of user association mechanisms have been proposed for 5G cellular networks. A survey of such mechanisms can be found in Ref. [9]. In Ref. [23], a context aware user association algorithm has been proposed for HetNets based on the context-aware analytic hierarchy process. In Ref. [33], a user association mechanism has been proposed for 5G networks based on a metric namely the reference base station efficiency (RBSE). The RBSE metric explicitly considers the cumulative effect of transmitted powers, traffic load and user's spectral efficiency to select the target network. In Ref. [34], a user association mechanism has been proposed for 5G ultra dense networks which can estimate achievable throughput values from different candidate access networks after handoff execution. However, these existing user association mechanisms are inefficient in RIS assisted environment as the effect of indirect channels are not taken care of.

B5G wireless systems are highly complex due to the exponential increase of traffic demand, service categories, end- user devices and time-sensitive applications. Hence, an automated network procedure is the need of the hour. Reinforcement learning (RL), Machine Learning (ML) and Deep Learning (DL) techniques have been proved to be the promising techniques in various domains such as health care, environmental modelling [35], automation [36] etc. In B5G also, a lot of application have been witnessed in the proceeding literature [37, 38]. However, training a supervised ML model requires labelled data to be generated using some simulated experiments. Features that are used to train the models are chosen based on domain knowledge. The DL and RL models are ahead of traditional supervised ML since they try to identify the high-level features from the training data [37]. It also eliminates the need to develop a new feature extractor for every problem.

Developing a user association mechanism for RIS assisted B5G systems to ensure requested throughput and low latency to the end users is a challenging research concern. The point of interest is to investigate DL-based techniques. Association mechanisms must explicitly consider the presence of an additional channel via RIS. Specifically, the major concerns of the investigations are as follows:

- How to capture the effect of RIS assisted B5G network characteristics in the decision process for network selection?
- Given a set of conflicting objectives (e.g., throughput vs energy consumption), how do we evaluate the performance of user association algorithms specific to RIS assisted B5G?
- Can we minimize the number of networks switching? Can we reduce the control overhead by serving a group of users via RIS intelligently?

4.2   Interference Management Using RIS

It is always a challenging research issue to determine the target network for an active user either for a homogeneous network [10] or for a heterogeneous network [18]. User association problem in 5G networks has been addressed in Ref. [9]. User association has been designed by taking care of user mobility in a survey paper described in Ref. [13]. Network load, throughput and interference relationship are significantly influenced by the choice of a target network of a user [14, 19].

Spectrum efficiency is significantly influenced by appropriate interference management in D2D enabled network for 5G and B5G. There can be a potentially large number of users in future wireless communications that would necessarily increase the required number of spectrum resources [30]. In D2D communication, spectrum efficiency is achieved through a direct communication avoiding the need of a supporting infrastructure. However, the potential benefit of D2D communication can only be achieved through appropriate interference management.

Deployment of RIS can play a pivotal role for interference management in D2D enabled network. RIS is a new paradigm for B5G and future wireless communications which not only alleviate the issue of interference but also can lead to an improved throughput. RIS is able to control the wireless propagation that results in a higher system capacity [12, 21]. The basic working principle of the RIS is shown in Fig. 1.

Here, we demonstrate *Tx* and *Rx* as the D2D transmitter and receiver, respectively, and their communication is assisted by RIS (a single RIS). Considering, h as the channel coefficient from the transmitter to the receiver, and Ω being the phase shift, the received signal can be represented as (for more than one RIS deployment):

Fig. 1 RIS based communication
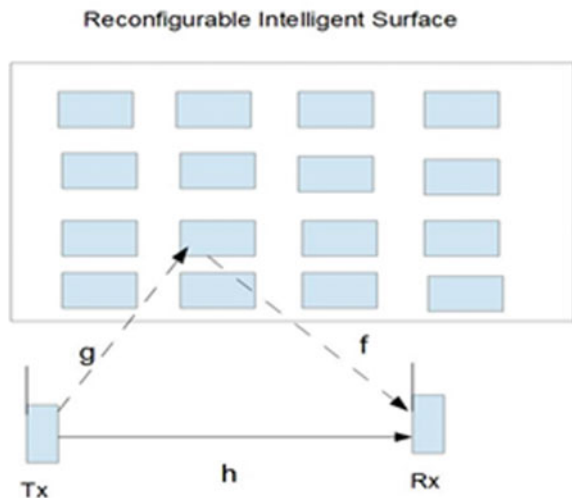
$$Y = \sum_{i=1}^{n} \left(h_{il} + f_l^T \Omega g_i \right) X_i + w_l \tag{1}$$

Note that X_i is the transmit data symbol of the user i, w_l is the additive white Gaussian noise at the lth receiver. Considering P as the transmit power, signal to noise plus interference ratio is given by:

$$Z_l = \frac{\left| h_{ll} + f_l^T \Omega g_l \right|^2 P}{\sum_{i=1}^{n} \left| h_{ll} + f_l^T \Omega g_l \right|^2 P + \sigma^2} \tag{2}$$

So, the achievable sum rate of the system is represented as follows:

$$\beta = \sum_{i=1}^{n} \log_2 (1 + Z_l). \tag{3}$$

As noted, the obtained data rate is motivated by the phase shift. So, in this context the challenging concerns are as follows:

- To determine an appropriate phase shift to avoid the interference among the intended signal and the reflective signal.
- How to take care of power optimization in the context of RIS to mitigate the interference.
- How to select the deployed number of RIS to control the interference. Here, exhaustive search can result in a high computational cost hence, DL- and ML-based approach may be followed.

4.3 Millimetre Wave (mm-Wave) Communication

In future wireless communication, mm wave has got significant attention as it is able to provide a very high data rate to the short-range communicating devices. It operates at a higher frequency band of up to 300 GHz [11] and thus is able to provide an extremely high data rate and network capacity. However, mm-wave has high propagation loss which results in major technical challenges in interference management in mm-wave assisted D2D communication. Furthermore, the mm-wave is prone to high packet losses due the presence of dynamic obstacles as it has very limited penetration capability, and thereby restricting the capacity of the communication. Therefore, significant effort has been initiated to deal with the dynamic obstacle management in D2D enabled mm wave communications [11].

5　Summary

Starting from Shannon's capacity formulae, in this work, an effort has been initiated to outline the different paradigms for capacity improvement. For each paradigm, we have listed the different technologies used and the works that have been done so far. Such a comprehensive analysis serves as a guideline towards developing new techniques for throughput improvement to the research community.

References

1. Gui G, Liu M, Tang F, Kato N, Adachi F (2020) 6G: opening new horizons for integration of comfort, security and intelligence. IEEE Wirel Commun 27(5):126–132
2. Tewari BP, Ghosh SC (2022) Wi-Fi assisted 5G D2D communications in unlicensed spectrum. J Amb Intel Humaniz Comput 13(4):1715–1734
3. Chen Y, Ai B, Zhang H, Nu Y, Song L, Han Z, Vincent Poor H (2021) Reconfigurable intelligent surface assisted Device-to-Device communications. IEEE Trans Wirel Commun 20(5):2792–2803
4. Elshaer H, Vlachos C, Friderikos V (2016) Interference aware decoupled cell association in Device-to-Device based 5G networks. In: Proceedings IEEE 83rd vehicular technology conference, pp 1–5
5. Singh D, Chattopadhyay A, Ghosh SC (2022) To continue transmission or to explore relays: millimeter wave D2D communication in presence of dynamic Obstacles. IEEE Trans Mob Comput. https://doi.org/10.1109/TMC.2022.3160764
6. Ganesan H, Ghosh SC (2022) Evidential Obstacle learning in millimeter wave D2D communication using spatial correlation. In: 14th international conference on communication systems & networks (COMSNETS), pp 344–352
7. Dev S, Ghosh SK, Ghosh SC (2021) A Multi-Arm bandit-based resource block allocation in RIS assisted wireless network. In: IEEE 20th International symposium on network computing and applications, pp 1–6
8. Pei X et al (2021) RIS-aided wireless communications: prototyping, adaptive beamforming, and indoor/outdoor field trials. https://arxiv.org/pdf/2103.00534.pdf
9. Liu D et al (2016) User association in 5G networks: a survey and outlook. IEEE Commun Surv Tutor 18(2):1018–1044
10. Tewari BP, Ghosh SC (2017) Joint frequency assignment and association control to maximize the aggregate throughput in IEEE 802.11 WLAN. Wirel Pers Commun 94(3):1193–1221
11. Jameel F, Hamid Z, Jabeen F, Zeadally S, Javed MA (2018) A survey of Device-to-Device communications: research issues and challenges. IEEE Commun Surv Tutor 20(3):2133–2168
12. Cao X et al (2021) AI-assisted MAC for reconfigurable intelligent surface-aided wireless networks: challenges and opportunities. IEEE Commun Mag 59(6):21–27
13. Waqas M et al (2020) A comprehensive survey on mobility-aware D2D communications: principles, practice and challenges. IEEE Commun Surv Tutor 22(3):1863–1885
14. Lei Y et al (2019) Delay-aware user association and power control for 5G heterogeneous network. Mob Netw Appl 24:491–503
15. Liang L, Li GY, Xu W (2017) Resource allocation for D2D-enabled vehicular communications. IEEE Trans Wirel Commun 65(7):3186–3197
16. Mukherjee S, Ghosh SC (2021) Scalable and fair resource sharing among 5G D2D Users and legacy 4G Users: a game theoretic approach. Ad Hoc Netw 115:102436
17. Ghoshal S, Ghosh SC (2021) A randomized algorithm for joint power and channel allocation in 5G D2D communications. Computer Commun 179:22–34

18. Zhou T, Zhao J, Qin D, Li X, Li C, Yang L (2021) Joint user association and time partitioning for load balancing in ultra-dense heterogeneous networks. Mob Netw Appl 26:909–922
19. Zhang H, Song L, Zhang YJ (2018) Load balancing for 5G ultra-dense networks using Device-to-Device communications. IEEE Trans Wirel Commun 17(6):4039–4050
20. Zhang H, Liao Y, Song L (2017) D2D-U: Device-to-Device communications in unlicensed band for 5G system. IEEE Trans Wirel Commun 16(6):3507–3519
21. Basar E et al (2019) Wireless communications through reconfigurable intelligent surfaces. IEEE Access 7:116753–116773
22. Liu R et al (2020) User association for millimeter-wave networks: a machine learning approach. IEEE Trans Commun 68(7):4162–4174
23. Habbal A, Goudar SI, Hassan S (2017) Context aware radio access technology selection in 5G ultra dense networks. IEEE Access 5:6636–6648
24. Alabani IA, Amer Arafah M (2021) An adaptive cell selection scheme for 5G heterogeneous ultra-dense networks. IEEE Access 9:64224–64240
25. Wu Q, Zhang R (2020) Beamforming optimization for wireless networks aided by intelligent reflecting surface with discrete phase shifts. IEEE Trans Commun 68(3):1838–1851
26. Cai C et al (2020) Reconfigurable intelligent surface assisted D2D underlay communications: a two-timescale optimization design. J Commun Inf Netw 5(4):369–380
27. Zhang HL, Di BY, Song LY, Han Z (2020) Reconfigurable intelligent surface assisted communications with limited phase shifts: how many phase shifts are enough? IEEE Trans Veh Tech 64(4):4498–4502
28. Di B et al (2020) Hybrid beamforming for reconfigurable intelligent surface based multi-user communications: achievable rate with limited discrete phase shifts. IEEE J Sel Areas Commun 38(8):1809–1822
29. Dev S, Ghosh SC (2021) An RIS deployment strategy to overcome static obstacles in millimeter wave D2D communication. In: IEEE 20th International symposium on network computing and applications, pp 1–6
30. Jayakumar S, Nandankumar S (2021) A review on resource allocation techniques in D2D communication for 5G and B5G technology. Peer-to-Peer Netw Appl 14:243–269
31. Gong S et al (2020) Towards smart wireless communications via intelligent reflecting surfaces, a contemporary survey. IEEE Commun Surv Tutor 22(4):2283–2314
32. Mao S, Chu X, Wu Q, Liu L, Feng J (2021) Intelligent reflecting surface enhanced D2D cooperative computing. arXiv:2103.04073v2
33. Orsino A, Araniti G, Molinaro A, Iera A (2015) Effective RAT selection approach for 5G dense wireless networks. In: Proceedings of the IEEE 81st vehicular technology conference (VTC spring), pp 1–5
34. Ghosh SK, Ghosh SC (2017) A predictive handoff mechanism for 5G ultra dense networks. In: Proceedings of the IEEE 16th international symposium on network computing and applications (NCA), pp 1–5
35. Fathima A, Alamelu Mangai J, Gulyani BB (2014) An ensemble model for predicting biochemical oxygen demand in river water using data mining techniques. Int J Riv Basin Manage Taylor Fr 12(4):357–366
36. Alamelu Mangai J, Kumar VS, Balamurugan SA (2012) A novel feature selection framework for automatic web page classification. Int J Autom Comput 9(4):442–448
37. Kaur J, Khan MA, Iftikhar M, Imran M, Emad Ul Haq Q (2021) Machine learning techniques for 5G and beyond. IEEE Access 9:23472–23488
38. Wang J et al (2021) Interplay between RIS and AI in wireless communications: fundamentals, architectures, applications, and open researchproblems. arXiv:2101.00250

Noise Performance of IMPATT Diode Oscillator at Different mm-Wave Frequencies

S. J. Mukhopadhyay, R. Dhar, and Aritra Acharyya

Abstract The performance of noise of Silicon (Si) DDR (Double Drift Region) IMPATT (Impact Ionization Avalanche Transit Time) devices at different millimeter-wave frequencies is studied and presented in this article. The motivation behind this study is to see how the device operates at high frequencies. The temperature for the system has been kept constant at 300 K. Double iterative method has been used for the simulation. The noise measure and the noise spectral density at the desired window frequencies has been studied, analyzed and presented in this article. The direct dependence of noise on frequency has not been presented in any previous work; however, the dependence of ionization on frequency has been presented in some articles which have been described here. The authors here have tried to provide a dependence of noise performance on the operating frequency based on the given literature and simulated results. Simulated results show that the noise measure improves significantly with increase in frequency and the device thus proves to be more effective in use at higher frequencies. Different doping and structural parameters for the Si IMPATTs at different operating frequencies have been reported and used in the present work.

S. J. Mukhopadhyay (✉)
Department of Electronics and Communication Engineering, Dr. Sudhir Chandra Sur Institute of Technology & Sports Complex, Kolkata, West Bengal 700074, India
e-mail: sangeeta.janamukhopadhyay@dsec.ac.in

R. Dhar
Department of Electronics Engineering, IIT (BHU), Varanasi, Uttar Pradesh 221005, India

A. Acharyya
Department of Electronics and Communication Engineering, Cooch Behar Government Engineering College, Cooch Behar, West Bengal 736170, India

1 Introduction

IMPATTs are high frequency generators and amplifier devices with frequencies ranging from a few gigahertz to several hundred gigahertz. IMPATTs have proven to be the most popular in military, defense, and radar applications, as well as non-military ones. IMPATTs have to be mounted on resonators to be used for sustainable use; otherwise they cannot be used for very high power applications. In DDR IMPATTS both the holes and electrons have different individual drift regions which help in more power handling and more efficient operations. The theory and development of SDR and DDR IMPATTs over the years presented in Refs. [1–5], have made it possible for the devices to be used for high power RF applications.

Although IMPATTs are very useful devices, their main drawback is that they are very noisy devices with noise measures ranging between 30 and 60 dB or even more—a cause for decrease in their efficiency. The main source of noise in these devices is the avalanching process which includes the collision of electrons in a very thin avalanche region leading to the generation of Electron–Hole-Pairs or EHPs. There are a lot of other noises too like the shot noise, Johnson noise, etc., but their effect is suppressed by the avalanching noise. The avalanching region in IMPATT devices plays a very important role in determining the noise performance of the devices [6–8].

In this article, we have presented the noise performance on Si DDR IMPATTs over a range of different window frequencies at mm-wave. Gummel and Blue [9] have presented a small signal theory on the avalanche noise of these devices. They contemplated field-dependent charge carrier ionization rates in their model, which assumed that electron and hole drift velocity is saturated and independent of the electric field even at the depletion layer's boundaries. In their simulation with realistic diodes they have shown that IMPATT devices can achieve 20–30 dB Noise Measures using different current densities from 100 to 1000 A/cm^2, parasitic resistances of 0 and 1 Ω and frequencies ranging from 7 to 40 GHz. Hines [10] has on the other hand presented the large signal noise properties along with the frequency conversion effects in IMPATT devices for the X-band frequencies. The same motivation has been used in this article with much higher frequency ranges starting from 94 GHz to nearly 400 GHz, with a constant parasitic capacitance of 1.5 Ω. Frequency up-conversion at the test frequencies can affect the noise performance of these devices. Moreover the temperature is kept fixed at 300 K which is one of the idealities that we have considered here. Moreover, the high noise measures in the devices can affect the sustainability of the frequency output with considerable amount of power. Thus, noise performance of these devices at these frequencies is very necessary to study.

Since the noise depends on the ionization of the device at the junction, the way by which ionizations depend on the frequency of operation is an important aspect to study. Earlier [11, 12] the authors verified the following relation,

$$W = \frac{0.37 v_{sn}}{f_d}, \tag{1}$$

where W is the width of depletion layer, v_{sn} is the saturation drift velocity of the electrons and f_d is the design frequency.

2 Simulation Methods

In Ref. [13] the computer simulation of noise characteristics of the IMPATT diodes has been reported. Along with it in Refs. [14, 15] the small signal noise analysis and intrinsic noise theories have been reported for IMPATT devices. In Ref. [14] the IMPATT device used is a SDR or Single Drift Region type while the one that we have used in our study is a DDR or Double Drift Region type whose structure is shown in Fig. 1. In this figure, W = Wn + Wp represents the total active region of the diode. The region denoted by x_A represents the avalanching region of the diode. The J_0 is the total current density of the diode and it flows from the N-side to the P-side. Vp and Vn represent the drift velocities of the holes and electrons, respectively. x_0 is the center of the diode and it is considered that that the avalanching process starts at that point. Table 1 depicts the parameters used for the simulation purpose.

In a DDR diode, the regions are structured as p$^+$p-nn$^+$; there are two separate drift regions for the holes and electrons. An elemental current di_c in the avalanche region over a small region dx is given by,

$$di_c = (\alpha_p I_p + \alpha_n I_n) dx \tag{2}$$

where $\alpha_{p,n}$ are the hole and electron ionization coefficients and $I_{i,n}$ are the average hole and electron currents. Thus the mean-square of this current can be written as,
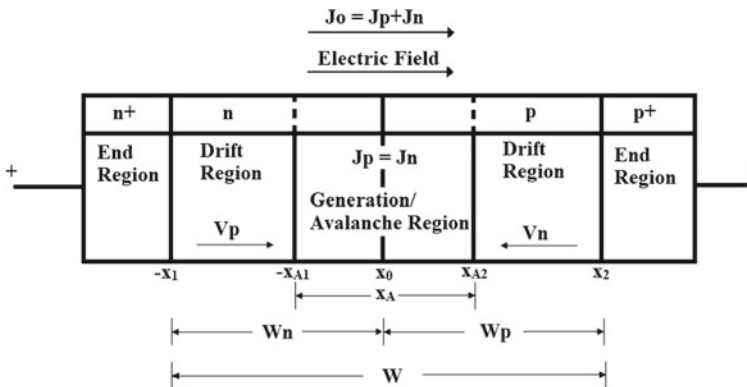
Fig. 1 1-D diagram of a Si DDR IMPATT

Table 1 Structural and doping parameters for Si for different operating frequencies

Operating frequency (GHz)	Wn (um)	Wp (um)	N_D ($\times 10^{23}/m^3$)	N_A ($\times 10^{23}/m^3$)	Nn+ ($\times 10^{26}/m^3$)	Np+ ($\times 10^{26}/m^3$)
94	0.32	0.30	1.50	1.55	5.0	2.7
140	0.28	0.245	1.80	2.10	6.2	3.5
220	0.18	0.16	3.95	4.59	7.5	4.7
300	0.132	0.112	6.00	7.32	9.0	5.9

$$< di_c^2 >= 2qdi_cdf = 2q(\alpha_p I_p + \alpha_n I_n)dxdf \tag{3}$$

The open-circuit mean-square noise voltage $<v^2>$ can be computed by integrating the mean square current given in (3) against the absolute square of the transfer impedance, as given by the following relation,

$$< v^2 > /df = 2q \int |Z_t(x, \omega)|^2(\alpha_p I_p + \alpha_n I_n)dx \tag{4}$$

The terminal noise voltage at a particular frequency ω is obtained by integrating the noise electric field over the whole space charge region,

$$v_t(x, \omega) = \int_{x=0}^{x=W} e_n(x, \omega)dx \tag{5}$$

The transfer impedance is measured by dividing the noise voltage by the noise current generated due to the noise source,

$$Z_t(x, \omega) = \frac{v_t(x, \omega)}{i_n(x, \omega)} \tag{6}$$

Thus by substituting Eq. (6) in Eq. (4), we can finally get the value of $<v^2>$. The noise measure (M_N) is given by the following expression,

$$M_N = \frac{\langle v_n^2 \rangle /df}{4k_B T_j(-Z_R - R_S)}, \tag{7}$$

3   Results and Discussion

The entire simulation has been done in MATLAB environment at different window or operating frequencies of 94 GHz, 140 GHz, 220 GHz and 300 GHz, respectively, and the following results have been obtained. The results show that the Noise Measure

decreases with the frequency which is shown by the following figures. It is noted that in all the figures the least measure of noise is not perfectly placed at the respective window frequencies but with a little offset from them. The reason is justified by the non-ideality of the diodes.

Figure 2 shows the noise measure at a window frequency of 94 GHz and the noise measure is around 36.36 dB at a frequency of 117 GHz.

Figure 3 shows the noise measure at a window frequency of 140 GHz and the noise measure is around 19.72 dB at a frequency of 218 GHz.

Figure 4 shows the noise measure at a window frequency of 200 GHz and the noise measure is around 11.16 dB at a frequency of 270 GHz.

Figure 5 shows the noise measure at a window frequency of 300 GHz and the noise measure is around 0.64 dB at a frequency of 117 GHz. Thus it can be seen that with the increase of operating frequencies the noise measure reduces significantly to less than 1 dB at around 300 GHz, which is shown in the following Fig. 6.

The validation for decrease in noise figure with frequency can be explained by the works done in Refs. [11, 12]. There it has been shown that as we increase the operating frequency the depletion width decreases and hence the avalanching process confines to a very small region. As a result, the collision between the ions decreases and hence the noise measure reduces significantly. Thus at high frequencies, it can be concluded that the diode can be used much more efficiently but at even higher frequencies the depletion width will reduce so much that the ionization will cease to occur, rendering the diode to be absolutely useless as there will be no production of power at any frequency.

The values of all the noise measures at different operating frequencies are given in Table 2.

Fig. 2 Noise measure versus frequency at 94 GHz atmospheric window frequency
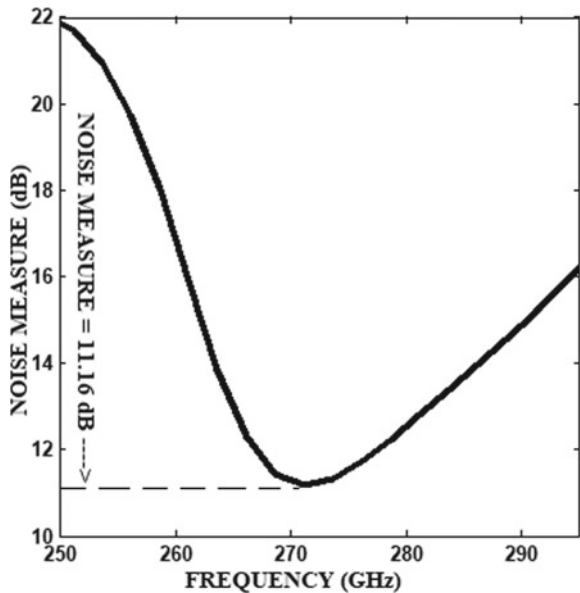
Figure 7 shows the noise spectral density over the desired operating frequency range. The points where the NSD takes the dip in the curve, are the points of desired frequency. The Noise Measure is then measured taking the values of NSD at those points.
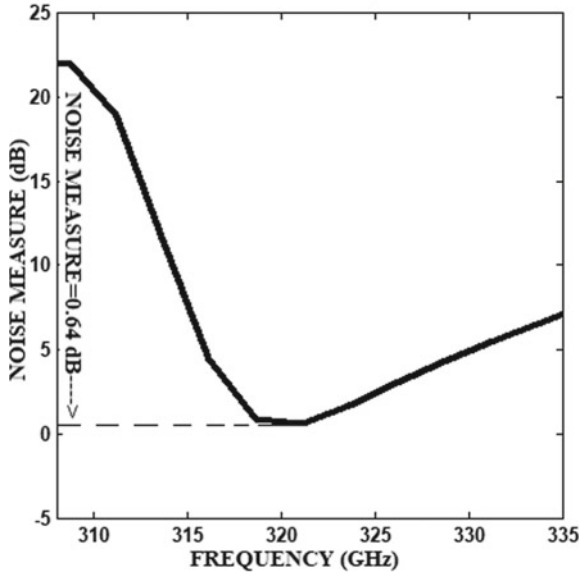
Fig. 5 Noise measure versus frequency at 300 GHz
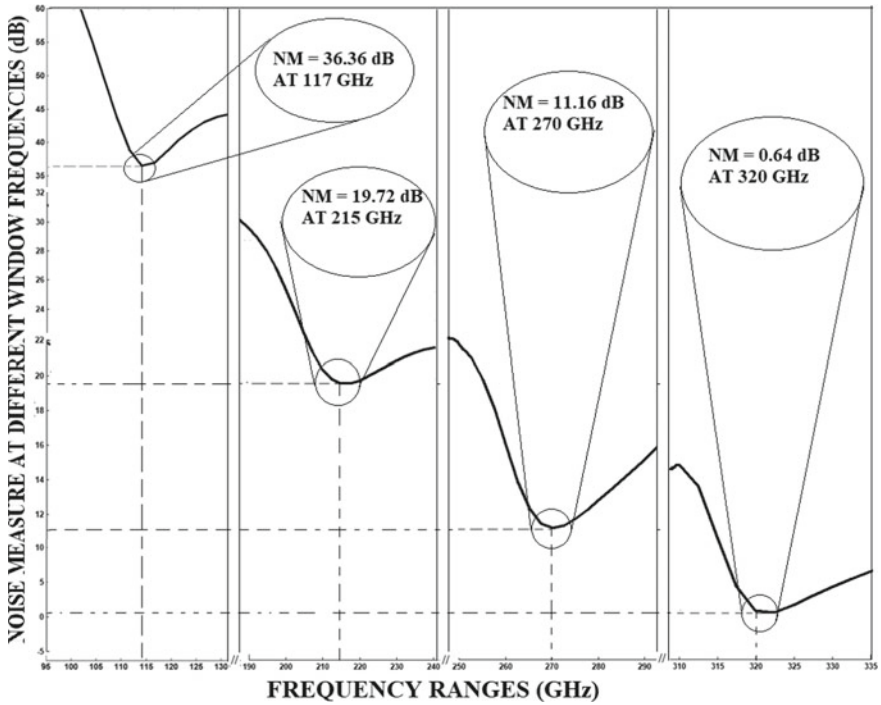
Fig. 6 Noise measure versus frequency for progressive atmospheric window frequencies

Table 2 Window frequencies and the respective noise measures

Window frequency (GHz)	Noise measure (dB)
94	36.36
140	19.72
200	11.16
300	0.64

Fig. 7 Noise spectral density versus frequency for the whole operating frequency range
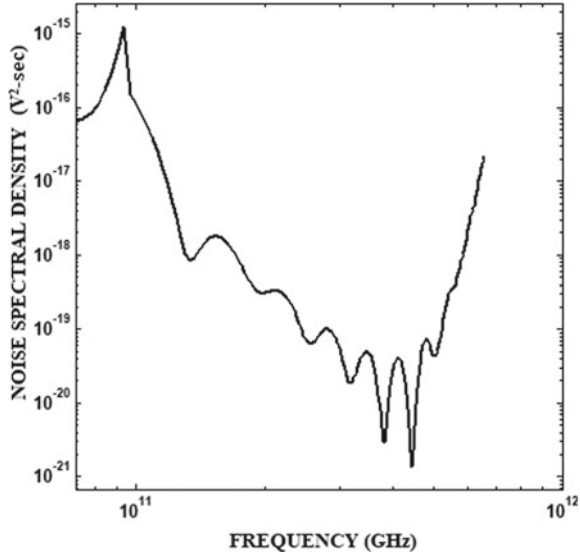
Z_R is the frequency dependent thing in the relation. The negative resistance is obtained from the Conductance-Susceptance curve or the G-B curve. The point of frequency where the lowest conductance is achieved is considered the operating frequency. The negative resistance is obtained from the inversion of the conductance value. Hence, the lowest conductance turns into the highest negative resistance at the desired frequency. Hence the value of the noise measure decreases with increase in negative resistance. According to the results shown above it can be assumed that increase in frequency leads to the increase in negative resistance which in turn leads to the decrease in Noise Measure.

Moreover at higher frequencies, according to Eq. 1, we find that as the operating frequency increases, the depletion width of the diode decreases, hence the space width for the noise to generate decreases, thus this also acts as a method of decreasing Noise Measure at higher frequencies.

4 Summary

After obtaining all the results we can conclude that operating the IMPATT Diodes at higher frequencies can help in reduction of the noise measures of the device, thus effectively improving the noise performance of the device. As discussed above, one of the reasons for reduction in Noise Measure at higher frequencies is the reduction of depletion width at high frequencies. The reduction in the depletion region also leads to the decrease in ionization and thus that may affect the performance of the device. The power handling capacity of the device reduces due to decrease in ionization which is not a property for IMPATT Diodes. Thus in order to achieve optimum performance from the device the trade-off between power and noise must be considered carefully. Thus to achieve a good balance between power and noise, the device must be carefully fabricated using proper structural and doping parameters required for the device to perform at that desired operating frequency.

References

1. Midford TA, Bernick RL (1979) Millimeter wave CW IMPATT diodes and Oscillators. IEEE Trans Microwav Theory Tech 27:483–492
2. Chang Y et al (1977) Millimeter-wave IMPATT sources for communication applications. In: IEEE MTT-S international microwave symposium digest, pp 216–219
3. Ghoshal D (2011) Measurement of electrical resistance of Silicon Single Drift Region IMPATT diode based on the study of the device and mounting circuit at threshold condition. J Electron Devices 11:625–631
4. Seidel TE, Scharfetter DL (July 1970) High-power millimeter wave IMPATT oscillators with both hole and electron drift spaces made by Ion Implantation. Proc IEEE 1135–1136
5. Seidel TE, Niehaus WC, Iglesias DE (1974) Double-drift silicon IMPATT's at X band. IEEE Trans Electron Devices 21(8):523–531
6. Gummel HK, Scharfetter DL (1966) Avalanche region of IMPATT diodes. BELL Syst Tech J 1797–1827
7. Gupta M-S (1971) Noise in avalanche transit-time devices. Proc IEEE, 1674–1687
8. Dallnan GC, Eustman LF (1968) Avalanche-diode microwave noise generation experiments. IEEE Trans Electron Devices 416
9. Gummel HK, Blue JL (1967) A small signal theory of avalanche noise in IMPATT diodes. IEEE Trans Electron Devices Ed-14(9):569–580
10. Hines ME (1972) Large-signal noise frequency conversion and parametric instabilities in IMPATT diode networks. Proc IEEE 60(12):1534–1548
11. Sze SM, Ryder RM (1971) Microwave avalanche diodes. Proc IEEE 59:1140–1142
12. Mukhopadhyay SJ, Mitra M (2018) DC and noise analysis of Si and 3C-SiC based IMPATTs at W-Band. In: Proceedings of international microwave and RF conference
13. Giblin RA, Scherer EF, Wierich RL (1973) Computer simulationo instability and noise in high-power avalanche devices. IEEE Trans Electron Devices 20(4):404–418
14. Mathur PC et al (1978) A small signal noise analysis for GaAs IMPATT diode. Phys Stat Sol (a) 46:321–326. Subject classification: 14.3.3; 22.2.1
15. Kuvas RL (1972) Noise in IMPATT diodes: intrinsic properties. IEEE Trans Electron Devices ED-19(2):220–233

Brief Introduction to High Frequency Passive Circuits

Hiranmay Mistri

Abstract Component used in any circuit, as per functionality, can be classified into two basic categories, passive and active components. Passive component can't provide energy to the circuit in the form of voltage or current i.e. provides no power gain to the circuit. As well as it can't amplify or process any signal. In low frequency (considerable up to 3 GHz, parasitic effect and radiation loss increases fatally beyond that) circuit where the component dimension is very less than operating wavelength (λ), i.e. Lumped parameter circuit, Resistor, Capacitor, Inductor or Conventional PN Junction diode can be the typical example of passive circuit components. Passive device or component characterized with monotonic I-V curve which must be within 1st or 3rd (or both) quadrant with always positive differential resistance. In high frequency where the dimension of λ is in order of the component dimension, Distributed parameter concept is applicable. Microwave device is the most suitable device to operate in this range. The frequency range can be from 3 to 100 GHz or even more. But at very high frequency dielectric and Ohmic losses became fatal and manufacturing devices for higher frequency became very demanding. Different waveguide sections like Attenuator, Terminator, Filter, Coupler and Ferrite devices are passive microwave components. Whereas, different types of Oscillators, Amplifiers, Mixers, Multipliers and detectors used in microwave frequency are the typical examples of active devices. Passive device in Microwave frequency range can be characterized based on several aspects. Transfer characteristics of a passive device must be linear, continuous wave signal must not get distorted and the S- parameter of the device have to be independent of power. For a two-port passive device or component, reflection at both port are identical, i.e. $|S_{11}|^2 = |S_{22}|^2$. And most of the passive components used in microwave circuit are reciprocal except Ferrite isolators and circulators [1]. In this chapter, we will discuss about different types of passive circuit components used in microwave frequency range.

H. Mistri (✉)
Department of Electronics and Communication Engineering, Ramkrishna Mahato Government Engineering College, Purulia, West Bengal 723103, India
e-mail: hiranmay.nitdgp@gmail.com

1   Waveguide TEE Junctions

Waveguide junction consists of three or more individual ports and is called a Tee junction. By connecting a section of waveguide with the main waveguide in series or parallel, a Tee junction can be formed. Based on structure, Tee junction can be of three types, such as.

1.1   H-Plane TEE

By connecting another rectangular waveguide section along the thinner side of the main waveguide, H-plane Tee is formed. The section which is connected to the main waveguide is called side arm and collinear arm is formed by both ends of the main waveguide. Here the plane containing the magnetic field of the main waveguide is parallel to the axis of the side arm; hence it is called H-plane Tee. Collinear arm contains port1 and port2 whereas side arm contains port3 (Figs. 1 and 2).

H-plane Tee is completely symmetric and port3 is perfectly matched. If any input signal is given at port3, get divided between port1 and port2 with equal magnitude and in phase components i.e. $S_{13} = S_{23}$, provides both collinear arms having an absolutely equal length.
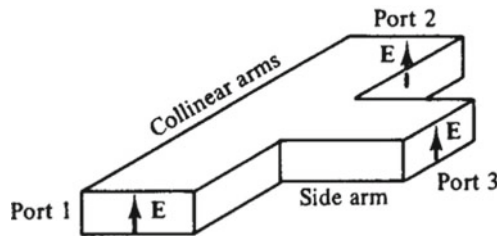
Fig. 1 H-plane TEE
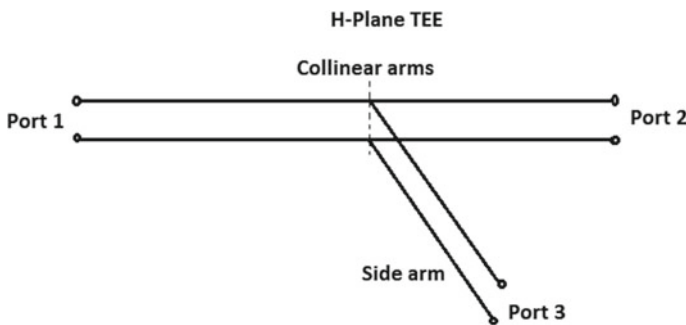
Fig. 2 Ports of H-plane TEE

1.1.1 S-Matrix of H-Plane TEE

Scattering matrix of a three port device must be a 3×3 matrix.

So, scattering matrix can be the form of,

$$S = \begin{bmatrix} S_{11} & S_{12} & S_{13} \\ S_{21} & S_{22} & S_{23} \\ S_{31} & S_{32} & S_{33} \end{bmatrix} \tag{1}$$

It is a symmetrical device i.e.

$$S_{ij} = S_{ji}, \ S_{21} = S_{12}, \ S_{31} = S_{13} \text{ and } S_{32} = S_{23} \tag{2}$$

Input power from port3 gets divided into two equal, in-phase parts at port1 and port2. So,

$$S_{13} = S_{23} \tag{3}$$

Port3 is perfectly matched $S_{33} = 0$,

From Eq. (1),

$$S = \begin{bmatrix} S_{11} & S_{12} & S_{13} \\ S_{21} & S_{22} & S_{23} \\ S_{31} & S_{32} & S_{33} \end{bmatrix} = \begin{bmatrix} S_{11} & S_{12} & S_{13} \\ S_{12} & S_{22} & S_{23} \\ S_{13} & S_{23} & 0 \end{bmatrix} \tag{4}$$

As per unitary property, $[S][S^*] = [I]$

So,
$$\begin{bmatrix} S_{11} & S_{12} & S_{13} \\ S_{12} & S_{22} & S_{23} \\ S_{13} & S_{23} & 0 \end{bmatrix} \begin{bmatrix} S_{11}^* & S_{12}^* & S_{13}^* \\ S_{12}^* & S_{22}^* & S_{23}^* \\ S_{13}^* & S_{23}^* & 0 \end{bmatrix} = \begin{bmatrix} 1 & 0 & 0 \\ 0 & 1 & 0 \\ 0 & 0 & 1 \end{bmatrix} \tag{5}$$

From Eq. (5),

$$R1^*C1 \Longrightarrow \quad |S_{11}|^2 + |S_{12}|^2 + |S_{13}|^2 = 1 \tag{6}$$

$$R2^*C2 \Longrightarrow \quad |S_{12}|^2 + |S_{22}|^2 + |S_{23}|^2 = 1 \tag{7}$$

$$R3^*C3 \Longrightarrow \quad |S_{13}|^2 + |S_{23}|^2 = 1 \tag{8}$$

But from Eq. (3) $S_{13} = S_{23}$

$$\text{So,} \quad S_{13} = S_{23} = \frac{1}{\sqrt{2}} \tag{9}$$

From Eqs. (6), (7) and (9) we have,

$$|S_{11}|^2 + |S_{12}|^2 = \frac{1}{2} \tag{10}$$

$$|S_{12}|^2 + |S_{22}|^2 = \frac{1}{2} \tag{11}$$

Again, from Eq. (5), $R1^*C3 => S_{11}S_{13}^* + S_{12}S_{23}^* = 0$

$$\text{Or, } S_{11}S_{13}^* + S_{12}S_{13}^* = 0 \qquad [\text{as, } S_{13} = S_{23}] \tag{12}$$

Or, $S_{13}^*(S_{11} + S_{12}) = 0$ but $S_{13}^* \neq 0$;
Hence, $S_{11} = -S_{12}$.
And from Eq. (10) we have, $S_{11} = \frac{1}{2}$ and $S_{12} = -\frac{1}{2}$.
Similarly, from Eq. (11) $S_{22} = \frac{1}{2}$.
Finally, the scattering matrix for H-plane Tee can be written as,

$$S = \begin{bmatrix} \frac{1}{2} & -\frac{1}{2} & \frac{1}{\sqrt{2}} \\ -\frac{1}{2} & \frac{1}{2} & \frac{1}{\sqrt{2}} \\ \frac{1}{\sqrt{2}} & \frac{1}{\sqrt{2}} & 0 \end{bmatrix} \tag{13}$$

1.1.2   Applications

(a) **As Power Divider**: Incident signal at port3 get divided into two equal, in-phase part at port1 and port2. Let's consider the incident signal at port3 having amplitude A and power P, then as, $S_{13} = S_{23} = \frac{1}{\sqrt{2}}$, signal appears at port1 and port2 is $\frac{A}{\sqrt{2}}$ and power is $\frac{P}{2}$. So it can act as a power divider. It is to be noted here that the input signal level at port3 reduced to port1 and port2 by a factor of $\frac{1}{\sqrt{2}}$ and in dB scale, it is equivalent to $20\log\left(\frac{1}{\sqrt{2}}\right) = -3$ dB. For that reason, H-plane TEE is called a 3 dB signal splitter.
(b) **As Power Combiner:** If the lengths of collinear arms are same, two in-phase input signals given through port1 and port2 get added and appear at port3. So, H-plane Tee can be used as a signal combiner.

Except that H-plane Tee can be used as a tuner or in duplexer assemblies of radar installation operating.

Illustrative Example 1: A 48 mW signal is fed into one of the collinear arm of a H-plane Tee. Determine the power that appears at all the ports when ports are terminated by a perfectly matched load.

Solution: We know that scattering element, $S_{ij} = \frac{v_i}{v_j}$ analogous to voltage ratio and power, $P \propto v^2$ so $P \propto S^2$ so $P_o = [S][S^*][P_i]$.

Let's consider input and output power of port1, port2 and port3 are P_{i1}, P_{i2}, P_{i3} and P_{o1}, P_{o2}, P_{03} respectively.

We have, $\begin{bmatrix} P_{o1} \\ P_{o2} \\ P_{o3} \end{bmatrix} = \begin{bmatrix} S_{11}^2 & S_{12}^2 & S_{13}^2 \\ S_{21}^2 & S_{22}^2 & S_{23}^2 \\ S_{31}^2 & S_{32}^2 & S_{33}^2 \end{bmatrix} \begin{bmatrix} P_{i1} \\ P_{i2} \\ P_{i3} \end{bmatrix}$.

Given that $P_{i1} = 48$ mW, $P_{i2} = 0$, $P_{i3} = 0$; and we know that s-matrix of a H-plane Tee is given as,

$$S = \begin{bmatrix} \frac{1}{2} & -\frac{1}{2} & \frac{1}{\sqrt{2}} \\ -\frac{1}{2} & \frac{1}{2} & \frac{1}{\sqrt{2}} \\ \frac{1}{\sqrt{2}} & \frac{1}{\sqrt{2}} & 0 \end{bmatrix} \qquad \text{Using all these values we have,}$$

$$\text{Or, } \begin{bmatrix} P_{o1} \\ P_{o2} \\ P_{o3} \end{bmatrix} = \begin{bmatrix} \frac{1}{4} & \frac{1}{4} & \frac{1}{2} \\ \frac{1}{4} & \frac{1}{4} & \frac{1}{2} \\ \frac{1}{2} & \frac{1}{2} & 0 \end{bmatrix} \begin{bmatrix} 48 \\ 0 \\ 0 \end{bmatrix}$$

$$\text{Or, } P_{o1} = 48 \cdot \left(\frac{1}{4}\right) + 0 \cdot \left(\frac{1}{4}\right) + 0 \cdot \left(\frac{1}{2}\right) = 12 \, \text{mW}$$

$$P_{o2} = 48 \cdot \left(\frac{1}{4}\right) + 0 \cdot \left(\frac{1}{4}\right) + 0 \cdot \left(\frac{1}{2}\right) = 12 \, \text{mW}$$

$$P_{o3} = 48 \cdot \left(\frac{1}{2}\right) + 0 \cdot \left(\frac{1}{2}\right) + 0 \cdot (0) = 24 \, \text{mW}$$

So, the power output at port1, port2 and port3 are 12 mW, 12 mW and 24 mW respectively.

1.2 E-Plane TEE

By connecting another rectangular waveguide along the width of the main waveguide E-plane TEE can be formed. As the electric field of the main waveguide is parallel to the axis of the side arm, it is called E-plane TEE (Fig. 3).

Input power at port3 gets divided into two parts and comes out from port1 and port2 with an equal magnitude but one signal is 180° out of phase with others i.e. $S_{23} = -S_{13}$.

a

b
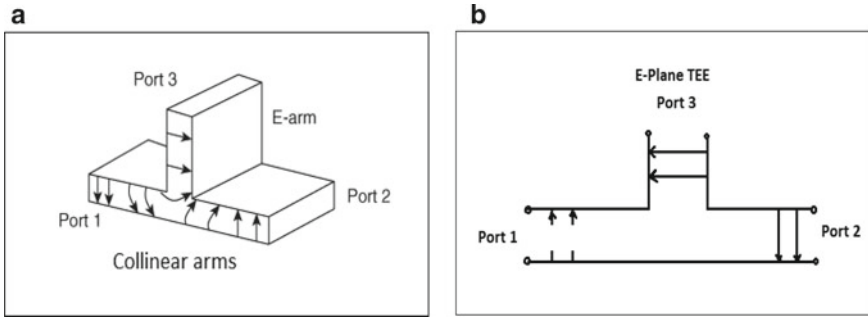
Fig. 3 E-plane TEE **a** schematic, **b** ports

1.2.1 S-Matrix for E-Plane TEE

Scattering matrix for E-plane Tee can be a 3×3 matrix.

$$\mathbf{S} = \begin{bmatrix} S_{11} & S_{12} & S_{13} \\ S_{21} & S_{22} & S_{23} \\ S_{31} & S_{32} & S_{33} \end{bmatrix}$$

As side arm i.e. port3 is perfectly matched $S_{33} = 0$.

$$\text{So,} \quad S_{23} = -S_{13} \text{ and } S_{33} = 0 \tag{14}$$

All the three ports are perfectly symmetric, hence $S_{ij} = S_{ji}$.

$$\text{So,} \quad S_{21} = S_{12}, S_{32} = S_{23} \text{ and } S_{31} = S_{13} \tag{15}$$

Using the values from Eqs. (14) and (15) the scattering matrix can be modified to

$$\mathbf{S} = \begin{bmatrix} S_{11} & S_{12} & S_{13} \\ S_{12} & S_{22} & -S_{13} \\ S_{13} & -S_{13} & 0 \end{bmatrix} \tag{16}$$

As per unitary property, $[S][S^*] = [I]$

$$\text{So,} \quad \begin{bmatrix} S_{11} & S_{12} & S_{13} \\ S_{12} & S_{22} & -S_{13} \\ S_{13} & -S_{13} & 0 \end{bmatrix} \begin{bmatrix} S_{11}^* & S_{12}^* & S_{13}^* \\ S_{12}^* & S_{22}^* & -S_{13}^* \\ S_{13}^* & -S_{13}^* & 0 \end{bmatrix} = \begin{bmatrix} 1 & 0 & 0 \\ 0 & 1 & 0 \\ 0 & 0 & 1 \end{bmatrix} \tag{17}$$

From matrix multiplication,

$$R1 \times C1 \Longrightarrow \quad |S_{11}|^2 + |S_{12}|^2 + |S_{13}|^2 = 1 \tag{18}$$

$$R2 \times C2 => \quad |S_{12}|^2 + |S_{22}|^2 + |S_{13}|^2 = 1 \tag{19}$$

$$R3 \times C3 => \quad |S_{13}|^2 + |S_{13}|^2 = 1 \tag{20}$$

$$\text{So,} \quad S_{13} = \frac{1}{\sqrt{2}} \quad \text{and} \quad S_{23} = -\frac{1}{\sqrt{2}} \tag{21}$$

From Eqs. (18), (19) and (21) we have,

$$|S_{11}|^2 + |S_{12}|^2 = \frac{1}{2} \tag{22}$$

$$|S_{12}|^2 + |S_{22}|^2 = \frac{1}{2} \tag{23}$$

Again, from Eq. (17), R1 $\times$ C3 $=> S_{11}S_{13}^* - S_{12}S_{13}^* = 0$

$$\text{Or,} \quad S_{11}S_{13}^* - S_{12}S_{13}^* = 0 \tag{24}$$

$$\text{Or,} \quad S_{13}^*(S_{11} - S_{12}) = 0 \quad \text{but} \quad S_{13}^* \neq 0;$$

Hence, $S_{11} = S_{12}$, putting this value in Eqs. (22) and (23) we have,

$$S_{11} = S_{12} = S_{22} = \frac{1}{2} \tag{25}$$

Substituting all these values in Eq. (16) we have

$$S = \begin{bmatrix} \frac{1}{2} & \frac{1}{2} & \frac{1}{\sqrt{2}} \\ \frac{1}{2} & \frac{1}{2} & -\frac{1}{\sqrt{2}} \\ \frac{1}{\sqrt{2}} & -\frac{1}{\sqrt{2}} & 0 \end{bmatrix}$$

1.2.2 Applications

(a) **As Power Divider**: If input signal of amplitude A and power P is given through port3 then output at ports1 and 2 having equal amplitude $\frac{A}{\sqrt{2}}$ and power $\frac{P}{2}$ but both outputs are 180° out of phase from one another i.e. $S_{23} = -S_{23}$.

(b) **As Power Combiner**: Conversely, when two input signals of opposite phase are given through ports1 and 2 it gets added and appears at port3. So, E-plane Tee can be used as a signal combiner.

Illustrative Example 2: An E-plane Tee made of waveguide section of 50 Ω characteristics impedance. A signal power of 40 mW is applied to E-arm which is perfectly matched. Determine the amount of power that is delivered to the load of 75 and 100 Ω connected to port1 and port2 respectively.

Solution: Clearly both of the collinear arms are not matched properly, so having a reflection from there. Ideally the 40 mW should be equally distributed to both of the arms having 20 mW each with opposite phase. But reflection due to load mismatch some of the power gets reflected.

$$\text{Reflection coefficient at portl,} \quad \rho_1 = \frac{Z_{L1} - Z_0}{Z_{L1} + Z_0} = \frac{75 - 50}{75 + 50} = 0.2$$

$$\text{Reflection coefficient at port2,} \quad \rho_2 = \frac{Z_{L2} - Z_0}{Z_{L2} + Z_0} = \frac{100 - 50}{100 + 50} = 0.33$$

Here, ideally received power at port1 and port2 should be 20 mW each, but it should be less practical due to the reflection present there. Actual received power P_1 and P_2 can be calculated as:

$$P_1 = 20[1 - \rho_1^2] = 20[1 - (0.2)^2] = 19.2\,\text{mW}$$
$$P_2 = 20[1 - \rho_2^2] = 20[1 - (0.33)^2] = 17.82\,\text{mW}$$

Hence power received at port1 and port2 is 19.2 mW and 17.82 mW respectively.

1.3 Magic TEE or Hybrid TEE

The structural combination of E-plane TEE and H-plane TEE is called Hybrid TEE or Magic TEE. It is formed by connecting two side arms along the broad and narrow side wall of the main waveguide. Two arms of the main waveguide i.e. port1 and port2 called collinear arms. Other two arms are E-arm and H-arm can be considered as port3 and port4 respectively or vice-versa (Figs. 4 and 5).

Fig. 4 Magic TEE
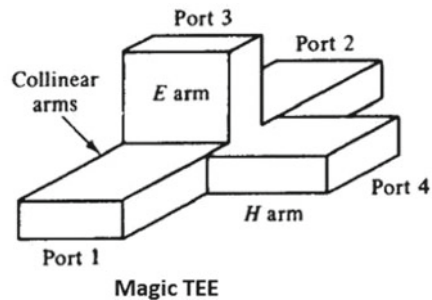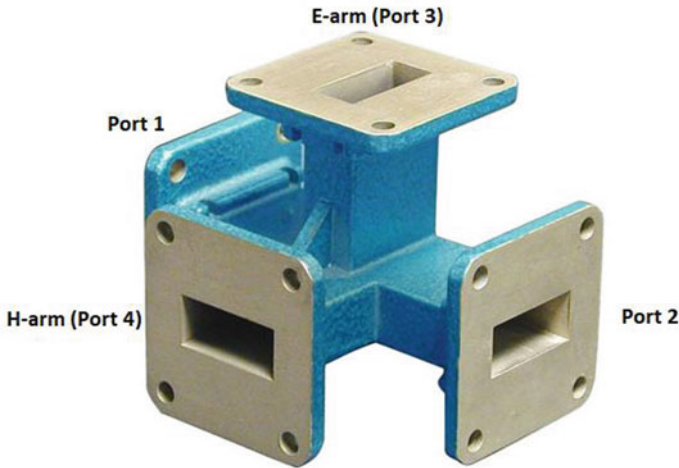
Magic TEE

Fig. 5 Illustration of ports of magic TEE

1.3.1 Characteristics of Magic TEE

(i) If two waves with equal amplitude and phase incident on port1 and 2 respectively then there will be zero output at port3 and the sum of the two waves will appear at port4.

(ii) If wave incident at port3, it gets equally divided between port1 and port2 but in opposite phase and no power appears at port4 i.e. $S_{43} = 0$.

(iii) If wave incident at port4 then it gets equally distributed between port1 and 2 and both of the parts are in-phase and no power appears at port3 i.e. $S_{34} = 0$.

(iv) If signal incident into one of the collinear arms then no output appears at other collinear arm as E-arm produces a phase delay and H-arm produce a phase advance to the wave. Hence $S_{21} = S_{12} = 0$.

1.3.2 Scattering Matrix of Magic TEE

Scattering matrix for any four port device can be given as

$$S = \begin{bmatrix} S_{11} & S_{12} & S_{13} & S_{14} \\ S_{21} & S_{22} & S_{23} & S_{24} \\ S_{31} & S_{32} & S_{33} & S_{34} \\ S_{41} & S_{42} & S_{43} & S_{44} \end{bmatrix}$$

For H-plane Tee section $S_{14} = S_{24}$ and for E-plane Tee section $S_{23} = -S_{13}$ (26)

From characteristics, we have $S_{43} = 0$, $S_{34} = 0$ and $S_{21} = S_{12} = 0$. (27)

Magic Tee is a symmetric device, hence $S_{ij} = S_{ji}$,

So, $S_{21} = S_{12}, S_{31} = S_{13}, S_{41} = S_{14}, S_{32} = S_{23}, S_{42} = S_{24}, S_{43} = S_{34}$ (28)

Port3 and port4 are perfectly matched, hence $S_{33} = 0$ and $S_{44} = 0$ (29)

Putting the above values in scattering matrix,

$$S = \begin{bmatrix} S_{11} & 0 & S_{13} & S_{14} \\ 0 & S_{22} & -S_{13} & S_{14} \\ S_{13} & -S_{13} & 0 & 0 \\ S_{14} & S_{14} & 0 & 0 \end{bmatrix}$$ (30)

As per unitary property, $[S][S^*] = [I]$

So, $$\begin{bmatrix} S_{11} & 0 & S_{13} & S_{14} \\ 0 & S_{22} & -S_{13} & S_{14} \\ S_{13} & -S_{13} & 0 & 0 \\ S_{14} & S_{14} & 0 & 0 \end{bmatrix} \begin{bmatrix} S_{11}^* & 0 & S_{13}^* & S_{14}^* \\ 0 & S_{22}^* & -S_{13}^* & S_{14}^* \\ S_{13}^* & -S_{13}^* & 0 & 0 \\ S_{14}^* & S_{14}^* & 0 & 0 \end{bmatrix} = \begin{bmatrix} 1 & 0 & 0 & 0 \\ 0 & 1 & 0 & 0 \\ 0 & 0 & 1 & 0 \\ 0 & 0 & 0 & 1 \end{bmatrix}$$ (31)

From matrix multiplication,

$$R1^*C1 \Rightarrow \quad |S_{11}|^2 + |S_{13}|^2 + |S_{14}|^2 = 1$$ (32)

$$R2^*C2 \Rightarrow \quad |S_{22}|^2 + |S_{13}|^2 + |S_{14}|^2 = 1$$ (33)

$$R3^*C3 \Rightarrow \quad |S_{13}|^2 + |S_{13}|^2 = 1$$ (34)

$$\text{So, } S_{13} = \frac{1}{\sqrt{2}}.$$

$$R4^*C4 \Rightarrow \quad |S_{14}|^2 + |S_{14}|^2 = 1$$ (35)

$$\text{So, } S_{14} = \frac{1}{\sqrt{2}}$$

Putting the values of S_{13} and S_{14} in Eqs. (32) and (33) we have $S_{11} = 0$ and $S_{22} = 0$.

Replacing these values into Eq. (30) we have

$$S = \begin{bmatrix} 0 & 0 & \frac{1}{\sqrt{2}} & \frac{1}{\sqrt{2}} \\ 0 & 0 & -\frac{1}{\sqrt{2}} & \frac{1}{\sqrt{2}} \\ \frac{1}{\sqrt{2}} & -\frac{1}{\sqrt{2}} & 0 & 0 \\ \frac{1}{\sqrt{2}} & \frac{1}{\sqrt{2}} & 0 & 0 \end{bmatrix} = \frac{1}{\sqrt{2}} \begin{bmatrix} 0 & 0 & 1 & 1 \\ 0 & 0 & -1 & 1 \\ 1 & -1 & 0 & 0 \\ 1 & 1 & 0 & 0 \end{bmatrix} \tag{36}$$

It is to be noted here that port3 can also be considered at H-arm and port4 as E-arm. In that case, scattering matrix will be different as, $S_{24} = -S_{14}$ and $S_{23} = S_{13}$ under that consideration.

1.3.3 Applications

(a) **Impedance Measurement**: Microwave source can be connected at port4, null detector at port3 and two collinear arms can form a bridge which can be used to measure the impedance.
(b) **As a Duplexer**: Duplexer is a circuit where a single antenna is used as transmitter and receiver. As both of the collinear arms are mutually isolated, it can be used as transmitter and receiver. Antenna is connected to E-arm and H-arm is perfectly matched.
(c) **As a Signal Mixer**: E-arm is to be connected to an antenna and H-arm is to be connected to a local oscillator. One of the collinear ports is perfectly matched and the other collinear port consisting the mixer circuit which gets half of the total signal and local oscillator power to produce the intermediate frequency (IF).

Illustrative Example3: If 1 W power is applied to the perfectly matched port3 of a magic Tee, what will be the power delivered to port1, port2 and port4 if it is terminated by a reflection of 0.5, 0.6 and 0.8 respectively?

Solution: Here port3 is perfectly matched but all other ports are having reflections, $\rho_1 = 0.5$, $\rho_2 = 0.6$, and $\rho_4 = 0.8$

We know that if [a] and [b] are the normalized parameter for input and output voltage then, [b] = [S] [a]

$$\text{So,} \quad \begin{bmatrix} b_1 \\ b_2 \\ b_3 \\ b_4 \end{bmatrix} = \begin{bmatrix} S_{11} & S_{12} & S_{13} & S_{14} \\ S_{21} & S_{22} & S_{23} & S_{24} \\ S_{31} & S_{32} & S_{33} & S_{34} \\ S_{41} & S_{42} & S_{43} & S_{44} \end{bmatrix} \begin{bmatrix} a_1 \\ a_2 \\ a_3 \\ a_4 \end{bmatrix}$$

Given that, $P_3 = 1$ W, power delivered at port3, $P_3 = \frac{1}{2}|a_3|^2 - \frac{1}{2}|\rho_3 a_3|^2$

$$P_3 = \frac{1}{2}|a_3|^2 - \frac{1}{2}|b_3|^2 \quad \text{and} \quad b_3 = \rho_3 a_3$$

where, $\rho_3 = 0$, so $P_3 = \frac{1}{2}|a_3|^2 = 1$ W or, $a_3 = \sqrt{2}$ V

Hence, $a_3 = \sqrt{2}$; $b_1 = \rho_1 a_1 = 0.5 a_1$; $b_2 = \rho_2 a_2 = 0.6 a_2$; $b_4 = \rho_4 a_4 = 0.8 a_4$

And s-matrix for magic Tee is, $[S] = \dfrac{1}{\sqrt{2}} \begin{bmatrix} 0 & 0 & 1 & 1 \\ 0 & 0 & -1 & 1 \\ 1 & -1 & 0 & 0 \\ 1 & 1 & 0 & 0 \end{bmatrix}$

Using these values, we have,

$$\begin{bmatrix} 0.5a_1 \\ 0.6a_2 \\ \sqrt{2} \\ 0.8a_4 \end{bmatrix} = \frac{1}{\sqrt{2}} \begin{bmatrix} 0 & 0 & 1 & 1 \\ 0 & 0 & -1 & 1 \\ 1 & -1 & 0 & 0 \\ 1 & 1 & 0 & 0 \end{bmatrix} \begin{bmatrix} a_1 \\ a_2 \\ a_3 \\ a_4 \end{bmatrix}$$

Or, $0.5a_1 = \frac{1}{\sqrt{2}}(a_3 + a_4)$; $0.6a_2 = \frac{1}{\sqrt{2}}(-a_3 + a_4)$; $\sqrt{2} = \frac{1}{\sqrt{2}}(a_1 - a_2)$

And $0.8a_4 = \frac{1}{\sqrt{2}}(a_1 + a_2)$.

Solving the above four equations we have $a_1 = 0.928$; $a_2 = -1.07$; $a_3 = 0.781$; $a_4 = -0.125$

Power delivered at Port1, $P_1 = \frac{1}{2}|a_1|^2[1 - |\rho_1|^2] = \frac{1}{2}|0.928|^2[1 - |0.5|^2]$

$$= 0.3225 \text{ W}$$

Power delivered at Port2, $P_2 = \frac{1}{2}|a_2|^2[1 - |\rho_2|^2] = \frac{1}{2}|-1.07|^2[1 - |0.6|^2]$

$$= 0.366 \text{ W}$$

Power delivered at Port3, $P_3 = \frac{1}{2}|a_3|^2[1 - |\rho_3|^2] = \frac{1}{2}|0.781|^2[1 - |0|^2]$

$$= 0.304 \text{ W}$$

Power delivered at Port4, $P_4 = \frac{1}{2}|a_4|^2[1 - |\rho_4|^2] = \frac{1}{2}|-0.125|^2[1 - |0.8|^2]$

$$= 0.0028 \text{ W}$$

2 Directional Coupler

It is a 4-port passive waveguide device that can couple a small fraction of total microwave power for measurement. It can measure incident and reflected power and VSWR values etc. It is a 4-port device where the main waveguide contains port1 (i.e. input port) and port2 (i.e. output port). And secondary auxiliary waveguide contains port3 (i.e. isolated port) and port4 (i.e. coupled port). Power at the coupled port is called forward power and the power at the isolated port is called back power. For bi-directional device, input can be given from port2 and for that case, port3 is coupled port and port4 is isolated port as shown in Fig. 6.

2.1 Properties of Directional Coupler

(i) All ports are perfectly matched i.e. $S_{11} = S_{22} = S_{33} = S_{44} = 0$.
(ii) When power travels from port1 to port2, some portion of it gets coupled to port4 but no power appears at port3 i.e. $S_{31} = 0$.
(iii) For bi-directional coupler, when power travels from port2 to port1, some portion of it gets coupled at port3 and no power appears at port4 $S_{42} = 0$.
(iv) Generally, same degree of coupling is used between port1 to port4 and port2 to port3.
(v) Output from directional couplers are always in phase quadrature.

A directional coupler can be characterized by four parameters,

i. Coupling Factor (C)
ii. Directivity (D)
iii. Isolation (I)
iv. Insertion Loss (IL)

Coupling Factor (C): It is the fraction of input power that is coupled at the coupling port. If the input power is P_1 and coupled power is P_4 then coupling factor is given by,

Port 1 (Input Power) P1   P2 Port 2 (Output Power)

Port 3 (Back Power) P3   P4 Port 4 (Forward Power)
(Isolated Port)   (Coupled Port)
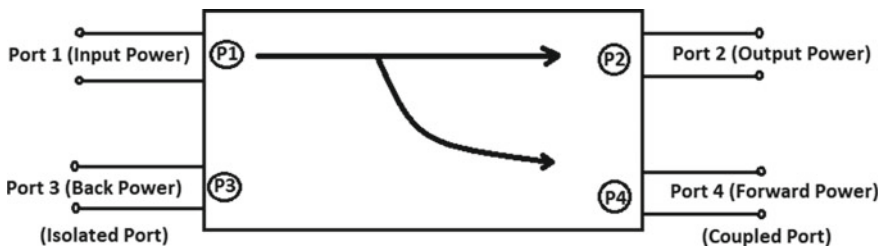
Fig. 6 Directional coupler

$$C = 10 \log \frac{P_1}{P_4} \text{ dB} = -20 \log(|S_{41}|) \text{ dB}. \tag{37}$$

Directivity (D): It is the ratio of forward power to the back power of a directional coupler.

$$D = 10 \log \frac{P_4}{P_3} \text{ dB} = 20 \log \frac{|S_{41}|}{|S_{31}|} \text{dB}. \tag{38}$$

Isolation (I): The ratio of incident power to the back power is called isolation.

$$I = 10 \log \frac{P_1}{P_3} \text{ dB} = -20 \log(|S_{31}|)\text{dB}.$$
$$= 10 \log \frac{P_1}{P_3} = 10 \log \left[\frac{P_1}{P_4} \cdot \frac{P_4}{P_3} \right] = \left[10 \log \frac{P_1}{P_4} + 10 \log \frac{P_4}{P_3} \right] \text{dB} = (C + D)\text{dB} \tag{39}$$

Insertion Loss (IL): It is the ratio of input power to output power.

$$IL = 10 \log \frac{P_1}{P_2} = -20 \log(|S_{21}|)\text{dB}. \tag{40}$$

2.2 *S-Matrix of Directional Coupler*

Scattering matrix of any 4-port device can be written as,

$$S = \begin{bmatrix} S_{11} & S_{12} & S_{13} & S_{14} \\ S_{21} & S_{22} & S_{23} & S_{24} \\ S_{31} & S_{32} & S_{33} & S_{34} \\ S_{41} & S_{42} & S_{43} & S_{44} \end{bmatrix} \tag{41}$$

As it is a symmetrical device, $S_{ij} = S_{ji}$,

So, $\quad S_{21} = S_{12}, S_{31} = S_{13}, S_{32} = S_{23}, S_{41} = S_{14}, S_{42} = S_{24}, S_{43} = S_{34}$ \qquad (42)

All ports are perfectly matched $S_{ii} = 0$.

So, $\quad S_{11} = S_{22} = S_{33} = S_{44} = 0.$ \qquad (43)

Again from property of isolation $S_{31} = S_{13} = 0$ and $S_{42} = S_{24} = 0$. (44)

Using Eqs. (42), (43) and (44), the above s-matrix reduced to

$$S = \begin{bmatrix} 0 & S_{12} & 0 & S_{14} \\ S_{12} & 0 & S_{23} & 0 \\ 0 & S_{23} & 0 & S_{34} \\ S_{14} & 0 & S_{34} & 0 \end{bmatrix}$$

As per unitary property, $[S][S^*] = [I]$

So, $\begin{bmatrix} 0 & S_{12} & 0 & S_{14} \\ S_{12} & 0 & S_{23} & 0 \\ 0 & S_{23} & 0 & S_{34} \\ S_{14} & 0 & S_{34} & 0 \end{bmatrix} \begin{bmatrix} 0 & S_{12}^* & 0 & S_{14}^* \\ S_{12}^* & 0 & S_{23}^* & 0 \\ 0 & S_{23}^* & 0 & S_{34}^* \\ S_{14}^* & 0 & S_{34}^* & 0 \end{bmatrix} = \begin{bmatrix} 1 & 0 & 0 & 0 \\ 0 & 1 & 0 & 0 \\ 0 & 0 & 1 & 0 \\ 0 & 0 & 0 & 1 \end{bmatrix}$ (45)

From matrix multiplication,

$$R1^*C1 \Longrightarrow \quad |S_{12}|^2 + |S_{14}|^2 = 1 \tag{46}$$

$$R2^*C2 \Longrightarrow \quad |S_{12}|^2 + |S_{23}|^2 = 1 \tag{47}$$

$$R3^*C3 \Longrightarrow \quad |S_{23}|^2 + |S_{34}|^2 = 1 \tag{48}$$

$$R4^*C4 \Longrightarrow \quad |S_{14}|^2 + |S_{34}|^2 = 1 \tag{49}$$

From Eqs. (46) and (47) $S_{14} = S_{23}$ and from (47) and (48) $S_{12} = S_{34}$ (50)

$$R1 * C3 \Longrightarrow \quad S_{12}S_{23}^* + S_{14}S_{34}^* = 0$$
$$\text{or, } S_{12}S_{23}^* + S_{23}S_{12}^* = 0 \quad \text{[from Eq. (50)]}$$
$$S_{12}S_{23}^* + S_{23}S_{12}^* = 0$$

Multiplied both sides by S_{12}, $|S_{12}|^2[S_{23} + S_{23}^*] = 0$,
Or, $S_{23} = -S_{23}^*$ only possible when S_{23} is purely imaginary. Whereas $S_{12} = S_{34}$ used to be real.
Let consider $S_{14} = S_{23} = jq$ and $S_{12} = S_{34} = p$ where p is purely real.
The scattering matrix of directional coupler used to be, using these values,

$$S = \begin{bmatrix} 0 & p & 0 & jq \\ p & 0 & jq & 0 \\ 0 & jq & 0 & p \\ jq & 0 & p & 0 \end{bmatrix}$$

2.3 Applications

(a) **As Reflectometer**: By connecting the power sensor at the coupled port, VSWR of the antenna system can be measured. Many RF devices need to have minimum VSWR or protection from excessive VSWR from the circuit.
(b) **As Signal Sampler**: Coupled port provides a fraction of the power of the main waveguide. This fraction is called coupling factor. By using this spectrum analysis, waveform monitoring etc. of any RF system can be done.
(c) **As Reference Signal Generator**: Signal of the coupled port can be used as a reference signal to control feedback circuitry.

Illustrative Example 4: Two identical couplers are used in a waveguide to sample the incident power of 5 mW and reflected power as 0.16 mW. What will be the value of VSWR?

Solution: Here reflection coefficient, $\rho = \sqrt{\frac{P_r}{P_i}} = \sqrt{\frac{0.16}{5}} = 0.179$.

Now, Voltage Standing Wave Ratio (VSWR) $= \frac{1+\rho}{1-\rho} = \frac{1+0.179}{1-0.179} \approx 1.44$.
So, VSWR $= 1.44$.

Illustrative Example 5: Two identical 40 dB directional couplers are used to sample incident and reflected power in a waveguide. Voltage standing wave ratio is 1.5 and the output of the coupler sampling incident power is 6 mW. Calculate the value of the reflected power.

Solution: Here VSWR $= \frac{1+\rho}{1-\rho} = 1.5$
Or, $1 + \rho = 1.5 - 1.5\rho$.
Or, $2.5\rho = 0.5$
Or, $\rho = \frac{0.5}{2.5} = 0.2$
Now, we know that $\rho = \sqrt{\frac{P_r}{P_i}} = \rho = \sqrt{\frac{P_r}{6}}$.
Or, $\rho^2 = \frac{P_r}{6}$ or, $\frac{P_r}{6} = 0.04$ or, $P_r = 0.24$ mW.
So, the reflected power is 0.24 mW.

Illustrative Example 6: Scattering matrix of a directional is given by

$$[S] = \begin{bmatrix} 0.03 & 0.85 & 0.10 & 0.03 \\ 0.85 & 0.03 & 0.03 & 0.10 \\ 0.10 & 0.03 & 0.06 & 0.85 \\ 0.03 & 0.10 & 0.85 & 0.03 \end{bmatrix}$$

Calculate Directivity, Coupling factor, Isolation and Insertion loss.

Solution: The port orientation of directional coupler is given by,
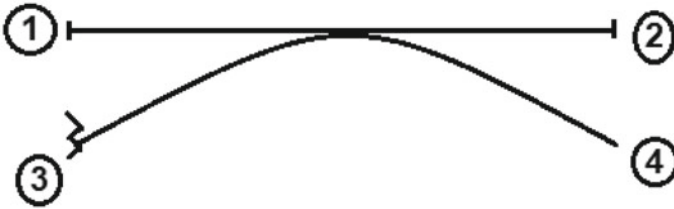
$$[S] = \begin{bmatrix} 0.03 & 0.85 & 0.10 & 0.03 \\ 0.85 & 0.03 & 0.03 & 0.10 \\ 0.10 & 0.03 & 0.06 & 0.85 \\ 0.03 & 0.10 & 0.85 & 0.03 \end{bmatrix} = \begin{bmatrix} S_{11} & S_{12} & S_{13} & S_{14} \\ S_{21} & S_{22} & S_{23} & S_{24} \\ S_{31} & S_{32} & S_{33} & S_{34} \\ S_{41} & S_{42} & S_{43} & S_{44} \end{bmatrix}$$

Directivity is given by, $D = 10 \log \frac{P_4}{P_3}$ dB $= 10 \log \left(\frac{P_4}{P_1} \cdot \frac{P_1}{P_3} \right)$ dB $= 20 \log \frac{|S_{41}|}{|S_{31}|}$ dB.

$D = 20 \log \left(\frac{0.03}{0.10} \right) = -10.46$ dB.

Coupling, $C = 10 \log \frac{P_1}{P_4}$ dB $= -20 \log (|S_{41}|)$ dB. $= -20 \log(0.03) = 30.46$ dB.

Isolation, $I = 10 \log \frac{P_1}{P_3}$ dB $= -20 \log (|S_{31}|) = -20 \log(0.10) = 20$ dB.

Here Isolation, $I = 30$ dB $= 30.46 + (-10.46) = C + D = $ Coupling + Directivity.

Insertion Loss, $IL = 10 \log \frac{P_1}{P_2} = -20 \log (|S_{21}|)$ dB. $= -20 \log(0.85) = 1.41$ dB.

3   Isolator

It is a passive, non-reciprocal two-port waveguide section that passes signals coming from one direction but blocks signals coming from other direction or any reflected signal (Fig. 7). Usually, an isolator is placed after the microwave source to pass the signal transmitted from the source but blocks any reflected wave to go to the source. That's how it isolates the source from other parts of the circuit.
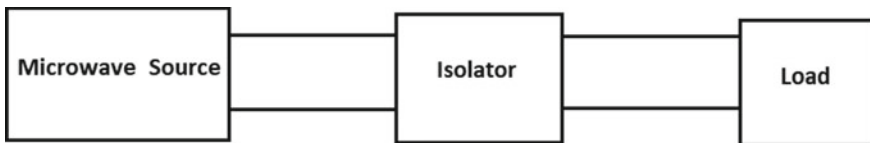
Fig. 7 Isolator
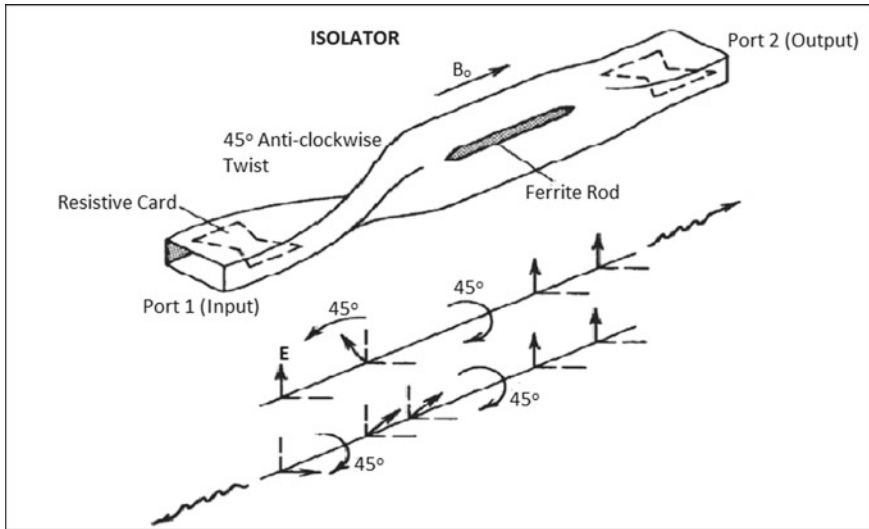
Fig. 8 Illustration of the working of an Isolator

Usually, an isolator consists of a waveguide section containing two slots of resistive card at both ends of it. A 45° anti-clockwise twist is used in between and after the twist a slot of ferrite rod so chosen that it can provide a 45° clockwise turn to the wave passing through it as illustrated in Fig. 8.

When wave travels from input to output port, resistive card at the input end blocks horizontally polarized wave and passes vertically polarized wave through it. Then this vertically polarized wave gets rotated by 45° anti-clockwise by the twist in the waveguide. Ferrite rod provides 45° further rotation to the wave so that it became vertically polarized again and gets easily passed through the resistive card at the output end.

But when wave travels from output side, resistive card at the output end passes vertically polarized wave but blocks horizontally polarized wave. Ferrite rod which provides rotation in the same direction to the wave coming from both directions provides 45° clockwise rotation to it. The twist in the waveguide provides further 45° clockwise (opposite due to wave coming from reverse side) rotation and ultimately it became horizontally polarized due to two consecutive turns of 45° each. This horizontally polarized wave gets blocked by a resistive card at the input side. Hence no power from output can appear at input side [2].

3.1 S-Matrix of Isolator

It is a two-port device. S-matrix of a two-port device can be written as,

$$S = \begin{bmatrix} S_{11} & S_{12} \\ S_{21} & S_{22} \end{bmatrix} \tag{51}$$

As both of the ports are perfectly matched, $S_{11} = 0$ and $S_{22} = 0$.
If signal is applied from port2 no power appears at port1, hence $S_{12} = 0$.
When signal is applied from port1, total output appears at port2 i.e. $S_{21} = 1$.

$$\text{So, s-matrix of isolator can be written as, } S = \begin{bmatrix} 0 & 0 \\ 1 & 0 \end{bmatrix} \tag{52}$$

3.2 Applications

(a) **As Protecting Device**: In the process of testing and measurement (T&M) it is very possible that any undesired reflection from device under test (DUT) can damage the original circuit. So, the Isolator is employed in between to suppress that undesired reflection.

Illustrative Example 7: Determine the scattering matrix of an isolator having insertion loss of 0.5 dB and that provides an isolation of 40 dB. Consider all the ports are perfectly matched.

Solution: As we know that isolator is a two-port device, the generic form of scattering matrix will be, $[S] = \begin{bmatrix} S_{11} & S_{12} \\ S_{21} & S_{22} \end{bmatrix}$.

Here, it is given that all the ports are perfectly matched, hence $S_{11} = S_{22} = 0$;
Insertion loss is given as 0.5 dB, hence $-20 \log|S_{21}| = 0.5$
Or, $S_{21} = 0.994$.
Again isolation is 40 dB so, $-20\log|S_{12}| = 40$.
Or, $S_{12} = 0.01$.
So, the s-matrix will be, $[S] = \begin{bmatrix} 0 & 0.01 \\ 0.994 & 0 \end{bmatrix}$.

4 Circulator

Circulator is a 3-port or 4-port device which can circulate RF signal in a particular direction (mainly clockwise but can be anti-clockwise as well). The structure is a combination of rectangular and circular waveguide and ferrite rod inserted in between, so that if input is given from port1 output can be obtained from port2 only, similarly if input is given from port2, output is available only at port3 and so on (Figs. 9 and 10).

Let's Consider RF signal of the dominant TE_{10} mode inserted from port1 of the rectangular waveguide section and get converted to TM_{11} dominant mode when it approaches circular waveguide section. But the orientation of port3 is completely out of phase with port1 so no output appears at port3. The ferrite rod between port3 and port4 provides 45° clockwise rotations to the signal and so that port4 became completely out of phase hence no output appears at port4. The RF signal then enters to rectangular waveguide section at port2 as the dominant TE_{10} mode. So the complete output appears at port2 [3].

Similarly, any input applied through port3 does appear at port1 as it is completely out of phase. But after 45° clockwise rotations through the ferrite rod, it appears at port4 and as port2 is again completely out of phase, no output appears at port2. Likewise, any input applied through port2 can appear at port3 only (Fig. 11).
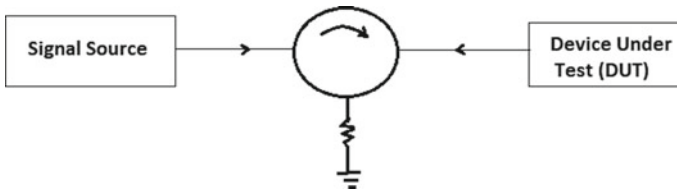
Fig. 9 Circulator
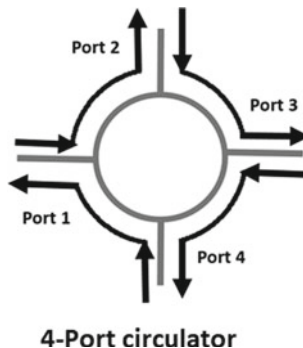
4-Port circulator

Fig. 10 Four-port circulator

Internal Structure of 4-port Circulator
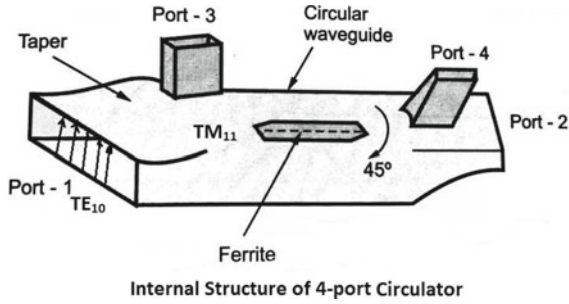
Fig. 11 Internal structure of a circulator

4.1 S-Matrix

For any 4-port device S-matrix can be the form of,

$$S = \begin{bmatrix} S_{11} & S_{12} & S_{13} & S_{14} \\ S_{21} & S_{22} & S_{23} & S_{24} \\ S_{31} & S_{32} & S_{33} & S_{34} \\ S_{41} & S_{42} & S_{43} & S_{44} \end{bmatrix} \tag{53}$$

As all the four ports are perfectly matched, $S_{ii} = 0$.

$$\text{So,} \quad S_{11} = S_{22} = S_{33} = S_{44} = 0. \tag{54}$$

Again from the property of isolation, $S_{14} = S_{12} = S_{32} = S_{43} = 1$ and all other elements are zero. So S-matrix reduce to the form of

$$S = \begin{bmatrix} 0 & 0 & 0 & 1 \\ 1 & 0 & 0 & 0 \\ 0 & 1 & 0 & 0 \\ 0 & 0 & 1 & 0 \end{bmatrix} \tag{55}$$

For exactly similar reason S-matrix of a 3-port circulator will be

$$S = \begin{bmatrix} 0 & 0 & 1 \\ 1 & 0 & 0 \\ 0 & 1 & 0 \end{bmatrix} \tag{56}$$

Here, $S_{13} = S_{21} = S_{32} = 1$ and all other elements are zero.

4.2   Applications

Due to its unique isolation property, circulator can be employed for several important applications like,

- As Duplexer
- As Reflection amplifier
- In Radar systems
- In Amplifier systems
- In Antenna transmitting or receiving Systems

Illustrative Example 8: Determine the scattering matrix of a 3-port circulator having an insertion loss of 0.5 dB, isolation of 40 dB and VSWR 0f 3.

Solution: The generic form of s-matrix of a 3-port device can be written as,

$$[S] = \begin{bmatrix} S_{11} & S_{12} & S_{13} \\ S_{21} & S_{22} & S_{23} \\ S_{31} & S_{32} & S_{33} \end{bmatrix}$$

For circulator, insertion loss is given by $S_{21} = S_{32} = S_{13}$
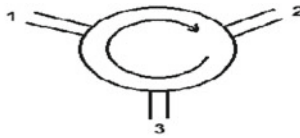
And isolation is given by, $S_{12} = S_{31} = S_{23}$.

And reflection coefficient which is related to VSWR is represented by $S_{11} = S_{22} = S_{33}$. In this case, all ports are not matched perfectly.

Here, $-20\log|S_{21}| = 0.5$, or $S_{21} = 0.994$; So, $S_{21} = S_{32} = S_{13} = 0.994$.

Again, $-20\log|S_{12}| = 40$, or, $S_{12} = 0.01$.

So, $S_{12} = S_{31} = S_{23} = 0.01$.

Now reflection coefficient, $\rho = S_{11} = S_{22} = S_{33} = \frac{VSWR-1}{VSWR+1} = \frac{3-1}{3+1} = 0.5$

So, $S_{11} = S_{22} = S_{33} = 0.5$

Putting all these values we have,

$$[S] = \begin{bmatrix} 0.5 & 0.01 & 0.994 \\ 0.994 & 0.5 & 0.01 \\ 0.01 & 0.994 & 0.5 \end{bmatrix}$$

5 Gyrator

Gyrator is a passive, 2-port, non-reciprocal, ferrite device which can provide a phase shift of 180° for RF signal transmission in the forward direction and 0° phase shift in the reverse direction [4]. It is a linear and lossless device which is very similar like a transformer but the fundamental difference is, a transformer does not provide any phase shift i.e. if voltage is at the primary end, induced secondary signal will be in the form of voltage only. But in the case of gyrator due to 180° phase reversal it will be in current form. Reverse transmission is very similar for both (Fig. 12).

Gyrator consists of two rectangular waveguide sections in both ends of port1 and port2, circular waveguide in between which contains ferrite rod to provide 90° F rotation in counter clockwise direction. There is a twist of 90° between rectangular waveguide and circular waveguide at port1.

Consider the figure shown below, for wave that propagates from left to right; it passes the twist and gets rotated by 90° in a counter clockwise direction. Again the ferrite rod provides another 90° rotation; the total rotation will be 180° at port2. The wave that propagates from right to left, experiences Faraday rotation of 90° in a similar manner. But while passing through the twist, it gets another 90° of rotation in a direction that cancels the Faraday rotation. For that reason, in transmission from port2 to port1, there is no phase shift (Fig. 13).

Fig. 12 Gyrator

Port1 π -Phase shift   Port2
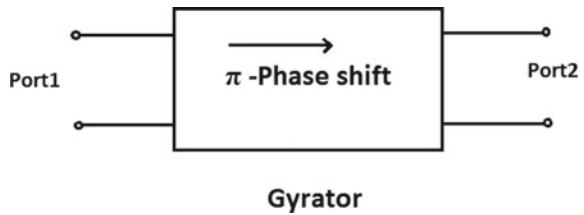
Gyrator

Fig. 13 Internal structure Gyrator

B_0

Port1   Ferrite Rod   Port2

E
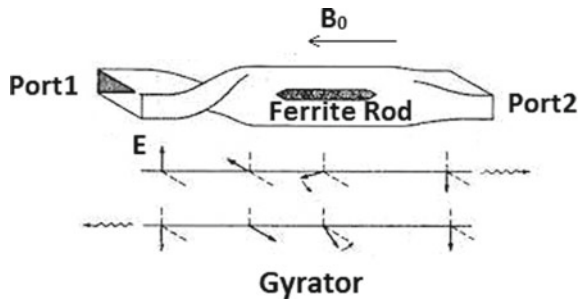
Gyrator

5.1 S-Matrix

S-matrix of a 2-port device having generic form of,

$$S = \begin{bmatrix} S_{11} & S_{12} \\ S_{21} & S_{22} \end{bmatrix} \tag{57}$$

As it is a symmetrical device, $S_{ii} = 0$;

$$\text{So,} \quad S_{11} = S_{22} = 0 \tag{58}$$

And from property of transmission $S_{21} = -1$ and $S_{12} = 0$; (59)

So, S-matrix for Gyrator is

$$S = \begin{bmatrix} 0 & 1 \\ -1 & 0 \end{bmatrix} \tag{60}$$

5.2 Applications

Gyrator can be employed for several applications like,

- As an Inductor
- As BPF
- In Telephony device that is connected to POTS
- As parametric equalizer.

6 Rat Race Coupler

Rat race or hybrid ring is a 4-port passive device that is used to combine two in-phase signals or nullify the signals having path differences. Total circumference of the ring is 1.5λ, where port1, port2 and port3 are 0.5λ apart and the distance between port1 to port4 is 0.75λ (Fig. 14).

When input is applied through port1, it appears as two equal parts one at port2 in clockwise direction and other at port4 in counter clockwise direction. As λ/4 path difference corresponds to 90° phase shift, port2 and port4 became in-phase and output appears there. And no output appears at port3 as it is out of phase.

Similarly, when input signal is applied to port3 it gets equally divided between port2 and port4 and no output appears at port1. Again if two different signals are applied to port1 half of the sum appears at port2 and another half appears at port4 and the difference appears at port3.

Fig. 14 Rat race coupler

Rat Race
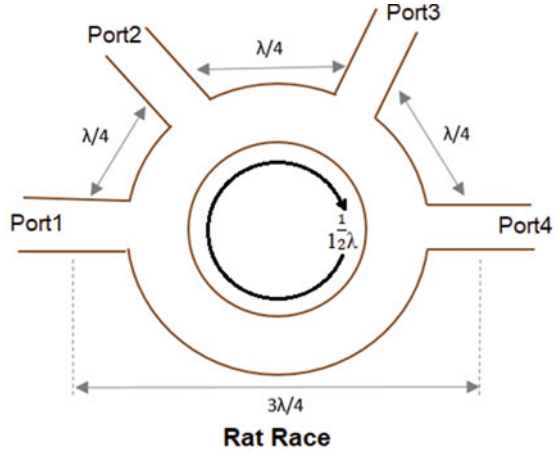
6.1 S-Matrix

S-matrix of a 4-port device can be written as,

$$S = \begin{bmatrix} S_{11} & S_{12} & S_{13} & S_{14} \\ S_{21} & S_{22} & S_{23} & S_{24} \\ S_{31} & S_{32} & S_{33} & S_{34} \\ S_{41} & S_{42} & S_{43} & S_{44} \end{bmatrix} \tag{61}$$

As it is a symmetrical device, $S_{ij} = S_{ji}$,

So, $S_{21} = S_{12}, S_{31} = S_{13}, S_{32} = S_{23}, S_{41} = S_{14}, S_{42} = S_{24}, S_{43} = S_{34}$ \quad (62)

All ports are perfectly matched $S_{ii} = 0$.

So, $S_{11} = S_{22} = S_{33} = S_{44} = 0.$ \quad (63)

Using Eqs. (62) and (63) above s-matrix reduced to

$$S = \begin{bmatrix} 0 & S_{12} & 0 & S_{14} \\ S_{12} & 0 & S_{23} & 0 \\ 0 & S_{23} & 0 & S_{34} \\ S_{14} & 0 & S_{34} & 0 \end{bmatrix} \tag{64}$$

Considering input from port1, $S_{21} = -S_{41}$ and $S_{31} = 0$;
For input from port2, $S_{12} = S_{32}$ and $S_{42} = 0$;
For input from port3, $S_{23} = S_{43}$ and $S_{13} = 0$;

For input from port4, $S_{34} = -S_{14}$ and $S_{24} = 0$;

For perfect matching from the feed line to the ring, impedance at the port should be $\frac{1}{\sqrt{2}}$ times of the impedance of the ring. For example, it can be 75 Ω for ring and 50 Ω for ports and it is imaginary by nature. Combining all these, Eq. (64) can be reduced as

$$S = \frac{-j}{\sqrt{2}} \begin{bmatrix} 0 & 1 & 0 & -1 \\ 1 & 0 & 1 & 0 \\ 0 & 1 & 0 & 1 \\ -1 & 0 & 1 & 0 \end{bmatrix} \tag{65}$$

6.2 Application

- Combiner of signal
- Splitter of signal.

7 Matched Termination

It is a two-port passive waveguide section which used to absorb all the incident power without any reflection or radiation from it. Though it is a two-port waveguide section port2 is perfectly matched and terminated by characteristics impedance (Fig. 15).

Practical circuit includes a tapered section of waveguide with one end terminated and a lossy dielectric inside it. Any input from port1 is absorbed at port2 due to the presence of lossy dielectric which formed matched termination (Fig. 16).

Fig. 15 Matched terminator

Fig. 16 Internal structure of matched terminator

Matched Termination
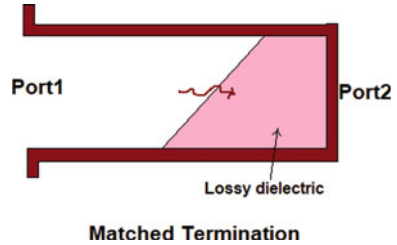
7.1 S-Matrix

As port2 is terminated by characteristics impedance, $Z_{in} = Z_{out}$ and there is no reflection from port2 as it is perfectly matched. Thus the reflection coefficient is $\Gamma = S_{11} = 0$.

7.2 Application

The Matched Termination is used to terminate the waveguide transmission line with no reflection at all.

8 Attenuator

It is a passive waveguide device that is used to diminish the strength of the signal without affecting the characteristics impedance (Z_0) of the waveguide. If characteristics impedance is not maintain fixed, there caused impedance discontinuity and hence undesired reflection. Generally, a resistive material is placed in parallel to the electric field line, current induce in the resistive material which introduced I^2R loss that introduces attenuation (Fig. 17).

Basically, attenuator is of three types,

- Fixed type attenuator
- Electronically or Mechanically variable type
- Series of fixed step type

A fixed slab of dielectric is placed inside the waveguide to provide a fixed amount of attenuation, in fixed type attenuator.

Variable attenuator is used to provide fixed or variable attenuation. The depth of attenuation depends on the insertion depth of the plate containing absorbing material into the waveguide. The attenuation is maximum when the dielectric slab is inserted totally into the waveguide. Variable attenuator can be of different types, like.

Fig. 17 Variable attenuator

Variable Attenuator
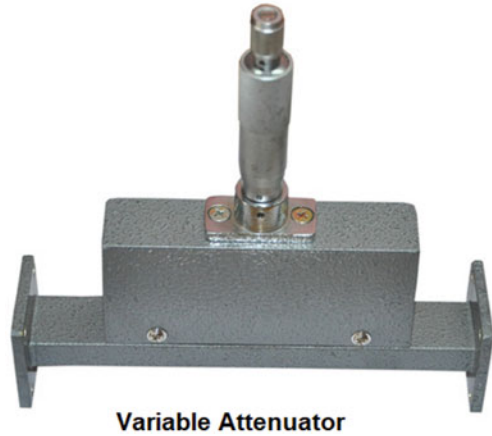
- Resistive card type (flap type) attenuator
- Slide vane attenuator
- Rotary vane attenuator

Among these, rotary vane attenuator is the most widely employed attenuator. It is having two tapered sections of rectangular to circular waveguide along with an intermediate circular waveguide section which is free to rotate. All the three waveguide section contains thin resistive cards [5]. When dominant TE_{10} mode enters from rectangular to circular waveguide, input resistive card allows only perpendicular components to pass. Resistive card inside the circular waveguide is available to rotate and adjust its orientation as per attenuation required. Inside circular waveguide TE_{11} mode have parallel and perpendicular components. Parallel component absorbed through resistive card and perpendicular component passes through it. Output resistive card further attenuates parallel components and perpendicular components appear at the output. The output power can be controlled by rotating circular waveguide to change the orientation of the resistive card inside it which can change the attenuation (Fig. 18).

Fig. 18 Rotary vane attenuator
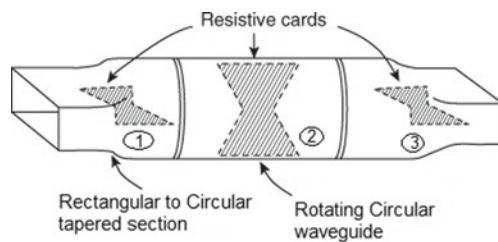
Rotary Vane Attenuator

As the basic property of the attenuator is to maintain characteristics impedance (Z_0) fixed, it does not introduce any reflection to the waveguide, hence no additional scattering property for it.

8.1 Applications

It provides attenuation to the waveguide where a signal with lower strength is required.

9 Phase-Shifter

Microwave phase-shifter is a passive device which can alter the phase of oscillation of electromagnetic wave at the output of the transmission line with respect to the phase at the input. Microwave phase-shifter can be used as power divider, beam forming network, phase discriminator and in phase-array antenna. The main difference between phase-shifter and attenuator is, the phase-shifter alters the phase of RF signal in a desired manner without doing any change in signal strength, whereas attenuator changes signal strength without altering the phase of the signal. There are different types of phase-shifter available in the industry, among them the two most widely employed phase-shifter are,

- Dielectric Phase-Shifter
- Precision Rotary Phase-Shifter

The working principle of all the phase-shifter is fundamentally similar. If we consider two arbitrary points having phases φ_1 and φ_2 and distance L among them. The phase difference, $\Delta\varphi = (\varphi_2 - \varphi_1) = \beta L = \left(\frac{2\pi}{\lambda}\right)L$. Where β is phase constant. This means, by changing the distance between two points, phase alteration is possible. Alternatively, if the velocity of RF signal can get changed, that is equivalent to the change in distance travel considering the time as constant. This implies that any retardation in velocity can have a net effect on the phase of the signal. Applying this principle different phase-shifter is developed.

9.1 Dielectric Phase-Shifter

Inside a rectangular waveguide a slab of dielectric of thickness 't' and height 'h' is inserted so that 'h' is in parallel orientation to the electric field. When the dominant TE_{10} mode is propagated through the waveguide, due to the presence of dielectric constant ε, the effective path length increased and hence velocity of propagation is reduced. Due to that, ultimately phase of the signal gets delayed [6].
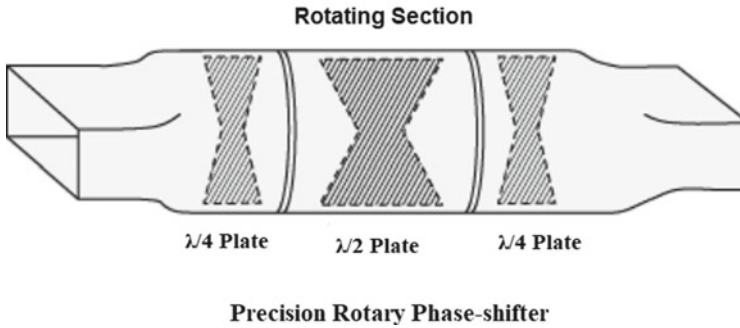
Fig. 19 Precision Rotary Phase-Shifter

9.2 Precision Rotary Phase-Shifter

This is one of the most widely employed phase-shifter, where a particular waveguide structure, one half-wave plate and two quarter-wave plate are used. Two rectangular to circular tapered section contains a quarter-wave plate inside it, mounted at 45° angles with the broad wall of the rectangular waveguide. The rotating circular waveguide contains half-wave plate at 0° default angle and precision over there (Fig. 19).

Both of the quarter-wave plates provides a phase shift of 90° each and a 180° phase shift for the half-wave plate. So when the signal of the dominant TE_{10} mode is applied to the input end it gets converted to TE_{11} mode inside the circular waveguide section and reaches the half-wave plate as a parallel and perpendicular component. Perpendicular component passes it with a net phase delay of $(90° + 180°) = 270°$ for quarter-wave and half-wave plate respectively when half-wave plate is in 0th or default position. Ultimately it passes the quarter-wave with an accumulated phase of $(270° + 90°) = 360°$. So there is no phase alteration of the signal. But when the half-wave plate rotates from 0th position to an angle of θ, the output signal experienced a total phase delay of 2θ. So, by rotating the circular waveguide section, i.e. changing the orientation of half-wave plate, the output phase of the signal can be regulated in the desired manner.

9.3 Applications

Microwave phase-shifter can be employed in different types of communication systems, radar systems, microwave measurement systems and in different industrial operations.

10 Waveguide Bends and Twists

Sometimes it became necessary to have bends in the waveguide structure to direct the signal in the desired direction. But any abrupt variation in the size or shape of the waveguide can cause reflection and hence a loss in efficiency. When such a change is required, certain conditions must be satisfied to prevent unwanted reflection. In general, bends can be of four types,

- Gradual E-Bend
- Gradual H-Bend
- Sharp E-Bend
- Sharp H-Bend

Gradual E-Bend: It is a gradual bend that distorts the E-field only. The bend gradually follows a radius of curvature where radius r must satisfy the condition of r > $2\lambda_g$ to avoid unwanted reflection (Fig. 20).

Gradual H-Bend: It is a gradual bend that distorts H-field only. Radius of curvature of the bend is greater than twice the wavelength i.e. r > $2\lambda_g$ to avoid any unwanted reflection through it (Fig. 21).

Sharp E-Bend: Two sharp bends of 45° on E-field waveguide placed quarter-wave $\left(\frac{\lambda_g}{4}\right)$ apart so that reflection caused by one sharp bend can be canceled by another, leaving no net reflection at all (Fig. 22).

Fig. 20 Gradual E-Bend

$r > 2\lambda_g$

Gradual E-Bend

Fig. 21 Gradual H-Bend

$r > \lambda_g$

Gradual H-Bend

Fig. 22 Sharp E-Bend
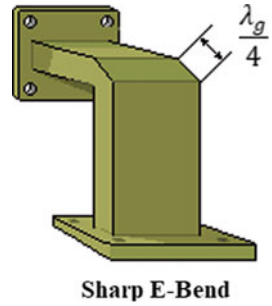
Sharp E-Bend

Sharp E-Bend: Two sharp bends of 45° on H-field waveguide placed quarter-wave $\left(\frac{\lambda_g}{4}\right)$ apart so that reflection caused by one sharp bend can be canceled by another, leaving no net reflection at all (Fig. 23).

Twist: For some particular use, sometimes it is required to rotate the RF signal in such a way that it can get the desired phase for phase adjustment at load. That can be achieved by using a twist in the waveguide which is gradual in nature and greater than $2\lambda_g$ (Fig. 24).

Fig. 23 Sharp H-Bend

Sharp H-Bend
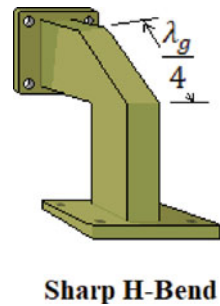
Fig. 24 Waveguide twist

Waveguide Twist

Some special kinds of lossy bends can also be used that consist of wound ribbons of conducting material like brass with chromium plated inner surface. It is used for a short section when no other solution is possible.

11 Cavity Resonator

Cavity resonator is a closed metallic structure that encloses electromagnetic energy. The structure can be hollow or filled with dielectric material. Cavity resonator can be formed by introducing metallic walls at a distance d apart both ends of a rectangular or circular waveguide along z direction. The microwave signal bounces back and forth inside the cavity to form a standing wave. Thus it can act like a Band Pass Filter (BPF) allowing a particular band of frequency to pass through it and blocking all other frequencies. Microwave cavity resonator acts as a very low loss resonant device at its resonance frequency and offers a quality factor as high as 10^6. At resonance stored electrical energy is equal to stored magnetic energy and impedance is purely real in nature. Here we will discuss about the cavity resonator made of rectangular i.e. rectangular cavity resonator and of circular waveguide i.e. cylindrical cavity resonator [7].

11.1 Rectangular Cavity Resonator

Rectangular waveguide closed from both ends by a metallic wall along z direction at a distance of d (Fig. 15). The transverse component of electric field can be written as (Fig. 25),

$$E_t(x, y, z) = \hat{e}(x, y) \left\{ A^+ e^{-j\beta}_{mnZ} + A^- e^{+j\beta}_{mnZ} \right\} \tag{66}$$

$$\text{where } \beta_{mn} = \sqrt{K^2 - K_c^2} = \sqrt{K^2 - \left(\frac{m\pi}{a}\right)^2 - \left(\frac{n\pi}{b}\right)^2} \quad \text{and} \quad K = \omega\sqrt{\mu\varepsilon} \tag{67}$$

Putting boundary condition $E_t = 0$ for $z = 0$;
We have, $\hat{e}(x, y)\{A^+ + A^-\} = 0$;

$$\text{Or,} \quad \{A^+ + A^-\} = 0; \quad \text{so,} \quad A^+ = -A^- \tag{68}$$

Second boundary condition is $E_t = 0$ for $z = d$;
Or, $\hat{e}(x, y)\left\{A^+ e^{-j\beta}_{mn}d + A^- e^{+j\beta}_{mn}d\right\} = 0$;
Or, $\left\{A^+ e^{-j\beta}_{mn}d + A^- e^{+j\beta}_{mn}d\right\} = 0$;
Or, $\left\{A^+ e^{-j\beta}_{mn}d - A^+ e^{+j\beta}_{mn}d\right\} = 0$;   [using Eq. (67)].

Fig. 25 Rectangular cavity
resonator
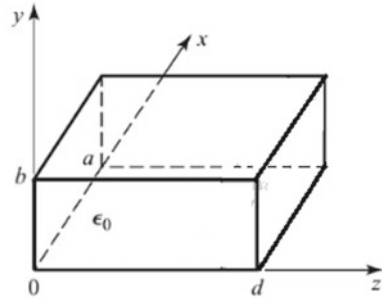
Rectangular Cavity Resonator

Or, $A^+\left[-2j\ \sin(\beta_{mn}d)\right] = 0$ $\left[\text{as } \frac{e^{jx}-e^{-jx}}{2j}\ \sin(x)\right].$
That implies, $\beta_{mn}d = p\pi$ where $p = 0,1,2,3, \ldots\ldots$

$$\text{Or,}\quad \beta_{mn} = \frac{p\pi}{d} \tag{69}$$

From Eq. (67) we have,

$$\beta_{mn} = \sqrt{K^2 - \left(\frac{m\pi}{a}\right)^2 - \left(\frac{n\pi}{b}\right)^2}\quad \text{or,}\quad K_{mnp}\sqrt{\beta^2 + K_c^2} = \sqrt{\beta^2 + \left(\frac{m\pi}{a}\right)^2 + \left(\frac{n\pi}{b}\right)^2}$$

$$\text{or,}\quad K_{mnp} = \sqrt{\left(\frac{m\pi}{a}\right)^2 + \left(\frac{n\pi}{b}\right)^2 + \left(\frac{p\pi}{d}\right)^2} \tag{70}$$

Now resonance frequency for different modes can be presented as,

$$f_{mnp} = \frac{1}{2\pi\sqrt{\mu\varepsilon}}\sqrt{\left(\frac{m\pi}{a}\right)^2 + \left(\frac{n\pi}{b}\right)^2 + \left(\frac{p\pi}{d}\right)^2} \tag{71}$$

For dominant mode i.e. TE_{101}

$$f_{101} = \frac{c}{2\pi}\sqrt{\left(\frac{m\pi}{a}\right)^2 + \left(\frac{p\pi}{d}\right)^2} \tag{72}$$

Illustrative Example 9: Determine the lowest resonant frequency of a rectangular
cavity resonator having dimensions 3 cm × 4 cm × 5 cm. Also find the change in
length required to have a resonant frequency of 1.5 times than the earlier one.

Solution: Here given that a = 3 cm; b = 4 cm; d = 5 cm;
    Dominant mode is TE_{101} here.
    Resonant frequency, $f_r = \frac{c}{2}\sqrt{\left(\frac{m}{a}\right)^2 + \left(\frac{n}{b}\right)^2 + \left(\frac{p}{d}\right)^2}$

For TE$_{101}$ mode, $f_r = \dfrac{c}{2}\sqrt{\left(\dfrac{1}{3}\right)^2 + \left(\dfrac{0}{4}\right)^2 + \left(\dfrac{1}{5}\right)^2} = \dfrac{3 \times 10^{10}}{2}\sqrt{\dfrac{1}{9} + \dfrac{1}{25}} = 0.583 \times 10^{10}$

$$= 5.83 \times 10^9\,\text{Hz} = 5.83\,\text{GHz}$$

Now for the second part, consider the new length of cavity is d,
New resonant frequency to be $f_r' = 1.5 \times f_r = 8.745$ GHz.
So, $f_r' = \frac{c}{2}\sqrt{\left(\frac{1}{3}\right)^2 + \left(\frac{0}{4}\right)^2 + \left(\frac{1}{d'}\right)^2}$ or, $8.745 \times 10^9 = \frac{3\times10^{10}}{2}\sqrt{\frac{1}{9} + \frac{1}{d'^2}}$.
Or, $d' = 2.08$ cm.
Length of the resonator must be reduced by $(5.00 - 2.08) = 2.92$ cm.

Illustrative Example 10: Calculate the resonant frequency for TE$_{111}$ mode of a rectangular cavity resonator of dimension 8 cm $\times$ 6 cm $\times$ 4 cm. What will be the new resonant frequency if the cavity is filled with a dielectric of $\varepsilon_r = 2.2$?

Solution: Here, a $= 8$ cm; b $= 6$ cm; d $= 4$ cm

$$\text{Resonant frequency, } f_r = \dfrac{c}{2}\sqrt{\left(\dfrac{m}{a}\right)^2 + \left(\dfrac{n}{b}\right)^2 + \left(\dfrac{p}{d}\right)^2} = \dfrac{3 \times 10^{10}}{2}\sqrt{\dfrac{1}{64} + \dfrac{1}{36} + \dfrac{1}{16}}$$

$$= 4.88\,\text{GHz}$$

Now, filling the cavity will reduce the resonant frequency of the cavity resonator.
New resonant frequency, $f_r' = \dfrac{f_r}{\sqrt{\varepsilon_r}} = \dfrac{4.88}{\sqrt{2.2}}$ GHz $= 3.29$ GHz.

Illustrative Example 11: A rectangular waveguide cavity resonator filled with dielectric $\varepsilon_r = 2.5$ and having a cross section of 5 cm $\times$ 4 cm. Find the length of the cavity resonator required to have the resonant frequency of 3 GHz at dominant TE$_{101}$ mode.

Solution: Given as a $= 5$ cm; b $= 4$ cm and $f_r = 3$ GHz.
We know that $f_r' = \dfrac{c}{2\sqrt{\varepsilon_r}}\sqrt{\left(\dfrac{m}{a}\right)^2 + \left(\dfrac{n}{b}\right)^2 + \left(\dfrac{p}{d}\right)^2}$.
For TE$_{101}$ mode, $f_r = 3$ GHz $= 3 \times 10^9 = \dfrac{3\times10^{10}}{2\sqrt{2.5}}\sqrt{\dfrac{1}{25} + \dfrac{1}{d^2}}$.
Or, $\sqrt{\dfrac{1}{25} + \dfrac{1}{d^2}} = \dfrac{\sqrt{2.5}}{5}$.
Or, $\dfrac{1}{25} + \dfrac{1}{d^2} = \dfrac{2.5}{25}$ or, $\dfrac{1}{d^2} = \dfrac{1.5}{25}$.
Or, $d^2 = \dfrac{25}{1.5}$ or, d $= 4.08$ cm.
So the length of the resonator should be 4.08 cm.

11.2 Cylindrical Cavity Resonator

It is made of a circular waveguide where both ends are shorted by a metallic wall along the z-axis at $z = 0$ and $z = d$ (Fig. 26). At resonant frequency total electrical energy

stored equals to the total stored magnetic energy. The transverse modes supported by cavity resonators are the TE and TM modes.

The transverse component of the electric field can be written as,

$$E_t(x, y, z) = \hat{e}(x, y)\left\{A^+ e^{-j\beta}_{mnZ} + A^- e^{+j\beta}_{mnZ}\right\}$$

Putting boundary condition $E_t = 0$ for $z = 0$;
We have, $\hat{e}(x, y)\{A^+ + A^-\} = 0$;

$$\text{Or,} \quad \{A^+ + A^-\} = 0; \quad \text{so,} \quad A^+ = -A^- \tag{73}$$

Second boundary condition is $E_t = 0$ for $z = d$;
Or, $\hat{e}(x, y)\left\{A^+ e^{-j\beta}_{mn} d + A^- e^{+j\beta}_{mn} d = 0\right\}$;

Or, $\left\{A^+ e^{-j\beta}_{mn} d + A^- e^{+j\beta}_{mn} d\right\} = 0$;

Or, $\left\{A^+ e^{-j\beta}_{mn} d - A^+ e^{+j\beta}_{mn} d\right\} = 0$ [using Eq. (72)].

Or, $A^+\left[-2j \ \sin(\beta_{mn}d)\right] = 0$ $\left[\text{as } \frac{e^{jx}-e^{-jx}}{2j} = \sin(x)\right]$.

That implies, $\quad \beta_{mn}d = p\pi$.

Or, $\quad \beta_{mn} = \frac{p\pi}{d}$.

So, for TE mode $\beta_{mn} = \frac{p\pi}{d}$ where $p = 1, 2, 3, \ldots\ldots$

And for TM mode $\beta_{mn} = \frac{p\pi}{d}$ where $p = 0, 1, 2, \ldots$

$$\text{Now,} \quad \beta_{mn} = \sqrt{K^2 - \left(\frac{X_{mn}}{\rho}\right)^2} \tag{74}$$

Dominant mode to be transmitted here is TE_{101} and TM_{010}.
The resonant frequency can be given as,

Fig. 26 Cylindrical cavity resonator
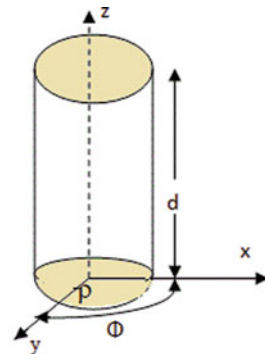
Cylindrical Cavity Resonator

Table 1 Order Zero X_{mn} for $J_n(x)$: (TM mode)

n	m					
	0	1	2	3	4	5
1	2.405	3.832	5.136	6.380	7.588	8.771
2	5.520	7.016	8.417	9.761	11.065	12.339
3	8.654	10.173	11.620	13.01	14.372	
4	11.792	13.324	14.796			

Table 2 Order Zero X'_{mn} for $J'_n(x)$: (TE mode)

n	m					
	0	1	2	3	4	5
1	3.832	1.841	3.054	4.201	5.317	6.416
2	7.016	5.331	6.706	8.015	9.282	10.520
3	10.173	8.536	9.969	11.346	12.682	13.987
4	13.324	11.706	13.170			

$$f'_{mnp} = \frac{1}{2\pi\sqrt{\mu\varepsilon}}\sqrt{\left(\frac{X'_{mn}}{\rho}\right)^2 + \left(\frac{p\pi}{d}\right)^2} \quad \text{for TE mode} \tag{75}$$

$$f_{mnp} = \frac{1}{2\pi\sqrt{\mu\varepsilon}}\sqrt{\left(\frac{X_{mn}}{\rho}\right)^2 + \left(\frac{p\pi}{d}\right)^2} \quad \text{for TE mode} \tag{76}$$

Here the values of X_{mn} can be determined from Bessel function values. The following two tables (Tables 1 and 2) can be used to determine the same for TM as well as TE mode.

11.3 Applications

- As microwave sensors
- Microwave oscillator
- Amplifier
- Wave meter
- Band pass filter at microwave frequency.

Illustrative Example 12: A circular cavity resonator having a diameter of 14 cm and length of 6 cm. Determine the resonant frequency if the resonator is operating at TM_{012} mode.

Solution: The resonant frequency of the circular waveguide can be given as,

$$f_{mnp} = \frac{1}{2\pi \sqrt{\mu\varepsilon}} \sqrt{\left(\frac{X_{mn}}{\rho}\right)^2 + \left(\frac{p\pi}{d}\right)^2} = f_{mnp} = \frac{c}{2\pi} \sqrt{\left(\frac{X_{mn}}{\rho}\right)^2 + \left(\frac{p\pi}{d}\right)^2}$$

For TM_{012} mode $f_r = \frac{c}{2\pi} \sqrt{\left(\frac{X_{01}}{7}\right)^2 + \left(\frac{2\pi}{6}\right)^2}$ D = 14 cm; $\rho = \frac{14}{2} = 7$ cm
  $X_{01} = 2.405$ for m = 0, n = 1; for TM mode (See table given above)

$$f_r = \frac{3x\,10^{10}}{2\pi} \sqrt{\left(\frac{2.405}{7}\right)^2 + \left(\frac{2\pi}{6}\right)^2} = 5.26\,\text{GHz}$$

Illustrative Example 13: A circular waveguide cavity resonator has a radius of 5 cm and operating at TM011 mode. Determine the length of the resonator if it has to resonate at 12 GHz.

Solution: Given that $\rho = 5$ cm; $f_r = 12$ GHz.

  Resonant frequency can be calculated as, $f_r = \frac{c}{2\pi} \sqrt{\left(\frac{X_{mn}}{\rho}\right)^2 + \left(\frac{p\pi}{d}\right)^2}$.

  For TM_{011} mode $X_{01} = 2.405$ (See table of Bessel function above for TM mode), and p = 1.

  So, $f_{011} = \frac{3\times 10^{10}}{2\pi} \sqrt{\left(\frac{2.405}{5}\right)^2 + \left(\frac{\pi}{d}\right)^2} = 12 \times 10^9$

  Or, $\sqrt{\left(\frac{2.405}{5}\right)^2 + \left(\frac{\pi}{d}\right)^2} = \frac{2\pi \times 12 \times 10^9}{3 \times 10^{10}} = 2.51$

  Or, $\left(\frac{\pi}{d}\right)^2 = 6.069$

  Or, d = 1.275 cm

  So the length should be 1.275 cm.

Illustrative Example 14: A cylindrical waveguide providing the same resonant frequency for TE as well as TM mode. Comment on the lowest possible mode of operation.

Solution: We know that the resonant frequency of circular waveguide,

$$f'_{mnp} = \frac{c}{2\pi} \sqrt{\left(\frac{X'_{mn}}{\rho}\right)^2 + \left(\frac{p\pi}{d}\right)^2} \quad \text{for TE mode}$$

where m = 0,1,2,3..;   n = 1,2,3,..;   and   p = 1,2,3,...;

$$f_{mnp} = \frac{c}{2\pi} \sqrt{\left(\frac{X_{mn}}{\rho}\right)^2 + \left(\frac{p\pi}{d}\right)^2} \quad \text{for TE mode}$$

where m = 0,1,2,3..;   n = 1,2,3,..;   and   p = 0,1,2,3,...;
  As per the problem statement $f_{mnp} = f'_{mnp}$.

So, $\frac{c}{2\pi}\sqrt{\left(\frac{X_{mn}}{\rho}\right)^2 + \left(\frac{p\pi}{d}\right)^2} = \frac{c}{2\pi}\sqrt{\left(\frac{X'_{mn}}{\rho}\right)^2 + \left(\frac{p\pi}{d}\right)^2}.$

As the resonator is same, all the parameters like radius (ρ) and length (d) are same.

So the above condition must be satisfied if and only if $X_{mn} = X'_{mn}$ and a suitable value of p is chosen. From the above table of Bessel function, it can be easily observed that $X_{mn} = X'_{mn}$ satisfies under the condition given below.

$X_{10} = X'_{01} = 3.832; X_{12} = X'_{02} = 7.016; X_{13} = X'_{03} = 10.173;$

and $X_{14} = X'_{04} = 13.324$ (Please refer table given above).

So the lowest ever value is $X_{10} = X'_{01} = 3.832$ and if p $= 1$ for both of the cases. Hence the mode of operation is TM$_{101}$ and TE$_{011}$.

Here p can never be zero for TE mode so TE$_{010}$ mode is not possible.

Very similar pattern can be observed for the higher order modes where $X_{mn} = X'_{mn}$. As per example $X_{12} = X'_{02} = 7.016$, $X_{13} = X'_{03} = 10.173$ and $X_{14} = X'_{04} = 13.324$ etc.

Problems

1. When input power is divided in the ratio of 2:1 in a T- junction coupler and the characteristic impedance of the two output lines is 150Ω and 75Ω, calculate the impedance of the input line.

2. If a signal of power 32 mW is fed into one of the collinear arm of a H-plane Tee. Determine the power that appears at all the ports when ports are terminated by matched load.

3. Design a lossless T-junction signal divider with a 80 Ω source impedance to give a 3:1 power split. Design quarter-wave matching transformers to convert the impedances of the output lines to 80 Ω. Determine the magnitude of the scattering parameters for this circuit, using a 80 Ω characteristic impedance.

4. An E-plane Tee made of waveguide section of 50Ω characteristics impedance. A signal power of 20 mW is applied to E-arm which is perfectly matched. Determine the power delivered to the load of 60Ω and 75Ω connected to port1 and port2 respectively.

5. If 500 mW power is applied to the perfectly matched port3 of a magic Tee, what will be the power delivered to port1, port2 and port4 if it is terminated by a reflection of 0.4, 0.6 and 0.7 respectively?

6. Two couplers with identical natures are used in a waveguide to sample the incident power of 10 mW and reflected power as 0.20 mW. What will be the value of VSWR?

7. Two 20 dB identical directional couplers are used to sample incident and reflected power in a waveguide. Voltage standing wave ratio is 1.5 and the output of the coupler sampling incident power is 8 mW. Calculate the value of the reflected power.

8. A directional coupler has the scattering matrix given below. Find the return loss, coupling factor, directivity, and insertion loss. Assume that all ports are terminated by matched load.

$$S = \begin{bmatrix} 0.1\angle 30° & 0.9\angle 90° & 0.18\angle 180° & 0.005\angle 90° \\ 0.9\angle 90° & 0.1\angle 30° & 0.005\angle 90° & 0.18\angle 180° \\ 0.18\angle 180° & 0.005\angle 90° & 0.1\angle 30° & 0.9\angle 90° \\ 0.005\angle 90° & 0.18\angle 180° & 0.9\angle 90° & 0.1\angle 30° \end{bmatrix}$$

9. A 20 dBm power source is connected to the input of a directional coupler having a coupling factor of 20 dB, a directivity of 35 dB, and an insertion loss of 0.5 dB. If all ports are matched, find the output powers (in dBm) at the through, coupled, and isolated ports.

10. Two 40 dB directional couplers with identical properties are used for sampling incidents and reflected power in a waveguide. The value of VSWR is 7 and the output of the coupler sampling incident power is 5 mw. Find the reflected power.

11. Design a single-section coupler with coupled line having a coupling of 19 dB, a system impedance of 60 Ω, and a center frequency of 8 GHz. If the coupler is to be made in strip line (edge-coupled), with r = 2.2 and b = 0.32 cm, find the necessary strip widths and separation.

12. A four port directional coupler has a 4:1 power splitting ratio and has a dissipation loss of 3 dB. The coupler directivity is 40 dB. What fraction of input power P_1 will go to port P_2 (output port) and P_3 (coupled port)?

13. Design a field displacement isolator in an X-band waveguide to operate at 11 GHz. The ferrite has 4π Ms = 2500 G and r = 13. Ignore ferrite losses.

14. A thin ferrite rod with 4π Ms = 600 G is magnetically biased along its axis. Find the external bias field strength required to produce a gyro-magnetic resonance at 2.52 GHz.

15. A lossless circulator having a return loss of 12 dB. Find the value of isolation? What will be the isolation if the return loss changes to 24 dB?

16. A two-port is known to have the following scattering matrix:

$$[S] = \begin{bmatrix} 0.15\angle 0° & 0.85\angle -45° \\ 0.85\angle 45° & 0.2\angle 0° \end{bmatrix}$$

Determine if the network is reciprocal and lossless. If port2 is terminated by matched load, then what is the return loss seen at port1?

17. A circular waveguide, filled with air, has a radius of 3 cm and is acting as a resonator for TE_{01} mode at 10 GHz by placing two perfectly conducting plates at its two ends. Determine the minimum distance between the two end plates.

18. A rectangular cavity resonator has dimensions of a = 5 cm, b = 2 cm, and d = 15 cm. Compute:

   a. The resonant frequency of the dominant mode for an air-filled cavity
   b. The resonant frequency of the dominant mode for a dielectric-filled cavity of ε_r = 2.56

19. Determine the lowest resonant frequency of a rectangular cavity resonator having dimensions 4 cm × 5 cm × 6 cm. Also find the change in length required to have a resonant frequency of 1.2 times than earlier one.
20. Calculate the resonant frequency for TE_{111} mode of a rectangular cavity resonator of dimension 6 cm × 5 cm × 4 cm. What will be the new resonant frequency if the cavity is filled with a dielectric of $\varepsilon_r = 4$?
21. A rectangular waveguide cavity resonator filled with dielectric $\varepsilon_r = 2.2$ and having a cross section of 4 cm × 3 cm. Find the length of the cavity resonator required to have the resonant frequency of 3 GHz at dominant TE_{101} mode.
22. A circular cavity resonator having diameter of 12 cm and length of 5 cm. Determine the resonant frequency if the resonator is operating at TM_{012} mode.
23. A circular waveguide cavity resonator has a radius of 6 cm and operating at TM011 mode. Determine the length of the resonator if it has to resonate at 10 GHz.
24. A circular waveguide providing same resonant frequency for TE as well as TM mode. Comment on all possible modes of operation.

References

1. Pozar DM (2012) Microwave engineering. Wiley, Hoboken, NJ
2. Rizzi PA (1988) Microwave engineering: passive circuits. Prentice Hall
3. Cohn SB (1968) Microwave band pass filters containing high-q dielectric resonators. IEEE Trans Microw Theory Tech 16:218–227
4. Bailey AE (ed) (1985) Microwave measurement. Peter Peregrinus, London
5. Montgomery CG, Dicke RH, Purcell EM (1948) Principles of microwave circuits, MIT radiation laboratory series, vol 8. McGraw-Hill, New York
6. Collin RE (2001) Foundations for microwave engineering, 2nd edn. Wiley–IEEE Press, Hoboken, N. J
7. Heaviside O (1950) Electromagnetic theory, vol 1, 1893. Reprinted by Dover. New York

Impact of Negative Bottom Gate Voltage for Improvement of RF/Analog Performance in Asymmetric Junctionless Dual Material Double Gate MOSFET

Arighna Basak, Arpan Deyasi, and Angsuman Sarkar

Abstract Research on double-gate MOSFET has already exhibited several novel solutions of existing problems like reducing leakage current or short-channel effect. For both long-channel structure or microscopic devices, the role of the bottom-gate becomes more critical for making higher ON-to-OFF current ratio, and therefore, individual-gate architecture becomes more popular than tied-gate architecture owing to the possibility of individual tuning. Junctionless devices come into the limelight due to better mobility control than the other DG configurations, and considered the subject of investigation in the last few years. The current chapter investigates the effect of negative bottom gate voltage on the analog and RF performances of Asymmetric Junctionless Dual Material Double Gate (AJDMDG) MOSFET. TCAD device simulator was used to investigate the effect of negative bottom gate voltage on analog and RF parameters. The results show that utilizing a low value of the work function of the bottom gate terminal improved the analog and RF performance.

1 Introduction

Due to the growing use of lower frequency bands, higher frequency utilization has become mandatory as a result of new innovations in the field of communication.

A. Basak
Department of Electronics and Communication Engineering, Brainware University, Barasat 700125, India
e-mail: arighnabsk060891@gmail.com

A. Deyasi (✉)
Department of Electronics and Communication Engineering, RCC Institute of Information Technology, Kolkata 700015, India
e-mail: deyasi_arpan@yahoo.co.in

A. Sarkar
Department of Electronics and Communication Engineering, Kalyani Government Engineering College, Kalyani 741235, India
e-mail: angsumansarkar@ieee.org

As a result of its destructive downscaling capabilities and requirement for high frequency management competency that spreads up to multiple Giga hertz (GHz) range, MOSFET devices have been popular in recent years for communication or wireless applications. However, MOSFET devices face the most significant hurdles in device manufacturing due to unwanted short channel effects (SCEs) caused by continual downscaling [1–3]. As a result, new device architectures such as double gate (DG) MOSFETs, junctionless MOSFETs [4–8], Surrounding gate MOSFETs [9], Dual Material Double Gate MOSFET (DMDG MOSFET), junctionless DMDG MOSFETs [10, 11], and asymmetric DMDG MOSFET [12] have become necessary for future device technology to alleviate these undesirable SCEs. AJDMDG Stack MOSFET device topology is one of the most successful candidates for suppressing SCEs among various possibilities.

Major work on long-channel double gate structure is pioneered by Taur [13, 14] and thereafter Ortiz-Conde [15, 16] at the beginning of this decade followed by several works that were reported on independent-gate structures with hetero-interfaces [17–19] for investigating surface potential variation. A few modified computational models are also proposed later for incorporating quantum effect [20, 21] with the ultrathin structure, and the corresponding transconductance and differential conductance [22] provide better characteristics.

Moreover, numerous researchers study the analog/RF performance of various topologies for communication and wireless applications, such as DG MOSFETs [23, 24], junctionless MOSFETs [25], SRG MOSFETs [26], DMDG MOSFETs [27–33], Ultrathin ID-DG FET [34–36], Surrounding gate MOSFETs [37, 38] and so on. These advanced architectures provide superior gate control as evident through a comparative analysis with an identical single-gate structure [39, 40].

An explicit analytical model of surface potential, field distribution, threshold roll-off and drain current for AJDMDG MOSFETs was created in Ref. [28], where the device structure integrates the benefits of junctionless, DMDG structure, asymmetry condition and high dielectric material. Because of the asymmetric oxide thickness and work function of the gate terminal, the AJDMDG MOSFET has lower SCEs and better device performance. In addition, the effect of the work function of the bottom gate on analog and RF characteristics of the AJDMDG MOSFET, such as intrinsic gain, f_{max} and f_T asymmetry was employed to lower intrinsic gain, enhance f_T, f_{max} and GBW, although investigated. As a result, the influence of negative bottom gate voltages on analog and RF performance has been explored in this chapter, and the analog and RF performance of the AJDMDG MOSFET structure has been enhanced further. As a result, the goal of this chapter is to look at how negative bottom gate voltages affect the RF and analog performances of the mentioned structure.

2 Device Structure and Simulation Setup

The 2-D construction of the AJDMDG MOSFET is exposed in Fig. 1. For this structure, in region I and region II, the work functions of the material present in the
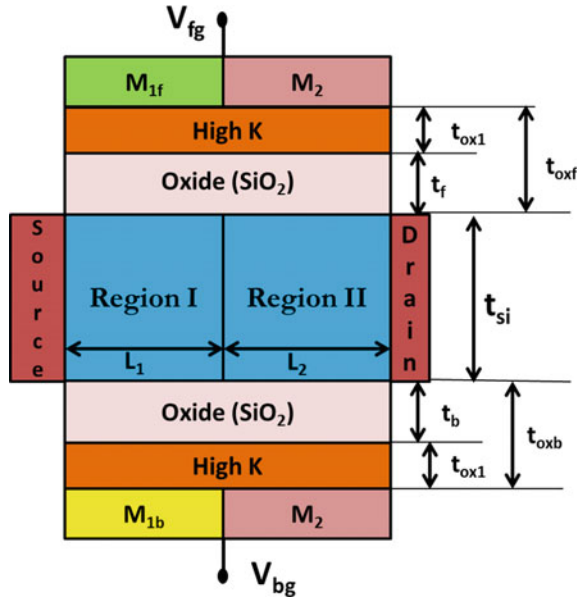
gate terminals are $\phi_{M1f} = 4.9$ eV, $\phi_{M2} = 4.5$ eV, $\phi_{M1b} = 4.0$ eV, respectively. The concentration of carriers is 3×10^{19} cm^{-3} Moreover, for this structure the value of t_{si} (channel thickness), t_{oxf} (effective oxide thickness of top gate), t_{oxb} (effective oxide thickness of bottom gate) are 10 nm, 1.1 nm and 2.1 nm, respectively.

TCAD Device Simulator [42] was used for this project. To study carrier transport, the Fermi–Dirac statistic model and a Drift diffusion were employed in simulation. The Shockley–Read–Hall (SRH) recombination model was merged with the Auger recombination model for the carrier recombination model [43]. Numerical solutions and differential equations were solved using the Newton and Gummel techniques [44]. For the quantum effect, the quantum density gradient model [45] was utilized.

3   Result and Discussion

The influence of negative values of bottom gate voltages on drain current (I_D) of AJDMDG MOSFET is shown in Fig. 2. It is depicted from Fig. 2 that I_D increases significantly for more negative values of the bottom gate voltage due to rise in carrier transport efficacy. Furthermore, Fig. 2 distinctly shows that reducing the value of bottom gate voltages enhances the ON state current, with greater ON current attained for $V_{bg} = -1.5$ V.

Figure 3 depicts the transconductance (g_m) of AJDMDG MOSFET at various negative V_{bg}. At a constant V_{DS}, transconductance is well-defined as

Fig. 2 Graphical variation of drain current (I_D) with V_{fg} for different negative values of V_{bg}
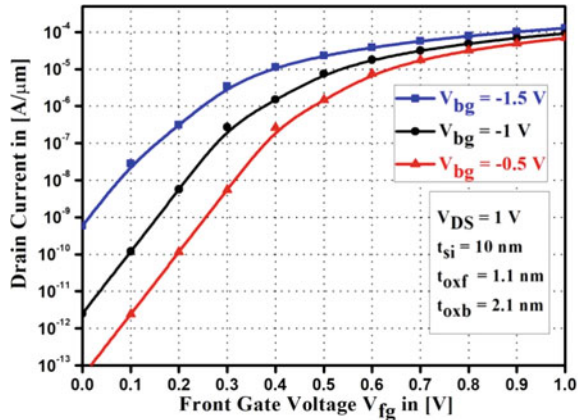
$$g_m = \frac{\partial I_D}{\partial V_{fg}} \tag{1}$$

Figure 3 illustrates that a drop in V_{bg} results in a high value of g_m.

Figure 4 depicts the TGF of an AJDMDG MOSFET for various negative V_{bg} values. TGF drops at lower values of V_{bg} as seen in the graph, with a smaller value of TGF achieved at $V_{fg} = 0.5$ V for $V_{bg} = -1.5$ V. As a result, TGF improves in terms of lowering negative V_{bg} values.

Figure 5 depicts the r_{out} of an AJDMDG MOSFET for various negative values of V_{bg}. This device's gain is evaluated using rout. According to Fig. 5, the value of rout lowers with negative values of V_{bg}, indicating an improvement in the device structure's driving capabilities. As a result, a lower rout value suggests greater analog performance.

Fig. 3 Plot of g_m with respect to the value of V_{fg} of AJDMDG MOSFET for various negative values of V_{bg}

Fig. 4 Plot of TGF with respect to the value of V_{fg} of AJDMDG MOSFET for various negative values of V_{bg}

Fig. 5 Plot of r_{out} with respect to the value of V_{fg} of AJDMDG MOSFET for various negative values of V_{bg}

Figure 6 depicts the intrinsic gain of an AJDMDG MOSFET for various negative values of V_{bg}. The product of g_m and r_{out} is clearly characterized as an intrinsic gain. The value of gain decreases as the negative values V_{bg} grow, and a lower gain for $V_{bg} = -1.5$ V indicates a higher analog performance.

The cut-off frequency (f_T), maximum frequency of oscillation (f_{max}) and gain bandwidth product (GBW) are significant factors for analyzing RF performance. The frequency at which the short circuit gain equals one is termed as the cut-off frequency [9, 41].

$$f_T = \frac{g_m}{2\pi(C_{GD} + C_{GS})} \tag{2}$$

where CGD and CGS are capacitance in gate-drain and gate-source regions.

Fig. 6 Plot of intrinsic gain with respect to the value of V_{fg} of AJDMDG MOSFET for various negative values of V_{bg}
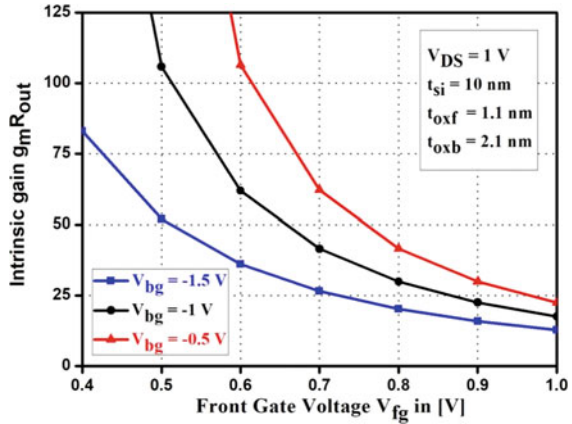
Figure 7 represents the effect of negative V_{bg} values on the cut-off frequency of an AJDMDG MOSFET. Figure 7 shows that at $V_{bg} = -1.5$ V, a higher f_T is produced. As a result, raising the negative values of V_{bg} improves f_T, as seen in Fig. 7.

f_{max} is characterized as [9, 41]

$$f_{max} = \frac{g_m}{2\pi C_{GS}\sqrt{4\left(g_{DS} + g_m \frac{C_{GD}}{C_{GS}}\right)(R_i + R_S + R_g)}} \tag{3}$$

whereas gate resistance (R_g) is 2.6 kΩ for a 20 nm thick molybdenum metal gate, R_i equals 20Ω and R_S equals 160 Ω.

Figure 8 represents the effect of negative V_{bg} values on the f_{max} of an AJDMDG MOSFET. According to Fig. 8, increasing the negative values of V_{bg} causes a rise in f_{max}, with a larger value of f_{max} found for $V_{bg} = -1.5$ V.
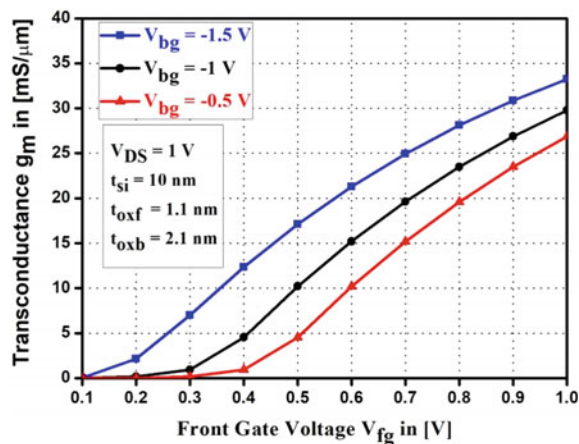
Fig. 7 Plot of f_T with respect to the value of V_{fg} of AJDMDG MOSFET for various negative values of V_{bg}
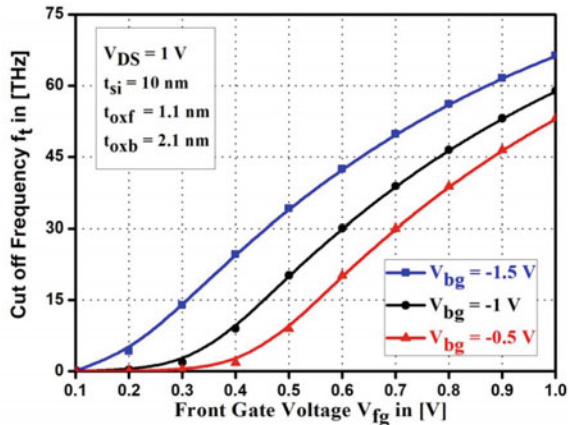
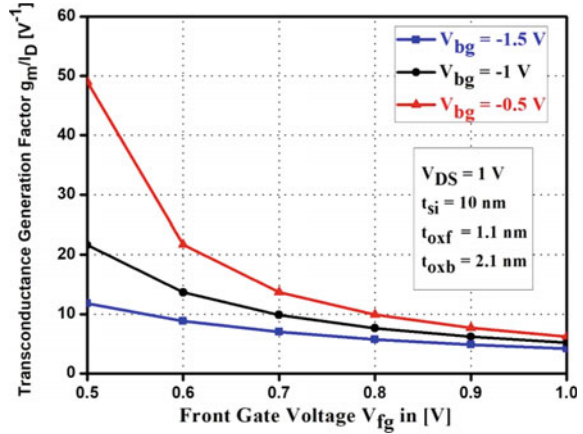**Fig. 8** Plot of f_{max} with respect to the value of V_{fg} of AJDMDG MOSFET for various negative values of V_{bg}
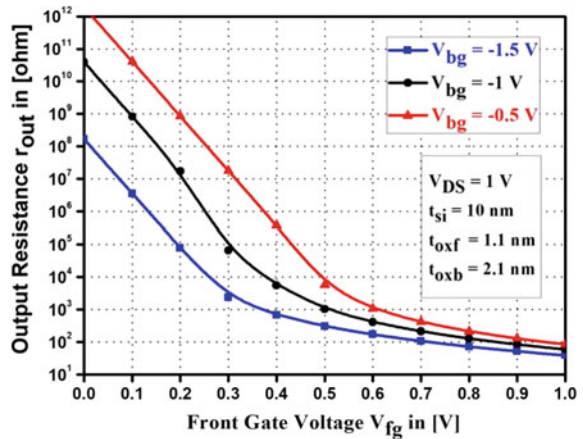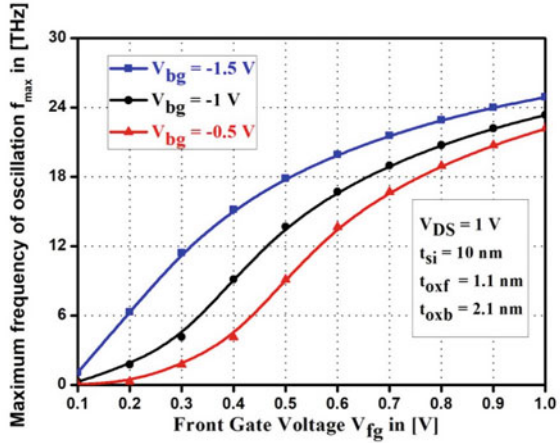
GBWt is characterized as [9, 41]

$$GBW = \frac{g_m}{20\pi C_{GD}} \qquad (4)$$

Figure 9 represents the effect of negative V_{bg} values on the GBW of an AJDMDG MOSFET. According to Fig. 9, a greater value of GBW is achieved when $V_{bg} = -1.5$ V.

Lower values of V_{bg} are required for circuit application reasons as a consequence of the analog and RF analyses.

Fig. 9 Plot of GBW with respect to the value of V_{fg} of AJDMDG MOSFET for various negative values of V_{bg}
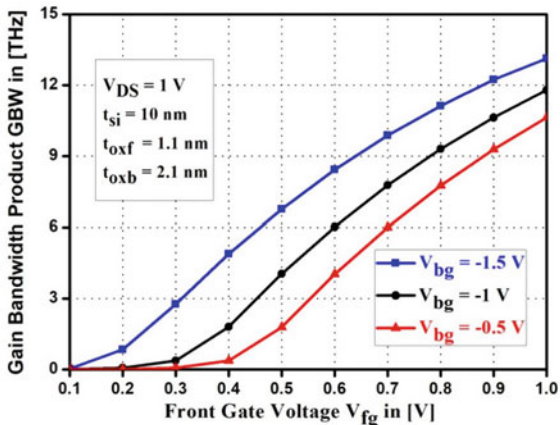
4 Summary

TCAD simulator is used to conduct a simulation investigation of the influence of negative bottom gate voltages on the analog and RF performance of AJDMDG MOSFETs. The simulation findings demonstrate that raising the negative values of V_{bg} can improve g_m, r_{out}, $g_m r_{out}$ and TGF. Furthermore, at $V_{bg} = -1.5$ V, the values of f_T, fmax and GBW are superior. As a result, a negative bottom gate voltage is appropriate for improving the analog and RF performance and is employed in wireless or communication applications.

References

1. International technology roadmap for semiconductors 2009 Edition and 2010 Update. http://www.itrs.net. Accessed 2018
2. Mohsenifar S, Shahrokhabadi MH (2015) Gate stack high-κ materials for Si-based MOSFETs past, present, and futures. Microelectron Solid State Electron 4:12–24
3. Datta S (2013) Recent advances in high performance CMOS transistors: from planar to non-planar. Electrochem Soc Interfac 22:41–46. https://doi.org/10.1149/2.F04131if
4. Chiang TK (2016) A short-channel-effect-degraded noise margin model for junctionless double-gate MOSFET Working on subthreshold CMOS logic gates. IEEE Trans Electron Devices 63
5. Hong S (2019) Compact charge modeling of double-gate MOSFETs considering the density-gradient equation. IEEE J Electron Devices Soc 7
6. Xie Q, Wang Z, Taur Y (2017) Analysis of short-channel effects in junctionless DG MOSFETs. IEEE Trans Electron Devices 64:3511–3514
7. Gnudi A, Reggiani S, Gnani E, Baccarani G (2013) Semianalytical model of the subthreshold current in short-channel junctionless symmetric double-gate field-effect transistors. IEEE Trans Electron Devices 60:1342–1348
8. Bari S, De D, Sarkar A (2015) Effect of gate engineering in JLSRG MOSFET to suppress SCEs: an analytical study. Physica E Low-dimens Syst Nanostruct 67:143–151
9. Biswal SM, Baral B, De D, Sarkar A (2015) Analytical subthreshold modeling of dual material gate engineered nano-scale junctionless surrounding gate MOSFET considering ECPE. Superlattices Microstruct 82:103–112
10. Reddy GV, Kumar MJ (2005) A new dual-material double-gate (DMDG) nanoscale SOI MOSFET-two-dimensional analytical modeling and simulation. IEEE Trans Nanotechnol 4:260–268
11. Singh J, Gadi V, Kumar MJ (2016) Modeling a dual-material-gate junctionless FET under full and partial depletion conditions using finite-differentiation method. IEEE Trans Electron Devices 63:2282–2287
12. Kumari V, Modi N, Saxena M, Gupta M (2015) Theoretical investigation of dual material junctionless double gate transistor for analog and digital performance. IEEE Trans Electron Devices 62:2098–2105
13. Taur Y (2000) An analytical solution to a double-gate MOSFET with undoped body. IEEE Electron Device Lett 21(5):241–247
14. Taur Y (2001) Analytic solutions of charge and capacitance in symmetric and asymmetric double-gate MOSFETs. IEEE Trans Electron Devices 48(12):2861–2869
15. Ortiz-Conde A, Garcia-Sanchez FJ, Muci J (2005) Rigorous analytic solution for the drain current of undoped symmetric dual-gate MOSFETs. Solid State Electron 49(4):640–647

16. Ortiz-Conde A, García-Sánchez FJ, Muci J, Malobabic S, Liou JJ (2007) A review of core compact models for undoped double-gate SOI MOSFETs. IEEE Trans Electron Devices 54(1):131–140

17. Roy K, Chowdhury AR, Deyasi A, Sarkar A (2019) Computing surface potential and drain current in nanometric double-gate MOSFET using Ortiz-Conde model. In: Advances in intelligent systems and computing book serie: contemporary advances in innovative and applicable information technology, vol 812, pp 41–47

18. Chakraborty D, Bhowmick S, Deyasi A (2018) Computing surface potential of double gate MOSFET for both free and doped carrier concentrations. In: IEEE 2nd international conference on electronics, materials engineering & nano-technology, Kolkata, India, pp 1–4

19. Nath A, Khanam F, Mukhopadhyay S, Deyasi A (2021), Surface potential computation for asymmetric Si–Si1−xGex ID-DG MOSFET following Ortiz-Conde model. In: Lecture notes in electrical engineering: nanoelectronics, circuits and communication systems, vol 692, pp 239–246

20. Vimala P, Balamurugan NB (2012) Quantum mechanical compact modeling of symmetric double-gate MOSFETs using variational approach. J Semicond 33(3):034001

21. Deyasi A, Chowdhury AR, Roy K, Sarkar A (2018) Effect of high-K dielectric on drain current of ID-DG MOSFET using Ortiz-Conde model. In: IEEE electron devices Kolkata conference, pp 176–181

22. Chakraborty R, Mondal D, Deyasi A (2020) Investigating effect of structural parameters on static characteristics of ultrathin DG MOSFET using Taur's model. In: Lecture notes in networks and systems: information, photonics and communication, vol 79, Chapter 2, pp 11–19

23. Biswas K, Sarkar A, Sarkar CK (2015) Impact of barrier thickness on Analog, RF and Linearity performance of nanoscale DG heterostructure MOSFET. Superlattices Microstruct 86:95–104

24. Sarkar A, Sarkar CK (2013) RF and analogue performance investigation of DG tunnel FET. Int J Electron Lett 1:210–217

25. Biswas K, Sarkar A, Sarka CK (2018) Fin shape influence on analog and RF performance of junctionless accumulation-mode bulk FinFETs. Microsyst Technol 24:2317–2324

26. Sarkar A, De S, Dey A, Sarkar CK (2011) A new analytical subthreshold model of SRG MOSFET with analogue performance investigation. Int J Electron 99:267–283

27. Basak A, Chanda M, Sarkar A (2019) Drain current modelling of unipolar junction dual material double-gate MOSFET (UJDMDG) for SoC applications. Microsyst Technol 27(11):3995–4005

28. Koley K, Syamal B, Kundu A, Mohankumar N, Sarkar CK (2012) Subthreshold analog/RF performance of underlap DG FETs with asymmetric source/drain extensions. Microelectron Reliab 52:2572–2578

29. Koley K, Dutta A, Syamal B, Saha SK, Sarkar CK (2013) Subthreshold analog/RF performance enhancement of underlap DG FETs with high- K spacer for low power applications. IEEE Trans Electron Devices 60:63–69

30. Chebaki E, Djeffal F, Hichem F, Bentrcia T (2016) Improved analog/RF performance of double gate junctionless MOSFET using both gate material engineering and drain/source extensions. Superlattices Microstruct 92:80–91

31. Sharma RK, Bucher M (2012) Device design engineering for optimum analog/RF performance of nanoscale DG MOSFETs. IEEE Trans Nanotechnol 11:992–998

32. Roy NC, Gupta A, Rai S (2015) Analytical surface potential modeling and simulation of junctionless double gate (JLDG) MOSFET for ultra-low-power analog/RF circuits. Microelectron J 46:916–922

33. Ghosh D, Pariha MS, Armstrong GA, Kranti A (2012) High-performance junctionless MOSFETs for ultralow-power analog/RF applications. IEEE Electron Device Lett 33:1477–1479

34. Deyasi A, Sarkar A, Roy K, Chowdhury AR (2021) Effect of high-K dielectric on differential conductance and transconductance of ID-DG MOSFET following Ortiz-Conde model. Microsyst Technol 27(11):3967–3975

35. Deyasi A, Chakraborty R, Mondal D, Pramanik N, Mukhopadhyay S (2021) Analytical investigation of transconductance and differential conductance of ultrathin ID-DG MOSFET with gradual channel approximation. In: Lecture notes in electrical engineering: fifth international conference on microelectronics, computing and communication systems, vol 748, pp 117–126
36. Mukhopadhyay S, Ray P, Deyasi A (2020) Computing gate asymmetric effect on drain current of DG-MOSFET following Ortiz-Conde model. In: IEEE national conference on emerging trends on sustainable technology and engineering applications, pp 1–5
37. Sarkar A, De S, Dey A et al (2012) Analog and RF performance investigation of cylindrical surrounding-gate MOSFET with an analytical pseudo-2D model. J Comput Electron 11:182–195
38. Sarkar A (2014) Study of RF performance of surrounding gate MOSFET with gate overlap and underlap. Adv Natl Sci Nanosci Nanotechnol 5
39. Bhowmick S, Chakraborty D, Deyasi A (2017) Computation of electrical parameters for single-gate high-K nanoscale MOSFET with cylindrical geometry. In: Advances in intelligent systems and computing: international conference on modelling and simulation, vol 749, pp 47–53
40. Deyasi A, Mukherjee S, Bhattacharjee AK, Sarkar A (2020) Classification of single and double-gate nanoscale MOSFET with different dielectrics from electrical characteristics using soft computing techniques. Int J Inf Technol 12(1):165–174
41. Basak A, Sarkar A (2020) Impact of back gate work function for enhancement of analog/RF performance of AJDMDG Stack MOSFET. Solid State Electron Lett 2:117–123
42. Abdullah G (2015) ATLAS device simulation software, Santa Clara, CA, USA
43. Goudan T, Miljanović V, Schmeiser C (2006) On the Shockley-Read-Hall model: generation-recombination in semiconductors. SIAM J Appl Math
44. Ringhofer C, Schmeiser C (1989) An approximate newton method for the solution of the basic semiconductor device equations. SIAM J Numer Anal 26:507–516
45. Ferron A, Cottle B, Curatola G, Fiori G, Guichard E (2004) Schrödinger approach and density gradient model for quantum effects modeling. J Process Device Eng

Analog/RF Performance Analysis of GAA-GNR Tunnel Field-Effect Transistor (TFET)

Anuva Ganguly, Jayabrata Goswami, Nitai Paitya, Anirudhha Ghosal, and J. P. Banerjee

Abstract In this paper, we present a gate all round tunneling field-effect transistor (GAA TFET) with graphene nanoribbon (GNR) that improves DC and RF performance. The GAA TFET with GNR (GAA-GNR TFET) has an ultrathin tunneling layer on the source side wall and a 5 nm wavelength GNR layer. The analysis of the GAA-GNR TFET was discussed using computer-aided design (TCAD) simulation technology. Simulations show that the proposed structure provides higher drain currents (Id), steeper mean threshold oscillations, and also very good RF performance. A detailed study of the analog/RF performance parameters includes gate capacitance, conductance (g_m), gain bandwidth product (GBP), transmission time (τ), and cutoff frequency (f_T) of the evaluated device. The TCAD simulation results show the improved DC and analog/RF performance of the proposed GAA-GNR TFET compared to the conventional GAA TFET. Single-port GAA-GNR TFET over 0 V with high ON current density, conductivity (g_m), cut-off frequency (f_T), gain bandwidth product (GBP), and low oscillation frequency the maximum (f_{max}) is 38 μA/μm, 7.8 μs/μm, 96 GHz, 19 GHz, and 16.3 THz when Vgs is equal to 1.2 V.

A. Ganguly
Department of Electronics and Communication Engineering, Dr. Sudhir Chandra Sur Institute of Technology and Sports Complex, 540, Dum Dum Road, Near Dum Dum, Surer Math, Dum Dum, Kolkata 700074, West Bengal, India

J. Goswami (✉)
Netaji Subhas Open University, DD 26, DD Block, Sector 1, Bidhannagar, Kolkata 700064, West Bengal, India
e-mail: goswamijayabrata@gmail.com

N. Paitya
Department of Computer Science and Engineering, Sikkim Manipal Institute of Technology, East Sikkim 737136, India
e-mail: nitai.p@smit.smu.edu.in

A. Ghosal · J. P. Banerjee
Institute of Radio Physics and Electronics, University of Calcutta, 92, APC Road, Kolkata 700009, West Bengal, India

1   Introduction

The tunnel field effect transistor (TFET) could be a semiconductor used at low power yet as high frequency applications largely because the typical metal–oxide–semiconductor field impact transistor (MOSFET) approached the thermal limits. The opposite essential physical limitation of MOSFET is that the short channel effects (SCEs) [1]. The semiconductor nanowire TFET is additionally used as a promising device that has the wonderful gate controlled and extremely influenced electrical behavior to beat the issues caused by short channel effects [2–5] afterward device structures like double-gate (DG), surrounding-gate (SG), gate all around (GAA) and carbon nano tube (CNT) FinFETs and graphene-nano-ribbon (GNR) transistors are researched for breakdown the scaling matter of bulk transistors [6–11]. The key performance parameters of a TFET is that the drain current (Id), and quicker shift speed (ION/IOFF) that is expounded to the sub-threshold slope once the junction transistor operates at low voltage [12] alternative benefits of the TFETs are lower discharge current and better on-current than the MOSFET, higher electricity management, and bar of the short channel effects [13–17]. Thus, the TFETs are gaining quality over MOSFETs within the technology nodes [18] many wonderful article and summary are drained the previous couple of years past, that summarize the TFET [19]. Among these studies, several papers propose a TFET with associate ultrathin tunnel layer at supply sidewall that permits band-to-band tunneling (BTBT) perpendicular to the channel direction (vertical BTBT) [20–27]. It will improve particle yet as sub-threshold swing (SS) with the assistance of an outsized BTBT junction space and a brief tunnel barrier breadth. In this work, we have a tendency to investigate device style and analog/RF performances of the projected transistors with relevance to many key parameters. First, the device constructs, yet because the principle of operation, are mentioned in Section a pair of. Second, simulation results and issues are delineating in Section three. Finally, Section four attracts conclusions by summarizing the engaging properties of the SCNW GNR TFET.

2   Device Composition and Operation

The Si GAA-GNR TFET could be a structure with lower targeted P-type channel between heavily doped supply (p+) and therefore the drain (n+) region. By victimization band-to-band tunneling electronic transistor mechanism, GAA-GNR controls the tunneling between the channel and (source and drain) regions. To realize correct leads to the simulation, non-local band-to-band (BTB) tunneling model, current density model, Shockley–Read–Hall (SRH) recombination model, bandgap narrowing model, and field-dependent quality model have been enclosed for the projected GAA-GNR TFET model. Figure 1 presents the schematic read of GAA-GNR TFET. In distinction to traditional GAA-GNR TFET, a layer of GNR with breadth of 5 nm is incorporated. The intrinsic channel, i.e., tunnel region surrounds

the standard nanowire structure. All the materials of the supply channel and drain are Si. SiO_2 is employed as gate chemical compound. In TCAD simulation, a channel length (L) is ready by 30 nm to exclude short channel impact. The vital style parameters are summarized in Table 1. The simulation technique needs the supply terminals to be grounded (VS = 0 V) for the calculation of BTBT generation rate (G) per unit volume in uniform field of force, K.P. perturbation theory is employed.

The transfer curves are simulated as shown in Fig. 2a (log scale) and Fig. 2b (linear scale) with 0.7V drain to source voltage for GAA TFET and GAA-GNR TFET. The drain current density of GAA-GNR TFET and GAA TFET at 1.2 V V_{gs} are 38 $\mu A/\mu m$ and 30.9 $\mu A/\mu m$, respectively.

The drain current is extracted at 7 V Vds. The applied activate gate to supply voltage Vgs-ON is that the voltage at that the BTBT starts to occur, whereas lateral BTBT is predominant. As Vgs will increase, vertical BTBT starts to occur, at 0.4 V Vgs and at last surpasses the lateral BTBT at 2 V Vgs. The drain current of the projected structure is decoupled into two totally different BTBTs.

Fig. 1 Schematic view of GAA-GNR TFET with GNR
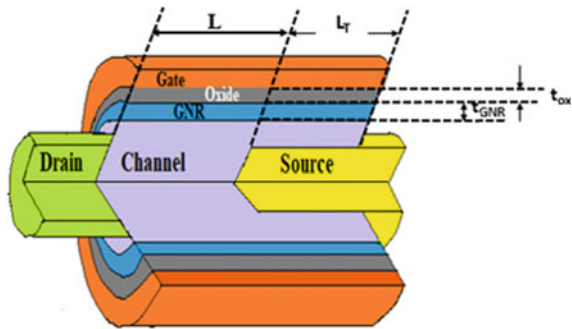
Table 1 GAA-GNR TFET design parameters used for TCAD simulation

Parameters	Value
Source doping concentration, p-type (N_s)	10^{20} cm^{-3}
Drain doping concentration, n-type (N_d)	10^{20} cm^{-3}
Channel doping concentration, p-type (N_{CH})	10^{14} cm^{-3}
Gate work function	4.05 eV
Channel length (L)	30 nm
Gate oxide thickness (t_{ox})	2 nm
Length of tunnel region (L_T)	Variable
Thickness of GNR (t_{GNR})	5 nm
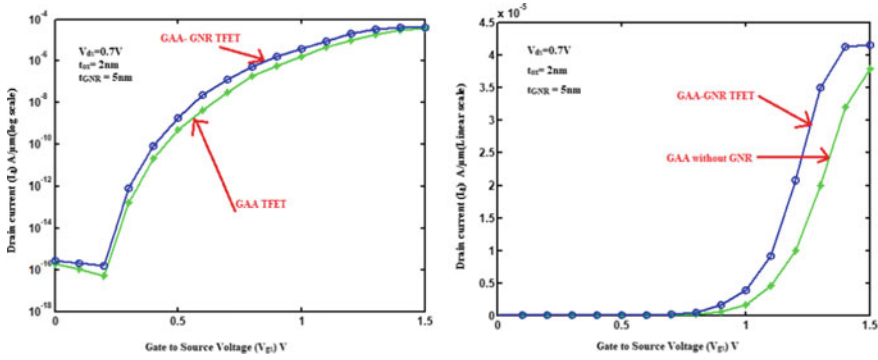
Fig. 2 a $\log(I_d)$ versus V_{gs} curve b I_d versus V_{gs} curve of GAA-GNR TFET

3   Analog/RF Performance Analysis

In this section, we've targeted on the analysis of RF performance parameters during this discussion, that embody transconductance (gm), gate to empty capacitance (Cgd), gate to supply capacitance (Cgs), cut-off frequency (fT), gain information measure product (GBP). The entire parameters area unit is calculated at 1 MHz tiny signal input frequency. All told oftenest figures of deserves, metric weight unit plays a key role to boost the RF performance of the device. Transconductance(gm) is outlined as ability of the device to replicate gate voltage (Vgs) into drain current (Id). The primary order differentiation of drain current (Id) w.r.t. Vgs is thought as metric weight unit as mentioned in equation one. The worth of metric weight unit is set to examine the device speed. The next price of metric weight unit, quicker change response of device [28].

$$g_m = \frac{\partial I_d}{\partial V_{gs}} \tag{1}$$

Figure 3 shows curves for the g variation of the device with individual to Vgs with totally different Vds voltages as 1 V, 0.7 V, and 0.5 V. For the projected structure, Id changes greatly with Vgs, whereas drain current maintains a high price, leading to the next gram. Additionally, it is inferred that gram will increase with the rise of Vgs till it enters the saturation region. The rise of the BTBT generation rate directly ends up in a rise in gram. However, it decreases at higher Vgs because of reduced quality. The gate-gate capacitance is especially composed of 2 capacitances Cgd and metric system, The parasitic capacitances metric system and Cgd is outlined by mathematical expression as equations a pair of and three severally [29].

$$C_{gs} = \frac{\partial Q_s}{\partial V_{gs}} \qquad (2)$$

$$C_{gd} = \frac{\partial Q_s}{\partial V_{gd}} \qquad (3)$$

Equations 2 and 3 play a pivotal role to extract device performance and responsible for parasitic oscillation at various operating frequencies. Figure 4 shows the gate to drain (C_{gd}) and gate to source (C_{gs}) of the device with respect to gate voltage.

Fig. 3 Variation of transconductance (g_m) along V_{gs} of the GAA-GNR TFET
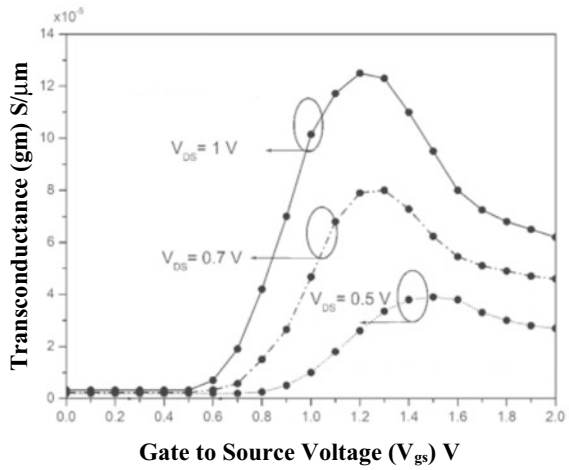
Fig. 4 Analysis of C_{gs} and C_{gd} for different V_{ds} values
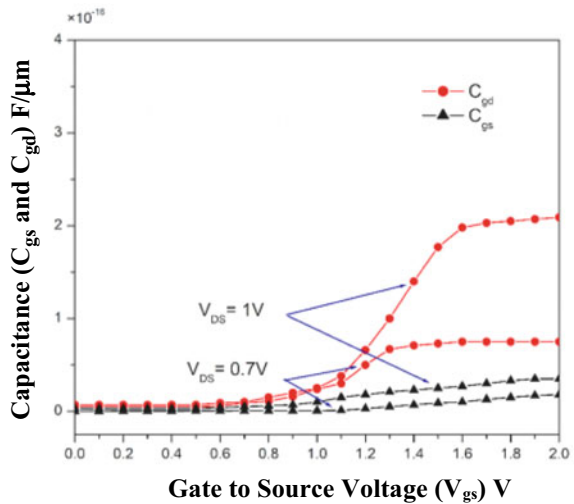
Fig. 5 Analysis of cut-off frequency (f_T)
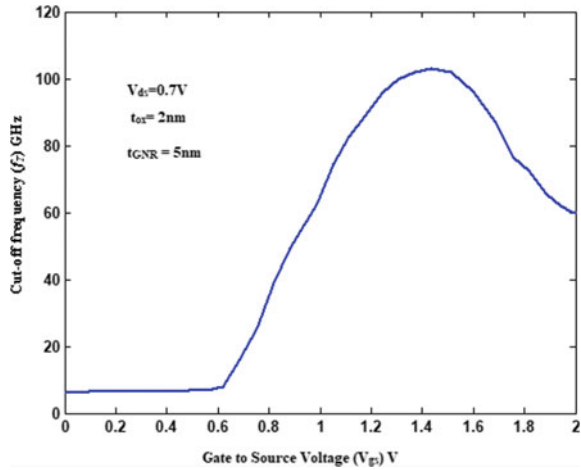
Another necessary device parameter is f_T; it's the utmost frequency at that a given device works properly with none performance debasement. f_T is additionally taken as associate operative frequency at that contact gain becomes adequate to unity. To analyze, the foot parameter of the device w.r.t. parasitic capacitances, the relation between each is given in Eq. 4.

$$f_T = \frac{g_m}{2\pi \left(C_{gs} + C_{gd}\right)} \tag{4}$$

Figure 5 shows the dependence of f_T on V_{gs}. It can be inferred that significant improvement in f_T of the proposed device is due to its larger g_m. It can be clearly seen from the figure that this rapid increase in g_m and an increase in gate capacitance results in an increase in f_T until V_{gs} reaches 1.2 V. After that a sharp drop in g_m and an increase in gate capacitance results in a decrease in the f_T. The proposed device achieves a maximum f_T of 103 GHz at 1.4v V_{gs} voltage.

The mathematical expression for GBP is given by equation five. As per the equation, it's directly in proportion to gram price and reciprocally proportional to Cgd price of the device [30, 31]. A high price of GBP is needed for superior high-frequency performance.

$$GBP = \frac{g_m}{2\pi C_{gd}} \tag{5}$$

Figure 6 shows the analysis of gain bandwidth product (GBP). The proposed device achieves a maximum GBP of 29.73 GHz at V_{gs} equal to 1v. The characteristics curve of GBP follows the same trends as f_T. Additionally, f_{max} is defined as maximum oscillation frequency at which power gain is unity. f_{max} is given by the formula.

Fig. 6 Data plot of GBP for proposed device
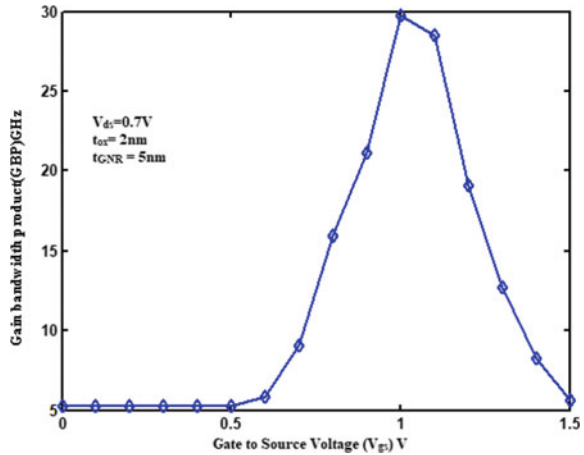
$$f_{\max} = \frac{f_T}{\sqrt{4R_g\left(g_d + 2\pi C_{gd}\right)}} \tag{6}$$

The maximum oscillation frequency variation with respective to V_{gs} is presented in Fig. 7. The value of fmax is 16THz at $V_{gs} = 1$ V. Another crucial operational issue for RF analysis is transit time that is outlined because the time needs to charge carriers to be shifted from supply to channel, given by equation half-dozen. Consistent with mathematical equation, transit time is reciprocally proportional to. If the worth will increase the transit time decreases [32].

$$\tau = \frac{1}{2\pi f_T} \tag{7}$$

Figure 8 shows the data plots for transit time. From Fig. 6, it can be analyzed that transit time becomes very less for V_{gs} greater than 0.7 V. The simulation analysis shows that GAA-GNR TFET seems to be additional appropriate for RF applications.

4   Summary

A new GAA-GNR TFET is proposed and dealing principle is investigated very well exploiting the second TCAD machine. The projected modification in GAA TFET improves ON-state current. Alongside these blessings, projected device conjointly consists of low Cgd and metric system that are causative for improved device controllability. Analog/RF parameters like metric system, Cgd, gm, f_T, GBP, $f_{\max}$, and transit time are analyzed to determine the practicableness of the GAA-GNR TFET for prime frequency application with low power operation. It is found that the projected device shows a higher performance for prime frequency parameters.

Fig. 7 f_{max} versus V_{gs} characteristics curve
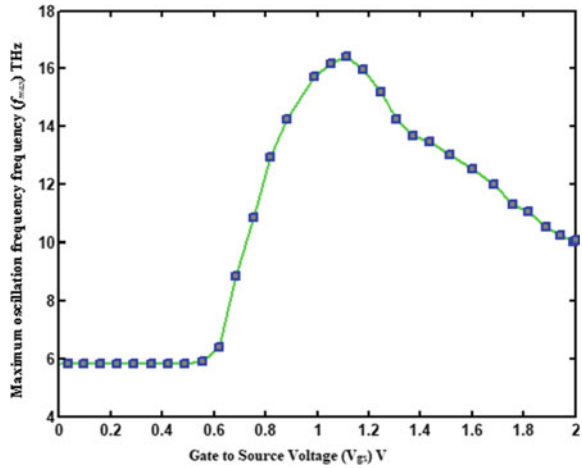
Fig. 8 Data plot of transit time(τ)
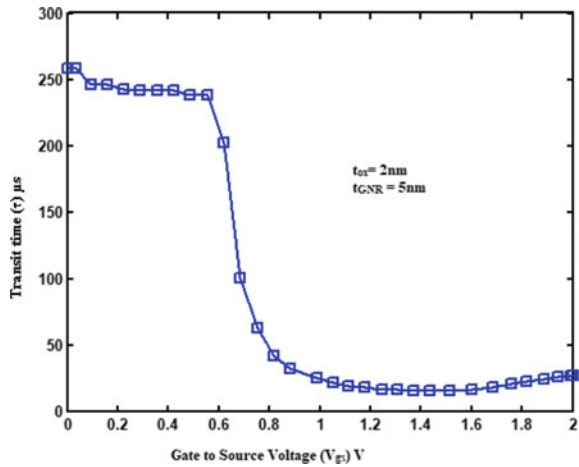
References

1. Neisser M, Wurm S (2015) ITRS lithography roadmap: 2015 challenges. Adv Opt Technol 4(4):235–240
2. Bangsaruntip S et al (2009) High performance and highly uniform gate-all-around silicon nanowire MOSFETs with wire size dependent scaling. IEEE Int Electron Dev Meeting Baltimore, 1–4
3. Hashim Y, Sidek O (2013) Dimensional effect on DIBL in silicon nanowire transistors. Adv Mater Res 626:190–194
4. Al Ariqi HT, Jabbar WA, Hashim Y, Manap HB (2019) Characterization of silicon nanowire transistor. TELKOMNIKA Telecommun Comput Electron Control 17(6):2860–2866
5. Hashim Y (2018) Optimization of resistance load in 4T-static random-access memory cell based on silicon nanowire transistor. J Nanosci Nanotechnol 18(2):1199–1201

6. Srivastava VM, Yadav KS, Singh G (2011) Design and performance analysis of cylindrical surrounding doublegate MOSFET for RF switch. Microelectron J 42(10):1124–1135

7. Bayani AH, Dideban D, Voves J, Moezi N (2017) Investigation of sub-10nm cylindrical surrounding gate germanium nanowire field effect transistor with different cross-section areas. Superlattices Microstruct 105(1):110–116

8. Srivastava VM (2015) Small signal model of cylindrical surrounding double-gate MOSFET and its parameters. Int Conf Trends Autom Commun Comput Technol, 1–5

9. Dargar SK, Srivastava VM (2019) Analysis of short channel effects in multiple-gate (n, 0) carbon nanotube FETs. J Eng Sci Technol 14(6):3282–3293

10. Singh N et al (2006) High-performance fully depleted silicon nanowire (diameter/spl les/5 nm) gate-all-around CMOS devices. IEEE Electron Device Lett 27(5):383–386

11. Dargar SK, Srivastava VM (2019) Performance analysis of 10 nm FinFET with scaled fin-dimension and oxide thickness. International conference on automation, computational and technology management

12. Bansal AK et al (2018) 3-D LER and RDF matching performance of nanowire FETs in inversion, accumulation, and Junctionless modes. IEEE Trans Electron Devices 65(3):1246–1252

13. Guan Y, Li Z, Zhang W, Zhang Y (2017) An accurate analytical current model of double-gate heterojunction tunneling FET. IEEE Trans Electron Dev 64(3):938–944

14. Seabaugh AC, Zhang Q (2010) Low-voltage tunnel transistors for beyond CMOS logic. Proc IEEE 98(12):2095–2110

15. Jena B, Dash S, Mishra GP (2018) Improved switching speed of a CMOS inverter using work-function modulation engineering. IEEE Trans. Electron Dev 65(6):2422–2429

16. Kumar A, Bhushan S, Tiwari PK (2017) A threshold voltage model of silicon-nanotube-based ultrathin double gate-all-around (DGAA) MOSFETs incorporating quantum confinement effects. IEEE Trans Nanotechnol 16(5):868–875

17. Dura J et al (2011) Analytical model of drain current in nanowire MOSFETs including quantum confinement, band structure effects and quasi-ballistic transport: device to circuit performances analysis. International conference on simulation of semiconductor processes and devices (ICSSPD), pp 43–46

18. Khaveh HRT, Mohammadi S (2016) Potential and drain current modeling of gate-all-around tunnel FETs considering the junctions depletion regions and the channel mobile charge carriers. IEEE Trans Electron Dev 63(12):5021–5029

19. Glass S et al (2018) A novel gate-normal tunneling field-effect transistor with dual-metal gate. IEEE J Electron Dev Soc 6:1070–1076

20. Seo JH, Yoon YJ, Lee S, Lee JH, Cho S, Kang IM (2015) Design and analysis of Si-based arch-shaped gate-all-around (GAA) tunneling field-effect transistor (TFET). Curr Appl Phys 15:208–212. [CrossRef]

21. Kao KH, Verhulst AS, Vandenberghe WG, Soree B, Groeseneken G, De Meyer K (2012) Direct and indirect band-to-band tunneling in germanium-based TFETs. IEEE Trans Electron Dev 59:292–301. [CrossRef]

22. Kao KH, Verhulst AS, Vandenberghe WG, Sorée B, Magnus W, Leonelli D, Groeseneken G, De Meyer K (2012) Optimization of gate-on-source-only tunnel FETs with counter-doped pockets. IEEE Trans Electron Dev 59:2070–2077. [CrossRef]

23. Kao KH, Verhulst AS, Vandenberghe WG, De Meyer K (2013) Counterdoped pocket thickness optimization of gate-on-source-only tunnel FETs. IEEE Trans Electron Dev 60:6–12. [CrossRef]

24. Betti Beneventi G, Gnani E, Gnudi A, Reggiani S, Baccarani G (2015) Optimization of a pocketed dual-metal-gate TFET by means of TCAD simulations accounting for quantization-induced bandgap widening. IEEE Trans Electron Dev 62:44–51. [CrossRef]

25. Asai H, Mori T, Matsukawa T, Hattori J, Endo K, Fukuda K (2019) Steep switching less than 15 mV dec-1 in silicon-on-insulator tunnel FETs by a trimmed-gate structure. Jpn J Appl Phys 58, SBBA16. [CrossRef]

26. Ashita, Loan SA, Rafat M (2018) A high-performance inverted-C tunnel junction FET with source-channel overlap pockets. IEEE Trans Electron Dev 65:763–768. [CrossRef]

27. Devi WV, Bhowmick B, Pukhrambam PD (2020) Investigation of dual MOSCAP TFET with improved vertical tunneling and its near infra-red sensing application. Semicond Sci Technol. [CrossRef]
28. Tirkey S, Yadav DS, Sharma D, Controlling ambipolar behaviour and improving radio frequency performance of hetero junction double gate tfet by dual work-function, hetero gate dielectric, gate underlap assessment and optimization. In: 2017 international conference on information, communication, instrumentation and control (ICICIC). IEEE, pp 1–7
29. Imenabadi RM, Saremi M, Vandenberghe WG (2017) A novel pnpnlike z-shaped tunnel field-effect transistor with improved ambipolar behavior and rf performance. IEEE Trans Electron Devices 64(11):4752–4758
30. Debnath RG, Baruah K, Baishya S (2020) Dc and analog/rf performance analysis of gate extended u-shaped channel tunnel field effect transistor. Microsyst Technol 26(9):2793–2799
31. Pandey C, Dash D, Chaudhury S (2020) Improvement in analog/rf performances of soi tfet using dielectric pocket. Int J Electron 107(11):1844–1860
32. Guenifi N, Rahi S, Larbi M (2020) Suppression of ambipolar current and analysis of rf performance in double gate tunneling field effect transistors for low-power applications. Int J Nanoparticles Nanotech 6:033

On the Generalized Distribution Functions in Heavily Doped Nano Materials at Terahertz Frequency

P. K. Chakraborty and K. P. Ghatak

Abstract In this chapter, we present a simplified analysis of the generalized distribution function of the carriers in heavily doped materials in the form $F(\overline{E}) = [1 + A + \exp(y)]^{-1}$ where A is a constant and the other variables are defined in the text. The substitution $A = 0$ and -1 lead to the well-known Fermi–Dirac statistics and Maxwell–Boltzmann distribution, respectively. The substitutions $A = 0$ and $y = 0$ together with $A = -4$ and $y = 0$ lead to the well-known Pauli's exclusion principle ($\pm(1/2)$), whereas the substitutions $A = i - 1$ ($i = \sqrt{-1}$) and $y = 0$ together with $A = -3 - i$ and $y = 0$ lead to the complex values of the Pauli's spin in the tail zone as $\pm(1 - i)/2$, respectively. Because of the complex Pauli's spin value, the electron energy component due to the spin g factor along the direction of the magnetic field B in heavily doped electronic materials forming band tails in the tail zone generates the magnitude of the electron energy as 71% g times the cyclotron resonance energy together with the phase value $\pm(\pi/4)$ in this case. We have also shown the Bose Einstein statistics in this context. Besides, the cases of terahertz frequency, heavy doping and intense electric field can be covered by replacing the value of $\overline{E}$ under the mentioned conditions.

1 Introduction

The concept of distribution functions of the carriers in different materials and their nanostructures occupy a singular position in the arena of terahertz frequency, heavy doping forming band tails and intrinsic intense electric field in nano devices for not only the characterization of the low dimensional systems under the mentioned

P. K. Chakraborty
Department of Electronics and Communication Engineering, Indian Institute of Technology, Kharagpur 721302, West Bengal, India

K. P. Ghatak (✉)
Department of Basic Science, Institute of Engineering and Management, D-1, Management House, Salt Lake, Sector - V, Kolkata 700091, West Bengal, India
e-mail: kamakhyaghatakcu@gmail.com

conditions but also for the study of the transport features in different technologically important materials [1, 2]. Fermi and Dirac (both independently) formulated the Fermi–Dirac (FD) statistics for electrons [3, 4] whereas the Bose–Einstein (BE) statistics appeared in the literature in 1924 for bosons [5] together with the fact that both of them get simplified into well-known Maxwell–Boltzmann statistics under certain limiting conditions. The FD statistics is generally applicable for studying the transport features of low dimensional nano systems of degenerate materials, because in this case, the band structure prevails [6] and the Fermi energy (E_F) is above the edge of the conduction band (CB) and within the conduction band. Also, we know by Pauli's exclusion principle, the occupational probability of an electron at an energy state is (1/2) at E_F [7]. The simple FD function cannot explain the existence of band tailing phenomena observed in the case of heavily doped systems at low temperatures where the quantum effects become prominent. Therefore, some modifications must be expected in the mathematical form of the well-known FD distribution function.

It might be noted that in the case of disordered materials, the conduction band penetrates within the Forbidden Band (FB) and the carriers do exist in the tail region. We know that for a semiconductor with heavily doped conditions, the doping levels must satisfy the inequality $(a_D.Ni^{1/3}) > 1$, where a_D is the Bohr radius and Ni is the doping concentration of the carriers, and that for "non-degenerately doped case", the doping condition should satisfy the inequality [9–11] $\{(0.02 \leq [a_D.Ni^{1/3}] < 1.0)\}$ [8–12],. As we know the normal FD distribution function cannot explain the occupational probability of the carriers is the Tail-Zone (TZ), because it is valid for the Band gap zone (BZ) only. Also, in general, the FB zone is known as the imaginary band (IB). The TZ lies in the FBZ. Therefore, we might conclude that for the TZ region, the probability of the distribution of the carriers must be different from normal FD distribution function. In this chapter, an attempt is made in the theoretical background to derive the generalized FD and BE in a very simplified manner and we also note various important conclusions which emerge from it. This new probability of distribution in the TZ region, is termed as "Extended and Modified distribution functions. The sections three and four contain the result and discussions and the conclusion, respectively.

2   Theoretical Background

Let us assume that the probability of occupation of the energy level $\overline{E}$ by an electron is $F(\overline{E})$. Let us also assume that there are two initial energy levels namely $\overline{E}_1$ and $\overline{E}_2$ together with two final energy levels $\overline{E}_3$ and $\overline{E}_4$ respectively as show in Fig. 1.

The probability of forward transmission of an electron in the initial energy level $\overline{E}_1$ to the final energy level $\overline{E}_3$ and an electron in the initial energy level $\overline{E}_2$ to the final energy level $\overline{E}_4$ is proportional to $F(\overline{E}_1)[1 - F(\overline{E}_3)]F(\overline{E}_2)[1 - F(\overline{E}_4)]$.

Similarly the probability of reverse transmission is similarly proportional to

$$F(\overline{E}_3)[1 - F(\overline{E}_1)]F(\overline{E}_4)[1 - F(\overline{E}_2)]$$

Fig. 1 Energy levels

The application of the principle of detailed balance of Einstein leads to the result

$$F(\overline{E}_1)\big[1 - F(\overline{E}_3)\big]\big[F(\overline{E}_2)[1 - F(\overline{E}_4)\big] = F(\overline{E}_3)\big[1 - F(\overline{E}_1)\big]F(\overline{E}_4)\big[1 - F(\overline{E}_2)\big] \tag{1}$$

Dividing both sides by $[F(\overline{E}_1)F(\overline{E}_2)F(\overline{E}_3)F(\overline{E}_4)]$ and assuming $[F(\overline{E}_1)F(\overline{E}_2)F(\overline{E}_3)F(\overline{E}_4)] \neq 0$ we get

$$\left[\frac{1}{F(\overline{E}_1)} - 1\right]\left[\frac{1}{F(\overline{E}_2)} - 1\right] = \left[\frac{1}{F(\overline{E}_3)} - 1\right]\left[\frac{1}{F(\overline{E}_4)} - 1\right] \tag{2}$$

Energy conservation rule gives us

$$\overline{E}_1 + \overline{E}_2 = \overline{E}_3 + \overline{E}_4 \tag{3}$$

Let us assume

$$\frac{1}{F(\overline{E})} - 1 = A + \exp\left(\frac{\overline{E} - E_F}{k_B T}\right) \tag{4}$$

where A is a constant, k_B is the Boltzmann constant and T is the temperature. Using (2), (3) and (4) we get

$$\left[A + \exp\left(\frac{\overline{E}_1 - E_F}{k_B T}\right)\right]\left[A + \exp\left(\frac{\overline{E}_2 - E_F}{k_B T}\right)\right] = \left[A + \exp\left(\frac{\overline{E}_3 - E_F}{k_B T}\right)\right]\left[A + \exp\left(\frac{\overline{E}_4 - E_F}{k_B T}\right)\right] \tag{5}$$

From (5) we can write

$$\left[\exp\left(\frac{\overline{E}_1}{k_B T}\right) + \exp\left(\frac{\overline{E}_2}{k_B T}\right)\right]^{-1} = \left[\exp\left(\frac{\overline{E}_3}{k_B T}\right) + \exp\left(\frac{\overline{E}_4}{k_B T}\right)\right]^{-1} \tag{6}$$

If (6) is satisfied by (4) then the $F(\overline{E})$ as given by (4) is a solution. Now for heavily doped nano-materials which are being discussed in this chapter is a low temperature phenomena i.e. $T \to 0$ and under this condition, (6) is being satisfied by (4).

Thus the modified Fermi–Dirac function can be written from (4) as

$$F(\overline{E}) = \left[1 + A + \exp(y)\right]^{-1} \tag{7}$$

where, $y = ((\overline{E} - E_F)/(k_B T))$

The conclusions from (7) are written below:

1. When $A = 0$, we get the ordinary Fermi–Dirac function from (7) as

$$F(\overline{E}) = \left[1 + \exp((\overline{E} - E_F)/(k_B T))\right]^{-1} \tag{8}$$

2. When $A = -1$, from (7) we can write that the $F(\overline{E}) = C \exp(-\overline{E}/k_B T)$, where $C = \exp(E_F/k_B T)$ which is the well-known Maxwell–Boltzmann distribution.
3. The substitutions $A = 0$ and $\overline{E} = E_F$ together with $A = -4$ and $\overline{E} = E_F$ in (7) generate the well-known Pauli's exclusion principle as $(\pm 1/2)$.
4. For $A = i - 1 (i = \sqrt{-1})$ and $\overline{E} = E_F$ together with $A = -3 + i$ and $\overline{E} = E_F$ in (7) lead to a complex value of the Pauli's spin in the tail zone as $1/2(\pm 1 \mp i)$ respectively.
5. The substitution $A = 1 + B_0 i$ (where B_0 is a real constant) leads to the modified and extended complex Fermi–Dirac function as

$$F_c(\overline{E}) = \left[1 + B_0 i + \exp(y)\right]^{-1} \tag{9}$$

From (9) we can write

$$\mathrm{Re}[F(\overline{E})] = \left[1 + \exp(y)\right]\left[B_0^2 + (1 + \exp y)^2\right]^{-2} \tag{10}$$

and

$$\mathrm{Im}[F(\overline{E})] = -B_0\left[B_0^2 + (1 + \exp y)^2\right]^{-2} \tag{11}$$

Few important points can also be noted in this context:

1. We know the concept of "spin g-factor" is very important for semiconductors; while studying the electron energy $(\overline{E}_5)$ in the presence of a magnetic field B, applied to a semiconductor along z axis which in this case assumes the form

$$\overline{E}_5 = \pm(g/2)[\hbar\omega_B] \tag{12}$$

where $\hbar\omega_B$ is the cyclotron resonance frequency of electron in this case.

The (12), exhibits the fact that it has only magnitude but no phase value.

The electron energy in the presence of the complex spin value $\pm(1/2)(1-i)$ in the tail zone can be written as

$$\overline{E}_6 = \pm(g/2)(1-i)[\hbar\omega_B] \tag{13}$$

From (13), we observe that the electron energy $(\overline{E}_6)$ as the presence of a magnetic field, has both magnitude and phase value,

Thus the magnitude is given by

$$\left|\overline{E}_6\right| = \frac{g}{2}\hbar\omega_B\left(\sqrt{2}\right) = 0.707\left[\frac{g}{2}\hbar\omega_c\right] \approx 71\% \ of \ (g\hbar\omega_B) \tag{14}$$

and the phase value can be written as

$$\phi_{EX} = \tan^{-1}\left\{-\frac{\left[\pm\frac{g}{2}\hbar\omega_B\right]}{\left\{\pm\frac{g}{2}\hbar\omega_B\right\}}\right\} = \pm\frac{\pi}{4} \tag{15}$$

In the conventional case, Pauli's value is 50% and the phase value $\phi_c = 0°$. When an electron rotates in its orbit around the nucleus, the average electron energy is about 71% of its maximum value. The phase value ϕ_{EX} in this case is $\pm(\pi/4)$.

For Boson, Pauli's exclusion principle is not obeyed. Replacing (-1) in (2) and (4) by $(+1)$ we get

$$\left[\frac{1}{F(\overline{E}_1)}+1\right]\left[\frac{1}{F(\overline{E}_2)}+1\right] = \left[\frac{1}{F(\overline{E}_3)}+1\right]\left[\frac{1}{F(\overline{E}_4)}+1\right] \tag{16}$$

$$\frac{1}{F(\overline{E})}+1 = A + \exp\left(\frac{\overline{E}-E_F}{k_BT}\right) \tag{17}$$

Following the method as given above we note that the (17) is a solution of Eq. (16). Substituting $A = 0$, we note that

$$F(\overline{E}) = \left[\exp\left(\frac{\overline{E}-E_F}{k_BT}\right)-1\right]^{-1} \tag{18}$$

which is the well-known BE statistics.

3   Result and Discussions

The Figs. 2, 3 and 4 exhibit the ordinary Fermi–Dirac function, real and imaginary parts of the extended Fermi–Dirac functions as given by (8), (10) and (11), respectively, where for Figs. 3 and 4 we have taken $B_0 = 1$ for the purpose of numerical computations. The graphs (3) and (4) are new and should be used in dealing with all types of carrier properties in the tail zone of the HD quantum material.

In this chapter, we have derived the modified and extended form of (FD) distribution function for the carriers in the Tail-zone (TZ) region, while the carriers penetrate with is the (FB zone) in the form of tails.

These carriers are free carriers and posses finite effective masses. The transport properties of these carriers are not the same as those of the carriers in the normal semiconductors bands [2]. In this chapter, we have derived the modified FD distribution function as given by Eq. (7) which is valid for carriers in the tail-zone (TZ).

The validity of the generalized Eq. (7) for which we have given a very simplified derivation can easily be assessed from five special cases as given above where the first three lead to the well-known results and the last two generate new concepts.

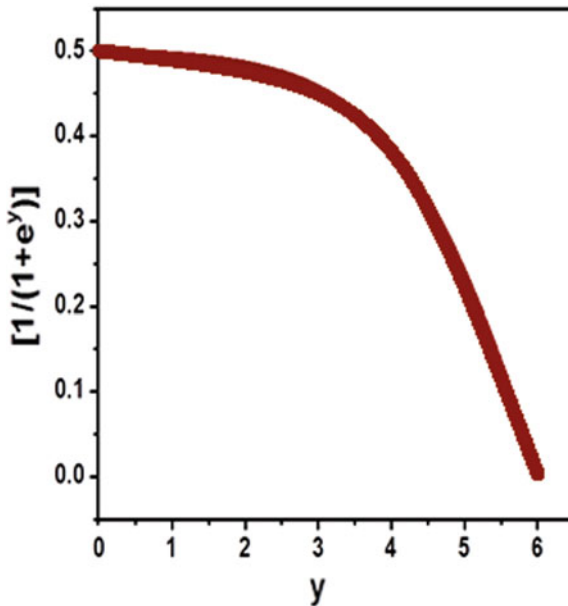**Fig. 2** Plot of the normal Fermi–Dirac probability distribution factor (Eq. 8) as a function of y
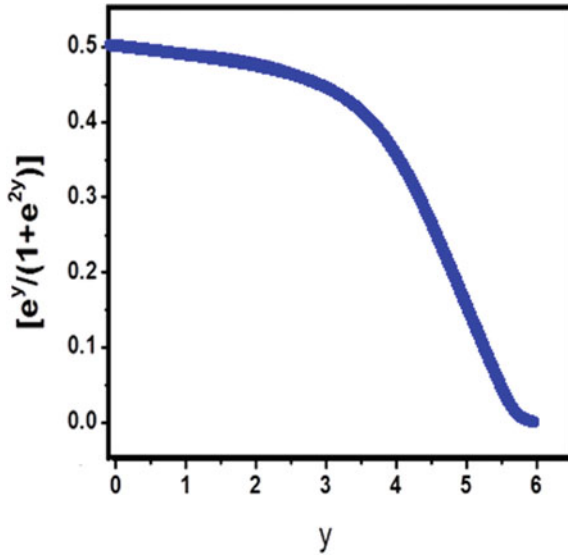
Fig. 3 Plot of the real part of the extended and modified Fermi–Dirac probability distribution factor as given by Eq. (10) as a function of y
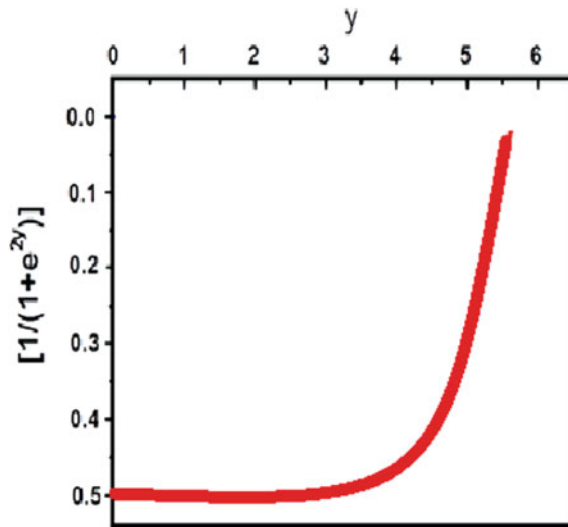

Fig. 4 Plot of the imaginary part of the extended and modified Fermi–Dirac probability distribution factor as given by Eq. (11) as a function of y

4 Summary

In this chapter, we present a simplified analysis of the generalized distribution function of the carriers in nano materials in the form $F(\overline{E}) = [1 + A + \exp(y)]^{-1}$ The substitution $A = 0$ and -1 lead to the well-known FD function and Maxwell–Boltzmann distribution, respectively. The substitutions $A = 0$ and $y = 0$ together with $A = -4$ and $y = 0$ lead to the well-known Pauli's exclusion principle ($\pm(1/2)$), whereas the substitutions $A = i - 1$ ($i = \sqrt{-1}$) and $y = 0$ together with $A = -3 - i$ and $y = 0$ lead to the complex values of the Pauli's spin in the tail zone as $\pm(1 - i)/2$, respectively. Because of the complex Pauli's spin value, the electron energy component due to the spin g factor along the direction of the magnetic field B in heavily doped electronic nano materials forming band tails in the tail zone generates the magnitude of the electron energy as 71% g times the cyclotron resonance energy together with the phase value $\pm(\pi/4)$ in this case. We have also shown the Bose–Einstein statistics in this context.

References

1. Modelung O (1978) Introduction to solid state theory. Springer Series Solid State Sci 2:25–41
2. Nag BR (1980) Electron transport in the compound semiconductors. Springer Series Solid State Sci 11:40–52
3. Fermi E (1926) For the quantization of the ideal monatomic gas. Z Phys 36:902–904
4. Dirac PAM (1926) On the theory of quantum mechanics. Proc Roy Soc 112:661–667
5. Bose SN (1924) Planck's law and light quantum hypothesis. Z Phys 26:1780180
6. Shaklovskii BI, Efros AL (1984) Electronic properties of doped semiconductors. Springer, Berlin, New York 45, pp 253–257
7. Pauli W (1925) The complex structure of the spectra is about the connection between the termination of the electron groups in the atom. Z. Physik 31:765
8. Choudhuri BK, Mondal BN, Chakraborty PK (2019) Fermi integral and density-of-states functions in a parabolic band semiconductor degenerately doped with impurities forming a band tail. Pramana J Phys 90:18–22
9. Chakraborty PK, Mondal BN, Choudhury BK (2019) Open access journal of mathematical and theoretical. Physics 2:22–28
10. Chakraborty PK, Biswas JC (1997) Conduction-band tailing in parabolic band semiconductors. J Appl Phys 82:7–12
11. Chakraborty PK, Mondal BN (2017) Fermi-statistics revised for degenerately doping with impurities forming band-tail. Quart Phys Rev 3:1–12
12. Kittle C (1980) Elementary Statistical mechanics. Dover Publications Inc., New York, pp 86–88

Influence of THz Frequency on the Gate Capacitance in 2D QWFETs

N. Debbarma, S. Debbarma, J. Pal, and K. P. Ghatak

Abstract Here we study C_g in the presence of THz frequency in 2D QW MOSFET's of III-V and opto-electronic materials on the basis of newly formulated 2D electron statistics. It is found taking quantum-well field effect transistors (QWFETs) of InAs, InSb, $Hg_{1-x}Cd_xTe$ and $Ga_{1-x}Al_x$ as C_g increasingly oscillates with changing V_g and d_z.with different numerical magnitudes.

1 Introduction

In recent years there has been considerable interest in studying the C_g in 2D MOSFETs under various external constraints [1–10]. In this chapter, we study the same in 2D QWMOSFETs made of the compounds as stated in the abstract. Section 2 contains the mathematical basis and the Sect. 3 explores the results and discussions in this context.

N. Debbarma · S. Debbarma
Department of Computer Science and Engineering, National Institute of Technology, Agartala, Tripura 799055, India

J. Pal
Department of Physics, Meghnad Saha Institute of Technology, Nazirabad Rd, Uchhepota, Kolkata, West Bengal 700150, India

K. P. Ghatak (✉)
Department of Basic Science and Humanities, Institute of Engineering and Management, Kolkata, West Bengal 700091, India
e-mail: kamakhyaghatakcu@gmail.com

2 Mathematical Basis

The 2D electron statistics assumes the form

$$\bar{n}_{2d} = C_1\left[\beta_0(\bar{E}_0, \lambda) - \bar{H}_{n_z}\right] \tag{1}$$

$$\bar{n}_{2d} = C_1\left[\omega_0(\bar{E}_0, \lambda) - \bar{H}_{n_z}\right] \tag{2}$$

$$\bar{n}_{2d} = C_1\left[\rho_0(\bar{E}_0, \lambda) - \bar{H}_{n_z}\right] \tag{3}$$

where $C_1 = \left(\frac{m_c}{\pi \hbar^2}\right) \sum_{n_z=1}^{n_{zmax}}$, $\bar{E}_0$ is the Fermi energy, $\bar{H}_{n_z} = \left(\frac{n_z \pi}{d_z}\right)^2 \left(\frac{\hbar^2}{2m_c}\right)$ and the other notations are defined in [6].

Using Eqs. (1)–(3) we can formulate and study C_g.
.

3 Result and Discussions

We have plotted normalized C_g versus V_g and d_z, respectively, as shown in Figs. 1, 2, 3 and 4, 5, 6, 7, and 8 and we briefly note the following:

Fig. 1 C_g versus V_g for the indicated compounds under the given constraints of band models
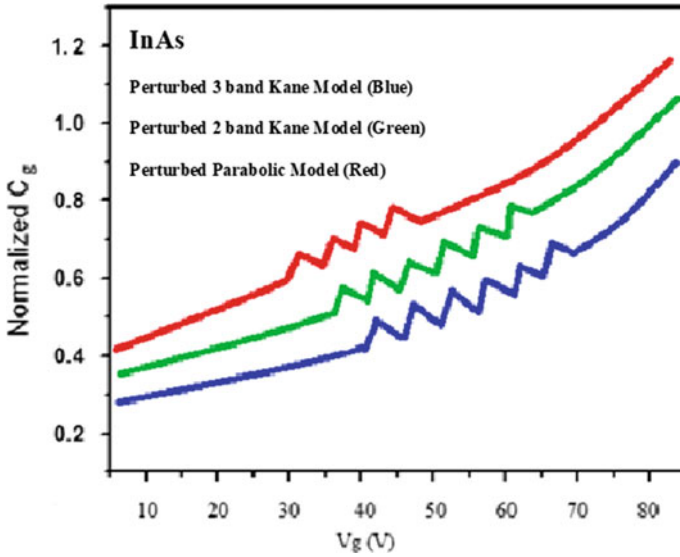
Fig. 2 C_g versus V_g for all cases of Fig. 1

Fig. 3 C_g versus V_g for all cases of Fig. 1

1. From Figs. 1, 2, 3 and 4 we observe that C_g increases with increasing V_g in an oscillatory way for all types of band models.
2. From Figs. 4, 5, 6, 7 and 8 we note that C_g increases with increasing d_z in different oscillatory manners.

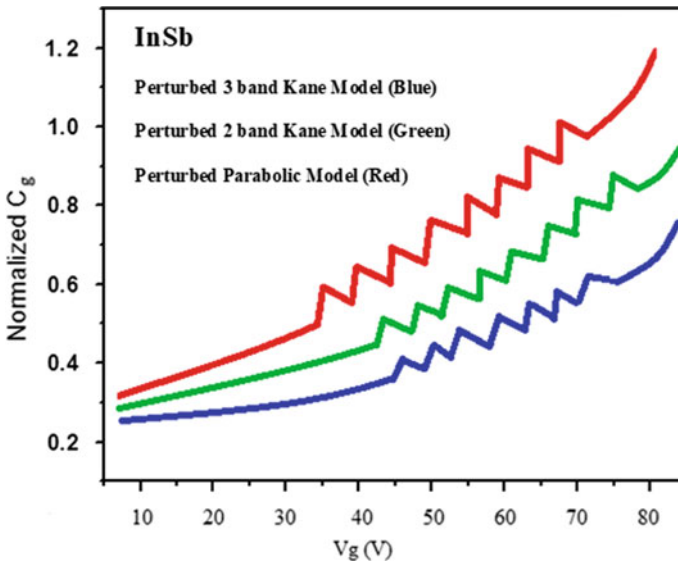**Fig. 4** C_g versus V_g for all cases of Fig. 1

Fig. 5 V_g versus d_z for the indicated compounds under the given constraints of band models

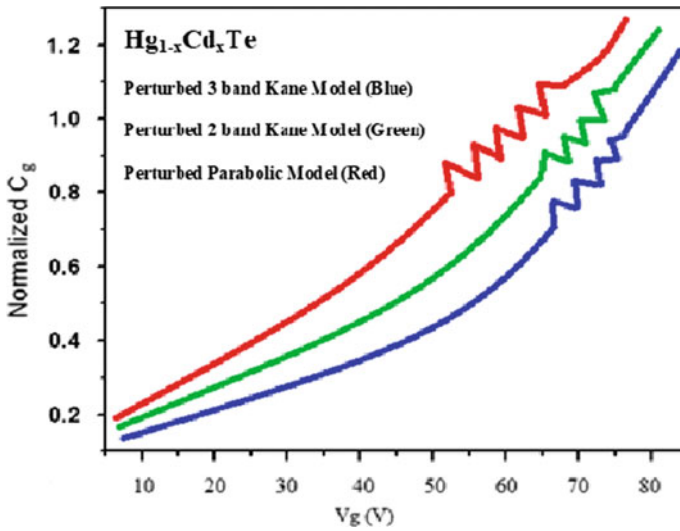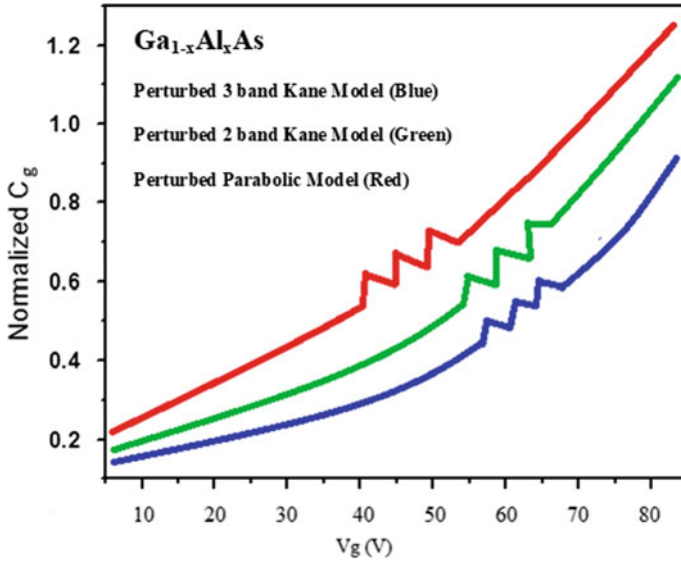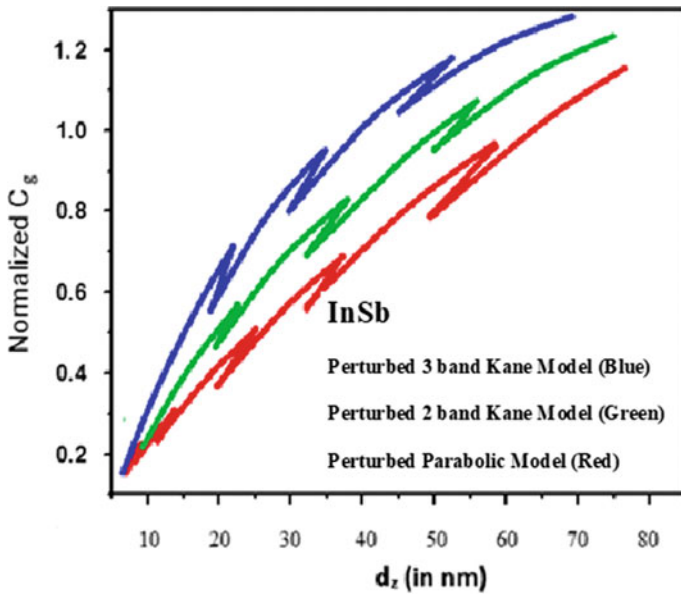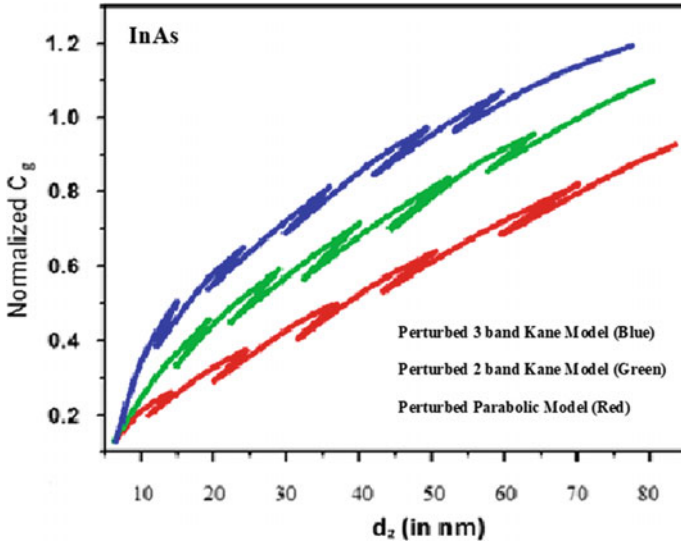**Fig. 6** C_g versus V_g for all cases of Fig. 5
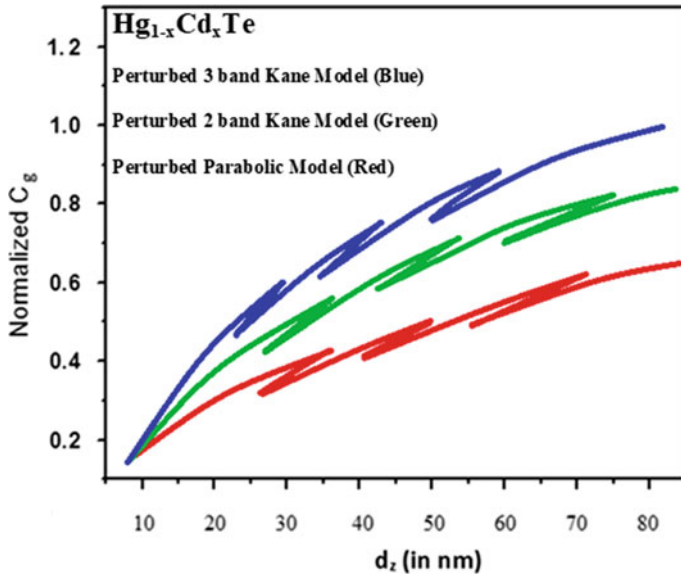
Fig. 7 C_g versus V_g for all cases of Fig. 5
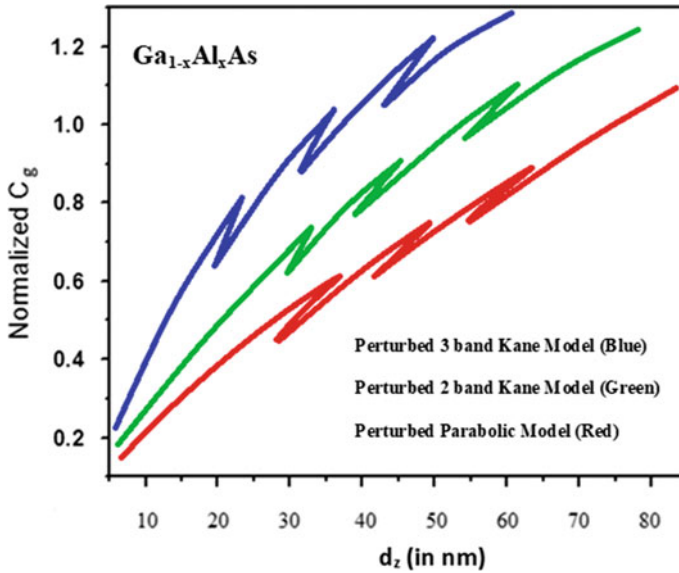
Fig. 8 C_g versus V_g for all cases of Fig. 5

References

1. Grove AS, Fitzgerald DJ (1966) Surface effects on *p-n* junctions: characteristics of surface space-charge regions under non-equilibrium conditions. Solid State Electron 9:783–806
2. Voshchenkov AM, Zemel JN (1974) Erratum: Admittance studies of surface quantization in [100]-oriented Si metal-oxide-semiconductor field-effect transistors. Phys Rev B 9:4410
3. Djuric Z, Spasojevic Z, Tjapkin D (1976) Electron ground state in the semiconductor inversion layer and low frequency MIS capacitance. Solid State Electron 19:931–934
4. Antcliffe GA, Bate RT, Reynolds RA (1971) Physics of semi-metals and narrow-gap semiconductors. In: Carter DL, Bate RT (eds) Proceeding of the international conference physics of semi-metals and narrow gap semiconductors, Pergamon Press, Oxford, pp 499
5. Daeer A, Kotthaus JP, Koch JF (1975) Surface cyclotron resonance in InSb. Solid State Commun 17(4):455–458
6. Ghatak KP (2016) Dispersion relations in heavily doped nanostructures. Springer, Germany
7. Dornhaus R, Nimtz S (1976) Springer tracts in modern physics, vol 78. Springer, Berlin, Heidelberg, New York, p 1
8. Weinberg ZA (1977) Tunneling of electrons from Si into thermally grown SiO₂. Solid State Electron 20:11–18
9. Dorda G (1973) Advances in solid state physics. In: Queisser HJ (ed) Festkorperprobleme, vol 13. Vieweg, Braunschweig, p 215
10. Lax B (1963) In: Smith RA (ed) Proceedings of the international school "Enrico Fermi" (Course XXII). Academic Press, New York, p 240

An Alternative Scheme of Quantum Optical Superfast Tristate CNOT Gate Using Frequency Encoding Principle of Light with Semiconductor Optical Amplifier

Snigdha Hazra and Sourangshu Mukhopadhyay

Abstract Photon is established as a strong and promising candidate in all-optical signal processing and superfast computing. Again, it is found that photon has a successful approach to be used as a quantum mechanical particle. For this reason, it is used as a carrier of information in optical systems instead of electrons in electronic systems. All-optical quantum systems can provide very high speed, secured and noise free communication and computation. Over the last few decades, several all-optical logic processors, algebraic processors, logic gates and their integrated systems are developed by many researchers. All-optical quantum logic gates with qubit data are the basic building block of an optical quantum computer. In quantum computation, qubits or quantum bits are the quantum analogue of classical boolean bits and are used to store information. Several popular encoding techniques (like phase encoding, frequency encoding, intensity encoding, polarization encoding etc.) are used to develop the qubits. Here, in this paper, the gate matrix for quantum optical tristate CNOT logic gate is developed for the first time with a frequency encoding technique. Quantum optical CNOT gate is one of the most important logic gates in the logic family that is extensively used for performing information processing task in optical systems. Tristate-based optical logic operations are proved to increase the data handling capacity. Also, the speed of different types of optical logic operations can be increased with tristate-based optical logic systems. Introduction of contradiction state is another advantage of tristate logic systems. Frequency encoding principle is the best way to encode tristate, quaternary state and multivalued logic states. In the article, the authors have developed a proper truth table and gate matrix of frequency encoded tristate CNOT gate. The all-optical scheme for tristate CNOT gate can be implemented with semiconductor optical amplifier (SOA)-based optical switches. At the same time advantages of quantum optical operations are exploited.

S. Hazra (✉) · S. Mukhopadhyay
Department of Physics, The University of Burdwan, Burdwan, West Bengal 713104, India
e-mail: snigdhahazra29@gmail.com

1 Introduction

All-optical signal processing has received great attention from scientists and technicians as it can overcome speed limitation problems encountered in electronic systems [1, 2]. Optical digital systems have several advantages over electronics and electrical counterparts. Here, the photon is used as the carrier of data instead of the electron found in electronic systems. Due to strong inherent parallelism and superfast speed of operation, photons can be used for very high-speed data processing, data handling, image processing in optical computing systems [3, 4]. Again, being a chargeless particle, photons cannot interact with other charged particles or even among themselves, so cross-talk related problems can also be avoided in optical systems [5]. In electrical systems, one can work with binary logic only, but in optical systems one can use the coding of binary, ternary, quaternary or multi-valued data with the optical signal [6]. Different physical properties of light like frequency, intensity, phase, polarization etc. are used to encode the bits of data. Some important encoding processes are frequency encoding, intensity encoding, phase encoding, polarization encoding, hybrid encoding etc. In intensity encoding, the presence of light is considered as '1' state and the absence of light is considered as '0' state. In the phase encoding technique, one specific phase of light is encoded as '1' state and another specific phase is encoded as '0' state, whereas in polarization encoding, two orthogonal sates of light are used to encode '1' and '0' states. In frequency encoding, two different frequencies of light are used to encode '1' state and '0' state, respectively. For long distance communication, the intensity of light may dropdown, phase may change and the state of polarization may alter due to reflection, refraction, scattering, absorption etc. so that '1' state may wrongly appear as '0' state which leads to the bit error problem [5–7]. In general, frequency is the fundamental property of a light signal which undergoes no change during reflection, refraction, scattering, absorption etc. in case of signal transmission. So, bit error rate can be reduced by using the frequency encoding technique [7, 8]. For this reason, it is the most reliable and useful encoding technique. Various types of all-optical logic systems were developed in the past few years using different encoding processes [9–12]. Again, the semiconductor optical amplifier (SOA) is considered as a promising switch for all-optical logic operations because of its small size, high gain, large bandwidth, small power requirement and flexibility for integration in the optical network [13, 14]. Over the last few decades, several works have been done using the semiconductor optical amplifier-based optical switches [1, 3–8, 15–20]. Here, in this article, an all-optical approach for realization of frequency encoded tristate CNOT logic gate is proposed. To implement such systems, semiconductor optical amplifier (SOA)-based optical switches like add/drop multiplexers, frequency converters etc. will be used. Since the proposed system is all-optical in nature, factors such as superfast speed of operation (at least THz), high degree of parallelism, less noise, no cross-talk, high bit rate, low bit error rate, very high signal to noise ratio etc. can be achieved with this system.

2 Usefulness of the Applications of Tristate Logic

In binary logic, there are two states of information, '0' and '1'. It restricts large data handling capacity and limits the speed of different optical logic operations. In tristate logic, there are three states of information. If '0' state is considered as 'no' and '1' state is considered as 'yes', then there must be a state that is neither 'yes' nor 'no'. This state is known as the state of contradiction and it is denoted by '$\bar{1}$'. Tristate logic operations can increase the data handling capacity [21]. Also, the speed of operations can be enhanced with tristate logic [22]. Frequency encoding principle is the best way to encode tristate, quaternary state, decimal, hexadecimal and multivalued logic state. In the proposed scheme, '0' state is encoded by frequency ν_1, '1' state by ν_2 and '$\bar{1}$' state by ν_3.

3 Semiconductor Optical Amplifier (SOA) as an Optical Switch

Semiconductor optical amplifier (SOA) is an important optoelectronic device which can amplify an input light signal by stimulated emission without optical pumping and it is massively used nowadays due to its small size, high gain, large bandwidth, low power consumption, high stability, fast switching speed (order of nanoseconds), flexibility for integration in photonic integrated circuits and ability to achieve a high extinction ratio [23]. The device shows different types of nonlinear effects such as cross gain modulation (XGM), cross phase modulation (XPM), self-phase modulation (SPM), four-wave mixing (FWM) etc. and for this the device is suitable for optical switching, all-optical signal processing, wavelength conversion and amplification.

3.1 Wavelength Conversion by SOA

Wavelength conversion refers to transfer of information at one wavelength to another signal at different wavelength. The basic principle of wavelength conversion is based on the XGM character of SOA. Cross gain modulation (XGM) is a nonlinear process that exploits the gain saturation property of SOA [23–25]. The schematic diagram of the SOA-based wavelength converter in the co-propagating scheme is shown in Fig. 1 [4]. When a strong pump beam of wavelength λ_1 (frequency ν_1) and a weak probe beam of wavelength λ_2 (frequency ν_2) are injected from the same side of the SOA, then at the output one can obtain a converted strong probe beam of wavelength λ_2 (frequency ν_2). The high intensity pump beam compresses the gain of SOA and cross gain modulation takes place. As a result, the pump beam transfers its total power to
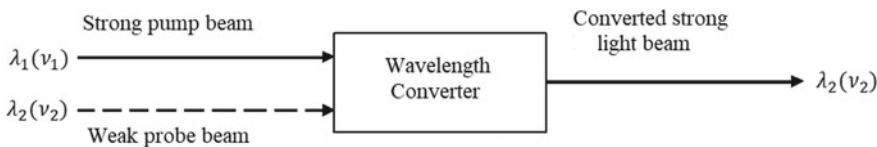
Fig. 1 Schematic diagram of SOA-based wavelength converter
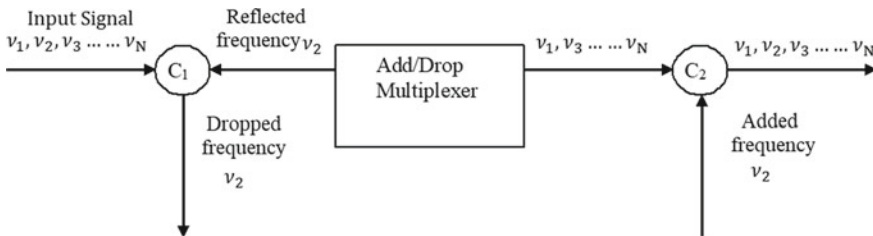
Fig. 2 Schematic diagram of Add/drop multiplexer

the probe beam and one can get a strong probe beam converted at the output. No output is obtained in the absence of either the pump or the probe beam.

3.2 *SOA-Based Add/Drop Multiplexer*

Add/drop multiplexer is an extremely useful device for routing of wavelength channel in wavelength division multiplexing network [24]. It has the ability to add or drop a particular wavelength (frequency) without any interference from the adjacent wavelength (frequency) channel. The schematic diagram of SOA-based add/drop multiplexer is shown in Fig. 2 [4]. The input light signal consists of the frequency channel $v_1, v_2, v_3, \ldots \ldots v_N$. When the add/drop multiplexer is tuned at a frequency v_2, then it reflects this frequency and this reflected frequency is dropped by the circulator. The dropped frequency can be added again at the output by another circulator.

4   Frequency Encoded Tristate CNOT Gate

Quantum CNOT gate is a two qubit reversible logic gate which is widely used in quantum computation. The first qubit is called the control qubit and the second qubit is called as the target qubit. The truth table of frequency encoded quantum optical tristate CNOT gate is given in Table 1.

The gate matrix of tristate CNOT gate will be of 9×9 order that is it will have 81 elements. Let the gate matrix of quantum optical tristate CNOT gate be:

Table 1 Truth table of frequency encoded tristate CNOT gate

Inputs		Outputs	
A	B	O_1	O_2
$v_1(0)$	$v_1(0)$	$v_1(0)$	$v_1(0)$
$v_1(0)$	$v_2(1)$	$v_1(0)$	$v_2(1)$
$v_1(0)$	$v_3(\bar{1})$	$v_1(0)$	$v_3(\bar{1})$
$v_2(1)$	$v_1(0)$	$v_2(1)$	$v_1(0)$
$v_2(1)$	$v_2(1)$	$v_2(1)$	$v_3(\bar{1})$
$v_2(1)$	$v_3(\bar{1})$	$v_2(1)$	$v_2(1)$
$v_3(\bar{1})$	$v_1(0)$	$v_3(\bar{1})$	$v_2(1)$
$v_3(\bar{1})$	$v_2(1)$	$v_3(\bar{1})$	$v_1(0)$
$v_3(\bar{1})$	$v_3(\bar{1})$	$v_3(\bar{1})$	$v_3(\bar{1})$

$$Tristate\,CNOT = \begin{pmatrix} a_1 & a_2 & a_3 & a_4 & a_5 & a_6 & a_7 & a_8 & a_9 \\ b_1 & b_2 & b_3 & b_4 & b_5 & b_6 & b_7 & b_8 & b_9 \\ c_1 & c_2 & c_3 & c_4 & c_5 & c_6 & c_7 & c_8 & c_9 \\ d_1 & d_2 & d_3 & d_4 & d_5 & d_6 & d_7 & d_8 & d_9 \\ e_1 & e_2 & e_3 & e_4 & e_5 & e_6 & e_7 & e_8 & e_9 \\ f_1 & f_2 & f_3 & f_4 & f_5 & f_6 & f_7 & f_8 & f_9 \\ g_1 & g_2 & g_3 & g_4 & g_5 & g_6 & g_7 & g_8 & g_9 \\ h_1 & h_2 & h_3 & h_4 & h_5 & h_6 & h_7 & h_8 & h_9 \\ i_1 & i_2 & i_3 & i_4 & i_5 & i_6 & i_7 & i_8 & i_9 \end{pmatrix}_{9\times9}$$

The state of light is represented by a 9×1 column matrix.

$$State\,of\,light = \begin{pmatrix} C_1 \\ C_2 \\ C_3 \\ C_4 \\ C_5 \\ C_6 \\ C_7 \\ C_8 \\ C_9 \end{pmatrix}_{9\times1}$$

Let, $|0\rangle = \begin{pmatrix} 1 \\ 0 \\ 0 \end{pmatrix}$ $|1\rangle = \begin{pmatrix} 0 \\ 0 \\ 1 \end{pmatrix}$ $|\bar{1}\rangle = \begin{pmatrix} 0 \\ 1 \\ 0 \end{pmatrix}$

From the truth table it is clear that, when tristate CNOT gate operates on $|00\rangle$, the state remains unchanged that is,

$$Tristate\,CNOT\,|00\rangle = |00\rangle \tag{1}$$

$$\text{or,}\quad \begin{pmatrix} a_1 & a_2 & a_3 & a_4 & a_5 & a_6 & a_7 & a_8 & a_9 \\ b_1 & b_2 & b_3 & b_4 & b_5 & b_6 & b_7 & b_8 & b_9 \\ c_1 & c_2 & c_3 & c_4 & c_5 & c_6 & c_7 & c_8 & c_9 \\ d_1 & d_2 & d_3 & d_4 & d_5 & d_6 & d_7 & d_8 & d_9 \\ e_1 & e_2 & e_3 & e_4 & e_5 & e_6 & e_7 & e_8 & e_9 \\ f_1 & f_2 & f_3 & f_4 & f_5 & f_6 & f_7 & f_8 & f_9 \\ g_1 & g_2 & g_3 & g_4 & g_5 & g_6 & g_7 & g_8 & g_9 \\ h_1 & h_2 & h_3 & h_4 & h_5 & h_6 & h_7 & h_8 & h_9 \\ i_1 & i_2 & i_3 & i_4 & i_5 & i_6 & i_7 & i_8 & i_9 \end{pmatrix} \begin{pmatrix} 1 \\ 0 \\ 0 \\ 0 \\ 0 \\ 0 \\ 0 \\ 0 \\ 0 \end{pmatrix} = \begin{pmatrix} 1 \\ 0 \\ 0 \\ 0 \\ 0 \\ 0 \\ 0 \\ 0 \\ 0 \end{pmatrix}$$

Solving this matrix equation, we have, $a_1 = 1$, $b_1 = 0$, $c_1 = 0$, $d_1 = 0$, $e_1 = 0$, $f_1 = 0$, $g_1 = 0$, $h_1 = 0$, $i_1 = 0$.

Similarly, solving the following equations we have the remaining 72 elements. Out of these 72 elements we have, $b_2 = 1$, $c_3 = 1$, $d_6 = 1$, $e_5 = 1$, $f_4 = 1$, $g_7 = 1$, $h_9 = 1$, $i_8 = 1$ and all other elements are zero.

$$Tristate\,CNOT\,|01\rangle = |01\rangle \tag{2}$$

$$Tristate\,CNOT\,\big|0\bar{1}\big\rangle = \big|0\bar{1}\big\rangle \tag{3}$$

$$Tristate\,CNOT\,|10\rangle = |10\rangle \tag{4}$$

$$Tristate\,CNOT\,|11\rangle = |1\bar{1}\rangle \tag{5}$$

$$Tristate\,CNOT\,\big|1\bar{1}\big\rangle = \big|11\big\rangle \tag{6}$$

$$Tristate\,CNOT\,\big|\bar{1}0\big\rangle = \big|\bar{1}1\big\rangle \tag{7}$$

$$Tristate\,CNOT\,\big|\bar{1}1\big\rangle = \big|\bar{1}0\big\rangle \tag{8}$$

$$Tristate\,CNOT\,\big|\bar{1}\bar{1}\big\rangle = \big|\bar{1}\bar{1}\big\rangle \tag{9}$$

Therefore, the gate matrix of quantum optical tristate CNOT gate will be,

$$Tristate\,CNOT = \begin{pmatrix} 1\,0\,0\,0\,0\,0\,0\,0\,0 \\ 0\,1\,0\,0\,0\,0\,0\,0\,0 \\ 0\,0\,1\,0\,0\,0\,0\,0\,0 \\ 0\,0\,0\,0\,0\,1\,0\,0\,0 \\ 0\,0\,0\,0\,1\,0\,0\,0\,0 \\ 0\,0\,0\,1\,0\,0\,0\,0\,0 \\ 0\,0\,0\,0\,0\,0\,1\,0\,0 \\ 0\,0\,0\,0\,0\,0\,0\,0\,1 \\ 0\,0\,0\,0\,0\,0\,0\,1\,0 \end{pmatrix}_{9\times9}$$

Since, $(Tristate\,CNOT)(Tristate\,CNOT)^{\dagger} = I$, tristate CNOT gate shows unitary property.

5   Proposed SOA-Based Frequency Encoded Tristate CNOT Gate

The block diagram of the proposed ultrafast quantum optical tristate CNOT gate with semiconductor optical amplifier (SOA)-based switches is shown in Fig. 3.

A and B are input optical channels that may have either ν_1 or ν_2 or ν_3 frequency of light signal. O_1 and O_2 are output optical channels. ν_1 frequency is encoded for '0' state, ν_2 for '1' state and ν_3 for '$\bar{1}$' state. Light from the input optical channel A is divided into two parts by using a beam splitter BS and one part of it is directly transferred to the output optical channel O_1. Other part is used as a triggering signal which can control the SOA-based logic infrastructure. The output of the SOA-based logic infrastructure appears at the output optical channel O_2 as per the truth table.
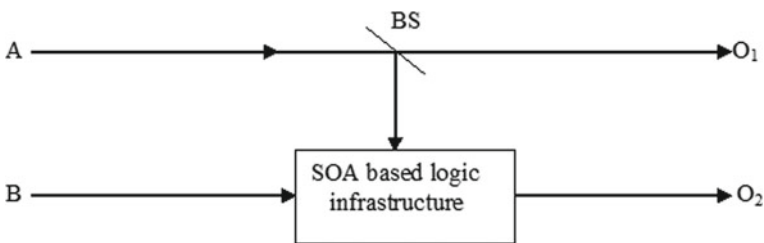

Fig. 3   Block diagram of proposed SOA-based frequency encoded tristate CNOT gate

6 Summary

The proposed scheme is all-optical in nature. So, the system exhibits a strong inherent parallelism and very high speed of operation (above THz). Semiconductor optical amplifier (SOA)-based optical switches like wavelength converters and add/drop multiplexers are used to implement the tristate logic system. The fast-switching speed (order of nanoseconds) of the semiconductor optical amplifier also ensures the superfast speed of operation of the system. The advantage of using the frequency encoding technique is that frequency is the fundamental property of light and it remains unaltered under reflection, refraction, scattering, absorption etc. in a long-haul data communication system. So, bit error rate can be removed easily and also signal to noise ratio remains unchanged at the same time. Again, a large number of data can be handled through a single optical channel. So, cross-talk related problems can be overcome by this encoding technique. It is also easy to represent multibit logic states by the frequency encoding principle. Introduction of contradiction state is another advantage of our proposed scheme and the scheme can be extended to realize multibit logic operations using the same mechanism. In our future work we will develop the complete circuit as stated in Fig. 3.

References

1. Dutta S, Mukhopadhyay S (2012) A new alternative approach of all optical frequency encoded clocked S-R flip-flop exploiting the nonlinear character of semiconductor optical amplifiers. Optik Int J Light Electron Optics 123(22) https://doi.org/10.1016/j.ijleo.2011.10.011
2. Mukhopadhyay S (2010) Role of optics in super-fast information processing. Indian J Phys 84:1069–1074. https://doi.org/10.1007/s12648-010-0101-4
3. Dutta S, Mukhopadhyay S (2010) All optical frequency encoding method for converting a decimal number to its equivalent binary number using tree architecture. Optik Int J Light Electron Optics 122(2):125–127. https://doi.org/10.1016/j.ijleo.2009.11.018
4. Dutta S, Mukhopadhyay S (2011) Alternating approach of implementing frequency encoded all-optical logic gates and flip-flop using semiconductor optical amplifier. Optik Int J Light Electron Optics 122(12):1088–1094. https://doi.org/10.1016/j.ijleo.2010.06.046
5. Saha S, Biswas S, Mukhopadhyay S (2017) Optical scheme of conversion of a positionally encoded decimal digit to frequency encoded Boolean form using Mach-Zehnder interferometer-based semiconductor optical amplifier. IET Optoelectron 11(5):201–207. https://doi.org/10.1049/iet-opt.2016.0078
6. Saha S, Biswas S, Mukhopadhyay S An alternative approach for binary to decimal conversion of frequency encoded optical data using MZI-SOA switch. J Optics https://doi.org/10.1007/s12596-021-00786-9
7. Garai SK (2015) Conversion of intensity encoded binary to frequency encoded data, and its regeneration in optical domain. JAST 1(1) ISSN: 2395–4353
8. Dutta S, Mukhopadhyay S (2012) A new approach of parallel data transmission through optical waveguide with SOA based frequency encoding/decoding technique. Optik Int J Light Electron Optics 123(3):212–216. https://doi.org/10.1016/j.ijleo.2011.02.028

9. Hazra S, Mukhopadhyay S (2020) An all-optical scheme for developing a programmable and integrated Pauli X, Y & Z gate based logic system using phase and frequency encoding principles. In: Proceedings of National Conference on Materials, Devices and Circuits in Communication Technology, 2020, (MDCCT 2020), ISBN: 978–81–955389–3–5. pp. 5–7

10. Mandal M, Mukhopadhyay S (2021) Photonic scheme for implementing quantum square root controlled Z gate using phase and intensity encoding of light. IET Optoelectronics 15(31). https://doi.org/10.1049/ote2.12008

11. Dey S, Mukhopadhyay S (2019) All-optical integrated square root of Pauli-Z (SRZ) gates using polarization and phase encoding. J Optics 48(8). https://doi.org/10.1007/s12596-019-00568-4

12. Dey S, Mukhopadhyay S (2018) Implementation of all-optical Pauli-Y gate by the integrated phase and polarization encoding. IET Optoelectron 12(4):176–179. https://doi.org/10.1049/iet-opt.2017.0138

13. Connelly M (2002) Semiconductor optical amplifiers. Springer Science & Business Media. ISBN: 0–7923–7657–9. https://doi.org/10.1016/B0-12-369395-0/00662-X

14. Dutta NK, Wang Q, Zhu G, Jaques J, Piccirilii AB, Leuthold J (2004) Semiconductor optical amplifiers-functional applications. J Opt 33(4):197–219. https://doi.org/10.1007/BF03354765

15. Wang J, Meloni G, Berrettini G, Poti L, Bogoni A (2010) All-optical clocked flip-flops and binary counting operation using SOA based S-R latch and logic gates. IEEE J Sel Top Quantum Electron 16(5):1486–1494. https://doi.org/10.1109/JSTQE.2009.2039199

16. Guo LQ, Connelly M (2008) A novel approach to all optical wavelength conversion by utilizing a reflective semiconductor optical amplifier in a co-propagation scheme. Optics Commun 281(17):4470–4473. https://doi.org/10.1016/j.optcom.2008.04.054

17. Garai SK, Mukhopadhyay S (2009) Method of implementing frequency encoded multiplexer and demultiplexer systems using nonlinear semiconductor optical amplifiers. Opt Laser Technol 41(8):972–976. https://doi.org/10.1016/j.optlastec.2009.04.005

18. Dai B, Shimizu S, Wang X, Wada N (2013) Simultaneous all-optical half-adder and half-subtractor based on two semiconductor optical amplifiers. IEEE Photonics Technol Lett 25(1):91–93. https://doi.org/10.1109/LPT.2012.2228847

19. Kotb A, Zoiros K, Guo C (2019) 320 Gb/s all-optical XOR gate using semiconductor optical amplifier-Mach Zehnder interferometer and delayed interferometer. Photon Netw Commun 38(1):177–184. https://doi.org/10.1007/s11107-019-00844-0

20. Garai SK (2012) Novel method of designing all optical frequency-encoded Fredkin and Toffoli logic gates using semiconductor optical amplifiers. IET Optoelectron 5(6):247–254. https://doi.org/10.1049/iet-opt.2010.0077

21. Garai SK, Pal A, Mukhopadhyay S (2010) All-optical frequency encoded inversion operation with tristate logic using reflecting semiconductor optical amplifiers. Optik Int J Light Electron Optics 121(16):1462–1465. https://doi.org/10.1016/j.ijleo.2009.02.011

22. Garai SK (2010) A scheme of developing frequency encoded tristate optical logic operations using semiconductor optical amplifier. J Modern Optics 57(6):419–428. https://doi.org/10.1080/09500341003692989

23. Mazlan IZ, Wahid MH, Hasan AF, Azidin MA, Isa NFM (2014) Cross gain modulation (XGM) based on wavelength conversion using semiconductor optical amplifier and filter. Int J Microwave Optic Technol 9(1) https://www.researchgate.net/publication/290274773_Cross_gain_modulation_XGM_based_on_wavelength_conversion_using_semiconductor_optical_amplifier_and_filter

24. Mukhopadhyay S, Dey S, Saha S (2019) Photonics: a dream of modern technology. In: Photonics and fiber optics. CRC Press, pp. 39–66. https://doi.org/10.1201/9780429026584-2

25. Dutta S, Mukhopadhyay S (2010) An all optical approach of frequency encoded NOT based Latch using semiconductor optical amplifier. J Opt 39:39–45

Use of Frequency Encoding Principle for Implementing Nano-Photonic Ultrafast Tristate Pauli X Gate

Ayan Dey and Sourangshu Mukhopadhyay

Abstract Optics has been found significant to take part in Quantum Computation as a carrier signal. In the last few years number of research articles were published where optics is used massively for implementing Quantum gates. In this chapter, an all-optical tristate Pauli X Gate has been designed with SOA-based optical switches using Frequency-encoded principles. Here, this design has three input signals and three output channels as per the requirement of quantum gates. The three input signals have been encoded by a light signal of three different frequencies using the Frequency-encoded principle. This design has been implemented by two Semiconductor optical Amplifier (SOA)-based optical switches to provide a high gain signal at the output channel. In the middle input channel, there is no requirement of SOA. The designed scheme can be treated as a tristate Pauli X Gate i.e., two input signals are cross switched to each other and one input signal is directly carried out. The authors developed a SOA-based tristate Pauli X gate scheme. In this paper, a high intense beam is produced by SOA to obtain a good communication system. The advantages of tristate SOA-based quantum logic gate include ultrafast speed of operation in the order of THz limit as optics is used. The SOA-based Tristate Pauli X gate is all-optical and universal in nature. The advantages of tristate operation in Quantum Computation and that of the frequency-encoding principle are successfully exploited here.

1   Introduction

Quantum logic gates have an important role in various fields of computation and data processing due to very speedy computation, very high information handling capacity, low loss, fast response time and intrinsic Parallelism [1–3]. Quantum computation stands on a natural set of reversible quantum gates. Previously many quantum gates

A. Dey (✉) · S. Mukhopadhyay

Department of Physics, The University of Burdwan, Golapbag, Burdwan, West Bengal 713104, India

e-mail: ayandeybwn@gmail.com

are implemented using optical switches, using electro-optic materials like Kerr and Pockels materials [4]. All optical integrated Pauli's X, Y and Z quantum logic gates are developed using optical switches by Baishali and Mukhopadhyay [5]. Quantum logic gates are implemented by phase, intensity, polarization and frequency-encoding techniques [6]. The implementation of SRCZ (square root of controlled Z) quantum gate by using Lithium niobate-based electro-optic Pockels materials is established where the SRCZ gate works on two-qubit inputs. The benefit of this scheme is such that one can use phase change of the light beam by the proper biasing potential in Pockels material to develop the SRCZ quantum logic gate for very fast operation and also the external biasing potential is adjustable by increasing or reducing the size of the electro-optic (Lithium niobate) Pockels materials [7–14]. Shuvra Dey et al. in their paper established an all-optical Pauli-Y gate by using phase and polarization-encoding techniques together to work on the dibit and tribit mechanism as a replacement of the single qubit mechanism because of high degree of accuracy and sensitivity [15]. All optical NAND logic gate operations are implemented analytically using Squeezed state of light Hence XOR and NOT quantum logic gate operations are proposed by Pal and Mukhopadhyay [16, 17]. All optical NOR and controlled NOR quantum logic gates are implemented and verified by the simulation experiment using Semiconductor Optical Amplifier-based optical switches which act like frequency transformer, add-drop multiplexer and frequency-encoding/decoding system where quantum logic gates can act as a universal logic gate. This was proposed by et al. [18]. The frequency-encoding principle is established as the popular technique which is used in all optical logic gate processers using optical switches like Semiconductor Optical Amplifier (SOA) [19–21]. Saha et al. in their work established an all-optical scheme where the optical transformation from binary to decimal using the frequency-encoding technique is performed and the scheme is implemented by an all–optical non-linear optical switch like MZI-SOA to produce a rapid transformation rate [22–25]. All-optical Tristate Pauli X, Y and Z quantum logic gates are developed using phase-encoding techniques by Electro-optic modulators by Sarfaraj and Mukhopadhyay [26].

The main objectives of this chapter are to design and develop an all-optical tristate Pauli X Gate by using two SOA-based optical switches to provide a high gain of the used signal. The frequency-encoding principle based-logic operation is used here. The SOA-based all–optical tristate Pauli X gate is established here in such a way that it can act as a universal logic gate. In the proposed tristate logic system, the speed of operation is extremely high (~THZ limits) and here, it is beneficial in the field of Quantum Computing.

2   Tristate Logic System

Tristate Pauli X, Y and Z quantum logic gates are advantageous in the Quantum computing field. Tristate Pauli X, Y and Z gates are realized in 3×3 matrices. Within the tristate logic system, the quantum state is presented by 3×1 column

matrices specified by $\begin{pmatrix} C_0 \\ C_1 \\ C_2 \end{pmatrix}$ [27, 28]. Few years ago, an all-optical integrated Pauli X, Y and Z gate arrangements with a single bit information system was proposed.

$$\text{Pauli X matrix in Tristate (X)} = \begin{pmatrix} 0\ 0\ 1 \\ 0\ 1\ 0 \\ 1\ 0\ 0 \end{pmatrix}$$

$$\text{Pauli Y matrix in tristate (Y)} = \begin{pmatrix} 0\ 0\ -i \\ 0\ 1\ 0 \\ i\ 0\ 0 \end{pmatrix} \text{ and}$$

$$\text{Pauli Z matrix in tristate (Z)} = \begin{pmatrix} 1\ 0\ 0 \\ 0\ 1\ 0 \\ 0\ 0\ -1 \end{pmatrix}$$

In general one can describe tristate Pauli X, Y and Z gates to show the input to output transformation.

For tristate Pauli X gate, matrix representation is

$$\begin{pmatrix} 0\ 0\ 1 \\ 0\ 1\ 0 \\ 1\ 0\ 0 \end{pmatrix} \begin{pmatrix} C_0 \\ C_1 \\ C_2 \end{pmatrix} = \begin{pmatrix} C_2 \\ C_1 \\ C_0 \end{pmatrix}$$

The requirement for the unitary matrix is fulfilled here, as it is essential in quantum computing.

The tristate Pauli X matrix is unitary in nature i.e., $X^\dagger = \begin{pmatrix} 0\ 0\ 1 \\ 0\ 1\ 0 \\ 1\ 0\ 0 \end{pmatrix} = X$ and

$$XX^\dagger = \begin{pmatrix} 0\ 0\ 1 \\ 0\ 1\ 0 \\ 1\ 0\ 0 \end{pmatrix} \begin{pmatrix} 0\ 0\ 1 \\ 0\ 1\ 0 \\ 1\ 0\ 0 \end{pmatrix} = \begin{pmatrix} 1\ 0\ 0 \\ 0\ 1\ 0 \\ 0\ 0\ 1 \end{pmatrix} = I$$

where, "**I**" is represented as a 3×3 identity matrix.

Tristate Pauli X gate matrix has a reversible character like other quantum logic gates. Due to the reversible characteristics, the Tristate Pauli X gate matrix keeps getting back to the initial state by two step actions as shown below.

$$\begin{pmatrix} 0\ 0\ 1 \\ 0\ 1\ 0 \\ 1\ 0\ 0 \end{pmatrix} \begin{pmatrix} C_0 \\ C_1 \\ C_2 \end{pmatrix} = \begin{pmatrix} C_2 \\ C_1 \\ C_0 \end{pmatrix}$$

$$\begin{pmatrix} 0 & 0 & 1 \\ 0 & 1 & 0 \\ 1 & 0 & 0 \end{pmatrix} \begin{pmatrix} C_2 \\ C_1 \\ C_0 \end{pmatrix} = \begin{pmatrix} C_0 \\ C_1 \\ C_2 \end{pmatrix}$$

Both the unitary and reversible characteristics are satisfied in the tristate operation.

Similarly, the all-optical tristate Pauli Y and Z gate matrices obey the characteristics of unitary matrices in nature and the reversible characteristics of quantum logic gates also satisfy the tristate operation [25].

Tristate Pauli X gate includes three input channels I_1, I_2 and I_3 and three output channels O_0, O_1 and O_2, respectively. In this scheme, the three input signals C_0, C_1 and C_2 are encoded by three frequencies of light signals v_1, v_2 and v_3. The scheme is performed in such a way that two input signals swap each other keeping the middle input signal intact.

3 Semiconductor Optical Amplifier (SOA) as an Ultrafast Optical Switch

The Semiconductor Optical Amplifier behaves as an optical switch which works with the non-linear properties of some medium. The non-linear medium works on the carrier generation i.e., electron–hole pair generation. The non-linearity can be seen in the refractive index of the GaAs material. The refractive index is changed when the excitation of electrons is increased by photon energy absorption. Due to the current injection, the optical gain modulation continuously varies with the change of refractive index of the non-linear medium [29, 30]. The characteristics of electron–hole pair generation and fast pulse signal count are satisfied such that the Semiconductor Optical Amplifier (SOA) can act as an ultrafast optical switch. Four different types of non-linear operation are observed in Semiconductor Optical Amplifier (SOA)-based optical switches which are cross gain modulation (XGM), cross phase modulation (XPM), self phase modulation (SPM) and four wave mixing (FWM). In the XGM process, two optical signals i.e., one is a pump beam of frequency v_1 and another is a probe beam of frequency v_2 are received. The amplitude (intensity) and power of the pump beam is high and the amplitude (intensity) and power of the probe beam is low. When the pump beam (v_1) and the probe beam (v_2) are injected jointly into the SOA, then the gain of the probe beam (v_2) is amplified and the gain of the pump beam (v_1) is reduced when passing through into the SOA. The gain of the probe beam (v_2) becomes greater than the pump beam (v_1). The condition of frequency conversion is fulfilled by shifting of information from the pump to the probe beam by the cross gain modulation process of SOA. In the present proposed scheme, XGM type non-linearity of Semiconductor Optical Amplifier (SOA) is used. The whole system is shown in Fig. 1.

Fig. 1 Frequency conversion from pump to probe by XGM process of SOA

4   SOA-Based Tristate Pauli X Gate
with Frequency-Encoding Principle

In this scheme of Conversion the input C_0 is encoded by a light signal of frequency v_1 (Corresponding to wavelength λ_1), input C_1 is encoded by a light signal frequency v_2 (Corresponding to Wavelength λ_2) and Input C_2 is encoded by a light signal frequency v_3 (Corresponding to Wavelength λ_3), which is shown in Table 1. The whole scheme is constructed with two SOA (Semiconductor optical amplifier) switches (shown in Fig. 2). Here, we have three input channels marked as I_1, I_2 and I_3 and three output channels marked as O_0, O_1 and O_2, respectively, are used (the qubit wise truth table is shown in Table 2).The input $C_0(v_1)$ is divided in two parts by using a proper beam splitter so that, one part is applied as a pump beam (amplitude high) and the another part is used as a probe beam (amplitude low). Similarly, the input $C_2(v_3)$ is divided in two parts, one part is used as a pump beam (amplitude high) and the other part is applied as a probe beam (amplitude low); to do this a proper beam splitter is used. For the input signal $C_1(v_2)$, no SOA is needed and the input signal $C_1(v_2)$ is directly carried out at the output O_1. As a result at output O_1, one can get the same input signal beam $C_1(v_2)$ as the output signal. When the pump beam of the input signal $C_0(v_1)$ and probe beam of the input signal $C_2(v_3)$ are injected jointly into the SOA1, and in this situation, the pump signal $C_0(v_1)$ will force the probe signal $C_2(v_3)$ to be amplified at the output. So, the amplitude of the input $C_2(v_3)$ becomes greater than the amplitude of the pump beam $C_0(v_1)$ by the cross gain modulation(XGM) process. As a result, the amplitude of the input signal $C_0(v_1)$ will converted to the amplitude of another input signal $C_2(v_3)$ with a single frequency from the SOA1 because of its XGM character. Here, at output O_0, one can get the amplified probe beam $C_2(v_3)$. Similarly, when the pump beam of the input $C_2(v_3)$ and probe beam of the input $C_0(v_1)$ are injected jointly into the SOA2, and in this situation, the pump signal $C_2(v_3)$ will force the probe signal $C_0(v_1)$ to reach to the output O_2 being amplified. So, the amplitude of the input $C_0(v_1)$ becomes greater than the amplitude of the pump beam $C_2(v_3)$ by the cross gain modulation(XGM) process. Here, at the output O_2, one can get the amplified probe beam $C_0(v_1)$. Basically when the input pump signal is $C_0(v_1)$ then the output intense signal is $C_2(v_3)$ and when the input pump signal is $C_2(v_3)$ then the output intense signal is $C_0(v_1)$ due to the cross gain modulation(XGM) process. On the other side, the input pump signal beam of the upper region $C_0(v_1)$ is switched to the output channel of the lower region O_2 and the input pump signal beam of the lower region $C_2(v_3)$ is switched to the output channel of the upper region O_0 i.e., the input signal of the upper region $C_0(v_1)$ and

Table 1 Truth table of tristate Pauli X gate when all input are encoded by frequency of light using Frequency-encoded principle

Inputs			Outputs		
I_1	I_2	I_3	O_0	O_1	O_2
v_0	v_1	v_2	v_2	v_1	v_0
v_2	v_1	v_0	v_0	v_1	v_2
v_0	v_2	v_1	v_1	v_2	v_0
v_1	v_2	v_0	v_0	v_2	v_1
v_1	v_0	v_2	v_2	v_0	v_1
v_2	v_0	v_1	v_1	v_0	v_2

the input signal of the lower region $C_2(v_3)$ are cross swapped to each other at the outputs O_2 and O_0 respectively and the middle input signal beam $C_1(v_2)$ is directly carried out at the middle output channel O_1 and one can get the same input signal $C_1(v_2)$ as the output signal. The whole scheme of Pauli X-gate described in Fig. 2 can be implemented by a Nano-Photonic system as shown in Fig. 3.
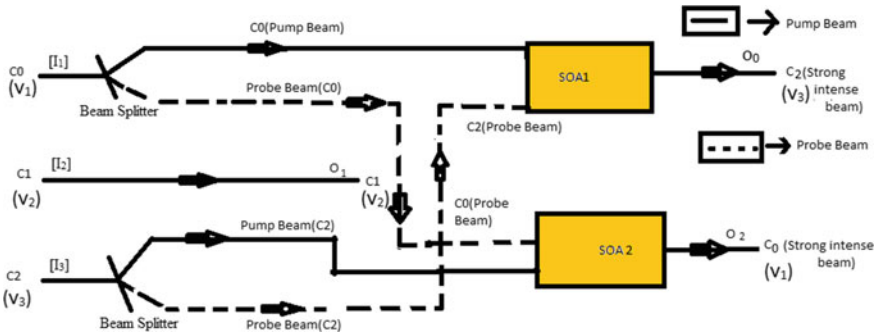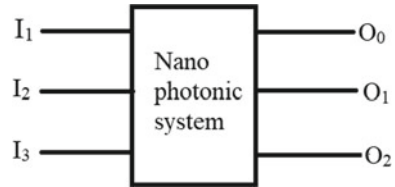

Fig. 2 Schematic layout of an all-optical tristate Pauli X Gate using SOA

Table 2 Truth table of tristate Pauli X gate (Q bit wise)

Inputs			Outputs		
I_1	I_2	I_3	O_0	O_1	O_2
C_0	C_1	C_2	C_2	C_1	C_0
C_2	C_1	C_0	C_0	C_1	C_2
C_0	C_2	C_1	C_1	C_2	C_0
C_1	C_2	C_0	C_0	C_2	C_1
C_1	C_0	C_2	C_2	C_0	C_1
C_2	C_0	C_1	C_1	C_0	C_2

Fig. 3 Frequency encoded nano-photonic system for implementing Quantum optical Pauli X gate

5 Summary

It is clear from the above scheme that the designed scheme can execute the tristate Pauli X gate by the frequency-encoding technique using Semiconductor Optical Amplifier (SOA)-based optical switches. The whole scheme is all-optical in nature. Using the Semiconductor Optical Amplifier (SOA), we get a high gain pulse at the output for a very good strong communication system. The advantages of tristate operation in quantum computing and the performance of the tristate device are superfast in order for THZ to limit. In our future work, the all-optical tristate Pauli X gate should be implemented and verified by a simulated experiment and analyzed by Finite-Difference Time-Domain (FDTD) and Plane Waves Expansion (PWE) methods. Simulation result is expected to be the validation of the truth tables shown in Tables 1 and 2.

References

1. Lloyd S (1995) Almost any quantum logic gate is universal. Phys Rev Lett 75:346
2. Sleator T, Weinfurter H (1995) Realizable universal quantum logic gates. Phys Rev Lett 74:4087
3. Fox AM, Fox M (2006) Quantum optics: an introduction, vol. 15. Oxford university press
4. Wang C, Zhang M, Chen X, Bertrand M, Shams-Ansari A, Chandrasekhar S (2018) Integrated lithium niobate electro-optic modulators operating at CMOS-compatible voltages. Nature 562:101–104
5. Sarkar B, Mukhopadhyay S (2017) An all optical scheme for implementing an integrated Pauli's X, Y and Z quantum gates with optical switches. J Optics 46:143–148
6. Mandal M, Goswami I, Mukhopadhyay S (2022) Implementation of programmable photonic one qubit quantum gates using intensity and phase encoding jointly. J Optics
7. Mandal M, Mukhopadhyay, S (2021) Photonic scheme for implementing quantum square root controlled Z gate using phase and intensity encoding of light. IET Optoelectron https://doi.org/10.1049/ote2.12008
8. Dey S, Mukhopadhyay S (2017) Approach of implementing phase encoded quantum square root of NOT gate. Electron Lett https://doi.org/10.1049/el.2017.2500
9. Goswami I, Mandal M, Mukhopadhyay S (2022) Alternative study of using electro-optic Pockels cell for massive reduction in the intensity of central frequency by multi-passing technique. J Optics 51:379–385

10. Lakshan S, Mukhopadhyay S (2022) All-optical method for measuring the electrical parameters of passive electronic elements with active use of pockels cells. J Optics
11. Lakshan S, Mukhopadhyay S (2022) Pockels cells-based intensity modulation using multiple biasing signals on a single-carrier light beam. J Optics 51:283–288
12. Lakshan S, Mukhopadhyay S Intensity and voltage controlled phase switching of light by joint effort of Kerr and Pockels material, vol. 258. Springer Proceedings in Physics, pp 691–694
14. Lakshan S, Mukhopadhyay S (2019) Optical scheme of obtaining highest transmission factor in case of KDP based electro-optic crystal by the adjustment of suitable biasing voltage and number of feedback passing. J Optic Commun
14. Mandal M, Mukhopadhyay S (2020) Analytical investigation to achieve the highest phase difference between two orthogonal components of light in lithium niobate based electro-optic system. Optoelectron Lett 16:338–342
15. Dey S, Mukhopadhyay S (2018) Implementation of all-optical Pauli-y gate by the integrated phase and polarisation encoding. IET Optoelectron https://doi.org/10.1049/iet-opt.2017.0138
16. Pal SK, Mukhopadhyay S (2011a) Analytical approach of using squeezed state formation of light for conducting all-optical noise free NAND logic operation. Optik 122(21):1943–1946
17. Pal SK, Mukhopadhyay S (2011b) Analytical approach of using the squeezed state formation of light for conducting all-optical noise free XOR and NOT logic operation. Optik 122(5):411–414
18. Sarkar PP, Satpati B, Mukhopadhyay S (2013) New simulative studies on performance of semiconductor optical amplifier based optical switches like frequency converter and add-drop multiplexer for optical data processors. J Optics 42:360–366
19. Pal SK, Mukhopadhyay S (2013) Analytical approach of using squeezed state formation of light for developing a highly noise reduced all-optical 1-bit memory cell. Optik 124(1):91–93
20. Dutta S, Mukhopadhyay S (2011) Alternating approach of implementing frequency encoded all-optical logic gates and flip-flop using semiconductor optical amplifier. Optik 122(12):1088–1094
21. Dutta S, Mukhopadhyay S (2010) An all optical approach of frequency encoded NOT based Latch using semiconductor optical amplifier. J Optics 39:39–45
22. Saha S, Biswas S, Mukhopadhyay S (2022) An alternative approach for binary to decimal conversion of frequency encoded optical data using MZI-SOA switch. J Optics 51:357–370
23. Saha SP, Mukhopadhyay S (2020) All optical frequency encoded quaternary memory unit using symmetric configuration of MZI-SOA. Optics Laser Technol 131:106386
24. Saha S, Biswas S, Mukhopadhyay S (2017) Optical scheme of conversion of a positionally encoded decimal digit to frequency encoded Boolean form using Mach–Zehnder interferometer-based semiconductor optical amplifier. IET Optoelectronics 2017. https://doi.org/10.1049/iet-opt.2016.0078
25. Reis C, Dionisio RP, Neto B, Teixeira A, Andre P (2010) All-optical XOR based on integrated MZI-SOA with co- and counter-propagation scheme. In: 2009 3rd ICTON Mediterranean Winter Conference (ICTON-MW). IEEE https://doi.org/10.1109/ICTONMW.2009.5385613
26. Sarfaraj MN, Mukhopadhyay S (2021) All-optical scheme for implementation of tri-state Pauli-X, Y and Z quantum gates using phase encoding. Optoelectron Lett 17:746–750
27. Garai SK, Pal A, Mukhopadhyay S (2010) All-optical frequency-encoded inversion operation with tristate logic using reflecting semiconductor optical amplifiers. Optik 121(16):1462–1465
28. Garai SK (2010) A scheme of developing frequency encoded tristate-optical logic operation using semiconductor optical amplifier. J Modern Optics 57(6)
29. Nakamura S, Tajima K, Sugimoto Y (1994) 10 ps all-optical switching in novel Mach–Zehnder configuration based on band-filling nonlinearity of GaAs. In: Conference on Lasers and Electro-Optics (CELO'94), CThS2
30. Tajima K (1993) All-optical switch with switch-off time unrestricted by carrier lifetime. Jpn J Appl Phys 32:L1746–L1749